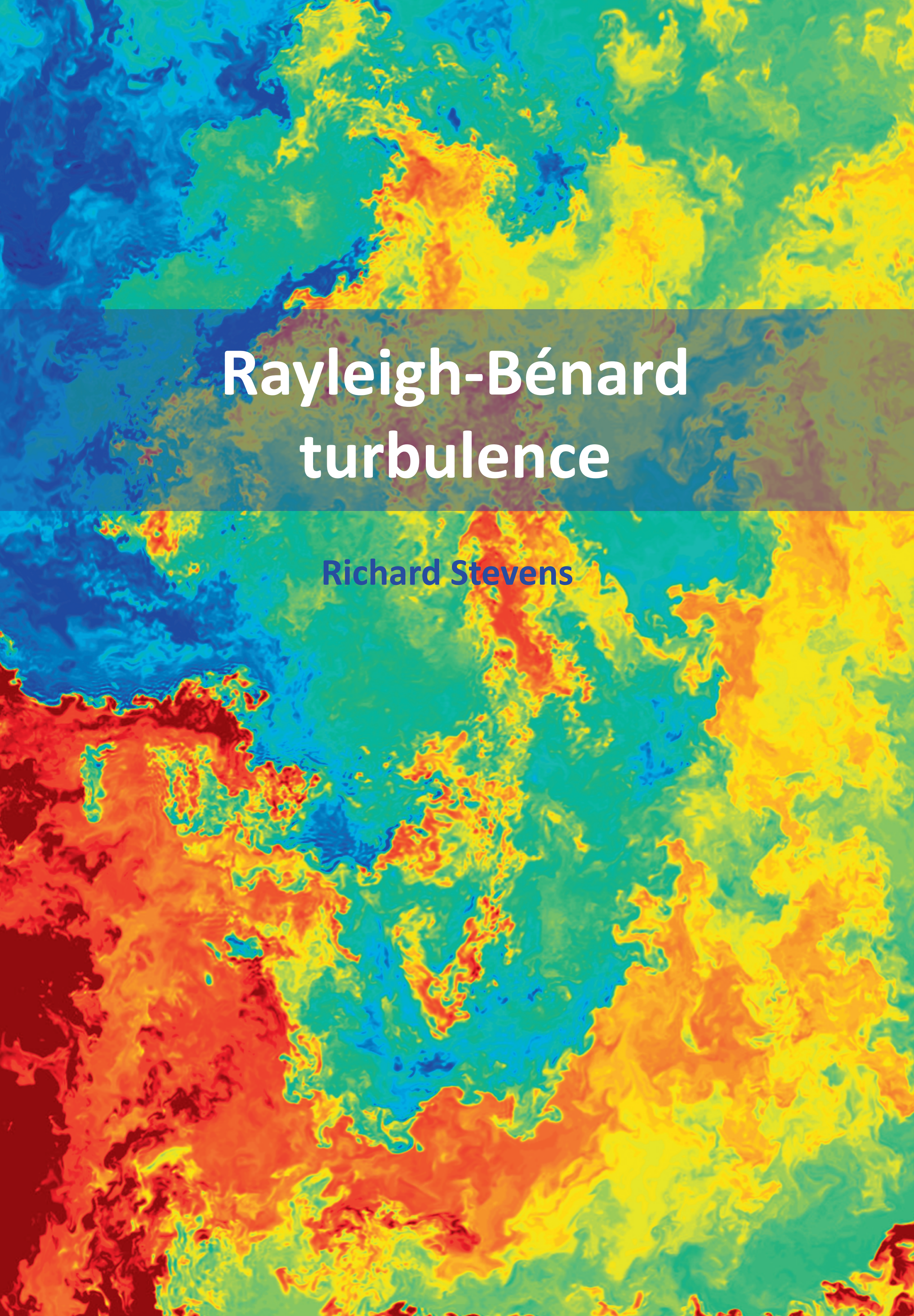

Rayleigh-Bénard turbulence

Richard Stevens

Rayleigh-Bénard turbulence

Richard Johannes Antonius Maria Stevens

Samenstelling promotiecommissie:

Prof. dr. Bene Poelsema (voorzitter)	Universiteit Twente
Prof. dr. Detlef Lohse (promotor)	Universiteit Twente
Prof. dr. Herman Clercx (promotor)	Universiteit Eindhoven & Twente
Prof. dr. GertJan van Heijst	Universiteit Eindhoven
Prof. dr. Guenter Ahlers	Universiteit van California at Santa Barbara
Prof. dr. Roberto Verzicco	Universiteit Twente & Rome
Prof. dr. dr. h. c. Siegfried Grossmann	Universiteit Marburg
Prof. dr. Bernard Geurts	Universiteit Twente

The work in this thesis was carried out at the Physics of Fluids group of the Faculty of Science and Technology of the University of Twente. It is part of the research programme of the Foundation for Fundamental Research on Matter (FOM), which is financially supported by the Netherlands Organisation for Scientific Research (NWO).

Nederlandse titel:
Rayleigh-Bénard turbulentie

Cover design: Menno Bokdam
Front cover - Visualization of the instantaneous temperature field for a direct numerical simulation at $Ra = 2 \times 10^{12}$ and $Pr = 0.7$ in an aspect ratio $\Gamma = 0.5$ sample, see figure 3.1.

Publisher:
Richard Stevens, Physics of Fluids, University of Twente,
P.O. Box 217, 7500 AE Enschede, The Netherlands
pof.tnw.utwente.nl

Print: Gildeprint B.V., Enschede

ISBN: 978-90-365-3203-7

RAYLEIGH-BÉNARD TURBULENCE

PROEFSCHRIFT

ter verkrijging van
de graad van doctor aan de Universiteit Twente,
op gezag van de rector magnificus,
Prof. dr. H. Brinksma,
volgens besluit van het College voor Promoties
in het openbaar te verdedigen
op donderdag 30 juni 2011 om 16:45 uur

door

Richard Johannes Antonius Maria Stevens

geboren op 15 November 1984

te Nijmegen

Dit proefschrift is goedgekeurd door de promotoren:

Prof. dr. rer. nat. Detlef Lohse
Prof. dr. Herman J.H. Clercx

Contents

1

Introduction

1.1 Conceptual beauty and relevance

Rayleigh-Bénard (RB) convection, i.e. the flow of a fluid heated from below and cooled from above, is the classical system to study thermally driven turbulence in confined space. It played a crucial role in the development of stability theory in hydrodynamics [1, 2] and had been paradigmatic in pattern formation and in the study of spatial-temporal chaos [3, 4]. The beauty of the system is that on one hand it is mathematically very well-defined, namely by the extended Navier Stokes equations with its appropriate boundary conditions, and can thus be analyzed in numerical simulations and theoretical studies. On the other hand, the system is easily accessible in experiments. Hence, RB convection is very well suited to test new techniques and concepts in Physics of Fluids. For this system, experiments, numerical simulations, and theoretical analysis are complementary: A combination of these techniques is mandatory to get a better understanding of the system.

Buoyancy-driven flow also plays a role in many natural phenomena and technological applications. In most cases the density differences within the fluid are due to temperature differences. In addition, there are many cases in which the fluid flow is affected by rotation, for example, in geophysical flows, astrophysical flows, and flows in technology.

On Earth, many large-scale fluid motions are driven by temperature-induced buoyancy, while the length scales of these phenomena are large enough to be influenced by the Earth's rotation. Key examples include the convection in the atmosphere [5] and oceans [6], including the global thermohaline circulation [7]. These natural phenomena are crucial for the Earth's climate. It is for example argued that the thermohaline circulation can have different distinct states and models show that the transitions between these states can be very sudden when a certain threshold is passed. There is evidence that past shutdowns of the circulation drastically cooled the climate all around the North Atlantic in a matter of years by stalling the current that brings warm water northwards [8, 9].

The interplay between rotation and convection has also been very important in human history, as this interplay causes the trade winds [10]. For centuries the trade winds were used to cross the world's oceans. They made the trade routes across the Atlantic and Pacific oceans possible and enabled the expansion of the European empire into the Americas. Nowadays, these winds are an important ingredient in weather prediction models as these winds act as a steering flow for tropical storms that form over the Atlantic, Pacific, and Southern Indian Oceans, before they make landfall in North America, Southeast Asia, and India, respectively. Similar zonal flows can be found on other planets in our solar system, for example on Neptune, Uranus, Saturn, and Jupiter [11, 12], although it is not known whether these are driven by convection alone. Rotating convection also plays a significant role in the spontaneous reversals of the Earth's magnetic field that protects the Earth from dangerous solar winds [13]. During reversals the strength of this magnetic field can decrease significantly, due to which solar winds can damage life and electronic equipment on Earth [14].

Knowledge about the influence of rotation on thermal convection is also important for the optimization of various industrial applications. Examples include the convective cooling in turbomachinery [15], and the efficient separation of carbon dioxide (CO_2) from nitrogen or methane gas. This efficient separation of CO_2 is one of the central processes in the energy context: This holds both for the separation of CO_2 from nitrogen in the emission gases of conventional carbon-based power plants to enable the long term storage of CO_2 and for the separation of CO_2 from methane gas in gas exploration fields. In both cases the method of choice is pressurization and cooling down of the gas mixture so that finally CO_2 condensates into droplets and can be separated in a centrifuge or in so-called rotational phase separators (RPS), which recently have been developed [16]. Due to the droplet condensation, considerable heat transfers emerge in this process which are strongly affected by rotation. It is therefore crucial to understand the effect of rotation on heat transfer within turbulent flow.

Hence, rotating RB convection, which is discussed in detail in part II of this thesis, is a relevant model for many geophysical, astrophysical, and industrial flows and the results can be used to better understand the basic physics of these problems.

The strength of the driving in RB convection is indicated by the Rayleigh number Ra, which indicates the dimensionless temperature difference in the system. In the beginning of the twentieth century a theoretical analysis of Lord Rayleigh [17] showed that the critical *Ra* number for the onset of convection is 1708. This analysis confirmed the earlier experimental results of Henry Bénard [18, 19]. In these experiments Bénard observed that just above the onset of convection a regular pattern of hexagonal convection cells is formed. A further increase in *Ra*, and thus in the driving of the system, first leads to time-dependent flow, chaotic time dependence, and eventually turbulence. All examples given above are in the turbulent regime, where the *Ra* number becomes very high. To understand this high *Ra* number regime better we study it in direct numerical simulations (DNS) in part I of this thesis, where the simulation results will be compared with experimental results from other groups. We emphasize again that numerical simulations and experiments on RB convection are complementary, because different aspects of the problem can be addressed. Namely, in accurate experimental measurements of the heat transfer a completely isolated system is needed. Therefore, one cannot visualize the flow while the heat transfer is measured. On the positive side, in experiments one can obtain very high *Ra* numbers and long time averaging. In DNS, on the other hand, one can simultaneously measure the heat transfer while the complete flow field is available for analysis. But the *Ra* number that can be obtained in simulations is lower than in experiments, due to the computational power that is needed to fully resolve the flow. Hence, a combination of experimental and numerical work is required to further improve our understanding of RB convection.

A way to simplify the sometimes difficult analysis of complex three-dimensional (3D) flows is to look at the two-dimensional (2D) analogue. In part III of this thesis we analyze the flow in the boundary layers, i.e. the flow close to the walls, in 2D RB simulations and experiments. In addition, we will look into the mechanism behind spontaneous flow reversals, which offers us insight to better understand similar spontaneous flow transitions in nature, such as the spontaneous reversals of the Earth's magnetic field.

In the next section we will introduce some general aspects of RB convection, that will be used throughout this thesis. After this general introduction we will give a detailed introduction to each part of this thesis.

1.2 Rayleigh-Bénard convection

1.2.1 Dimensionless parameters

There have been many investigations of non-rotating RB convection and a comprehensive summary of all this work is given in the review papers by Ahlers, Grossmann & Lohse [20] and Lohse and Xia [21]. For not too large temperature gradients, the system is usually described by the Oberbeck-Boussinesq approximation [22–24] in which the fluid density ρ is assumed to depend linearly on the temperature T,

$$\rho(T) = \rho(T_0)\left[1 - \beta(T - T_0)\right], \tag{1.1}$$

where β is the thermal expansion coefficient and T_0 is some reference temperature. In addition, it is assumed that the material properties of the fluid such as β, the viscosity ν, and the thermal diffusivity κ do not depend on temperature. The governing equations of the RB problem are then the Oberbeck-Boussinesq equations. When we take the z-axis parallel to gravity these equations read

$$\frac{\partial \mathbf{u}}{\partial t} + \mathbf{u} \cdot \nabla \mathbf{u} = -\nabla p + \nu \nabla^2 \mathbf{u} + \beta g \theta \hat{z}, \tag{1.2}$$

$$\frac{\partial \theta}{\partial t} + \mathbf{u} \cdot \nabla \theta = \kappa \nabla^2 \theta \tag{1.3}$$

for the velocity field $\mathbf{u}$, the kinematic pressure field p, and the temperature field θ relative to some reference temperature. Note that $\rho(T_0)$ has been absorbed in the pressure term. In addition to the Oberbeck-Boussinesq equations we have the continuity equation ($\nabla \cdot \mathbf{u} = 0$). A no-slip ($\mathbf{u} = 0$) velocity boundary condition is assumed at all the walls. Moreover, the hot bottom and the cold top plate are at a constant temperature, and no lateral heat flow is allowed at the sidewalls.

Within the Oberbeck-Boussinesq approximation and for a given cell geometry, the dynamics of the system is determined by two dimensionless control parameters, namely, the Rayleigh number

$$Ra = \frac{\beta g \Delta L^3}{\kappa \nu}, \tag{1.4}$$

where g is the gravitational acceleration, $\Delta = T_b - T_t$ the difference between the imposed temperatures T_b and T_t at the bottom and the top of the sample, respectively, and the Prandtl number

$$Pr = \frac{\nu}{\kappa}. \tag{1.5}$$

The cell geometry is described by its shape and an aspect ratio. All 3D cells considered in this thesis are cylindrical cells with aspect ratio $\Gamma = D/L$, where D is the cell diameter of the sample, and L is its height. For 2D cells the aspect-ratio is $\Gamma = w/L$, where w is the width of the RB cell. The key response of the system is the heat flux from bottom to top. The dimensionless heat flux is defined as

$$Nu = \frac{QL}{\lambda \Delta}, \tag{1.6}$$

where Q is the heat-current density and λ the thermal conductivity of the fluid in the absence of convection. Within the Oberbeck-Boussinesq approximation one obtains for incompressible flow

$$Nu = \frac{\langle u_z \theta \rangle_{A,t} - \kappa \partial_3 \langle \theta \rangle_{A,t}}{\kappa \Delta L^{-1}}. \tag{1.7}$$

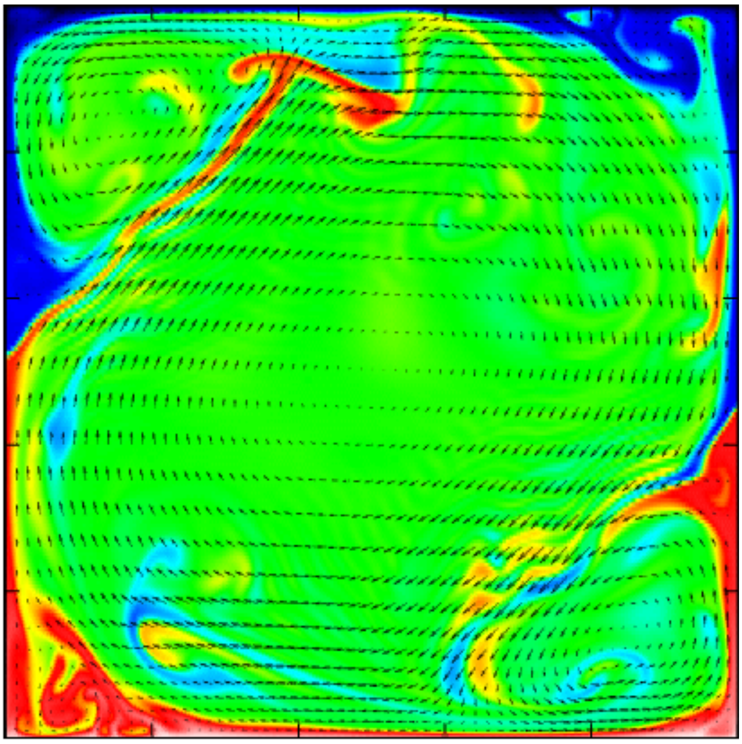

Figure 1.1: Visualization of the large scale circulation in 2D RB convection for $Ra = 10^9$ and $Pr = 4.38$. Here red indicates warm upflowing fluid and blue cold downflowing fluid. The vectors indicate the velocity field. See also part III of this thesis.

Here $\langle \cdot \rangle_{A,t}$ denotes the average over any horizontal plane and over time, and ∂_3 the spatial derivative in vertical direction.

The second key system response is the extent of turbulence, expressed in terms of a characteristic velocity amplitude U, non-dimensionalized by ν/L to define a Reynolds number

$$Re = \frac{UL}{\nu}. \tag{1.8}$$

There are various reasonable possibilities to choose a velocity, e.g., the components or the magnitude of the velocity field at different positions, local or averaged amplitudes, etc. Of particular interest is the velocity and the dynamic behavior of the large scale circulation (LSC), which is a domain filling circulation cell that is spontaneously generated in the fluid, see figure 1.1 for 2D Rayleigh-Benard convection.

1.2.2 The Grossmann-Lohse theory

The heat transfer in a non-rotating RB system can satisfactorily be described by the Grossmann-Lohse (GL) theory [25–28]. The basis of this theory is a set of two exact relations for the kinematic and thermal energy dissipation rates ε_u and ε_θ, respectively, namely

$$\varepsilon_u \equiv \nu\langle(\nabla\mathbf{u})^2\rangle_{V,t} = \frac{\nu^3}{L^4}(Nu-1)RaPr^{-2}, \tag{1.9}$$

$$\varepsilon_\theta \equiv \kappa\langle(\nabla\theta)^2\rangle_{V,t} = \kappa\frac{\Delta^2}{L^2}Nu. \tag{1.10}$$

Here $\langle\cdot\rangle_{V,t}$ indicates that volume and time averages are taken. The central idea of the theory is to split the volume averaged kinetic and thermal dissipation rate into the respective bulk and boundary layer contributions,

$$\varepsilon_u = \varepsilon_{u,BL} + \varepsilon_{u,bulk}, \tag{1.11}$$

$$\varepsilon_\theta = \varepsilon_{\theta,BL} + \varepsilon_{\theta,bulk}. \tag{1.12}$$

The motivation for this splitting is that the physics of the bulk and the boundary layer contributions to the dissipation rate is fundamentally different and thus the corresponding contributions must be modeled differently. Furthermore, the GL theory assumes that there exists a large scale circulation, which defines a Reynolds number $Re = UL/\nu$, and that the boundary layers behave, at least scalingwise, as is described by the laminar Prandtl-Blasius boundary layer theory for flow over an infinitely long flat plate, see section 1.2.3. The assumption that the kinetic and thermal dissipation rate can be splitted as indicated in equation (1.11) and (1.12 means that there are four different turbulent regimes, namely regime I in which both ε_u and ε_θ are dominated by the BL contribution, regime II in which ε_u is dominated by $\varepsilon_{u,bulk}$ and ε_θ by $\varepsilon_{\theta,BL}$, regime III in which ε_u is dominated by $\varepsilon_{u,BL}$ and ε_θ by $\varepsilon_{\theta,bulk}$, and regime IV in which both ε_u and ε_θ are dominated by their bulk contributions. The main result of the GL model is a set of equations, which describes $Nu(Ra,Pr)$ and $Re(Ra,Pr)$. Over the years the predictions resulting from this theory have shown to be very reliable. For a more detailed summary of the GL theory we refer to section II B of Ref. [20].

1.2.3 Prandtl-Blasius boundary layer theory

One of the basic assumptions of the GL-model is that the boundary layers in RB convection, at least scalingwise, behave as is described by the Prandtl-Blasius boundary layer theory for flow over an infinitely long flat plate. Discussions about the Prandtl-Blasius boundary layer theory can be found in several textbooks like, Loitsianski and Szablewski [29], Schlichting [30], Landau and Lifshitz [24], Guyon [31], and Kundu [32]. A detailed discussion of the Prandtl-Blasius boundary layer theory will be given in chapter 4. Here it suffices to say that according to the Prandtl-Blasius boundary layer theory the kinetic boundary layer thickness scales as

$$\frac{\lambda_u}{L} = aRe^{-1/2}, \tag{1.13}$$

where a is a dimensionless prefactor of order one, and the thermal boundary layer thickness scales as

$$\frac{\lambda_\theta}{L} \sim Re^{-1/2}Pr^{-1/2} \quad \text{for } Pr \ll 1, \tag{1.14}$$

$$\frac{\lambda_\theta}{L} \sim Re^{-1/2}Pr^{-1/3} \quad \text{for } Pr \gg 1. \tag{1.15}$$

Meanwhile it is well known [20] that most RB experiments and all RB simulations are in the regime where the kinetic boundary layers are expected to be governed by laminar flow dynamics. The experiments of Sun, Cheung & Xia [33] have found that, despite the intermittent emission of plumes, the Prandtl-Blasius type laminar boundary layer description is indeed a good approximation, in a time-averaged sense, both in terms of its scaling and its various dynamical properties. In order to further verify that the boundary layers in RB convection indeed behave as is described by the Prandtl-Blasius theory we will investigate the boundary layer profiles over a wide range of *Ra* and *Pr* numbers in chapter 13. Here we will use the method introduced by Zhou & Xia [34] to study the boundary layer profiles in the time dependent reference frame. The result of this analysis will show that the kinetic and thermal boundary layer profiles in RB convection are indeed well described by the Prandtl-Blasius boundary layer theory. In chapter 4 we will use this theory to derive a theoretical estimate for the minimum number of computational nodes that should be placed inside the thermal and kinetic boundary layers close to the horizontal plates in a DNS. The results from this analysis will be used throughout this thesis to check the numerical resolution of the presented simulations.

1.3 Guide through the thesis

This thesis contains three main parts. In part I we will study the results from high *Ra* number DNSs in cylindrical samples. In part II we will consider the effect of rotation on turbulent thermal convection both with experiments and DNSs and in part III we will study 2D RB convection, again both with experiments and DNSs. We will now give a more comprehensive introduction to the three part of this thesis.

1.3.1 Part I - High Rayleigh number thermal convection

The very high *Ra* number regime is of interest for astrophysical and geophysical applications, where *Ra* numbers can easily reach values of $Ra = 10^{20}$. However, the

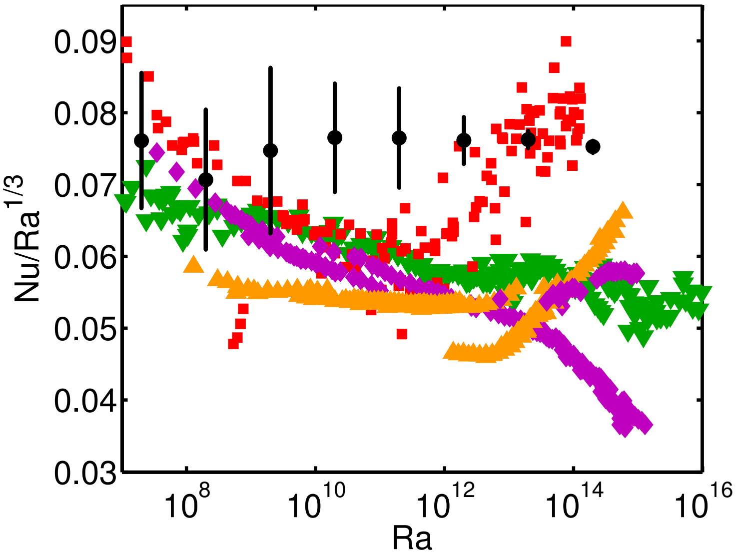

Figure 1.2: Nu vs Ra for $\Gamma = 0.23$ and $\Gamma = 0.5$. The green downward pointing triangles are experimental data from Niemela *et al.* [35]. [35, 36] after a reanalysis reported in Ref. [37], the red squares are from Chavanne *et al.* [38], the purple diamonds are from Ahlers *et al.* [39–42] (all $\Gamma = 0.5$), and the upward pointing cyan triangles are from Roche *et al.* [43] ($\Gamma = 0.23$). The DNS results of Amati *et al.* [44] are indicated by the black dots, the vertical black lines indicate the errorbars. Simulations in the same parameter regime, not shown in this figure, are discussed in chapter 2 and 3.

kinetic boundary layer is expected to become turbulent at $Ra \approx 10^{14}$ (for $Pr = 0.7$) and for higher Ra numbers the system is expected to enter the so-called ultimate regime [20]. In 1962, Kraichnan [*] [45], followed by Spiegel in 1971 [46], postulated that the heat transfer and strength of turbulence in this ultimate regime are not influenced by the thermal and kinetic boundary layers, and thus that the kinematic and thermal diffusivity do not play any significant role in the heat flux anymore. The flow would than become bulk dominated. He predicted that the heat transport in the ultimate regime should scale like

$$Nu \sim Ra^{1/2}(\ln Ra)^{-3/2}Pr^{+1/2} \quad \text{for } Pr < 0.15, \tag{1.16}$$

$$Nu \sim Ra^{1/2}(\ln Ra)^{-3/2}Pr^{-1/4} \quad \text{for } 0.15 < Pr \leq 1. \tag{1.17}$$

The logarithmic corrections follow from the to viscous sublayers induced by no-slip boundary conditions. Ever since Kraichnan's prediction scientist have tried to find evidence for this ultimate regime.

In numerical studies of Lohse and Toschi [47] and Calzavarini *et al.* [48] the scaling of this ultimate regime is observed in so-called homogeneous RB convection.

---

[*] For curiosity, we note that Robert Kraichnan was Albert Einstein's last postdoc and it was him who directed Kraichnan to turbulence.

In this system the top and bottom temperature boundary conditions are replaced with periodic ones, while a mean temperature gradient is imposed. In addition this system is horizontally periodic. Also confinement to the side with cylinders still leads to $Nu \sim Ra^{1/2}$, see Schmidt *et al.* [49], in spite of the sidewall boundaries. There are also some interesting experiments, which try to mimic this homogeneous RB system. Gilbert *et al.* [50] used a vertical channel with wide entrance and exit sections to avoid any influence of the thermal boundary layers on the Nusselt number. They found a scaling, which is consistent with the ultimate regime predicted by Kraichnan, when they redefined *Ra* in terms of the natural coherence length based on the amplitude of the temperature fluctuations instead of a geometric quantity. The same scaling was obtained in the experiments by Cholemari and Arakeri [51, 52]. These authors report on a new type of turbulent flow that is driven purely by buoyancy. The flow is induced by an unstable density difference, created by using brine and water, across the ends of a long vertical pipe. With the *Ra* number based on the local density gradient, they found a homogeneous turbulent region in the midlength of the pipe.

However, up to now the question remains whether this ultimate regime can also be achieved in real RB convection. Between 1996 and 2001 Chavanne *et al.* [38, 53, 54] performed experiments with helium at very low temperatures in an aspect ratio $\Gamma = 0.5$ cell. These experiments reached *Ra* numbers up to $Ra \approx 10^{15}$. In this dataset, see figure 1.2, one can see a strong increase in the heat transport at $Ra \approx 10^{11}$ and Chavanne *et al.* [38, 53, 54] interpreted this as a transition towards the ultimate state. In 2000 Niemela and coworkers [35–37, 55, 56] have performed experiments using cryogenic helium in an aspect ratio $\Gamma = 0.5$ sample. The data of these experiments reached *Ra* numbers up to $Ra \approx 10^{17}$. However, in these experimental measurements no strong heat transport enhancement, as it was found in the experiments of Chavanne *et al.* [38, 53, 54], was observed. Both these experiments have been performed with liquid helium near its critical point, and therefore the *Pr* number increases significantly when the *Ra* number is increased.

For more moderate *Ra* up to 2×10^{14} the DNS by Amati *et al.* [44] in a three dimensional cylindrical cell of aspect ratio $1/2$ with $Pr = 0.7$ showed a higher Nusselt number than measured in experiments, see figure 1.2. In order to explain this discrepancy it was suggested by Verzicco and Sreenivasan [57] that the experimental conditions are closer to fixed heat flux conditions than fixed temperature boundary conditions of the horizontal plates. However, the 2D simulations by Johnston and Doering [58] showed that the Nusselt number obtained in simulations with constant temperature and constant heat flux boundary conditions are identical for $Ra \gtrsim 5 \times 10^6$.

The work by Chavanne *et al.* [38, 53, 54] and Niemela *et al.* [35–37, 55, 56] initiated the work of Ahlers and coworkers in Göttingen in 2009. They used a RB cell with a height over 2 meters to perform measurements around room temperature with high-pressurized gases in order to keep the *Pr* number constant over a wide range of

Ra numbers [59]. The first results of Ahlers *et al.* [39–41] were in general agreement with the Niemela *et al.* data .[35–37, 55, 56], see figure 1.2. However, further measurements [42] revealed the presence of different turbulent states for very high *Ra*, which seem to be triggered by the temperature outside the convection apparatus.

Similar transitions between different turbulent states in this high *Ra* number regime are reported by Roche *et al.* [43, 60–62]. For $Ra \gtrsim 10^{12}$ and $\Gamma = 0.23$ they found two different scaling branches for $Nu(Ra)$. For lower fluid density an upper, less steep branch, and for higher density a lower, but steeper branch is found. In addition, they found that the *Ra* number at which the transition takes place depends on the aspect ratio, namely the smaller the aspect ratio, the larger the *Ra* number for which the transition is observed. Subsequently, the presence of these different turbulent states was explained by Grossmann and Lohse [63] by extending the GL-theory to the very large *Ra* number regime, where the kinetic boundary layer becomes turbulent. However, at the moment it remains unclear why a different turbulent state would be triggered by the fluid density or the temperature outside the cell.

It thus turns out that the practical realization of this high *Ra* number regime in RB convection comes with great technical difficulties, like the use of cryogenic gases close to the critical point, pressurized fluids, or simply very large systems. It has been argued that the disagreements between the experiments could be caused by the variations of the *Pr* number in some experiments, the use of constant temperature or a constant heat flux condition at the bottom plate, the finite conductivity of the horizontal plates and sidewall, non-Oberbeck-Boussinesq effects, i.e. the dependence of the fluid properties on the temperature, and even wall roughness and temperature conditions outside the cell might play a role [42].

From the above discussion it becomes clear that there are several open questions on high *Ra* number thermal convection. The main questions that will be addressed in part I of this thesis are:

- What effect causes the differences that are observed between the experimental and numerical results shown in figure 1.2?
- What numerical resolution should be used in the bulk and the boundary layers to assure that the flow in a DNS is properly resolved?
- What effect causes the differences observed between the several experiments for $Ra \gtrsim 10^{11}$?
- How can one determine from experimental sidewall temperature measurements whether a large scale circulation is present?

In chapter 2 and 3 we present results of DNSs, in which the Boussinesq approximation is unconditionally valid, the walls are perfectly smooth, and the boundary conditions are exactly defined. These simulations thus provide a good reference case for the intended model problem and are compared with available experimental data. In chapter 2 we show that in RB simulations it must be assured that the mesh size is of the same order (if possibly equal or smaller) than the smallest scales in the flow, to obtain an accurate measurement of the heat transport. In chapter 2 we showed that the difference between experiments and simulations shown in figure 1.2 was caused by insufficient numerical resolution. Based on the experience gained in the simulations presented here we formulate general resolution criteria that need to be satisfied in the bulk. In addition, we derive lower bound estimates for the number of computational nodes that should be placed inside the kinetic and thermal boundary layers close to the horizontal plates (chapter 4). These results have been used to check the resolution of the simulations presented in part II and III of this thesis. In chapter 3 we investigate the influence of the *Pr* number on the heat transport and we look into the effect of changing the constant temperature boundary condition at the bottom plate into a constant heat flux condition. Finally, in chapter 5 we use the data accessibility provided by DNSs to demonstrate a new method that can be used to determine whether a large scale circulation is present. This method can be applied to available experimental data for high *Ra* number and rotating RB convection, as we will show in chapter 12, to determine whether an LSC is present.

1.3.2 Part II - Rotating Rayleigh-Bénard convection

In part II of this thesis we study the influence of rotation on heat transport. For this we will analyze rotating RB, i.e. a cylindrical RB sample rotated around its symmetry axis. The corresponding system of equations is

$$\begin{aligned} \frac{\partial \mathbf{u}}{\partial t} + \mathbf{u}\cdot\nabla\mathbf{u} + 2\boldsymbol{\Omega}\times\mathbf{u} &= -\nabla p + \nu\nabla^2\mathbf{u} + \beta g\theta\hat{z}, & (1.18)\\ \frac{\partial \theta}{\partial t} + \mathbf{u}\cdot\nabla\theta &= \kappa\nabla^2\theta, & (1.19)\end{aligned}$$

where $\boldsymbol{\Omega}$ is the rotation rate of the system around the center axis, pointing against gravity, $\boldsymbol{\Omega} = \Omega\hat{\mathbf{z}}$. The rotation rate of the system is indicated by the Rossby number

$$Ro = \sqrt{\beta g\Delta/L}/(2\Omega), \tag{1.20}$$

which indicates the ratio between the buoyancy and Coriolis force. Note that the *Ro* number is an inverse rotation rate. Therefore in part of this thesis the rotation rate is expressed by $1/Ro$, which is proportional to Ω.

Nusselt number measurements in rotating Rayleigh-Bénard convection

The addition of rotation complicates experimental investigations on RB convection. Nevertheless, there have been several experiments on the influence of rotation on thermal convection. Early linear stability analysis, see e.g. Chandrasekhar [1], revealed that rotation has a stabilizing effect due to which the onset of heat transfer is delayed. This can be understood from the thermal wind balance, see appendix A, which implies that convective heat transport parallel to the rotation axis is suppressed. Experimental investigations concerning the onset of convective heat transfer and the pattern formation in cylindrical cells just above the onset under the influence of rotation have been performed by many authors, see e.g. [64–68]. Recently, Lopez, Rubio, Marques and coworkers. see e.g. [69–71], have carefully investigated the onset of thermal convection under the influence of rotation in DNSs.

Since the experiments by Rossby in 1969 [72], it is known that rotation can also enhance the heat transport. Rossby found that, when water is used as the convective fluid, the heat transport first increases with respect to the non-rotating value when the rotation rate is increased. He measured an increase of about 10%. This increase is counterintuitive as the stability analysis of Chandrasekhar [1] has shown that rotation delays the onset to convection and from this one would expect that the heat transport decreases. The mechanism responsible for this heat transport enhancement is Ekman pumping [72–76], i.e. due to the rotation, rising or falling plumes of hot or cold fluid are stretched into vertically-aligned-vortices that suck fluid out of the thermal boundary layers adjacent to the bottom and top plates. This process contributes to the vertical heat flux, see appendix A for details. For stronger rotation Rossby found, as expected, a strong heat transport reduction, due to the suppression of the vertical velocity fluctuations by the rotation. This means that a typical measurement of the heat transport enhancement as function of the rotation rate looks like the one shown in figure 1.3. After Rossby many experiments, e.g. [68, 74–80], have confirmed this general picture. The group of Niemela [81] has performed high *Ra* number experiments, in which no heat transport enhancement due to Ekman pumping is observed. As we will show in chapter 6 this is an effect of the high *Ra* number that is used in these experiments. In figure 11.1 (page 139) we give an overview of the parameter ranges that are covered in the various experimental studies.

Rotating RB experiments are more difficult than non-rotating RB experiments as a well controlled rotating table has to be available. In contrast, in numerical simulations it is sufficient to include the one simple term in the Boussinesq approximation in a non-rotating RB code to include rotation. Nevertheless, there have been only a limited number of numerical studies on rotating thermal convection. In most of these numerical simulations a horizontally unbounded domain is simulated. These simulations are relevant to understand large convective systems that are influenced by rotation, such as the atmosphere and solar convection. In 1991 Raasch & Etling [82] used a large-eddy simulation to simulate the atmospheric boundary layer. Julien and coworkers [73, 77, 83, 84], Kunnen *et al.* [85, 86] and King *et al.* [76] used DNSs at several *Ra* and *Ro* numbers to study the heat transport and the resulting flow patterns under the influence of rotation. Sprague *et al.* [87] numerically solved an asymptotically reduced set of equations valid in the limit of strong rotation. Finally,

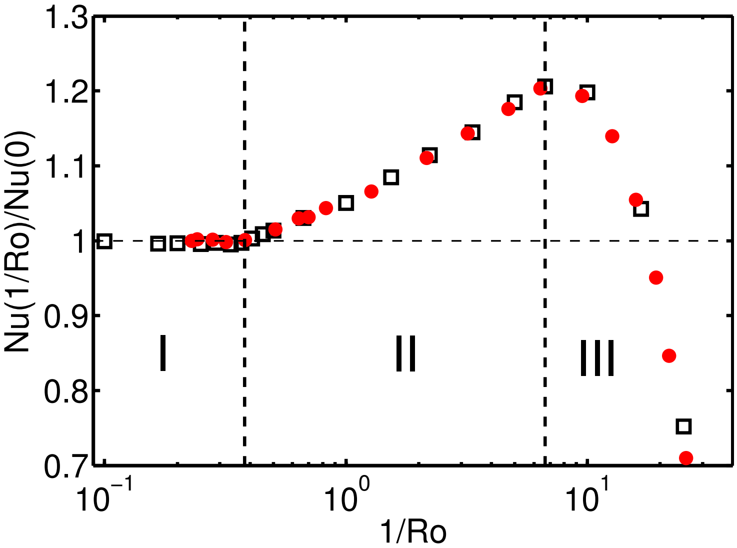

Figure 1.3: The scaled heat transfer $Nu(1/Ro)/Nu(0)$ as function of $1/Ro$ on a logarithmic scale. Experimental and numerical data for $Ra = 2.73 \times 10^8$ and $Pr = 6.26$ are indicated by red dots and open squares, respectively. Data taken from chapter 6 and 8 and are called run E2 in Zhong & Ahlers [80]. See also chapter 12.

Schmitz and Tilgner [88, 89] performed horizontally periodic simulations with no-slip and stress-free boundary conditions at the horizontal plates. They show that heat transport enhancement under the influence of rotation is only found when a no-slip boundary condition at the horizontal plates is used.

Oresta *et al.* [90] and Kunnen *et al.* [75, 91, 92] have studied turbulent rotating convection in a cylinder. They focus on the influence of rotation on the heat transport and the corresponding changes in the flow structure. In addition, it allowed Kunnen *et al.* [75, 91, 92] to make direct comparisons between experiments and simulations. An indication of the parameter regime that is covered by several numerical studies can be found in the phase diagram shown in figure 11.1 (page 139).

Different turbulent states

When the heat transport enhancement as function of the rotation rate is considered, a typical division in three regimes, see figure 1.3, is observed. Namely regime I (weak rotation), where no heat transport enhancement is observed, regime II (moderate rotation), where a strong heat transport enhancement is found, and regime III (strong rotation), where the heat transport starts to decrease [91, 93]. This division is based on several experimental efforts. The experiments of Boubnov & Golitsyn [93], Zhong, Ecke & Steinberg [68], and Sakai [94] first showed with flow visualization experiments that there is a typical ordering of vertically-aligned- vortices under the

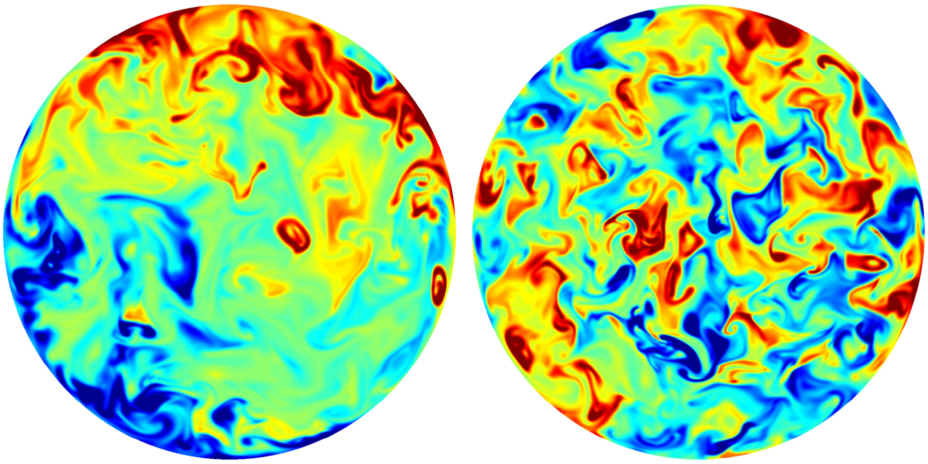

Figure 1.4: Visualization, based on a DNS, of the temperature field in the horizontal mid-plane of a cylindrical convection cell. The red and blue areas indicate warm and cold fluid, respectively. The left image is at a slow rotation rate ($1/Ro = 0.0046$) below the transition where the warm upflow (red) and cold downflow (blue) reveal the existence of a single convection roll superimposed upon turbulent fluctuations. The right image is at a somewhat larger rotation rate ($1/Ro = 0.6$) and above the transition, where vertically-aligned vortices cause disorder on a smaller length scale.

influence of rotation, see figure 1.4 for a visualization based on numerical simulations performed in this thesis. A three dimensional visualization of the vortices is made by Kunnen *et al.* [92]. The first local velocity (and temperature) measurements in the flow have been reported by Boubnov & Golitsyn [93] and Fernando *et al.* [95]. In both experiments the flow was analyzed using particle-streak photography. Vorobieff & Ecke [74, 96] used digital cameras to perform particle image velocimetry (PIV) measurements to study the flow with higher spatial and temporal resolutions. Special attention was given to obtain statistics on the vortices in the strongly rotating regime, see figure 1.4 and appendix B. In later experiments by Kunnen *et al.* [75, 91, 97] these experiments were extended by the application of stereoscopic PIV (SPIV): In this technique two cameras are used to obtain a stereoscopic view, which allows for a reconstruction of the out-of-plane velocity. This made new experimental data available, for example on the correlation between the vertical velocity and the vertical vorticity.

It is also well known that without rotation the LSC is the dominant flow structure, see e.g. [20, 98, 99] and figure 1.4. This has motivated Hart, Kittelman & Ohlsen [100], Kunnen *et al.* [75], and Ahlers and coworkers [80, 98] to study the influence of weak rotation on the LSC. In these investigations it was found that the LSC has a weak precession under the influence of rotation. In addition, it was shown by Zhong & Ahlers [80] that, although the Nusselt number is unchanged in regime I, there are various properties of the LSC that are changing when the rotation rate is increased in regime I. Based on an experimental and numerical study on the properties of the LSC Kunnen *et al.* [75] showed that the LSC disappears when a strong enough rotation is applied.

There have also been analytic modeling efforts by Portegies *et al.* [101] and Grooms *et al.* [102] to understand the heat transport in the rotating regime. In these models only the heat transfer in the vertically-aligned-vortices is considered as most heat transport in the strong rotating regime takes place inside these vortices.

From the above discussion it becomes clear that there are several open questions on rotating RB convection. The main questions that will be addressed in part II of this thesis are:

- How does the effect of Ekman pumping depend on *Ra* and *Pr*?
- What happens at the onset of heat transport enhancement?
- What is the influence of the aspect ratio in rotating RB convection?
- Can the Grossmann-Lohse model be extended in order to describe the heat transfer in rotating RB convection?
- How can changes in the flow structure due to rotation be detected from experimental sidewall temperature measurements?

In part II of this thesis we present experimental and numerical data on the heat transfer as function of the *Ra*, *Ro*, and *Pr* number and for different aspect ratios. The experiments have been performed in the group of Guenter Ahlers in Santa Barbara, see chapter 6 for a description of the setup, and in Eindhoven, see chapter 10 for a description of the setup, which is based on the Santa Barbara design. In chapter 6 we show that the effect of Ekman pumping, and thus the observed heat transport enhancement, strongly depends on the *Ra* and *Pr* number. The *Pr* number dependence will be discussed in more detail in chapter 7. In chapter 8 we show that there is a sharp transition between a regime where the LSC is dominant at weak rotation, to a regime that is dominated by vertically-aligned-vortices at stronger rotation. Subsequently, we will show in chapter 9 that the rotation rate at the onset of heat transport enhancement increases when the aspect ratio of the sample is decreased. Then we will study the influence of the aspect ratio for stronger rotation rates in chapter 10 to show that the heat transport in the strong rotating regime does not depend on the aspect ratio. After this we will discuss the behavior of the boundary layers under the influence of rotation in chapter 11. The results from this analysis will be used in a model that extends the GL theory to the rotating case to account for the smooth onset of heat transport enhancement that is found at relatively low *Ra* numbers. We emphasize that this model cannot be used to explain the onset of heat transport enhancement for larger *Ra*, which is discussed in chapter 9. Finally, in chapter 12 we will discuss, based on the results of experiments and numerical simulations, how the different flow regimes in rotating RB convection can be recognized from the azimuthal temperature (or vertical velocity) profiles close to the sidewall. For this analysis we will use some of the methods introduced in chapter 5 to determine whether the LSC is present. In addition, we will show that a weak secondary circulation is created due to rotation, which takes place in the Ekman boundary layer, close to the horizontal plates, and in the Stewartson boundary layers, close to the sidewall.

1.3.3 Part III - 2D Rayleigh-Bénard convection

The total amount of CPU time that is used in the simulations presented in this thesis well surpasses 10 million hours. However, unfortunately, CPU time is not available in unlimited amounts. Therefore we have also performed simulations on 2D RB convection. An obvious advantage of these 2D computations is that they are much cheaper than the three dimensional ones. However, one may wonder whether the dynamics of 3D RB convection are sufficiently captured in 2D RB simulations.

This question has been addressed by Schmalzl *et al.* [103] and the general conclusion was that various properties observed in 3D RB convection are well reflected in 2D simulations. Over the years 2D simulations have been used to investigate a number of aspects. Sugiyama *et al.* [104–106] used 2D simulations to verify and study the non-Oberbeck Boussinesq effects observed in 3D experiments of Ahlers *et al.* [105]. Johnston & Doering [58] used periodic 2D simulations to show that for high enough *Ra* numbers the heat transport in simulations with constant temperature condition and constant heat flux condition at the horizontal plates becomes equal. We note that we have shown the same for 3D DNS in cylindrical domains in chapter 3.

It thus becomes clear that 2D simulations can be used to better understand some aspects of 3D RB convection. The main questions that will be addressed in part III of this thesis are:

- Do the boundary layer profiles in RB convection agree with the prediction of the Prandtl-Blasius theory?
- What mechanism is responsible for the spontaneous flow reversals observed in 2D RB convection?

In chapter 13 we analyze experimental and numerical results on (quasi) 2D RB convection to characterize the boundary layer profiles. Here we find good agreement between the theoretical Prandtl-Blasius profiles and the numerically and experimentally obtained ones. This further confirms one of the key assumptions of the GL-theory, namely that the boundary layers behave in laminar way up to a certain *Ra* number. In chapter 14 we analyze the random flow reversals that are observed in (quasi) 2D experiments and simulations. Here we again find a perfect agreement between experiments and simulations. We find that the reversals are only observed in a certain parameter regime. The reversals are caused by a geometry effects as the flow rolls that build up in the diagonally opposing corners of the cell trigger the reversals.

1.4 Collaboration

In this thesis we used a combination of experimental, numerical and theoretical techniques to get a better understanding of RB convection. This was only possible due to the collaboration with several groups around the world.In particular, we would like to mention that Dr. Kazuyasu Sugiyama and Prof. Roberto Verzicco provided the 2D and 3D numerical codes for the simulations presented.

Some of the experiments presented in this thesis have been performed by ourselves in Eindhoven, while others have been performed elsewhere. In particular, many rotating RB experiments have been performed by Dr. Jin-Qiang Zhong, Dr. Stephan Weiss and Prof. Guenter Ahlers in Santa Barbara. The 2D experiments in part III are performed in the group of Prof. Ke-Qing Xia in Hong Kong. Dr. Quan Zhou and Prof. Ke-Qing Xia contributed to the analysis of the boundary layer profiles in part III.

Others have contributed to the more theoretical work presented. Here we mention the contributions of Dr. Olga Shiskina on the analysis that shows the minimum number of computational nodes that should be placed inside the boundary layers, the work of Prof. GertJan van Heijst on the analysis of the Stewartson boundary layers in rotating RB convection, and the contribution of Prof. Siegfried Grossmann on several chapters.

Part I

High Rayleigh number thermal convection

2

Radial boundary layer structure and Nusselt number in Rayleigh-Bénard *

Results from direct numerical simulations for three dimensional Rayleigh-Bénard convection in a cylindrical cell of aspect ratio $1/2$ *and* $Pr = 0.7$ *are presented. They span five decades of Rayleigh from* 2×10^6 *to* 2×10^{11}*. The results are in good agreement with the experimental data by Niemela* et al.*, Nature,* ***404****, 837 (2000). Previous direct numerical simulations results from Amati* et al.*, Phys. Fluids,* ***17****, 121701 (2005) showed a heat transfer that was up to* 30% *higher than the experimental values. The simulations presented in this chapter are performed with a much higher resolution to properly resolve the plume dynamics. We find that in underresolved simulations the hot (cold) plumes travel further from the bottom (top) plate than in the better resolved ones, due to insufficient thermal dissipation mainly close to the sidewall (where the grid cells are largest) and therefore the Nusselt number in underresolved simulations is overestimated. Furthermore, we compare the best resolved thermal boundary layer profile with the Prandtl-Blasius profile. We find that the boundary layer profile is closer to the Prandtl-Blasius profile at the cylinder axis than close to the sidewall, due to rising plumes close to the sidewall.*

---

[*] Based on: R.J.A.M. Stevens, R. Verzicco, and D. Lohse, Radial boundary layer structure and Nusselt number in Rayleigh-Bénard convection, J. Fluid Mech. 643, 495-507 (2010).

2.1 Introduction

Previous direct numerical simulations up to Rayleigh 2×10^{14} by Amati et al. [44] in a three dimensional cylindrical cell of aspect ratio $1/2$ with $Pr = 0.7$ showed a higher Nusselt Nu number than measured in experiments, see figure 2.1. In order to explain this discrepancy it was suggested by Verzicco & Sreenivasan [57] that the experimental conditions are closer to fixed heat flux conditions than fixed temperature boundary conditions of the horizontal plates. However, recent two dimensional simulations by Johnston & Doering [58] showed that the Nusselt number Nu obtained in simulations with constant temperature and constant heat flux boundary conditions are identical when $Ra \gtrsim 5 \times 10^6$. In this chapter we show that the Nusselt number obtained in the three dimensional simulations with constant temperature boundary conditions is in good agreement with the experimental data, see figure 2.1, when the resolution is sufficiently high.

2.2 Numerical method and results on the Nusselt number

We numerically solved the three-dimensional Navier-Stokes equations within the Boussinesq approximation,

$$\frac{D\mathbf{u}}{Dt} = -\nabla P + \left(\frac{Pr}{Ra}\right)^{1/2} \nabla^2 \mathbf{u} + \theta \hat{z}, \tag{2.1}$$

$$\frac{D\theta}{Dt} = \frac{1}{(PrRa)^{1/2}} \nabla^2 \theta, \tag{2.2}$$

with $\nabla \cdot \mathbf{u} = 0$. Here $\hat{z}$ is the unit vector pointing in the opposite direction to gravity, $D/Dt = \partial_t + \mathbf{u} \cdot \nabla$ the material derivative, $\mathbf{u}$ the velocity vector with no-slip boundary conditions at all walls, and θ the non-dimensional temperature, $0 \leq \theta \leq 1$. The equations have been made non-dimensional by using the length L, the temperature Δ, and the free-fall velocity $U = \sqrt{\beta g \Delta L}$. The numerical scheme is described in detail in Refs. [107–109].

The most important requirement for conducting DNS is to resolve all the relevant scales of the flow, i.e. the Kolmogorov length η and the Batchelor length η_T. According to Grötzbach [110], the maximum wave number to be recorded by the grid is $k_{max} = \pi/h$, where h=$(\Delta x \Delta y \Delta z)^{1/3}$ is the mean grid width. This wave number must be greater than $1/\eta$, where $\eta = (\nu^3/\varepsilon_u)^{1/4}$, and greater than $1/\eta_T$, where $\eta_T = (\kappa^3/\varepsilon_u)^{1/4}$. According to Grötzbach [110] this leads to the following restrictions on the mean grid widths:

$$h \leq \pi\eta = \pi(\nu^3/\varepsilon_u)^{1/4} \text{ for } Pr \leq 1 \ , \tag{2.3}$$

$$h \leq \pi\eta_T = \pi(\kappa^3/\varepsilon_u)^{1/4} \text{ for } Pr \geq 1 \ , \tag{2.4}$$

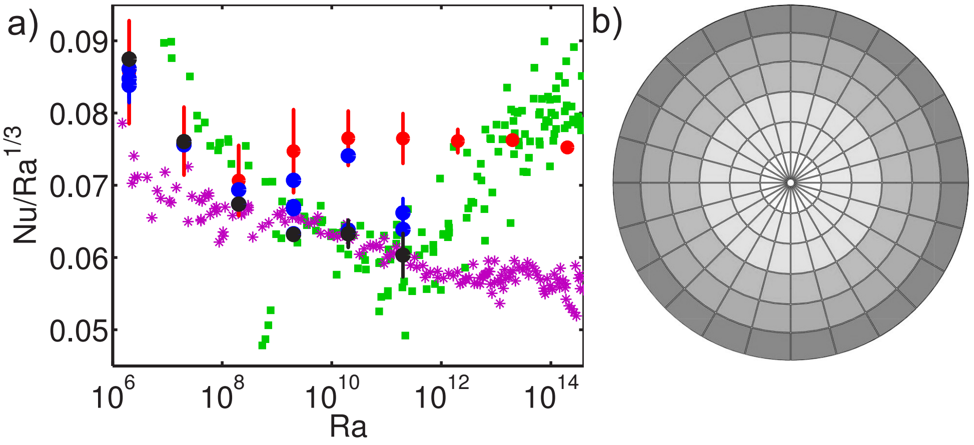

Figure 2.1: (a) compensated Nusselt number vs the Rayleigh number for $Pr = 0.7$. Purple stars are experimental data from Niemela et al. [35] and the green squares are from Chavanne et al. [38]. The DNS results from Verzicco & Camussi [109] and Amati et al. [44] are indicated in red and the present DNS results with the highest resolution are indicated by the black dots. When the vertical errorbar is not visible the error is smaller than the dot size. The results of the underresolved simulations of this study are indicated by the blue dots. (b) sketch of the grid geometry. The cells close to the sidewall are largest and therefore this region is least resolved.

However the simulations presented in this chapter show that it is necessary to properly resolve the flow in all directions of the flow. This means that the definition for h should read h = max$(\Delta x, \Delta y, \Delta z)$. Note that this adapted criterion requires a higher resolution in the horizontal plane, especially in the BLs close to the horizontal plates. This high resolution in the horizontal direction is necessary to properly resolve the plume dynamics in the BL as the (thermal) gradients in this region are large in all directions of the flow and not only in the vertical direction. The simulations presented in this chapter will show that it is crucial to properly resolve the plume dynamics to obtain accurate results for the Nusselt number.

When the vertical dissipation profile is assumed to be constant and is approximated by equating it to the production term due to buoyancy forces in the kinetic energy equation one obtains the following relations [110],

$$h \leq \pi\eta = \pi L \left(\frac{Pr^2}{RaNu}\right)^{1/4} \text{ for } Pr \leq 1 \;, \tag{2.5}$$

$$h \leq \pi\eta_T = \pi L \left(\frac{1}{RaPrNu}\right)^{1/4} \text{ for } Pr \geq 1 \;, \tag{2.6}$$

which are widely used in the literature. However one has to realize that RB convection is anisotropic and that the dissipation rates strongly fluctuate in time and space. It is widely know that the dissipation rates peak close to the walls and therefore there the relevant length scales are smallest. For DNS simulations in a cylindrical geometry this means that one has to take care that the azimuthal resolution is sufficient, because the grid spacing $\Delta\phi$ is largest close to the sidewall while the length scale that has to be resolved in that region is smallest. Furthermore, one also has to realize that the dissipation rates strongly fluctuate in time and thus also the relevant length scales that have to be resolved [111]. This means that when the relevant length scales in the simulation are determined from azimuthally and time averaged dissipation rate, the necessary resolution for a fully resolved simulation may locally or temporarily be even larger. How strong this effect is depends on the strength of the intermittency and therefore on the system parameters (Ra,Pr,Γ). Although the relations (2.5) and (2.6) can be used to get an estimate of the required resolution, one has to realize that the result underestimates the resolution that is required to have a fully resolved simulation, because the fluctuations in time and space are not incorporated in these relations

All simulations in this chapter are for $Pr = 0.7$ and therefore η is the smallest length scale in the flow. We simulated each Ra number on at least three different grids to test the influence of the grid scales. In table 2.1 the largest grid scale $\ell_{max} = \max(\Delta r, \Gamma L/2\Delta\phi, \Delta z)$ is compared to the Kolmogorov scale η for each simulation. We do this in two different ways, namely by looking at the global criterion (2.5), assuming an uniform distribution of the dissipation rates, see column ($\ell_{max,g}/\eta$). Furthermore, we also estimated this ratio by looking at the time averaged dissipation rates as function of the position ($\ell_{max,p}/\eta$). Note that the relation between $\ell_{max,p}$ and $\ell_{max,g}$ shows that the global criterion indeed underestimates the required resolution for a fully resolved DNS simulation. The grid density near the plates has been enhanced to keep a sufficient number of nodes in the thermal BL where the vertical temperature gradients are very high, see the column "N_{BL}" in table 2.1. According to Grötzbach [110] three points in the thermal BL should be sufficient. In the papers by Verzicco and Camussi [109] and Amati et al. [44] it was already noted that more than three grid points in the thermal BL are required. Indeed, the results clearly show that more grid points in the thermal BL are required to have a fully resolved simulation. In chapter 4 we will derive a lower bound estimate for the number of gridpoints that should be placed inside the BLs. Here we note that the strength of the plumes decreases slowly when the plumes travel further away from the plates and therefore the grid spacing from the plates to the bulk has to be increased gradually to prevent that the plumes become underresolved just above the thermal BL.

Table 2.1: The columns from left to right indicate Ra; the number of grid points in the azimuthal, radial, and axial direction ($N_\theta \times N_r \times N_z$), the Nusselt number ($Nu$) obtained after averaging the results of the three methods (see text) using the whole simulation length, the Nusselt number (Nu_h) after averaging the results of the three methods using the last half of the simulation, the maximum difference between the three methods (max-diff), the number (N_{BL}) of points in the thermal BL, the maximum grid scale compared to the Kolmogorov scale estimated by the global criterion ($\ell_{max,g}/\eta$), and the maximum grid scale compared to the Kolmogorov scale estimated by azimuthally and time averaged dissipation rate. The last two columns give the Nusselt number derived from the volume averaged kinetic $\langle \varepsilon_u \rangle$ and thermal $\langle \varepsilon_\theta \rangle$ dissipation rates compared to Nu indicated in column three. The *italic* lines indicates a simulation started with a different initial flow field.

Ra	$N_\theta \times N_r \times N_z$	Nu	Nu_h	max-diff	N_{BL}	$\frac{\ell_{max,g}}{\eta}$	$\frac{\ell_{max,p}}{\eta}$	$\frac{\frac{\langle \varepsilon_u \rangle}{\nu^3 Ra Pr^{-2}/L^4}+1}{Nu}$	$\frac{\frac{\langle \varepsilon_\theta \rangle}{\kappa \Delta^2/L^2}}{Nu}$
2×10^6	$97 \times 49 \times 129$	*10.85*	*10.92*	*0.32 %*	*18*	*0.42*	–	–	–
2×10^6	$97 \times 49 \times 129$	10.68	10.32	0.35 %	18	0.42	0.51	0.973	0.978
2×10^6	$129 \times 65 \times 193$	10.56	10.86	0.15 %	27	0.31	0.39	0.972	0.986
2×10^6	$193 \times 97 \times 257$	11.02	11.03	0.44 %	35	0.21	0.26	0.974	0.991
2×10^7	$129 \times 49 \times 193$	*20.52*	*20.56*	*0.36 %*	*17*	*0.66*	–	–	–
2×10^7	$193 \times 97 \times 257$	20.54	20.69	0.70 %	31	0.46	0.64	0.989	0.987
2×10^7	$289 \times 129 \times 353$	20.64	20.53	0.36 %	42	0.34	0.43	0.984	0.991
2×10^8	$97 \times 49 \times 193$	40.57	40.71	0.02 %	10	1.84	2.82	1.007	0.926
2×10^8	$193 \times 65 \times 257$	39.42	39.52	0.02 %	13	0.92	1.41	0.992	0.950
2×10^8	$257 \times 97 \times 385$	39.41	39.10	0.79 %	19	0.70	1.11	0.995	0.973
2×10^9	$129 \times 65 \times 257$	89.07	88.25	0.02 %	6	3.01	4.57	1.001	0.858
2 × 10^9	*193 × 65 × 257*	*84.49*	*84.46*	*0.45 %*	*7*	*1.99*	*3.10*	*1.002*	*0.879*
2×10^9	$193 \times 65 \times 257$	84.10	83.66	0.51 %	7	1.98	3.06	1.000	0.877
2×10^9	$385 \times 97 \times 385$	79.75	78.70	0.70 %	10	1.15	1.47	0.999	0.935
2×10^9	$513 \times 129 \times 513$	*79.60*	*78.89*	*0.45 %*	*17*	*0.93*	*1.22*	*1.006*	*0.962*
2×10^{10}	$129 \times 97 \times 385$	201.08	201.21	1.01 %	12	6.56	10.88	1.006	0.878
2×10^{10}	$513 \times 129 \times 513$	171.79	169.58	2.09 %	19	1.59	2.83	0.994	0.927
2×10^{10}	$385 \times 257 \times 1025$	173.13	173.30	0.98 %	29	2.12	–	–	–
2×10^{11}	$769 \times 193 \times 769$	387.07	387.53	2.18 %	16	2.31	–	–	–
2×10^{11}	$769 \times 257 \times 1025$	373.64	368.88	2.03 %	18	2.28	6.34	0.9883	0.9058
2×10^{11}	$1081 \times 351 \times 1301$	352.67	364.75	4.15 %	26	1.60	3.96	1.0244	0.9318

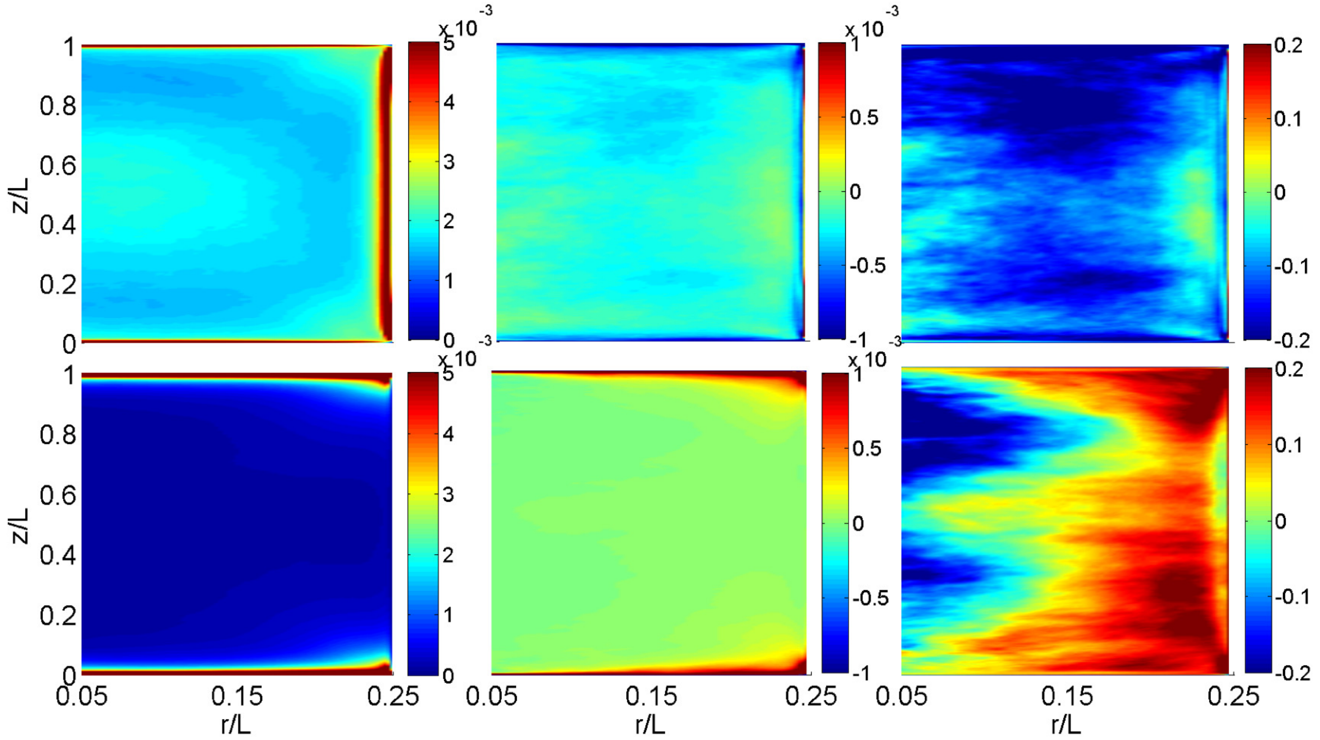

Figure 2.2: Dimensionless kinetic (upper) and thermal (lower) dissipation rates at $Ra = 2 \times 10^9$. The upper row gives $\widetilde{\varepsilon}_u" = \varepsilon_u"L/U^3$ and the lower row $\widetilde{\varepsilon}_\theta = \varepsilon_\theta L/(\Delta^2 U)$. The left column indicates the dimensionless kinetic $\widetilde{\varepsilon}_u$ and thermal $\widetilde{\varepsilon}_\theta$ dissipation rates for the high resolution case $(385 \times 97 \times 385)$. The middle column gives $\widetilde{\varepsilon}_u^H - \widetilde{\varepsilon}_u^L$ (upper plot), and $\widetilde{\varepsilon}_\theta^H - \widetilde{\varepsilon}_\theta^L$ (lower plot), where the superscripts H and L, respectively, mean the data obtained from the high $(385 \times 97 \times 385)$ and low resolution simulations $(129 \times 65 \times 257)$. The rightmost column gives $(\widetilde{\varepsilon}_u^H - \widetilde{\varepsilon}_u^L)/\widetilde{\varepsilon}_u^H$ (upper plot) and $(\widetilde{\varepsilon}_\theta^H - \widetilde{\varepsilon}_\theta^L)/\widetilde{\varepsilon}_\theta^H$ (lower plot). The difference for the thermal dissipation rates between the fully resolved and the underresolved simulations is largest (in absolute values) close to the sidewall.

For all simulations up to $Ra = 2 \times 10^{10}$ on the $129 \times 97 \times 385$ grid we simulated the flow for at least 200 dimensionless time units (2 dimensional time units equal 1 turnover time) to make sure to have reached the statistically stationary state and all transient effects are washed out, before we then started to collect data for an additional 400 dimensionless time units (and some cases even for 3000 dimensionless time units) so that the statistical convergence could be verified. In simulations where the flow field obtained at a lower Ra (or a new random flow field) is used as an initial condition, we observe a small overshoot in Nu, before it settles to its statistically stationary value. The long initialization runs we used prevent that this influences our results. This is double checked by the convergence of the different methods we use to calculate Nu. Since most simulations are started from an interpolated field obtained at a lower Ra, we recomputed Nu for $Ra = 2 \times 10^9$ on the $193 \times 65 \times 257$ grid with a new flow field to rule out the effect of hysteresis on the obtained Nusselt results. The result is shown in *italics* in table 2.1 and is in excellent agreement with the original result.

For the six most demanding simulations, i.e. the bottom five cases in table 2.1 and the simulation for $Ra = 2 \times 10^9$ on the $513 \times 129 \times 513$ grid, the criteria for time averaging had to be relaxed due to the limited CPU time available. Therefore we averaged these cases for 100 dimensionless time units (300 time units for the simulation at $Ra = 2 \times 10^{10}$ on the $385 \times 257 \times 1025$ grid, 200 dimensionless time units for for $Ra = 2 \times 10^9$ on the $513 \times 129 \times 513$ grid, and 40 dimensionless time units for $Ra = 2 \times 10^{11}$ on the $1081 \times 351 \times 1301$ grid). The simulations at $Ra = 2 \times 10^{10}$ have completely different initial conditions, i.e. different flow fields obtained at lower Ra are used as initial condition. Nonetheless, we observe good agreement.

We calculate Nu as volume average and also by using the temperature gradients at the bottom and top plate. The volume average is calculated from the definition of the Nusselt number $Nu = (\langle u_z \theta \rangle_A - \kappa \partial_3 \langle \theta \rangle_A) / \ \kappa \Delta L^{-1}$ [108]. In addition, we average over the entire volume and time. The averages of the three methods, i.e. the volume average and the averages based on the temperature gradients at the bottom and top plate. The value Nu in table 2.1 gives the average value of these three for the simulation length of the actual simulation, normally 400 dimensionless time units. We also determined Nu over the last half of our simulations, normally the last 200 dimensionless time units, see the column "Nu_h" in table 2.1. These values are within 1% of the value determined over the whole simulation, showing that our results are well converged. The maximum difference in Nu obtained from the three methods, i.e. volume average and using the temperature gradients at the plates, is given in the column "max-diff" in table 2.1.

Figure 2.1 shows that the DNS data converge to the experimental data when the resolution is increased. The results indeed show that a very high resolution is required to obtain converging results for the Nusselt number. The error bars in figure

2.1 indicate the maximum of the following three quantities. 1) The maximum difference between the three methods to determine the *Nu*. 2) The difference between *Nu* determined over whole simulation length and *Nu* determined over the last half of the simulation. 3) When the error bar based on criterion 1 and 2 is smaller than 1% after averaging over 400 dimensionless time units the error is assumed to be 1%. When the data is averaged over 100 dimensionless time units we take a minimal error of 3%. For 2×10^6 and 2×10^7 we also determined the variation in *Nu* at various distances from the horizontal plates [112] and found that the differences are smaller than 0.2%. We note that *Nu* fluctuates more in time than in space (after sufficient spatial averaging). This check also shows that the Nusselt number results in our simulation are well converged. The difference in *Nu* we get from independent simulations is normally well within these error margins when exactly the same grid is used, except for some cases at $Ra = 2 \times 10^6$.

2.3 Dissipation rates and PDFs of temperature distribution

Another way to calculate *Nu* is to look at the two exact global relations for the volume averaged kinetic and thermal energy dissipation rates $\langle \varepsilon_u \rangle = \nu^3 (Nu-1) Ra Pr^{-2}/L^4$, and $\langle \varepsilon_\theta \rangle = \kappa \Delta^2 Nu/L^2$, respectively [113]. We have calculated the azimuthally and time averaged energy dissipation rate $\varepsilon_u(\overrightarrow{x}) = \nu |\nabla \mathbf{u}|^2$ and the thermal dissipation rate $\varepsilon_\theta(\overrightarrow{x}) = \kappa |\nabla \theta|^2$. In addition we look at the quantity $\varepsilon_u^{''}(\overrightarrow{x}) := \mathbf{u} \cdot \nabla^2 \mathbf{u}$. The volume averaged value of $\varepsilon_u^{''}$ is the same as the volume averaged kinetic energy dissipation rate ε_u (although it differs locally), which can easily be derived using Gauss's theorem [20]. Figure 2.2 compares the difference between the dissipation rates obtained in the fully resolved and the underresolved simulations and reveals a higher thermal dissipation rate for the fully resolved simulations as it is calculated from the (temperature) gradients. In the underresolved simulations the gradients are smeared out and therefore ε_u and ε_θ are underestimated. To check the resolution, we calculated ε_u and ε_θ from the respective gradients and compared it with the values obtained from above global exact relations. Table 2.1 shows that for ε_u the relation is basically satisfied for all simulations, whereas for ε_θ the difference can be considerable. For the higher *Ra* numbers the temperature field is underresolved, because of the line structure of the plumes very close to the horizontal plates and close to the sidewalls. Since the thermal dissipation rate in these regions is much higher than the kinetic dissipation rate this effect is much more pronounced in the convergence of the thermal dissipation rate than in the convergence of the kinetic dissipation rate. We note that the value for the Nusselt number seems to be converged earlier than the convergence of the dissipation rates. Testing above exact relations seems to be the best way to verify the grid resolution. For 2×10^6 and 2×10^7 the kinetic dissipation rate is not converged because we can not properly resolve the kinetic dissipation rate close to

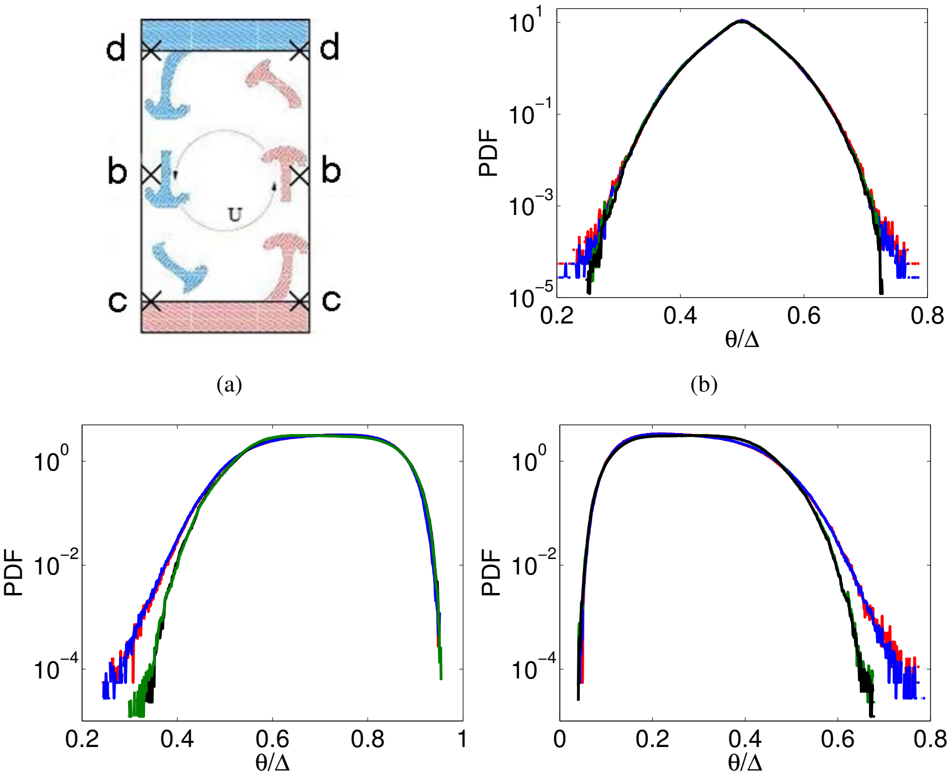

(a) (b)

(c) (d)

Figure 2.3: a) A sketch showing the locations (crosses) of the azimuthally averaged temperature PDFs, shown in figure 2.3 b, c, and d, for $Ra = 2 \times 10^8$ obtained on different grids. The radial position is $0.2342L$ for the underresolved ($97 \times 49 \times 193$) and $0.2314L$ for the better resolved ($193 \times 65 \times 257$) simulations. The temperature PDF for the better resolved simulations averaged over 3000 dimensionless time units is indicated in black. The green line indicates the result using half of the time series. The temperature PDF averaged over 3000 dimensionless time units for the underresolved simulations is indicated in blue, and the red indicates the result using half of the time series. b) Temperature PDF at mid height. c) Temperature PDF at the distance λ_θ^{sl} from the bottom plate. d) Temperature PDF at the distance λ_θ^{sl} from the top plate.

the cylinder axis due to the metric factors $1/r$, $1/r^2$,... that amplify the numerical errors in the squared gradients this region. At higher *Ra* the fraction of the kinetic dissipation that is in this region is smaller and therefore the convergence is better.

The vertical heat flux concentrates in the plume-dominated sidewall region where the vertical velocity reaches its maximum [114]. Therefore it is very important to properly resolve the region close to the sidewall. However, figure 2.2 reveals that in the underresolved simulations the region close to the sidewall is least resolved (red areas in the plot where the thermal dissipation rates are compared (right plot)), as

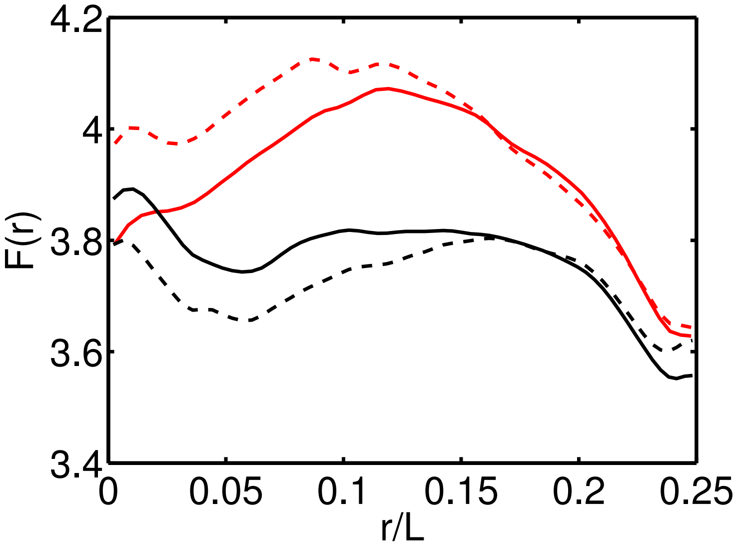

Figure 2.4: Flatness of the temperature PDF at mid height for $Ra = 2 \times 10^8$ for the underresolved (red (upper lines), $97 \times 49 \times 193$) and the better resolved simulations (black (lower lines), $193 \times 65 \times 257$). The solid lines indicate the result after averaging over 3000 dimensionless time units and the dashed lines the result after averaging over 1600 dimensionless time units. Both simulations are started from the same initial field obtained at a lower Ra and the data collecting is started when each simulation has reached the statistically stationary state.

there the finite volumes are largest, due to the cylindrical geometry of the grid (see figure 2.1b). When the resolution is insufficient close to the sidewall, the plumes in this region, which are important for the heat transfer, are not properly resolved and not sufficiently dissipated. Therefore too much heat is transported across the cell, leading to an overestimation of Nu in the underresolved simulations. Furthermore, figure 2.2 shows that the thermal dissipation rate in the underresolved simulations is overestimated in the central region. This is due to the flow organization at higher Ra, see figure 8 of Ref. [109], where it is shown that there is a double convection roll for $Ra = 2 \times 10^9$. Because the plumes close to the sidewall are insufficiently dissipated in the underresolved simulations the plumes that will reach the central region of the cell will be stronger in the underresolved simulations than in the better resolved ones. This leads to a higher dissipation in the central region in underresolved simulations with respect to better resolved simulations. Supplementary movies [115] reveal the dynamics of the system for the different grid resolutions. Movie 2.1 shows the temperature field in horizontal cross sections close to bottom plate and movie 2.2 at mid height. Note that the coarseness of the underresolving grids does not capture all the characteristics of the flow observed in the high resolution simulation.

To further investigate the influence of the grid resolution, we calculated azimuthally averaged PDFs, see also Refs. [112, 116–119], of the temperature averaged over

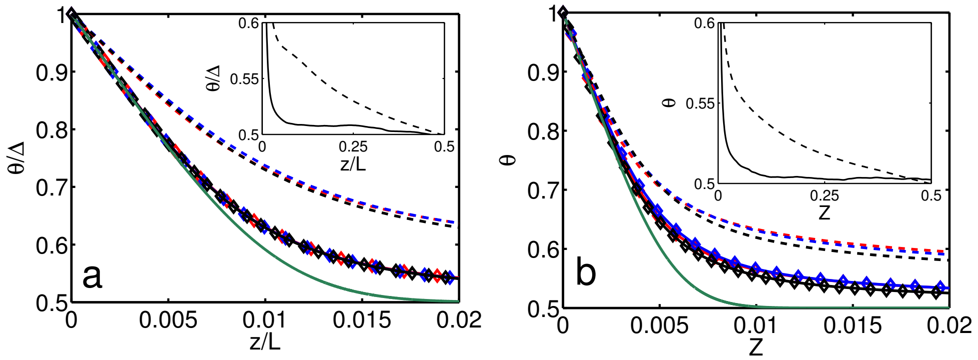

Figure 2.5: Azimuthally averaged temperature profiles obtained from the simulations at different grids. a) $Ra = 2 \times 10^8$, for the grids $97 \times 49 \times 193$ (red), $193 \times 65 \times 257$ (blue), $257 \times 97 \times 385$ (black) and b) $Ra = 2 \times 10^9$ for the grids $129 \times 65 \times 257$ (red), $193 \times 65 \times 257$ (blue), $385 \times 97 \times 385$ (black). The solid lines show the temperature profile at the cylinder axis ($r = 0$) (the diamonds indicate the data points obtained from the simulation) and the dashed lines at the radial position $0.225L$. The green line indicates the PB profile matched to the temperature gradient at the cylinder axis ($r = 0$) of the high resolution simulation. The insets show the temperature profile from the highest resolution data over a larger axial range. Here the solid line indicates the profile at the axis and the dashed line the temperature profile at the radial position $0.225L$.

3000 dimensionless time units for $Ra = 2 \times 10^8$, comparing the underresolved case ($97 \times 49 \times 193$) with the fully resolved one ($193 \times 65 \times 257$). Figure 2.3 shows that the temperature PDFs at mid height and at a distance λ_θ^{sl} (thermal BL based on the slope) from the plates have longer tails in the underresolved simulation than in the better resolved one. Again the reason lies in the rising (falling) plumes from the bottom (top) plate which are not properly dissipated in the underresolved simulations and therefore travel further from the plates. The comparison with the PDF obtained using half of the time series reveals that the differences in the PDFs are not due to a lack of averaging, but due to insufficient grid resolutions. We note that we observe similar differences at other radial positions, only the averaging around the cylinder axis ($r = 0$) leads to not fully converged results due to the cylindrical geometry. In figure 2.4 we show the effect of the grid resolution on the flatness $F = \langle(\theta - \langle\theta\rangle)^4\rangle / \langle(\theta - \langle\theta\rangle)^2\rangle^2$ obtained at mid height for the better resolved and underresolved simulations. Comparison between the solid and dashed lines show that the data are converged close to the sidewall where the statistics is best due to geometric reason. Comparison between black (well resolved) and red (underresolved) reveals that the insufficiently dissipated plumes mainly close to the sidewall leads to too large flatnesses in the underresolved simulations.

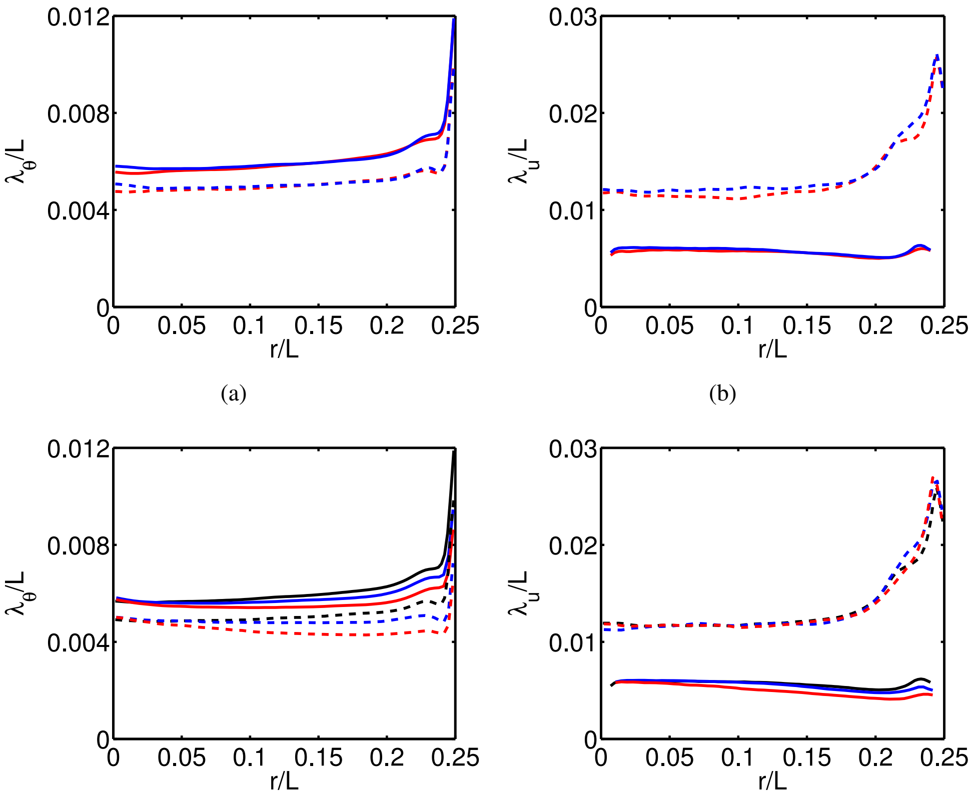

(a) (b)

(c) (d)

Figure 2.6: Azimuthally averaged BL thicknesses as function of the radial position for $Ra = 2 \times 10^9$. Figure 2.6a and b show data from the high resolution simulation ($385 \times 97 \times 385$). a) The solid line indicates λ_θ^{sl} and the dashed lines λ_θ^{rms}, where red and blue indicate the bottom and top plate, respectively. b) The solid line indicates $\lambda_u^{\epsilon_u''}$ and the dashed line λ_u^{rms} based on the azimuthal velocity (colors as in figure 2.6a). c) Now the colors indicate the different grid resolutions: Red ($129 \times 65 \times 257$), blue ($193 \times 65 \times 257$), and black ($385 \times 97 \times 385$). The solid lines indicate λ_θ^{sl} and the dashed lines λ_θ^{rms}. The data for the bottom and top BL are averaged for clarity. Note that the BL is thicker (especially close to the sidewall) in the higher resolution simulations, which is in agreement with the observed Nu trend. d) The solid lines indicate $\lambda_u^{\epsilon_u''}$ and the dashed lines λ_u^{rms} based on the azimuthal velocity for the different grid resolutions (colors as in figure 2.6c).

2.4 Boundary layers

Although the bulk is turbulent, scalingwise the BLs still behave in a laminar way due to the small BL Reynolds number [20]. In figure 2.5 we compare the thermal BL profile obtained from the simulations with the Prandtl-Blasius (PB) profile, as done by Sugiyama et al. [106] for $2D$ RB simulations. The temperature gradient of the PB profile is matched to the temperature gradient obtained in the high resolution simulation. The temperature profile obtained in the simulations best matches the PB profile around the cylinder axis ($r = 0$). Close to the sidewall the agreement is worse due to the rising (falling) plumes in this region. We therefore compare the difference between the PB profile and the result obtained from the simulation for different *Ra*. We determine, at the cylinder axis, $(\theta_{sim}\text{-}\theta_{PB})/(\Delta\text{-}\theta_{PB})$ for the bottom BL and $(\theta_{PB}\text{-}\theta_{sim})/(\theta_{PB})$ for the top BL. Here θ_{sim} is the mean temperature at a distance λ_θ^{sl} from the plate and θ_{PB} the temperature according to PB at this height, after having matched the gradient at the plate to the simulation data. If the simulation exactly matched PB (e.g. for very small *Ra*), this expression would be zero. In contrast 0.103, (0.130, 0.149) is obtained for $Ra = 2 \times 10^8$, (2×10^9, 2×10^{10}). As expected, the expression is smaller for the lower *Ra* numbers. We perform the same procedure for the results of chapter 6 at $Ra = 1 \times 10^8$ with $\Gamma = 1$ and now different *Pr*. For $Pr = 0.7$, $Pr = 6.4$, and $Pr = 20$ we now obtain 0.099, 0.040, and 0.033, respectively. Now the expression is closest to zero at the highest *Pr*, where the *Re* number of the flow is lowest and thus the flow better fulfills the assumptions of the PB approximation. The agreement with the PB profile becomes less when the distance from the plate is larger due to the rising (falling) plumes in this region. This phenomenon is discussed in detail by Sugiyama et al. [106].

Figure 2.6 shows the radial dependence of λ_θ^{sl}, λ_θ^{rms} (thermal BL thickness based on maximum rms value). First we determined the kinetic BL thickness by looking at λ_u^{rms} (kinetic BL thickness based on maximum azimuthal rms velocity). Although this definition is widely used in the literature it is clear that it overestimates the kinetic BL thickness because for $Pr = 0.7$ the kinetic BL thickness is smaller than the thermal BL thickness. One can see this in figure 2.2 where the BL region, indicated in red, is smaller for the kinetic BL than for the thermal BL. Therefore we also determine the kinetic BL thickness by looking at the axial profile of the kinetic energy dissipation. We define $\lambda_u^{\varepsilon''_u}$ (kinetic BL thickness defined as the axial position of the maximum value of ε''_u, multiplied by 2) because this definition selects the region where ε''_u is highest and it is this region where a particular good resolution is required. Such defined kinetic BL thickness now well agrees with that of the thermal BL, $\lambda_u^{\varepsilon''_u} \approx \lambda_\theta^{sl}$, as expected from PB theory for $Pr \approx 1$. Figure 2.6 shows that for both definitions the kinetic BL becomes thicker closer to the sidewall. This is due to the plumes traveling along the sidewall and lower velocities very close to the sidewall. We note that therefore very close to the sidewall the definition of $\lambda_u^{\varepsilon''_u}$ misrepresents the BL thickness. Thus the enhanced grid resolution in the vertical direction near the plates is most important around the cylinder axis ($r = 0$). In contrast, the azimuthal (and radial) resolution are most important to properly resolve the flow close to the sidewall. Note that the difference in the BL thicknesses between the fully resolved and underresolved simulations is largest close to the sidewall, demonstrating that this is indeed a delicate region from a resolution point of view.

2.5 Conclusions

In summary, results from DNS with sufficient resolution using constant temperature boundary conditions for the horizontal plates are in good agreement with the experimental data, see figure 2.1. Previous DNS results showed a Nu number that was up to 30% higher than the experimental results. The new simulations have been performed with much higher resolution than the previous simulations to properly resolve the plume dynamics. Because in underresolved simulations the hot (cold) plumes travel further from the bottom (top) plate than in the better resolved ones, due to insufficient thermal dissipation close to the sidewall (where the grid cells are largest), the Nusselt number is overestimated in underresolved simulations. It thus is crucial to properly resolve the plume dynamics to accurately determine the Nusselt number and based on the simulations we have defined the resolution criteria that have to be fulfilled to have a fully resolved DNS simulation. When the simulation is not fully resolved the exact relation $\varepsilon_\theta = \kappa\Delta^2 Nu/L^2$ for the thermal dissipation rate does not hold. This is because the temperature gradients are smeared out in underresolved simulations leading to an underestimation of the thermal dissipation rate. We also showed that there is a strong radial dependence of the BL structures. At the cylinder axis (r=0) the temperature profile obtained in the simulations agrees well with the PB case, whereas close to the sidewall the agreement is worse due to rising (falling) plumes in this region.

3

Prandtl and Rayleigh number dependence of heat transport in high Rayleigh number thermal convection [*]

Results from direct numerical simulation for three-dimensional Rayleigh-Bénard convection in samples of aspect ratio $\Gamma = 0.23$ *and* $\Gamma = 0.5$ *up to Rayleigh number* $Ra = 2 \times 10^{12}$ *are presented. The broad range of Prandtl numbers* $0.5 < Pr < 10$ *is considered. In contrast to some experiments, we do not see any increase in* $Nu/Ra^{1/3}$*, neither due to Pr number effects, nor due to a constant heat flux boundary condition at the bottom plate instead of constant temperature boundary conditions. Even at these very high Ra, both the thermal and kinetic boundary layer thicknesses obey Prandtl-Blasius scaling.*

3.1 Introduction

Most experiments for $Ra \gtrsim 2 \times 10^{11}$ are performed in samples with aspect ratios $\Gamma \equiv D/L = 0.5$ and $\Gamma = 0.23$ samples. The majority of these experiments are performed with liquid helium near its critical point [35–38, 43, 60, 61]. While [35, 36] and [37] found a Nu increase with $Nu \propto Ra^{0.31}$, the experiments by [38] and [43, 60, 61] gave a steep Nu increase with $Nu \propto Ra^{0.38}$. In these helium experiments the Pr number

---

[*] Based on : R.J.A.M. Stevens, D. Lohse, R. Verzicco, Prandtl and Rayleigh number dependence of heat transport in high Rayleigh number thermal convection, submitted to J. Fluid. Mech. (2011).

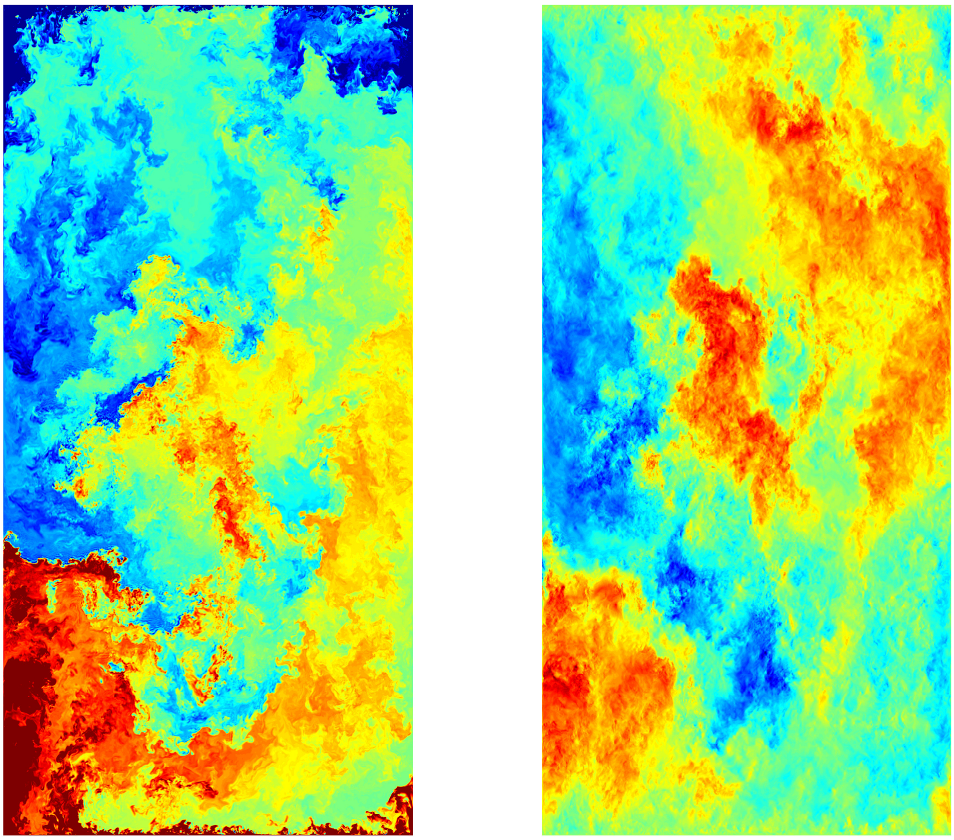

Figure 3.1: Visualization of the instantaneous temperature (left) and vertical velocity field (right) for the simulation at $Ra = 2 \times 10^{12}$ and $Pr = 0.7$ for $\Gamma = 0.5$. Red and blue indicate warm (up flowing) and cold (down flowing) fluid, respectively, in the left (right) panel. See also movie 3.1 in the supplementary material [115].

increases with increasing Ra. [39] and [40, 41] performed measurements around room temperature with high pressurized gases with nearly constant Pr and do not find such a steep increase. [120] found two $Nu \propto Ra^{1/3}$ branches in a $\Gamma = 1$ sample. The high Ra number branch is 20% higher than the low Ra number branch. By necessity, Nu increases more steeply in the transition region. The scaling in the transition region happens to be around $Nu \propto Ra^{0.5}$. There are thus considerable differences in the heat transfer obtained in these different experiments in the high Ra number regime. Very recently, Ahlers and coworkers (see [42] and addendum to [41]) even found two different branches in *one* experiment with the steepest branch going as $Nu \propto Ra^{0.36}$.

There is no clear explanation for this disagreement although it has been conjectured that variations of the Pr number, the use of constant temperature or a constant heat flux condition at the bottom plate, the finite conductivity of the horizontal plates

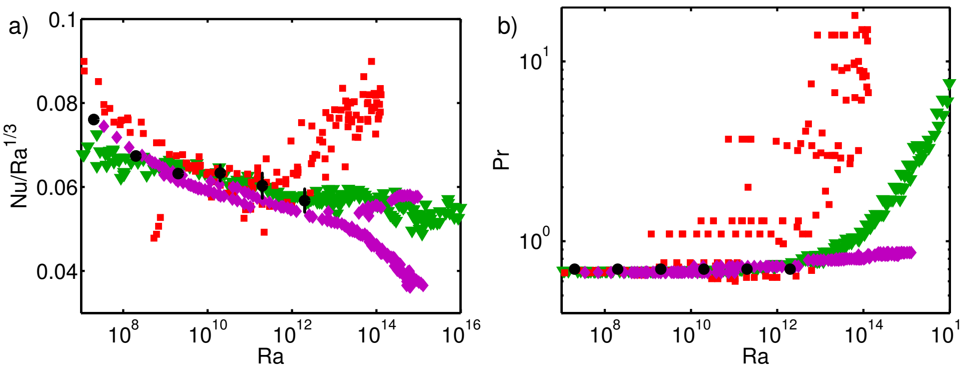

Figure 3.2: (a) *Nu* vs *Ra* for $\Gamma = 0.5$. The green downward pointing triangles are experimental data from [35, 36] after a reanalysis reported in [37], the red squares are from [38], the purple diamonds are from [39] and [40–42]. The DNS results for $Pr = 0.7$ are indicated in black and are from [121]. The data point for $Ra = 2 \times 10^{12}$ is from this study. When the vertical error bar is not visible the error is smaller than the dot size. (b) Parameter space for the data presented in panel a. Symbols as in panel a.

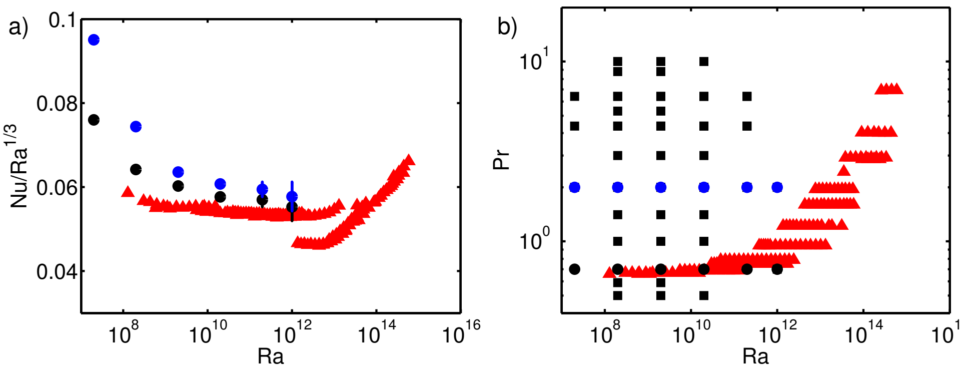

Figure 3.3: (a) *Nu* vs *Ra* for $\Gamma = 0.23$. The upward pointing red triangles are from [43]. The DNS results for $Pr = 0.7$ and $Pr = 2.0$ are indicated in black and blue, respectively. When the vertical error bar is not visible the error is smaller than the dot size. (b) Parameter space for the data presented in panel a. Symbols as in panel a. The black squares indicate DNS simulations presented in this chapter.

and side wall, non Oberbeck-Boussinesq effects, i.e. the dependence of the fluid properties on the temperature, the existence of multiple turbulent states [63], and even wall roughness and temperature conditions outside the sample might play a role. Since the above differences among experiments might be induced by unavoidable technicalities in the laboratory set–ups, within this context, direct numerical simulations are the only possibility to obtain neat reference data that strictly adhere to the intended theoretical problem and that could be used as guidelines to interpret the experiments: This is the main motivation for the present study.

We start this chapter with a description of the numerical procedure that is used to

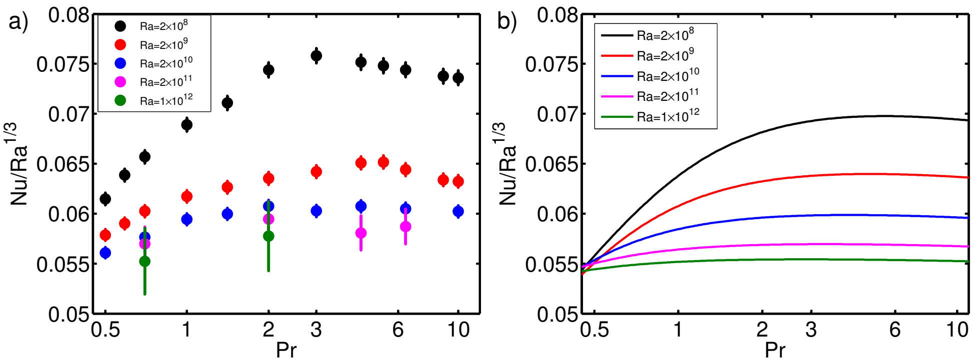

Figure 3.4: Nu vs Pr. The results for $Ra = 2\times10^8$, $Ra = 2\times10^9$, $Ra = 2\times10^{10}$, $Ra = 2\times10^{11}$ and $Ra = 10^{12}$ are indicated in black, red, blue, purple, and dark green, respectively. Panel a gives the DNS results for $\Gamma = 0.23$ and panel b the prediction from the GL model for $\Gamma = 1$. The slight decrease of Nu for $Pr \geq 3$ and not too large Ra is also seen in experiments [122, 123].

investigate the influence on the heat transfer for two of the issues mentioned above. First, we discuss the effect of the Pr number on the heat transport in the high Ra number regime. Subsequently, we will discuss the difference between simulations performed with a constant temperature at the bottom plate with simulations with a constant heat flux at the bottom plate. We take the constant heat flux condition only at the bottom plate, because in real setups the bottom plate is in contact with a heater while the top plate is connected to a thermostatic bath. Thus, the condition of constant heat flux applies at most only to the bottom plate [35–37]. At the top plate constant temperature boundary conditions are assumed to strictly hold, i.e., perfect heat transfer to the recirculating cooling liquid. We will conclude the chapter with a brief summary, discussion, and outlook to future simulations.

3.2 Numerical procedure

The flow is solved by numerically integrating the three-dimensional Navier-Stokes equations within the Boussinesq approximation. The numerical method is already described in [57, 109, 124] and chapter 2 and here it is sufficient to mention that the equations in cylindrical coordinates are solved by central second-order accurate finite-difference approximations in space and time. We performed simulations with constant temperature conditions at the bottom plate for $2\times10^7 < Ra < 1\times10^{12}$ and $0.5 < Pr < 10$ in an aspect ratio $\Gamma = 0.23$ sample. We also present results for a simulation at $Ra = 2\times10^{12}$ at $Pr = 0.7$ in a $\Gamma = 0.5$ sample. In addition, we performed simulation with a constant heat flux at the bottom plate and a constant temperature at the top plate [57] for $Pr = 0.7$, $\Gamma = 0.5$, and $2\times10^6 \leq Ra \leq 2\times10^{11}$. Because in all simulations the temperature boundary conditions are precisely assigned, the surfaces are infinitely smooth, and the Boussinesq approximation is unconditionally valid, the simulations provide a clear reference case for present and future experiments.

In chapter 2 we investigated the resolution criteria that should be satisfied in a fully resolved DNS simulation. In chapter 4 the minimal number of nodes that should be placed inside the boundary layers is determined. The resolutions used here are based on this experience and we stress that in this chapter we used even better spatial resolution than in chapter 2 to be sure that the flow is fully resolved.

To give the reader some idea of the scale of this study we mention the resolutions that were used in the most demanding simulations, i.e., simulations that take at least 100.000 DEISA CPU hours each. For $\Gamma = 0.23$ this are the simulations at $Ra = 2 \times 10^{11}$, which are performed on either a $641 \times 185 \times 1281$ (azimuthal, radial, and axial number of nodes) grid for $Pr = 0.7$ and $Pr = 2.0$ or on a $769 \times 257 \times 1537$ grid for $Pr = 4.38$ and $Pr = 6.4$. The simulations at $Ra = 1 \times 10^{12}$ are performed on a $1081 \times 301 \times 2049$ grid. The simulations for $Ra = 2 \times 10^{11}$ were run for at least 100 dimensionless time units (defined as $L/\sqrt{\beta g \Delta L}$), while these simulations at $Ra = 1 \times 10^{12}$ cover about $30 - 40$ time units. The simulation with a constant heat flux condition at the bottom plate and constant temperature condition at the top plate in a $\Gamma = 0.5$ sample with $Pr = 0.7$ at $Ra = 2.25 \times 10^{11}$ is performed on a $1081 \times 351 \times 1301$ grid. The simulation at $Ra = 2 \times 10^{12}$ with $Pr = 0.7$ in the $\Gamma = 0.5$ sample has been performed on a $2701 \times 671 \times 2501$ grid, which makes it the largest fully bounded turbulent flow simulation ever. This simulation takes about 100.000 vectoral CPU hours on HLRS (equivalent to $\approx 9 \times 10^6$ DEISA CPU hours). To store one snapshot of the field (T, u_1,u_3, because u_2 follows from continuity) costs 160 GB in binary format. A snapshot of this flow is shown in figure 3.1. Movies of this simulation are included in the supplementary material

3.3 Prandtl number dependence

In figure 3.2a and figure 3.3a the DNS results for $Pr = 0.7$ in the $\Gamma = 0.23$ and $\Gamma = 0.5$ samples are compared with experimental data. The result for $Ra = 2 \times 10^{12}$ in the $\Gamma = 0.5$ sample agrees well with the experimental data of Niemela et al. [35–37] and Ahlers et al. [39–41], while there is a visible difference with the results of Chavanne et al. [38]. A comparison of the results for $\Gamma = 0.23$ with the experimental data of Roche et al. [43] shows that there is a good agreement for higher Ra numbers, while for lower Ra we obtain slightly larger Nu than in those experiments. We again stress that we performed resolution checks for this $\Gamma = 0.23$ case (up to $Ra = 2 \times 10^{10}$), and in addition considering the good agreement with the results for $\Gamma = 0.5$, we exclude that our DNS results overestimate Nu.

Figure 3.2b and figure 3.3b shows that in some experiments the Pr number increases with increasing Ra. This difference in Pr is often mentioned as one of the

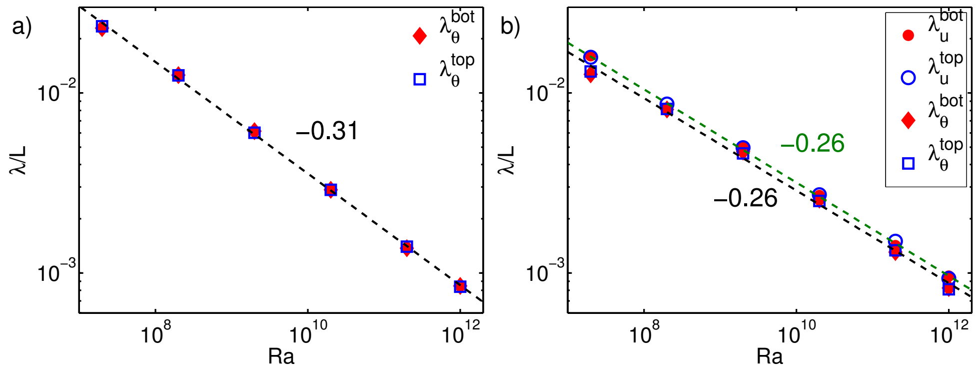

Figure 3.5: BL thicknesses for $Pr = 0.7$ in the $\Gamma = 0.23$ sample. a) The thermal BL thickness close to the bottom and top plate averaged over the entire horizontal area scales with $Ra^{-0.31}$ (black dashed line) b) The kinetic (dark green line) and thermal (black line) BL thicknesses averaged between $0.25D/2 < r < 0.50D/2$ scale with $Ra^{-0.26}$. Note that this is slightly less than in figure 3.5, when we average λ_θ over the full area.

possible causes for the observed differences in the heat transfer between the experiments. Figure 3.4 shows the Nu number as function of Pr for different Ra. This figure shows that the effect of the Pr number on the heat transfer decreases with increasing Ra. This means that the differences in the heat transport that are observed between the experiments for $Ra \gtrsim 10^{11}$, see figure 3.2a, are not a Pr number effect. This is in agreement with the theoretical prediction of the GL-model for $\Gamma = 1$, which is shown in figure 3.4.

3.4 Scaling of thermal and kinetic boundary layers

We determined the thermal and kinetic BL thickness for the simulations in the $\Gamma = 0.23$ sample. The horizontally averaged thermal BL thickness (λ_θ) is determined from $\lambda_\theta^{sl}(r)$, where $\lambda_\theta^{sl}(r)$ is the intersection point between the linear extrapolation of the temperature gradient at the plate with the behavior found in the bulk [125]. In figure 3.5a it is shown that the scaling of the thermal BL thickness is consistent with the Nu number measurements when the horizontal average is taken over the entire plate.

The horizontally averaged kinetic BL thickness (λ_u) is determined from $\lambda_u^{''}(r)$, where $\lambda_u^{''}(r)$ is based on the position where the quantity $\epsilon_u^{''} := \mathbf{u} \cdot \nabla^2 \mathbf{u}$ reaches its maximum. We use this quantity as [121] and [126] showed that it represents the kinetic BL thickness better than other available methods. [121, 125] also explained that this quantity cannot be used close to the sidewall as here it misrepresents the kinetic BL thickness. For numerical reasons, it can neither be calculated accurately in the center region. To be on the safe side we horizontally average the kinetic BL

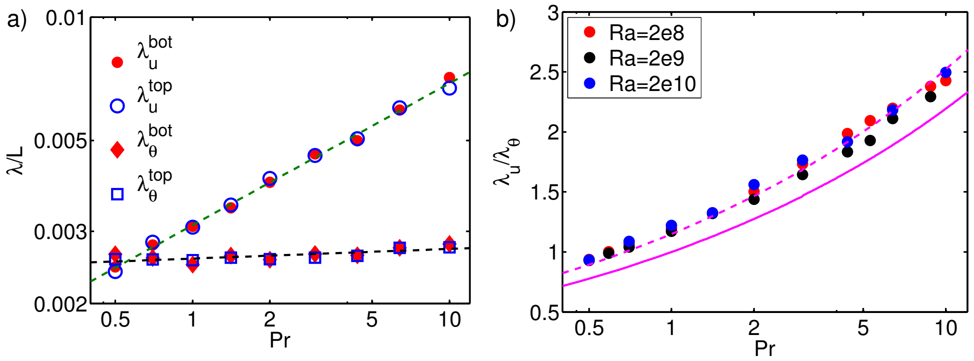

Figure 3.6: a) Kinetic and thermal BL thicknesses close to the bottom and top plate for $Ra = 2 \times 10^{10}$ for $\Gamma = 0.23$. b) The ratio between the kinetic and thermal BL thickness as function of Pr for different Ra for $\Gamma = 0.23$. The green solid line indicates the prediction from the Prandtl-Blasius theory [126]. The magenta dashed line, which lies 15% above the theoretical prediction, is a guide to the eye. All numerical data are horizontally averaged for $0.25D/2 < r < 0.50D/2$.

between $0.25D/2 < r < 0.50D/2$, where D indicates the diameter of the cell and all given values refer to that used.

Figure 3.5b reveals that for $Pr = 0.7$ the kinetic and thermal BL thickness have the same scaling and thickness over a wide range of Ra. In figure 3.6b the ratio λ_u/λ_θ is compared with results of the Prandtl-Blasius BL theory. We find a *constant* difference of about 15% between the numerical results and the theoretical PB type prediction, see e.g. [126]. We emphasize that this is a good agreement, because the PB BL. theory is for parallel flow over a infinitely flat plat plate, while in a aspect ratio $\Gamma = 0.23$ cell one can hardly find a region of parallel flow. Thus even for these large Ra numbers the scaling and the ratio of the kinetic and thermal boundary layer thickness are well described by Prandtl-Blasius BL theory. This result agrees with the experimental results of [127] and [33]. Indeed, [127] showed that the kinetic BL near the sidewall obeys the scaling law of the Prandtl-Blasius laminar BL and [33] showed the same for the boundary layers near the bottom plate. Recently, [34, 128] have developed a method of expressing velocity profiles in the time-dependent BL frame and found that not only the scaling obeys the PB expectation, but even the rescaled velocity and temperature profiles From all this we can exclude that at $Ra \lesssim 10^{12}$ the BL is turbulent.

3.5 Constant heat flux at bottom plate

It has also been argued that the different boundary conditions at the bottom plate, i.e. that some experiments are closer to a constant temperature boundary condition, and some are closer to a constant heat flux boundary condition, might explain the

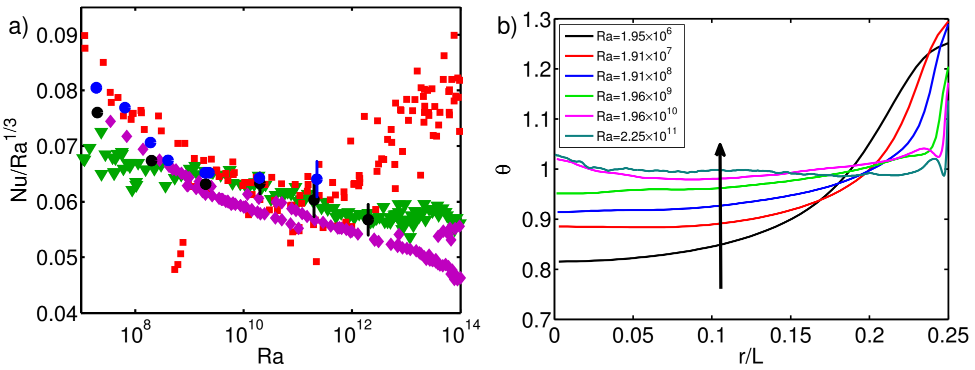

Figure 3.7: a) Nu vs Ra for $\Gamma = 0.5$. Data as in figure 3.2a. The numerical data for $Pr = 0.7$ with constant heat flux at the bottom and constant temperature at the top plate are indicted in blue and the numerical data with constant temperature condition at both plates in black. b) Time-averaged temperature at the bottom plate for simulations with constant heat flux at the bottom plate and constant temperature at the top plate. The arrow indicates the direction of increasing Ra.

differences in the heat transport that are observed in the high Ra number regime. Figure 3.7a compares the Nu number in the simulations with constant temperature and constant heat flux at the bottom plate. The figure shows that the difference between these both cases is small and even decreases with increasing Ra. For large Ra no difference at all is seen within the (statistical) error bars, which however increase due to the shorter averaging time (in terms of large eddy turnovers) at the very large $Ra \geq 2 \times 10^{11}$.

Figure 3.7b shows the time-averaged temperature of the bottom plate in the simulations with constant heat flux at the bottom plate for different Ra. The radial dependence at the lower Ra numbers can be understood from the flow structure in the sample: Due to the large scale circulation the fluid velocities are largest in the middle of the sample. Thus in the middle more heat can be extracted from the plate than close to the sidewall where the fluid velocities are smaller. It is the lack of any wind in the corners of the sample that causes the relative high time-averaged plate temperature there. The figure also shows that this effect decreases with increasing Ra. The reason for this is that the turbulence becomes stronger at higher Ra and this leads to smaller flow structures. Therefore the region close to the sidewall with relative small fluid velocities decreases with increasing Ra and this leads to a more uniform plate temperature at higher Ra. This effect explains that the simulations with constant temperature and constant heat flux condition at the bottom plate become more similar with increasing Ra.

The small differences between the simulations with constant temperature and constant heat flux at the bottom plate show that the differences between the experiments in the high Ra number regime can not be explained by different plate conductivity properties. This finding is in agreement with the results of Johnston and Doering [58]. In their periodic two-dimensional RB simulations the heat transfer for simulations with constant temperature and constant heat flux (both at the bottom and the top plate) becomes equal at $Ra \approx 5 \times 10^6$. For the three-dimensional simulations the heat transfer for both cases also becomes equal, but at higher Ra. This is due to the geometrical effect discussed before, see figure 3.7b, that cannot occur in periodic two-dimensional simulations [58].

3.6 Conclusions

In summary, we presented results from three-dimensional DNS simulations for RB convection in cylindrical samples of aspect ratios $\Gamma = 0.23$ and $\Gamma = 0.5$ up to $Ra = 2 \times 10^{12}$ and a broad range of Pr numbers. The simulation at $Ra = 2 \times 10^{12}$ with $Pr = 0.7$ in an aspect ratio $\Gamma = 0.5$ sample is in good agreement with the experimental results of Niemela *et al.* [35–37]. and Ahlers *et al.* [39–41], while there is a visible difference with the results of Chavanne *et al.* [38]. In addition, we showed that the differences in the heat transfer observed between experiments for $Ra \gtrsim 2 \times 10^{11}$ can neither be explained by Pr number effects, nor by the assumption of constant heat flux conditions at the bottom plate instead of constant temperature conditions. Furthermore, we demonstrated that the scaling of the kinetic and thermal BL thicknesses in this high Ra number regime is well described by the Prandtl-Blasius theory.

Several questions remain: Which effect is responsible for the observed difference in Nu vs Ra scaling in the various experiments? Are there perhaps different turbulent states in the highly turbulent regime as has been suggested for RB flow by [63], but also for other turbulent flows in closed systems by [129]? At what Ra number do the BLs become turbulent? As in DNSs both the velocity and temperature fields are known in the whole domain (including in the boundary layers where the transition between the states is suggested to take place), they will play a leading role in answering these questions.

4

Boundary layer structure in turbulent thermal convection and its consequences for the required numerical resolution [*]

Results on the Prandtl-Blasius type kinetic and thermal boundary layer thicknesses in turbulent Rayleigh-Bénard convection in a broad range of Pr numbers are presented. By solving the laminar Prandtl-Blasius boundary layer equations, we calculate the ratio of the thermal and kinetic boundary layer thicknesses, which depends on the Pr number only. It is approximated as $0.588Pr^{-1/2}$ *for* $Pr \ll Pr^*$ *and as* $0.982Pr^{-1/3}$ *for* $Pr^* \ll Pr$*, with* $Pr^* \equiv 0.046$*. Comparison of the Prandtl-Blasius velocity boundary layer thickness with that evaluated in the direct numerical simulations presented in chapter 2 gives very good agreement. Based on the Prandtl-Blasius type considerations, we derive a lower-bound estimate for the minimum number of the computational mesh nodes, required to conduct accurate numerical simulations of moderately high (boundary layer dominated) turbulent Rayleigh-Bénard convection, in the thermal and kinetic boundary layers close to bottom and top plates. It is shown that the number of required nodes within each boundary layer depends on Nu and Pr and grows with* $\sim Ra^{0.15}$*. This estimate agrees excellently with empirical results, which were based on the convergence of the Nusselt number in numerical simulations.*

---

[*] Based on: O. Shishkina, R. J. A. M Stevens, S. Grossmann, D. Lohse, Boundary layer structure in turbulent thermal convection and its consequences for the required numerical resolution, New J. Phys. 12, 075022 (2010).

4.1 Introduction

Major progress in the understanding of the Rayleigh–Bénard (RB) system has been made over the last decades, see e.g. the recent reviews [20, 21]. Meanwhile it has been well established that the general heat transfer properties of the system, i. e. $Nu = Nu(Ra, Pr)$ and $Re = Re(Nu, Pr)$, are well described by the Grossmann–Lohse (GL) theory [25–28]. In that theory, in order to estimate the thicknesses of the kinetic and thermal boundary layers (BL) and the viscous and thermal dissipation rates, the boundary layer flow is considered to be scalingwise laminar Prandtl–Blasius flow over a plate. Here we use the conventional definitions for the Ra and Pr number, see chapter 1. The Reynolds number $Re = UH/\nu$ is defined with the wind amplitude U which forms in the bulk of the RB container.

The assumption of a laminar boundary layer will break down if the shear Reynolds number Re_s in the BLs becomes larger than approximately 420 [24]. Most experiments and direct numerical simulations (DNS) currently available are in regimes where the boundary layers are expected to be still (scalingwise) laminar, see [20]. Indeed, experiments have confirmed that the boundary layers scalingwise behave as in laminar flow [33], i.e., follow the *scaling predictions* of the Prandtl–Blasius theory [24, 30, 130–133]. In chapter 13 and Ref. [34] it is shown that not only the scaling of the thickness, but also the experimental and numerical *boundary layer profiles* in Rayleigh–Bénard convection agree perfectly with the Prandtl–Blasius profiles, if they are evaluated in the time dependent reference frames, based on the respective *momentary* thicknesses. This confirms that the Prandtl–Blasius boundary layer theory is indeed the relevant theory to describe the boundary layer dynamics in Rayleigh–Bénard convection for not too large Re_s.

The aim of this chapter is to explore the consequences of the Prandtl–Blasius theory for the required numerical grid resolution of the BLs in DNSs. Hitherto, convergence checks can only be done *a posteriori*, by checking whether the Nusselt number does not considerably change with increasing grid resolution, see Refs. [112, 118, 124, 134, 135] and chapter 2 or by guaranteeing (e.g. in ref. [48] and chapter 2) that the Nusselt numbers calculated from the global energy dissipation rate or thermal dissipation rate well agree with that one calculated from the temperature gradient at the plates or the ones obtained from the overall heat flux. The knowledge that the profiles are of Prandtl–Blasius type offers the opportunity to *a priori* determine the number of required grid points in the BLs for given Rayleigh number and Prandtl number, valid in the boundary layer dominated ranges of moderately high Ra numbers.

In section 4.2 we will first revisit the Prandtl–Blasius BL theory – see refs. [24, 30, 130–133] or for more recent discussions in the context of RB refs. [28, 136] – and derive the ratio between the thermal boundary layer thickness δ_θ and the velocity boundary layer thickness δ_u as functions of the Prandtl number Pr extending previous

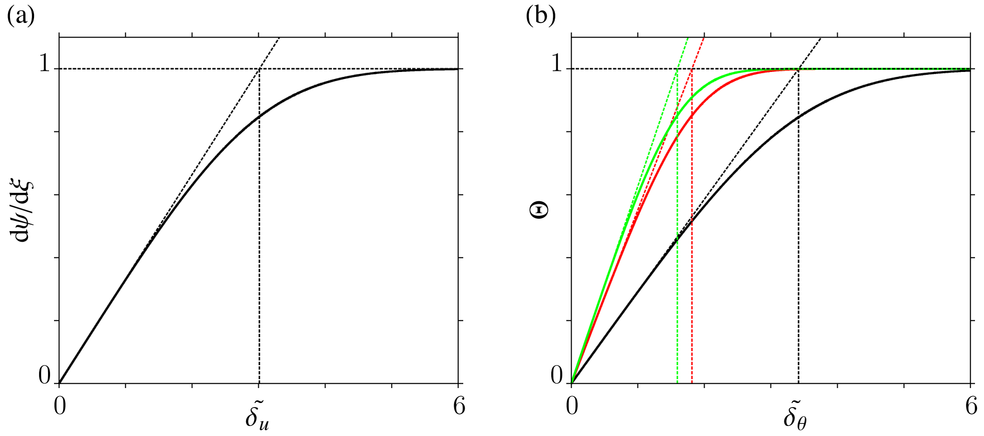

Figure 4.1: Solution of the Prandtl–Blasius equations (4.4)–(4.7): (*a*) Longitudinal velocity profile $\frac{d\Psi}{d\xi}(\xi)$ (solid curve) with respect to the similarity variable ξ. The tangent to the longitudinal velocity profile at the plate ($\xi = 0$) and the straight line $d\Psi/d\xi = 1$ (both dashed lines) intersect at $\xi = \tilde{\delta}_u \equiv A^{-1} \approx 3.012$, for all Pr. We define this value $\tilde{\delta}_u$ as the thickness of the kinetic boundary layer. (*b*) Temperature profile $\Theta(\xi)$ as function of the similarity variable ξ for $Pr = 0.7$ (black solid curve), $Pr = 4.38$ (red solid curve) and $Pr = 6.4$ (green solid curve). The tangents to the profile curves at the plate ($\xi = 0$) and the straight line $\Theta = 1$ (dashed lines) define the edges (thicknesses) of the corresponding thermal boundary layers, i. e., $\xi = \tilde{\delta}_\theta \equiv C(Pr)$. For the presented cases $Pr = 0.7$, 4.38, and 6.4 one has $C(0.7) \approx 3.417$, $C(4.38) \approx 1.814$, and $C(6.4) \approx 1.596$, respectively.

work (section 4.3). We will also discuss the limiting cases for large and small Pr, respectively. The transitional Prandtl number between the two limiting regimes turns out to be surprisingly small, namely $Pr^* = 0.046$. The crossover range is found to be rather broad, roughly four orders of magnitude in Pr. In section 4.4 we note that the Prandtl–Blasius velocity BL thickness is different from the velocity BL thickness based on the position of the maximum r.m.s. velocity fluctuations (widely used in the literature), but well agrees with a BL thickness based on the position of the maximum of an energy dissipation derivate that was introduced in chapter 2 We then derive the estimate for the minimum number of grid points that should be placed in the boundary layers close the top and bottom plates, in order to guarantee proper grid resolution. Remarkably, the number of grid points that must have a distance smaller than δ_u from the wall *increases* with increasing Ra, roughly as $\sim Ra^{0.15}$. This estimate is compared with *a posteriori results* for the required grid resolution obtained in various DNSs of the last three decades, finding good agreement. Section 4.5 is left to conclusions.

4.2 Prandtl boundary layer equations

The Prandtl–Blasius boundary layer equations for the velocity field $\mathbf{u}(x,z)$ (assumed to be two-dimensional and stationary) over a semi-infinite horizontal plate [24, 30, 130–133] read

$$u_x \partial_x u_x + u_z \partial_z u_x = \nu \partial_z \partial_z u_x, \tag{4.1}$$

with the boundary conditions $u_x(x,0) = 0$, $u_z(x,0) = 0$, and $u_x(x,\infty) = U$. Here $u_x(x,z)$ is the horizontal component of the velocity (in the direction x of the large-scale circulation), $u_z(x,z)$ the vertical component of the velocity (in the direction z perpendicular to the plate), and U the horizontal velocity outside the kinetic boundary layer (wind of turbulence). Correspondingly, the equation determining the (stationary) temperature field $T(x,z)$ reads

$$u_x \partial_x T + u_z \partial_z T = \kappa \partial_z \partial_z T, \tag{4.2}$$

with the boundary conditions $T(x,0) = T_{plate}$ and $T(x,\infty) = T_{bulk}$, which under Oberbeck–Boussinesq conditions is the arithmetic mean of the upper and lower plate temperature. Applying these equations to RB flow implies that we assume the temperature field to be passive.

The dimensionless similarity variable ξ for the vertical distance z from the plate measured at the distance x from the plate's edge is

$$\xi = z\sqrt{\frac{U}{x\nu}}. \tag{4.3}$$

Since the flow in Prandtl theory is two-dimensional, a streamfunction $\hat{\Psi}$ can be introduced, which represents the velocity field. The streamfunction is non-dimensionalized as $\Psi = \hat{\Psi}/\sqrt{x\nu U}$, and the temperature is measured in terms of $\Delta/2$, giving the non-dimensional temperature field Θ. Rewriting eqs. (4.1) and (4.2) in terms of Ψ and Θ one obtains

$$\begin{aligned} d^3\Psi/d\xi^3 + 0.5\Psi d^2\Psi/d\xi^2 &= 0, & (4.4) \\ d^2\Theta/d\xi^2 + 0.5 Pr \Psi d\Theta/d\xi &= 0. & (4.5) \end{aligned}$$

Here the boundary conditions are

$$\begin{aligned} &\Psi(0) = 0, \qquad d\Psi/d\xi(0) = 0, \qquad d\Psi/d\xi(\infty) = 1, & (4.6) \\ &\Theta(0) = 0, \qquad \Theta(\infty) = 1. & (4.7) \end{aligned}$$

The temperature and velocity profiles obtained from numerically solving equations (4.4)–(4.7) (for particular Prandtl numbers) are already shown in textbooks [24, 30, 133] and in the context of RB convection in refs. [136, 137]: From the momentum equation (4.6) with above boundary conditions one immediately obtains the horizontal velocity $d\Psi/d\xi$. The dimensionless kinetic boundary layer thickness $\tilde{\delta}_u$ can be defined as that distance from the plate at which the tangent to the function

$d\Psi/d\xi$ at the plate ($\xi = 0$) intersects the straight line $d\Psi/d\xi = 1$ (see figure 4.1 *a*). As equation (4.4) and the boundary conditions (4.6) contain no parameter whatsoever, the *dimensionless* thickness $\tilde{\delta}_u$ of the kinetic boundary layer with respect to the similarity variable ξ is universal, i.e., independent of *Pr* and *U* or *Re*,

$$\tilde{\delta}_u = A^{-1} \approx 3.012 \quad \text{or} \quad A \approx 0.332. \tag{4.8}$$

Solving numerically equation (4.5) with the boundary conditions (4.7) for any fixed Prandtl number, one obtains the temperature profile with respect to the similarity variable ξ (see figure 4.1 *b*). Note that in contrast to the longitudinal velocity $d\Psi/d\xi$, the temperature profile Θ depends not only on ξ but also on the Prandtl number, since *Pr* appears in equation (4.5) as the (only) parameter. The distance from the plate at which the tangent to the Θ profile intersects the straight line $\Theta = 1$ defines the dimensionless thickness of the thermal boundary layer,

$$\tilde{\delta}_\theta = C(Pr), \tag{4.9}$$

where $C(Pr)$ is a certain function of Prandtl number. E.g. one numerically finds $C \approx 3.417$, 1.814, and 1.596 for $Pr = 0.7$, 4.38, and 6.4, respectively (see figure 4.1 *b*).

From (4.8) and (4.9) one obtains the ratio between the (dimensional) thermal boundary layer thickness δ_θ and the (dimensional) kinetic boundary layer thickness δ_u:

$$\frac{\delta_\theta}{\delta_u} = \frac{\tilde{\delta}_\theta}{\tilde{\delta}_u} = AC(Pr). \tag{4.10}$$

As discussed above, the constant A and the function $C = C(Pr)$ are found from the solutions of equations (4.4)–(4.7) for different *Pr*. A and $C(Pr)$ reflect the slopes of the respective profiles,

$$A = \frac{d^2\Psi}{d\xi^2}(0), \quad C(Pr) = \left[\frac{d\Theta}{d\xi}(0)\right]^{-1}. \tag{4.11}$$

With (4.3) the physical thicknesses are $\delta_u = \tilde{\delta}_u/\sqrt{\frac{U}{x\nu}}$ and $\delta_\theta = \tilde{\delta}_\theta/\sqrt{\frac{U}{x\nu}}$, generally depending on U and the position x along the plate. The *physical* thermal BL thickness then is

$$\delta_\theta = \frac{C(Pr)}{\sqrt{U/(x\nu)}} = \left[\sqrt{\frac{U}{x\nu}}\frac{\partial\Theta}{\partial\xi}(0)\right]^{-1} = \left[\frac{\partial\Theta}{\partial z}(0)\right]^{-1}. \tag{4.12}$$

Thus, explicitly it depends neither on U nor on the position x along the plate. Reminding the definition of the thermal current $J = \langle u_z T\rangle - \kappa\partial_z\langle T\rangle$, we get $\langle \frac{\partial\Theta}{\partial z}(0)\rangle =$

$\frac{1}{\Delta/2}\langle\frac{\partial T}{\partial z}(0)\rangle = \frac{2}{\kappa\Delta}J = 2H^{-1}Nu$, i. e., on x-average we have

$$\delta_\theta = \frac{H}{2Nu}. \tag{4.13}$$

δ_θ is the so-called slope thickness, see Sect. 2.4 of reference [136]. In contrast to the thermal BL thickness δ_θ the physical velocity BL thickness $\delta_u = A^{-1}/\sqrt{\frac{U}{x\nu}}$ depends explicitly both on the position x and on the wind amplitude U. In a Rayleigh–Bénard cell we choose for x a representative value $x = \tilde{a}L = \tilde{a}\Gamma H$. Then the famous Prandtl formula [130] results

$$\delta_u = \frac{aH}{\sqrt{Re}}. \tag{4.14}$$

Here $a = \sqrt{\frac{\tilde{a}\Gamma}{A^2}} = A^{-1}\sqrt{\tilde{a}\Gamma}$. The constant a has been obtained empirically [27], based on the experimental measurements by [138] performed in a cylindrical cell of aspect ratio one, filled with water. The result was [27]

$$a \approx 0.482. \tag{4.15}$$

We note that this value probably depends on the aspect ratio, on the shape of the RB container, and can also be different for numerical 2D Rayleigh–Bénard convection [103, 106, 139]. It will also be different for the slope thickness as considered here or other definitions as e. g. the 99% -thickness.

It seems worthwhile to note that similarly to the case of δ_θ also δ_u can be expressed by a profile slope at the plate. Analogously to the temperature case one calculates for the kinetic thickness $\delta_u = U/\frac{\partial u_x}{\partial z}(0)$. Here U appears explicitly and the derivative may depend on $\mathbf{x}$. The denominator is the local stress tensor component, which – after averaging – describes the momentum transport, just as the temperature profile derivative at the plate characterises the heat transport. In combination with eq. (4.14) it says that the kinetic stress behaves as $\langle\frac{\partial u_x}{\partial z}(0)\rangle \sim U\sqrt{Re}/(aH)$.

From eqs. (4.10) and (4.14) we also find the useful (and known) relation for Prandtl-Blasius boundary layers

$$\delta_\theta = a_\theta C(Pr)\frac{H}{\sqrt{Re}} \quad \text{with} \quad a_\theta = A\cdot a \approx 0.160. \tag{4.16}$$

From solving equations (4.4)–(4.7) together with relations (4.11) one obtains that the BL thickness ratio (4.10) has two limiting cases, namely $\delta_\theta/\delta_u \sim Pr^{-1/2}$ for very small $Pr \ll 1$ and $\delta_\theta/\delta_u \sim Pr^{-1/3}$ for very large $Pr \gg 1$. We thus present the ratio of the thermal and kinetic boundary layer thicknesses normalised by $Pr^{-1/3}$ in figure 4.2 for different Pr from $Pr = 10^{-6}$ to 10^{6}. The figure confirms that the scaling of the ratio between the thermal and kinetic boundary layer thicknesses in the low

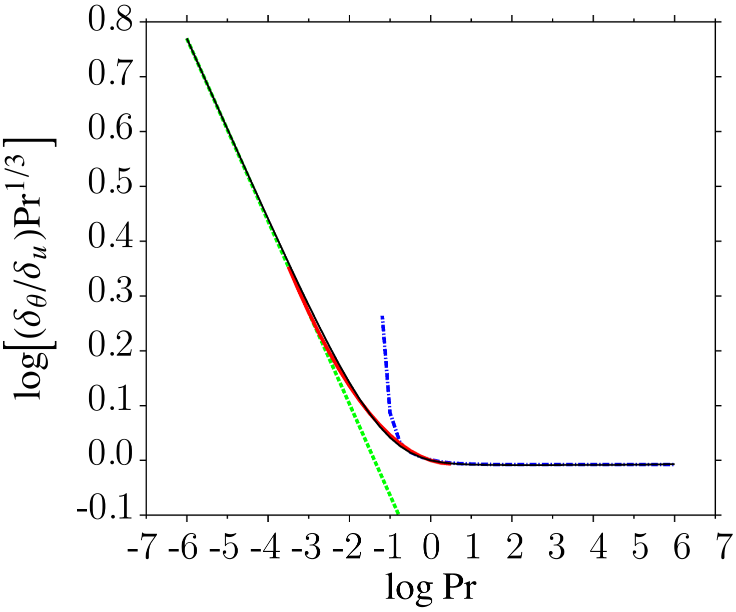

Figure 4.2: Double-logarithmic plot of the ratio of the thermal and kinetic boundary layer thicknesses, normalised by $Pr^{-1/3}$, as obtained from numerical solution of equations (4.4)–(4.7) as function of Pr (solid black line). For large Pr the curve through the data is constant, for small Pr the (plotted, reduced) curve behaves $\propto Pr^{-1/6}$. Approximation (4.22) (green dotted line) is indistinguishable from δ_θ/δ_u in the region $Pr < 3\times 10^{-4}$. Approximation (4.24) (blue dashed-dotted line) well represents δ_θ/δ_u for $Pr > 0.3$; for $Pr > 3$ it practically coincides with approximation (4.25). Approximation (4.26) (red solid curve) connects the analytical approximations in the transition range $3\times 10^{-4} \le Pr \le 3$ between the lower and upper Prandtl number regimes.

and high Prandtl number regimes is $Pr^{-1/2}$ and $Pr^{-1/3}$, respectively. Between these two limiting regimes there is a transition region, whose width is about 4 orders of magnitude in Pr. In the next section we will derive analytic expressions for the ratio δ_θ/δ_u in the respective regimes, which will be used in the remainder of the chapter to analyse the resolution properties for DNS in the BLs of the Rayleigh–Bénard system.

In the Prandtl–Blasius theory the asymptotic velocity amplitude U is a given parameter; the resulting heat current Nu is a performance of the boundary layers only. In contrast, in Rayleigh–Bénard convection the heat transport is determined by the BLs together with the bulk flow. Therefore in RB convection the wind amplitude U no longer is a passive parameter, but U and Nu are actively coupled properties of the full thermal convection process.

The Reynolds number Re is defined as the dimensionless wind amplitude,

$$Re = \frac{UH}{\nu}. \tag{4.17}$$

From the law for the kinetic BL thickness (4.14), the thermal BL thickness δ_θ (4.13), and the BL thickness ratio (4.10) one obtains

$$Re = \left(\frac{aH}{\delta_u}\right)^2 = \left(\frac{\delta_\theta}{\delta_u}\right)^2 \left(\frac{aH}{\delta_\theta}\right)^2 = 4a^2 Nu^2 \left(\frac{\delta_\theta}{\delta_u}\right)^2 . \qquad (4.18)$$

This $Re \sim Nu^2$ law is in perfect agreement with the GL theory [25–28]. In that theory several sub-regimes in the (Ra, Pr) parameter space are introduced, depending on the dominance of the BL or bulk contributions. In regimes I and II the BL of the temperature field dominates, while in III and VI it is the thermal bulk. Regimes I and II differ in the velocity field contributions: It either is the u-BL (I) or the u-bulk (II) which dominates; analogously the pair III and IV is characterized. The labels ℓ (for **l**ower Pr) and u (for **u**pper Pr) distinguish the cases in which the thermal BL is thicker or smaller than the kinetic one. All ranges in the GL theory, which are thermal boundary layer dominated, show the $Re \sim Nu^2$ behaviour, namely I_l, I_u, II_l, II_u. In the thermal bulk dominated ranges of RB convection the relation between Re and Nu is different. In III_u we have $Re \sim Nu^{4/3}$, in IV_l it is $Re \sim Nu$, and in IV_u also $Re \sim Nu^{4/3}$ holds; but here the Prandtl–Blasius result (4.18) is not applicable, since the heat transport mainly depends on the heat transport properties of the bulk. In the range I_∞, although boundary layer dominated, also a different relation ($Re \sim Nu^3$) holds; here the upper and the lower kinetic BLs fill the whole volume and therefore there is no free flow outside the BLs, in contrast to the Prandtl–Blasius assumption of an asymptotic velocity with the LSC amplitude U.

4.3 Approximations for the ratio δ_θ/δ_u

In this section we will derive analytical approximations for the ratio δ_θ/δ_u for the three regimes identified in the previous section, cf. figure 4.2. We start by discussing the low ($Pr < 3 \times 10^{-4}$) and the high ($3 < Pr$) Prandtl number regimes, before we discuss the transition region $3 \times 10^{-4} \leq Pr \leq 3$.

4.3.1 Approximation of δ_θ/δ_u for $Pr < 3 \times 10^{-4}$

In the case of very small Prandtl number, $Pr \ll 1$, the thickness of the velocity boundary layer is negligible compared with the thickness of the temperature boundary layer, i.e., $\delta_\theta \gg \delta_u$. Hence, in most of the thermal boundary layer it is $u_x \approx U$. Introducing the similarity variable as in ref. [30]

$$\eta = \frac{z}{2}\sqrt{\frac{U}{x\kappa}}, \qquad (4.19)$$

one obtains the following equation for the temperature as a function of η:

$$d^2\Theta/d\eta^2 + 2\eta\, d\Theta/d\eta = 0, \quad \text{with} \quad \Theta(0) = 0, \quad \Theta(\infty) = 1.$$

The solution of this boundary value problem is the Gaussian error function

$$\Theta(\eta) = \operatorname{erf}(\eta) \equiv \frac{2}{\sqrt{\pi}} \int_0^\eta e^{-t^2} dt. \tag{4.20}$$

According to (4.3) and (4.19), the similarity variable ξ used in the Prandtl equations and the similarity variable η used in the approximation for $Pr \ll 1$ are related as follows

$$\eta = \frac{1}{2} Pr^{1/2} \xi. \tag{4.21}$$

Applying now the formulae (4.20), (4.21) and (4.11) we obtain the following equalities:

$$\frac{2}{\sqrt{\pi}} = \frac{d\Theta}{d\eta}(0) = \frac{d\Theta}{d\xi}(0) \cdot \frac{d\xi}{d\eta} = \frac{1}{C(Pr)} \cdot 2Pr^{-1/2}.$$

This leads to the approximation for the function $C(Pr) = \sqrt{\pi} Pr^{-1/2}$ for very small Pr.

$$\frac{\delta_\theta}{\delta_u} = A\sqrt{\pi} Pr^{-1/2} \approx 0.588 Pr^{-1/2}, \quad Pr \ll 1. \tag{4.22}$$

In figure 4.2 one can see that for very small Prandtl numbers, $Pr < 3 \times 10^{-4}$, the approximation (4.22) is as expected indistinguishable from the numerically obtained δ_θ/δ_u.

4.3.2 Approximation of δ_θ/δ_u for $Pr > 3$

Meksyn [133], based on the work by Pohlhausen [132], derived that the solution of the temperature equation (4.5), together with relation (4.7) equals

$$\Theta\left(\frac{\xi}{\sqrt{2}}\right) = D \int_0^{\xi/\sqrt{2}} e^{-F(t)Pr} dt, \qquad F(t) = \frac{1}{\sqrt{2}} \int_0^t \Psi(q) dq. \tag{4.23}$$

The constant D can be found as usual from the boundary condition at infinity and was approximated in [132, 133] for $Pr > 1$ as follows

$$D = \frac{0.478 Pr^{1/3}}{c(Pr)}, \qquad c(Pr) \approx 1 + \frac{1}{45Pr} - \frac{1}{405Pr^2} + \frac{161}{601425Pr^3} - \ldots$$

From this and (4.23) one derives

$$\frac{0.478 Pr^{1/3}}{c(Pr)} = D = \frac{d\Theta}{d(\xi/\sqrt{2})}(0) = \sqrt{2}\frac{d\Theta}{d\xi}(0) = \frac{\sqrt{2}}{C(Pr)}.$$

This connects $c(Pr)$ and $C(Pr)$ as follows

$$C(Pr) \approx \frac{\sqrt{2}}{0.478} c(Pr) Pr^{-1/3} \approx 2.959 c(Pr) Pr^{-1/3},$$

resulting in the approximation

$$\frac{\delta_\theta}{\delta_u} = AC(Pr) = EPr^{-1/3} c(Pr), \quad E \approx A \frac{\sqrt{2}}{0.478} \approx 0.982. \tag{4.24}$$

For Pr $\gg$ 1, the function $c(Pr)$ approaches 1, hence $C(Pr) \approx 2.959 Pr^{-1/3}$, implying

$$\frac{\delta_\theta}{\delta_u} = EPr^{-1/3}, \quad Pr \gg 1. \tag{4.25}$$

In figure 4.2 the approximation (4.24) is presented as a blue dash-dotted curve. For $Pr > 3$ the function $(\delta_\theta/\delta_u)Pr^{1/3}$ almost coincides with the constant E.

4.3.3 Approximation of δ_θ/δ_u in the crossover range $3 \times 10^{-4} \leq Pr \leq 3$

As one can see in figure 4.2, the approximation (4.22) well represents δ_θ/δ_u in the region $Pr < 3 \times 10^{-4}$, while (4.25) is a good approximation of δ_θ/δ_u for $Pr > 3$. An approximation of the ratio of the thermal and kinetic boundary layer thicknesses in the transition region $3 \times 10^{-4} \leq Pr \leq 3$ is obtained by applying a least square fit to the numerical solutions of the Prandtl–Blasius equations (4.4)-(4.7). One finds:

$$\frac{\delta_\theta}{\delta_u} \approx Pr^{-0.357+0.022\log Pr}, \quad 3 \times 10^{-4} \leq Pr \leq 3. \tag{4.26}$$

As seen in figure 4.2, this relation is a good fit of the full solution in the transition regime.

4.3.4 Summary

For the ratio δ_θ/δ_u of the thicknesses of the thermal and kinetic boundary layers, which depends strongly (and only) on Pr, we find according to (4.22), (4.25), and (4.26)

$$\frac{\delta_\theta}{\delta_u} = \begin{cases} A\sqrt{\pi} Pr^{-1/2},\ A \approx 0.332, & Pr < 3 \times 10^{-4}, \\ Pr^{-0.357+0.022\log Pr}, & 3 \times 10^{-4} \leq Pr \leq 3, \\ E Pr^{-1/3},\ E \approx 0.982, & Pr > 3. \end{cases} \tag{4.27}$$

The crossover Prandtl number Pr^* between the asymptotic behaviours, cf. first and last line of (4.27), is defined as the intersection point $Pr^* = 0.046$ of the asymptotic approximations. Note that this crossover between the small-Pr behaviour $\delta_\theta/\delta_u \propto$

$Pr^{-1/2}$ and the large-Pr behaviour $\delta_\theta/\delta_u \propto Pr^{-1/3}$ does not happen at a Prandtl number of order 1, but at the more than 20 times smaller value $Pr^* = 0.046$. In this sense most experiments are conducted in the large Pr regime. However, also note that other definitions of the BL thicknesses lead to other crossover Prandtl numbers.

Finally, we also give the thickness of the kinetic BL in the three regimes, as obtained from (4.27) and (4.13), namely

$$\delta_u = \begin{cases} 0.5Nu^{-1}Pr^{1/2}A^{-1}\pi^{-1/2}H, & Pr < 3\times 10^{-4}, \\ 0.5Nu^{-1}Pr^{0.357-0.022\log Pr}H, & 3\times 10^{-4} \le Pr \le 3, \\ 0.5Nu^{-1}Pr^{1/3}E^{-1}H, & Pr > 3. \end{cases} \tag{4.28}$$

We compare this Prandtl–Blasius result (4.28) for the kinetic boundary layer thickness in terms of Nu and Pr (thus valid if the heat transport is BL dominated) with the estimate given in chapter 2, where the kinetic boundary layer thickness in a cylindrical cell is identified as two times that height at which the averaged quantity

$$\varepsilon''_u := \langle \mathbf{u} \cdot \nabla^2 \mathbf{u} \rangle_{t,\phi,r} \tag{4.29}$$

has a maximum, because it was empirically found that the maximum of ε''_u is approximately in the middle of the velocity boundary layer. Here $\mathbf{u}$ is the velocity field and the averaging is over time t, the azimuthal direction ϕ, and over the radial direction $0.1R < r < 0.9R$, with R the radius of the cylindrical convective cell. The restricted range for the radial direction has been used in order to exclude the singularity region close to the cylinder axis and the region close to the sidewall, where the definition misrepresents the kinetic boundary layer thickness. Figure 4.3 shows that there is a very good agreement between the theoretical Prandtl–Blasius slope boundary layer thickness and that obtained using (4.29). The figure also shows that the position of the maximum r.m.s. velocity fluctuations is not a good indicator for the velocity boundary layer edge; it rather seems to identify the position where the LSC is the strongest.

4.4 Resolution requirements within the boundary layers

We now come to the main point of this chapter: What can we learn from the Prandtl–Blasius theory for the required mesh resolution in the BLs of DNS of turbulent RB convection? Obviously, a "proper" mesh resolution should be used in order to obtain accurate results. In a perfect DNS the local mesh size should be smaller than the local Kolmogorov $\eta_K(\mathbf{x},t)$ and Batchelor $\eta_B(\mathbf{x},t)$ scales (see e.g. ref. [140]), and the resolution in the boundary layers should be also sufficient, see e.g. Refs. [110, 134, 137, 141] and chapter 2. It indeed has been well established that the Nusselt number is very sensitive to the grid resolution used in the boundary layers; when DNS is underresolved, the measured Nusselt number is too high, see Refs. [44, 57, 109, 110,

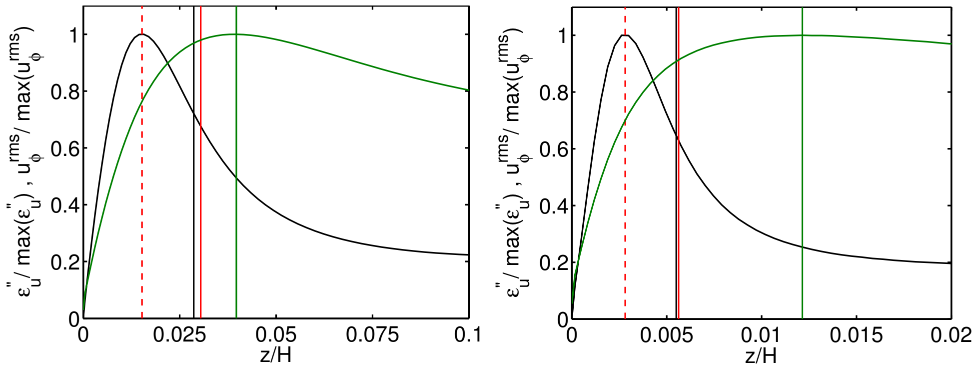

(a) (b)

Figure 4.3: Profiles of ε_u'' (4.29) (black), and the r.m.s. velocity fluctuations for the azimuthal velocity component u_ϕ (green) for (a) $Ra = 10^8$ and $Pr = 6.4$ and (b) $Ra = 2 \times 10^9$ and $Pr = 0.7$. The profiles have been normalised with the respective maxima for clarity. The vertical black lines indicate the velocity boundary layer thickness based on (4.28). The red dashed and solid lines indicate the heights at which the quantity ε_u'' (4.29) has a maximum and two times this height, respectively. The vertical green line indicates the position of the maximum r.m.s. velocity fluctuations.

134, 142] and chapter 2. Hitherto, the standard way to empirically check whether the mesh resolution is sufficient is to try a finer mesh and to make sure that the Nusselt number is not too different. In this way the minimal number of grid points that is needed in the boundary layer is obtained by trial and error: Grötzbach [110] varied the number of grid points in the boundary layer between 1 and 5 in simulations up to $Ra = 3 \times 10^5$ with $Pr = 0.71$ and found that 3 grid points in the boundary layers should be sufficient. Verzicco and Camussi [109] tested this at $Ra = 2 \times 10^7$ and $Pr = 0.7$ and stated that at least 5 points should be placed in the boundary layers. In chapter 2 several the grid resolution for $Ra = 2 \times 10^6$ to 2×10^{11} and $Pr = 0.7$ are tested. Here it is found that for $Ra = 2 \times 10^9$ the minimum number of nodes in the boundary layers should be around 10 and that this number increases for increasing Ra. Together with the earlier series of papers the data clearly suggest that indeed there is an increase of required grid points in the BL with increasing Rayleigh number.

However, one must be careful. The empirical determination of the required number of grid points in the BL is not only intensive in computational cost, but also difficult. The Nusselt number obtained in the simulations not only depends on the grid resolution in the BLs at the top and bottom plates, but also on the grid resolution in the *bulk* and at the side walls where the thermal plumes pass along (see chapter 2). So obviously a general theory-based criterion for the required grid resolution in the thermal and kinematic boundary layers will be helpful for performing future simulations. In this section we will derive such a universal criterion, harvesting above results from the Prandtl–Blasius boundary layer theory.

We first define the (local) kinetic energy dissipation rates per mass,

$$\varepsilon_u(\mathbf{x},t) \equiv \frac{\nu}{2}\sum_i\sum_j\left(\frac{\partial u_i(\mathbf{x},t)}{\partial x_j}+\frac{\partial u_j(\mathbf{x},t)}{\partial x_i}\right)^2. \tag{4.30}$$

Its time and space average for incompressible flow with zero velocity b.c. is $\langle\varepsilon_u\rangle_{t,V} = \nu\sum_i\sum_j\langle\left(\frac{\partial u_i(\mathbf{x},t)}{\partial x_j}\right)^2\rangle_{t,V}$. It is connected with the Nusselt number through the exact relation

$$\langle\varepsilon_u\rangle_{t,V} = \frac{\nu^3}{H^4}(Nu-1)RaPr^{-2}. \tag{4.31}$$

This follows directly from the momentum equation for Rayleigh–Bénard convection in Boussinesq approximation [143]. Here, $\langle\cdot\rangle_{t,V}$ denotes averaging over the whole volume of the convective cell and over time and (later) $\langle\cdot\rangle_{t,A}$ denotes averaging over any horizontal plane and time.

We start with the well established criterion that in a perfect DNS simulation the (local) mesh size must not be larger than the (local) Kolmogorov scale [144] $\eta_K(\mathbf{x},t)$, which is locally defined with the energy dissipation rate of the velocity,

$$\eta_K(\mathbf{x},t) = \left(\nu^3/\varepsilon_u(\mathbf{x},t)\right)^{1/4}. \tag{4.32}$$

η_K is the length scale at which the inertial term $\sim u_r^2/r$ and the viscous term $\sim \nu u_r/r^2$ of the Navier-Stokes equation balance, where $u_r \sim (\varepsilon_u r)^{1/3}$ has been assumed for the velocity difference at scale r. A corresponding length scale η_T follows from the balance of the advection term $\sim u_r T_r/r$ and the thermal diffusion term $\kappa T_r/r^2$ in the advection equation; it is

$$\eta_T(\mathbf{x},t) = \left(\kappa^3/\varepsilon_u(\mathbf{x},t)\right)^{1/4} = \eta_K(\mathbf{x},t)Pr^{-3/4}. \tag{4.33}$$

However, for large Pr the velocity field is smooth at those scales at which the temperature field is still fluctuating. Then the velocity difference $u_r \sim \sqrt{\varepsilon_u/\nu}r$ and advection term and thermal diffusion term balance at the so-called Batchelor scale [145] η_B, which is defined as

$$\eta_B(\mathbf{x},t) = \left(\nu\kappa^2/\varepsilon_u(\mathbf{x},t)\right)^{1/4} = \eta_K(\mathbf{x},t)Pr^{-1/2}. \tag{4.34}$$

For small $Pr < 1$ obviously $\eta_T > \eta_B > \eta_K$ and for comparison with the grid resolution, the Kolmogorov scale η_K seems to be the most restrictive (i.e., smallest) length scale. In contrast, for large $Pr > 1$ it $\eta_T < \eta_B < \eta_K$ and one may argue that η_T is the most restrictive length scale. This indeed may be the case in the Prandtl number regime in which the velocity field can still be described through Kolmogorov scaling $u_r \sim (\varepsilon_u r)^{1/3}$, but for even larger Pr the velocity field becomes smooth $u_r \sim \sqrt{\varepsilon_u/\nu} r$ and then the grid resolution should be compared to the Batchelor scale η_B as smallest relevant length scale. In below analysis, for $Pr > 1$ we will restrict ourselves to this limiting case.

We now define *global* Kolmogorov and Batchelor length scales $\eta_K^{global} \equiv \frac{\nu^{3/4}}{\langle\varepsilon_u\rangle_{t,V}^{1/4}}$ and $\eta_B^{global} \equiv \frac{\nu^{1/4}\kappa^{1/2}}{\langle\varepsilon_u\rangle_{t,V}^{1/4}}$, respectively, (and also the global length scale $\eta_T^{global} \equiv \frac{\kappa^{3/4}}{\langle\varepsilon_u\rangle_{t,V}^{1/4}}$). Using the exact relation (4.31), one can find how the global Kolmogorov length η_K^{global} depends on Ra, Pr, and Nu, namely

$$\eta_K^{global} \equiv \frac{\nu^{3/4}}{\langle\varepsilon_u\rangle_{t,V}^{1/4}} = \frac{Pr^{1/2}}{Ra^{1/4}(Nu-1)^{1/4}}H. \tag{4.35}$$

The admissible global mesh size h^{global} should clearly be smaller than both η_K^{global} and η_B^{global}, which implies that one is on the safe side provided that

$$h^{global} \le \frac{Pr^{1/2}}{Ra^{1/4}(Nu-1)^{1/4}}H \quad \text{for} \quad Pr \le 1 \tag{4.36}$$

or with the relation (4.34) between the Kolmogorov and Batchelor length

$$h^{global} \le \frac{1}{Ra^{1/4}(Nu-1)^{1/4}}H \quad \text{for} \quad Pr > 1. \tag{4.37}$$

A similar way to estimate mesh requirements in the bulk was suggested for the first time by Grötzbach [110]. Note that with these estimates for the required bulk resolution for most times and locations one is on the safe side, as equation (4.31) is an estimate for the volume averaged energy dissipation rate, which is localized in the boundary layers. However, not only the background field but also plumes detaching from the boundary layers do require an adequate resolution.

To estimate the number of nodes that should be placed in the boundary layers, we will first estimate the area averaged energy dissipation rate in a horizontal plane in the velocity BL, $\langle\varepsilon_u\rangle_{t,A\in BL}$. Employing eqs. (4.17), (4.14) and (4.30), one can find a lower bound for this quantity, namely

$$\begin{aligned}\langle\varepsilon_u\rangle_{t,A\in BL} &\ge \nu\left\langle\left(\frac{\partial u_x}{\partial z}\right)^2\right\rangle_{t,A} \ge \nu\left(\left\langle\frac{\partial u_x}{\partial z}\right\rangle_{t,A}\right)^2 \approx \nu\left(\frac{U}{\delta_u}\right)^2 = \\ &= \nu\left(\frac{\nu Re}{H}\frac{Re^{1/2}}{aH}\right)^2 = \frac{\nu^3 Re^3}{a^2H^4}.\end{aligned} \tag{4.38}$$

From eqs. (4.31), (4.38), (4.18) and (4.27) it follows a lower bound for the ratio

$$\frac{\langle\varepsilon_u\rangle_{t,A\in BL}}{\langle\varepsilon_u\rangle_{t,V}} \ge \frac{Pr^2Re^3}{a^2RaNu} = 64a^4Nu^5\frac{Pr^2}{Ra}\left(\frac{\delta_\theta}{\delta_u}\right)^6$$

$$= \begin{cases} 64\pi^3a^4A^6Nu^5Pr^{-1}Ra^{-1}, & Pr < 3\times10^{-4}, \\ 64a^4Nu^5Pr^{-0.15+0.132\log Pr}Ra^{-1}, & 3\times10^{-4} \le Pr \le 3, \\ 64a^4E^6Nu^5Ra^{-1}, & Pr > 3. \end{cases} \tag{4.39}$$

For the Kolmogorov length η_K^{BL} in the velocity BL one can therefore write

$$\eta_K^{BL} \equiv \left\langle\left(\frac{\nu^3}{\varepsilon_u}\right)^{1/4}\right\rangle_{t,A\in BL} \approx \left(\frac{\langle\varepsilon_u\rangle_{t,V}}{\langle\varepsilon_u\rangle_{t,A\in BL}}\right)^{1/4}\eta_K^{global}. \tag{4.40}$$

The mesh size h^{BL} in the BL must be smaller than η_K^{BL} and η_B^{BL}, i.e., one is on the safe side if

$$h^{BL} \lesssim \begin{cases} 2^{-3/2}a^{-1}Nu^{-3/2}Pr^{3/4}A^{-3/2}\pi^{-3/4}H, & Pr < 3\times10^{-4}, \\ 2^{-3/2}a^{-1}Nu^{-3/2}Pr^{0.5355-0.033\log Pr}H, & 3\times10^{-4} \le Pr \le 1, \\ 2^{-3/2}a^{-1}Nu^{-3/2}Pr^{0.0355-0.033\log Pr}H, & 1 < Pr \le 3, \\ 2^{-3/2}a^{-1}E^{-3/2}Nu^{-3/2}H, & Pr > 3, \end{cases} \tag{4.41}$$

according to (4.39), (4.40), (4.36) and (4.37).

From the relations (4.41), (4.27) and (4.13) one can estimate the minimum number of nodes of the computational mesh, which must be placed in each thermal and kinetic boundary layer close the plates. We find that this minimum number of nodes in the thermal boundary layers is

$$\begin{aligned} N_{\texttt{th.BL}} &\equiv \frac{\delta_\theta}{h^{BL}} \\ &\gtrsim \begin{cases} \sqrt{2}aNu^{1/2}Pr^{-3/4}A^{3/2}\pi^{3/4}, & Pr < 3\times10^{-4}, \\ \sqrt{2}aNu^{1/2}Pr^{-0.5355+0.033\log Pr}, & 3\times10^{-4} \le Pr \le 1, \\ \sqrt{2}aNu^{1/2}Pr^{-0.0355+0.033\log Pr}, & 1 < Pr \le 3, \\ \sqrt{2}aNu^{1/2}E^{3/2}, & Pr > 3, \end{cases} \end{aligned} \tag{4.42}$$

while the minimum number of nodes in the kinetic boundary layers is

$$\begin{aligned} N_{\texttt{v.BL}} &\equiv \frac{\delta_u}{h^{BL}} = \frac{\delta_u}{\delta_\theta}\frac{\delta_\theta}{h^{BL}} \\ &\gtrsim \begin{cases} \sqrt{2}aNu^{1/2}Pr^{-1/4}A^{1/2}\pi^{1/4}, & Pr < 3\times10^{-4}, \\ \sqrt{2}aNu^{1/2}Pr^{-0.1785+0.011\log Pr}, & 3\times10^{-4} \le Pr \le 1, \\ \sqrt{2}aNu^{1/2}Pr^{0.3215+0.011\log Pr}, & 1 < Pr \le 3, \\ \sqrt{2}aNu^{1/2}Pr^{1/3}E^{1/2}, & Pr > 3. \end{cases} \end{aligned} \tag{4.43}$$

The number of nodes in the thermal boundary layer looks very restrictive for very low *Pr*; however, one should realise that for very low *Pr* the thermal boundary layer also becomes much thicker than the velocity boundary layer. Hence, the criterion for the number of nodes in the thermal boundary layers determines the ideal distribution of nodes above the viscous boundary layer. For very high *Pr* the kinetic boundary layer becomes much thicker than the thermal boundary layer, and hence the restriction for the velocity boundary layer determines the ideal distribution of nodes above the thermal boundary boundary layer. Note that for large *Pr* equation (4.42) suggests that the number of grid points in the thermal boundary layer becomes independent of *Pr* (for fixed *Nu*): Indeed, as the velocity field is smooth anyhow, with increasing *Pr* no extra grid points are necessary in the thermal BL.

In figure 4.4 we show the minimum number of nodes $N_{\mathtt{th.BL}}$ and $N_{\mathtt{v.BL}}$, respectively, necessary to simulate the cases which have been investigated experimentally so far, for different *Ra* and *Pr*. The data points are generated by introducing the experimental values of Ra, Pr, and the (measured) corresponding *Nu* into the formulas (4.42), (4.43). Based on these quasi-data points, one can give e.g. the following fits for the minimum number of nodes within the boundary layers for the case of $Pr \approx 0.7$:

$$N_{\mathtt{th.BL}} \approx 0.35 Ra^{0.15}, \quad 10^6 \leq Ra \leq 10^{10}, \tag{4.44}$$

$$N_{\mathtt{v.BL}} \approx 0.31 Ra^{0.15}, \quad 10^6 \leq Ra \leq 10^{10}. \tag{4.45}$$

Note that the numerical pre-factors in these estimates significantly depend on the Prandtl number and on the empirically determined (ref. [27]) value of a, cf. eq. (4.15). The minimum node numbers for other values of *Pr* can be calculated directly using the relations (4.42)–(4.43). Apparently the scaling exponent depends much less on *Pr*. Note that all these estimates only give lower bounds on the required number of nodes in the boundary layers.

As discussed at the beginning of this section, previous studies by Grötzbach [110], Verzicco and Camussi [109], and the study presented in chapter 2 found an increasing number of nodes that should be placed in the thermal and kinetic boundary layers. The theoretical results thus confirm all above studies, because the increasing number of nodes was due to the increasing *Ra* number at which the tests were performed. To be more specific: according to the estimates (4.44) and (4.45) for $Pr = 0.7$ the minimum number of nodes that should be placed in the thermal and kinetic boundary layers is $N \approx 2.3$ for $Ra = 3 \times 10^5$, $N \approx 4.4$ for $Ra = 2 \times 10^7$, and $N \approx 8.7$ for $Ra = 2 \times 10^9$. The empirically found values at the respective *Ra* with $Pr \approx 0.7$ are 3 for $Ra = 3 \times 10^5$, 5 for $Ra = 2 \times 10^7$, and 10 for $Ra = 2 \times 10^9$. Thus there is very good agreement between the theoretical results and the empirically obtained values, especially if one considers the difficulties involved in determining these values empirically, and the empirical value for the constant a (4.15) that is used in the theoretical

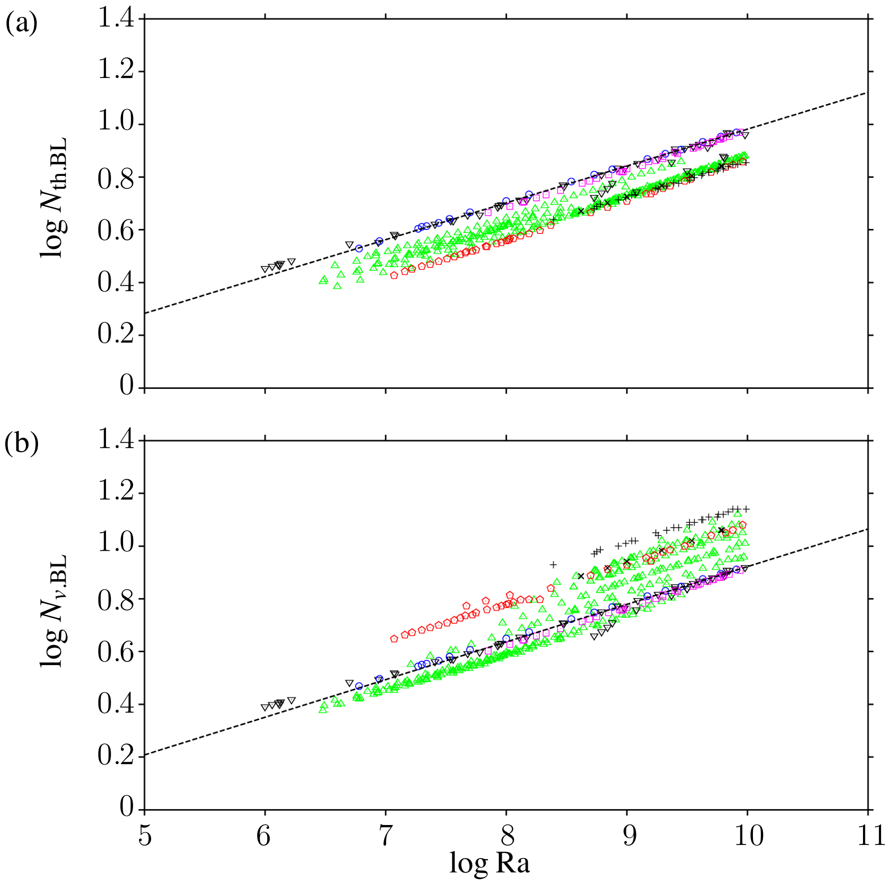

Figure 4.4: Minimum number of BL nodes necessary in DNS of boundary layer dominated, moderately high RB convection. (a) $N_{\mathtt{th.BL}}$ (4.42) in the thermal boundary layers and (b) $N_{\mathtt{v.BL}}$ (4.43) in the kinetic boundary layers, required to simulate the experimentally investigated cases, references [59] (lilac squares, $Pr = 0.67$), [38] (black triangles, $0.60 \leq Pr \leq 7.00$), [146] (blue circles, $0.68 \leq Pr \leq 5.92$), [62] (green triangles, $0.73 \leq Pr \leq 6.00$), [147] (red pentagons, $3.76 \leq Pr \leq 5.54$), [123] (black crosses, $Pr = 4.2$) and [127] (black pluses, $Pr = 7.0$). Dashed lines are fits to the quasi-data (measured values introduced into eqs. (4.42), (4.43)), with precision $\mathrm{O}(10^{-4})$; rounding the respective numbers to their upper bounds gives (a) $N_{\mathtt{th.BL}} \approx 0.35Ra^{0.15}$ (4.44) and (b) $N_{\mathtt{v.BL}} \approx 0.31Ra^{0.15}$ (4.45) for the quasi-data in the ranges $10^6 \leq Ra \leq 10^{10}$ and $0.67 \leq Pr \leq 0.73$.

estimates. We want to emphasize that not only the boundary layers close to the plates, but also the kinetic boundary layers close to the vertical walls must be well resolved.

To sum up, the mesh resolution should be analysed *a priori* using the resolution requirements in the bulk (4.36), (4.37) *and* in the boundary layers (4.42), (4.43). Having conducted the DNS, the Kolmogorov and Batchelor scale should be checked *a posteriori*, to make sure that the mesh size was indeed small enough (as it has been done, for example, in refs. [112, 118]).

4.5 Conclusions

In summary, we used laminar Prandtl–Blasius boundary layer theory to determine the relative thicknesses of the thermal and kinetic boundary layers as functions of *Pr*, see equation 4.27.

We found that neither the position of the maximum r.m.s. velocity fluctuations nor the position of the horizontal velocity maximum reflect the slope velocity boundary layer thickness, although many studies use these as criteria to determine the boundary layer thickness. In contrast to them, the algorithm introduced in chapter 2 agrees very well with the theoretical estimate of the kinetic slope boundary layer thickness.

We used the results obtained from the Prandtl–Blasius boundary layer theory to derive a lower bound on the minimum number of nodes that should be placed in the thermal and kinetic boundary layers close to the plates. We found that this minimum number of nodes increases not slower than $\sim Ra^{0.15}$ with increasing Ra. This result is in excellent agreement with results from several numerical studies over the last decades, in which this minimum number of nodes was determined empirically. Hence, the derived estimates can be used as guideline for future direct numerical simulations.

5

Effect of plumes on measuring the large scale circulation in Rayleigh-Bénard convection *

We studied the properties of the large-scale circulation (LSC) in turbulent Rayleigh-Bénard (RB) convection by using results from direct numerical simulations in which we placed a large number of numerical probes close to the sidewall. The LSC orientation is determined by either a cosine or a polynomial fit to the azimuthal temperature or azimuthal vertical velocity profile measured with the probes. We study the LSC in $\Gamma = D/L = 1/2$ *and* $\Gamma = 1$ *samples, where D is the diameter and L the height. For* $Pr = 6.4$ *in an aspect ratio* $\Gamma = 1$ *sample at* $Ra = 1 \times 10^8$ *and* 5×10^8 *the obtained LSC orientation is the same, irrespective of whether the data of only* 8 *or all* 64 *probes per horizontal plane are considered. In a* $\Gamma = 1/2$ *sample with* $Pr = 0.7$ *at* $Ra = 1 \times 10^8$ *the influence of plumes on the azimuthal temperature and azimuthal vertical velocity profiles is stronger. Due to passing plumes and/or the corner flow the apparent LSC orientation obtained using a cosine fit can result in a misinterpretation of the character of the large-scale flow. We introduce the relative LSC strength, which we define as the ratio between the energy in the first Fourier mode and the energy in all modes that can be determined from the azimuthal temperature and azimuthal vertical velocity profiles, to further quantify the large-scale flow. For* $Ra = 1 \times 10^8$ *we find that this relative LSC strength is significantly lower in a* $\Gamma = 1/2$ *sample than in a* $\Gamma = 1$ *sample, reflecting that the LSC is much more pronounced in a* $\Gamma = 1$ *sample than in a* $\Gamma = 1/2$ *sample. The determination of the relative LSC strength can be ap-*

---

*Based on: R.J.A.M. Stevens, H.J.H. Clercx, and D. Lohse, Effect of Plumes on Measuring the Large Scale Circulation in Turbulent Rayleigh-Bénard Convection, submitted to Phys. Fluids (2011).

plied directly to available experimental data to study high Rayleigh number thermal convection and rotating RB convection.

5.1 Introduction

In experiments the LSC is measured by using thermistors that are embedded in the sidewall, see e.g. [148], or by using small thermistors that are placed in the flow at different azimuthal positions and different heights, see e.g. [149]. Since the LSC transports warm (cold) fluid from the bottom (top) plate up (down) the side wall, the thermistors can detect the location of the up-flow (down-flow) by showing a relatively high (low) temperature. The properties of the LSC have recently been intensively studied in experiments [36, 75, 98, 149–163], numerical simulations [75, 109, 119, 164, 165], and models [75, 156–158, 163, 166–169]. For a complete overview of all literature in which certain aspect of the LSC are studied we refer to the recent review of Ahlers, Grossmann, and Lohse [20]. In part II of this thesis we investigate several properties of the LSC in experiments and numerical simulations of rotating RB convection. In chapter 14 in part III of this thesis we model the reversal behavior of the LSC, which we observe in (quasi)-two-dimensional experiments and DNS simulations.

In experiments the LSC is measured by using thermistors that are embedded in the sidewall, see e.g. [148], or by using small thermistors that are placed in the flow at different azimuthal positions and different heights, see e.g. [149]. Since the LSC transports warm (cold) fluid from the bottom (top) plate up (down) the side wall, the thermistors can detect the location of the up-flow (down-flow) by showing a relatively high (low) temperature. In addition, there have also been a number of direct measurements of the LSC by particle image velocimetry (PIV) and laser Doppler velocimetry (LDV) (see, for example Refs. [99, 150, 152]) that complement the thermistor method.

In this chapter we investigate the properties of the LSC with results from direct numerical simulations (DNS). Though DNSs are limited both in Ra and in duration, i.e. in number of LSC turnover times, to smaller values than the experimental analogues the advantage is that in contrast to the experiments the full spatial information is available. We will take advantage of this in order to verify the algorithms employed in experiments to identify the LSC orientation based on a limited number of probes. We will introduce two existing methods to determine the LSC orientation over time. The first method [98] determines the LSC orientation from a cosine fit to the azimuthal temperature profile measured with the probes. This method has been extremely successful in revealing important features, i.e. azimuthal meandering, reversals, and cessations, of the LSC [98, 155, 156, 161]. In the second method the LSC orientation is determined by using a second order polynomial fit around the

Table 5.1: The columns from left to right indicate the following: *Ra*, *Pr*, Γ, the number of grid points in the azimuthal, radial and axial directions ($N_\theta \times N_r \times N_z$). The last two columns indicate the relative LSC strength determined using equation (5.2), see section 5.6, using the data of only 8 ($\bar{S}_m(8)$) and all 64 ($\bar{S}_m(64)$) probes in the horizontal midplane, respectively.

Ra	Pr	Γ	$N_\theta \times N_r \times N_z$	$\bar{S}_m(8)$	$\bar{S}_m(64)$
1×10^8	6.4	1.0	$257 \times 129 \times 257$	0.74	0.70
1×10^8	6.4	1.0	$385 \times 193 \times 385$	0.65	0.68
5×10^8	6.4	1.0	$257 \times 129 \times 257$	0.68	0.73
5×10^8	6.4	1.0	$385 \times 193 \times 385$	0.70	0.76
1×10^8	0.7	$1/2$	$193 \times 65 \times 257$	0.45	0.57
1×10^8	0.7	$1/2$	$257 \times 97 \times 385$	0.42	0.54
1×10^8	6.4	$1/2$	$193 \times 65 \times 257$	0.06	0.27

maximum and the minimum. Using this method the sloshing mode of the LSC, which is caused by an off-center motion of the LSC, was discovered [149, 162, 163]. We note that this can not be obtained by the cosine fit method as this method assumes that there is no off-center motion of the LSC.

So far these procedures have been applied to experimental data where the data of 8 azimuthally equally spaced probes were available. The benefit of the simulations over the experiments is that it is easy to place a large number of probes in the flow. Here we placed up to 64 azimuthally equally spaced numerical probes at different heights into the numerical RB sample. With an arrangement of up to 64 probes we can determine how the extracted information on the LSC and plume dynamics depends on the number of probes that is used. We also visualized the flow by movies that show the flow dynamics in horizontal or vertical planes, see the accompanying material [115].

The chapter is organized as follows. In section 5.2 we start with a discussion of the numerical method that has been used. This is followed in section 5.3 by a discussion of the traditional methods that are used in experiments to determine the LSC orientation. Based on the results obtained by these methods we discuss the characteristics of the LSC in a $\Gamma = 1$ (section 5.4) and $\Gamma = 1/2$ (section 5.5) sample. An important question for both high Ra number [39, 170] and rotating RB convection (see part II of this thesis) is whether or not there is a single LSC present. Therefore we will discuss a new method in section 5.6, which is based on the energy in the different Fourier modes of the azimuthal temperature and azimuthal vertical velocity profile, to determine whether a single LSC is present. In section 5.7 we will look into time resolved properties of the LSC. The general conclusions of this chapter will be presented in section 5.8.

5.2 Numerical method and procedure

The flow is solved by numerically integrating the three-dimensional unsteady Navier-Stokes equations within the Boussinesq approximation. For a detailed discussion of the numerical code we refer to Refs. [107–109] and chapter 2 of this thesis. The flow is simulated in a cylindrical sample in order to keep the geometry identical to the one used in most experiments. In chapters 2 and 3 and part II of this thesis it is shown that the simulation results obtained with this code agree excellent with experimental results. The cases we studied are based on the most common experimental setups that are available, namely $Pr \approx 6.4$ and $Pr \approx 0.7$ at an aspect ratio $\Gamma = D/L$ of 1 and $1/2$. A detailed overview of the simulations can be found in table 5.1.

In the simulations we placed up to 64 azimuthally equally spaced numerical probes per horizontal plane that provide simultaneous point-wise measurements of the temperature and the three velocity and vorticity components at the heights $0.25L$, $0.50L$, and $0.75L$ and a distance $0.45D$ from the cylinder axis. Grid refinement tests were performed because the region close to the sidewall, where the LSC properties are sampled, is most sensitive from a resolution point of view, see chapter 2. The simulations are fully resolved according to the criteria of chapters 2 and 4 and the LSC properties we find do not depend on the grid resolution. Note that the azimuthal and radial number of grid points required to get the same resolution with respect to the turbulent length scales is less for the $\Gamma = 1/2$ cases than for the $\Gamma = 1$ cases because for the latter a larger horizontal extent has to be simulated.

5.3 Methods to determine the LSC orientation

Following Ahlers and coworkers [20, 98, 156], the orientation and strength of the LSC can be determined by fitting the function

$$\theta_i = \theta_m + \delta_m \cos(\phi_i - \phi_m) \tag{5.1}$$

to the temperatures recorded by the numerical probes at the height $z = 0.5L$ and the azimuthal positions $\phi_i = 2i\pi/n_p$, where n_p indicates the number of probes. The three parameters θ_m, δ_m, and ϕ_m are obtained from least square fits. Here δ_m is a measure of the temperature amplitude of the LSC and ϕ_m is the azimuthal orientation of the LSC at midheight. The azimuthal average of the temperature at the horizontal midplane is given by θ_m. We calculated temperatures θ_t and θ_b, orientations ϕ_t and ϕ_b, and amplitudes δ_t and δ_b for the top and bottom levels at $z = 0.75L$ and $z = 0.25L$ separately by the same method. For experiments [20, 98, 156] exactly this method is applied to the data of 8 equally spaced thermistors, see figure 5.1.

A second method that is applied to determine the LSC orientation is to make a polynomial fit around the sensor that records the highest (lowest) temperature

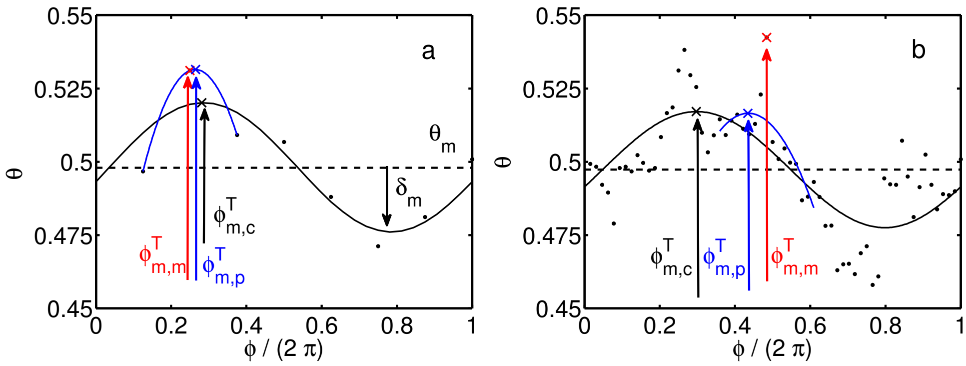

Figure 5.1: Azimuthal temperature profile averaged over $4\tau_f$ at midheight for $Ra = 5 \times 10^8$, $Pr = 6.4$, and $\Gamma = 1$. The measured data from the numerical probes are indicated by the dots. The solid black line shows the cosine fit (eq. (5.1)) to the data with offset θ_m (dashed line) and amplitude δ_m. The black cross indicates the position of $\phi^T_{m,c}$. The red cross indicates the position of the probe that records the highest temperature and thus the position of $\phi^T_{m,m}$. The blue solid line gives the polynomial fit around the maximum. Its maximum, indicated by the blue cross, indicates the position of $\phi^T_{m,p}$. The $\phi(x)$ range that is considered in the polynomial fit is $\frac{1}{2}\pi$. Panel a and b shows the procedure applied to the data of 8 and 64 equally spaced probes at midheight, respectively. The corresponding azimuthal vertical velocity profiles are given in figure 5.8.

Table 5.2: The LSC orientation in this chapter is determined from the azimuthal temperature or azimuthal vertical velocity profile with different methods. In addition, the LSC orientation is also determined at different heights. As explained in the text this information is indicated in the notation $\phi^3_{1,2}$. In this table the meaning of the symbols at the index locations 1, 2, and 3, is summarized.

Index	Symbol	Meaning
1	b	Height $0.25L$
1	m	Height $0.50L$
1	t	Height $0.75L$
2	c	Cosine fit
2	p	Polynomial fit
2	m	Maximum
3	T	Azimuthal temperature profile
3	w	Azimuthal vertical velocity profile

[149, 162]. Finally, since we have a large number of numerical probes, i.e. up to 64 azimuthally equally spaced per horizontal level, we also determine the LSC orientation by finding the probe that records the highest (lowest) temperature. Again the LSC orientation based on these two methods is determined separately for all three levels, see figure 5.1.

To distinguish the different methods we introduce a notation with a second index, i.e. $\phi_{*,[c,p,m]}$. Here c indicates that ϕ is determined using a cosine fit to the azimuthal temperature profile, p that ϕ is determined using a polynomial fit around the maximum (or minimum) observed in the azimuthal profile, and m indicates that the maximum (or minimum) observed in the azimuthal profile is used. Because the numerical probes record both the temperature and vertical velocity component we use both to determine the LSC orientation. In the rest of this chapter we will use the notation $\phi^{T}_{*,*}$ to indicate that the orientation is based on the azimuthal temperature profile and $\phi^{w}_{*,*}$ when it is based on the azimuthal vertical velocity profile. Hence ϕ has three indices, i.e. $\phi^{3}_{1,2}$, see table 5.2 for a detailed overview. In the rest of this chapter we will indicate the numerical value of an index when this index is varied.

Because the numerically obtained azimuthal profiles can be very noisy, we applied a moving averaging filter to the data obtained from the numerical probes to eliminate the detection of very small plumes. In experiments these events are not detected anyhow by thermistors, since these need time to react to temperature changes in the flow. We decided to apply a moving averaging filter of $4\tau_f$, where τ_f is defined with respect to the free-fall velocity U_f as $\tau_f = L/U_f$ (L is the height of the sample). Recently, Bailon-Cuba et al. [171] showed the characteristic convective velocity U_c of the LSC is approximately $U_f/5$ for the parameter ranges $Ra = 10^7 - 10^9$, $\Gamma = 1/2 - 12$, and $Pr = 0.7$. This means that the LSC turnover time τ_{LSC} defined as $\tau_{LSC} = 2L/U_c$ is about 10 τ_f.

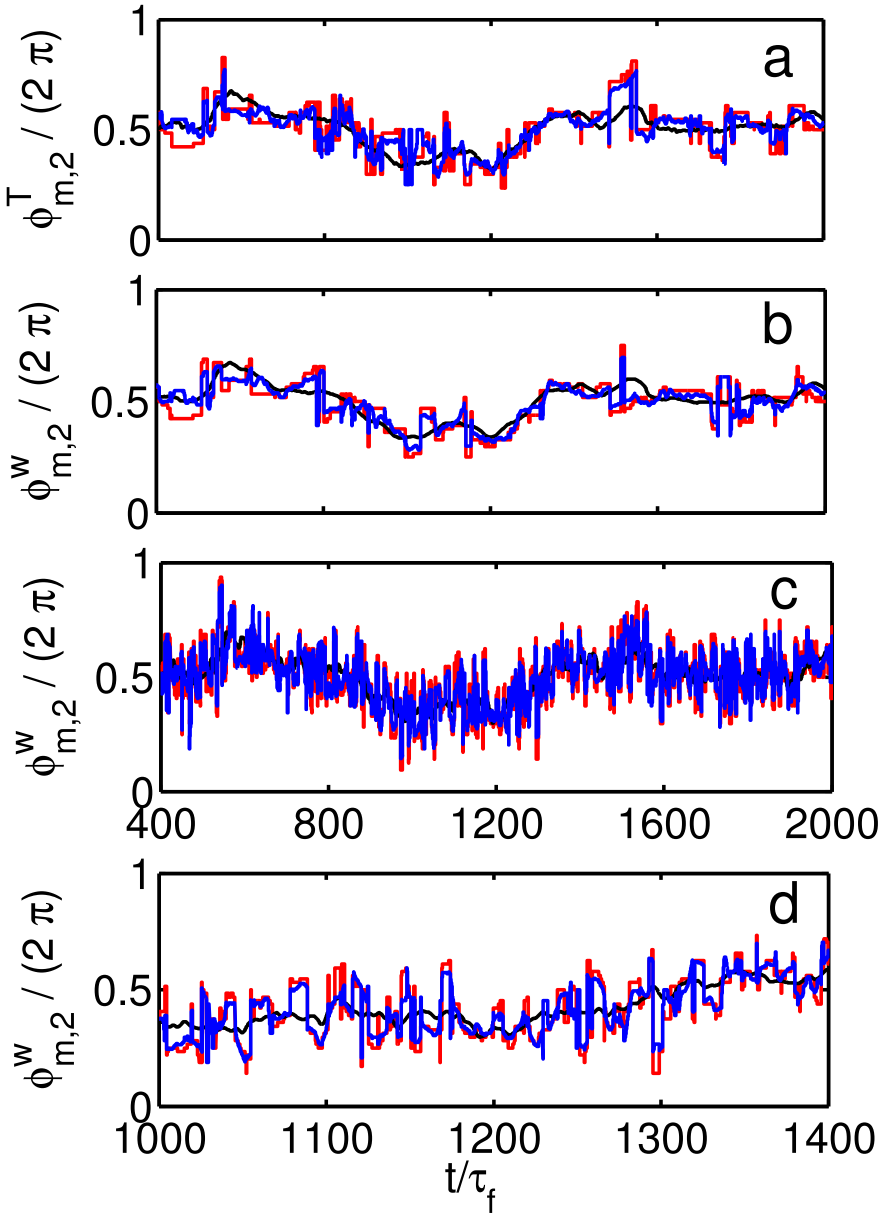

Figure 5.2: The LSC orientation for $Ra = 1 \times 10^8$, $Pr = 6.4$, and $\Gamma = 1$ on the $257 \times 129 \times 257$ grid based on the data of 64 azimuthally equally spaced probes per horizontal level. The black, red, and blue line indicate $\phi^3_{m,c}$ $\phi^3_{m,m}$, and $\phi^3_{m,p}$, respectively. a) $\phi^T_{m,2}$ based on the azimuthal temperature profile averaged over $50\tau_f$ ($\approx$ 5 LSC turnover times), b) $\phi^w_{m,2}$ based on the azimuthal vertical velocity profile averaged over $50\tau_f$, c) $\phi^w_{m,2}$ based on the azimuthal vertical velocity profile averaged over $4\tau_f$. d) Enlargement of the graph shown in panel c to reveal more details.

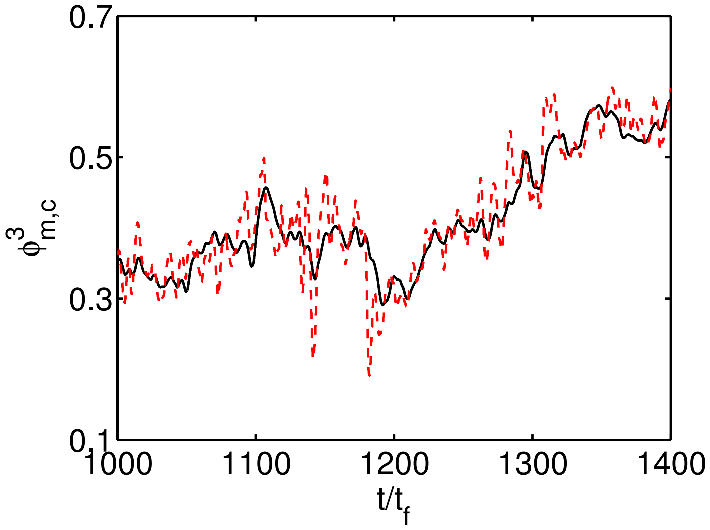

Figure 5.3: $\phi^w_{m,c}$ (solid black line) and $\phi^T_{m,c}$ (red dashed line) for $Ra = 1 \times 10^8$, $Pr = 6.4$, and $\Gamma = 1$ on the $257 \times 129 \times 257$ grid, and based on the azimuthal vertical velocity and azimuthal temperature profile averaged over $4\tau_f$. Here the data of all 64 azimuthally equally spaced probes at midheight have been used.

5.4 Results for $\Gamma = 1$

Figure 5.2 shows the typical behavior of the LSC orientation for $Pr = 6.4$ in a $\Gamma = 1$ sample. The figure shows $\phi^T_{m,2}$ and $\phi^w_{m,2}$. In order to show that the LSC orientation based on the temperature and the vertical velocity data is almost identical we consider first a long averaging time ($50\tau_f$). The results are displayed in figure 5.2a and b. The similarity is expected since the LSC carries warm fluid from the bottom plate up the sidewall and vice versa. To show the influence of this long time averaging we show $\phi^w_{m,2}$ based on the azimuthal vertical velocity profile after averaging over $4\tau_f$, see figure 5.2c and 5.2d. When no time averaging is applied the graph looks similar, with some additional peaks due to very small plumes, to the one where the data is averaged over $4\tau_f$. Figure 5.3 shows that the LSC orientation can be determined more precisely from the vertical velocity than from the temperature even for this relatively high Pr (i.e. small thermal diffusivity). The difference between the LSC orientation determined from the vertical velocity and the temperature seems to depend on several parameters such as the Ra and the Pr number, and the aspect ratio. However, at the moment we do not have enough numerical data available to systematically study this. For $\Gamma = 1$ the obtained LSC orientation at midheight is the same when the data of only 8 or all 64 probes is used, but not when the data of only 2 probes is used.

From figure 5.2 it becomes clear that the LSC orientation, obtained by the polynomial and cosine fit, can differ significantly. This is due to the off-center mo-

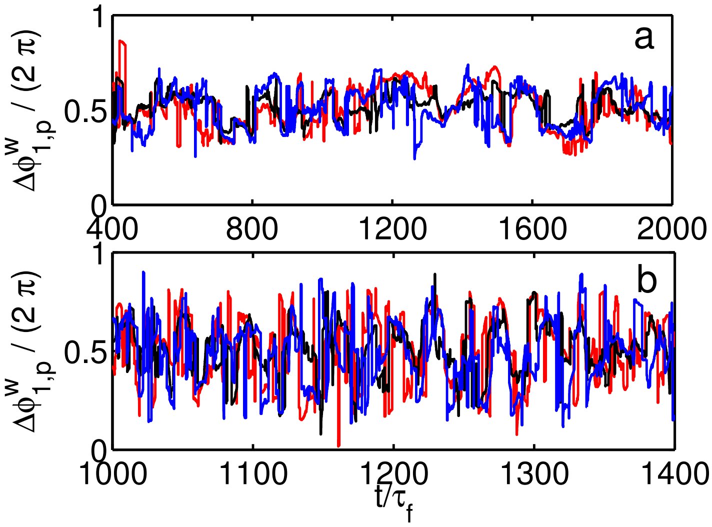

Figure 5.4: The red, black, and blue lines indicate $\Delta\phi^{w}_{b,p}$, $\Delta\phi^{w}_{m,p}$, and $\Delta\phi^{w}_{t,p}$, respectively for $Ra = 1 \times 10^8$, $Pr = 6.4$, and $\Gamma = 1$ on the $257 \times 129 \times 257$ grid. Panel a and b show $\Delta\phi^{w}_{1,p}$ when the azimuthal vertical velocity profile is averaged over $50\tau_f$ and $4\tau_f$, respectively. The average of $\Delta\phi^{w}_{1,p}$ is π and this is in agreement with a cosine fit. The deviations from this value are due to plumes and the off-center motion of the LSC. Here the data of all 64 azimuthally equally spaced probes per horizontal level have been used.

tion of the LSC [149, 162, 163]. Figure 5.4 shows $\Delta\phi = \phi_{max} - \phi_{min}$, i.e. the difference between the orientation of the strongest up (ϕ_{max}) and down going motion (ϕ_{min}) obtained using the polynomial fit, fluctuates around $\Delta\phi = \pi$. To quantify the strength of these fluctuations we calculate $\langle(\Delta\phi^{w}_{1,p} - \pi)^2\rangle^{1/2}$. The values based on the data of 64 (8) probes per horizontal level for the case presented in figure 5.4 are $\langle(\Delta\phi^{w}_{t,p} - \pi)^2\rangle^{1/2} \approx 1.09(1.04)$, $\langle(\Delta\phi^{w}_{b,p} - \pi)^2\rangle^{1/2} \approx 0.84(0.77)$, and $\langle(\Delta\phi^{w}_{m,p} - \pi)^2\rangle^{1/2} \approx 1.11(1.01)$. Because the fluctuation strength is the same when the data of 8 and 64 equally spaced probes per horizontal level are considered we conclude that the use of 8 probes is sufficient to capture these statistics in a $\Gamma = 1$ sample. In figure 5.5 it is shown that the LSC orientation, obtained using the polynomial fit method, can be different at the different heights. We note that the same is observed when the LSC orientation based on a cosine fit is considered. This indicates that the LSC is not always flowing straight up and down, but is also moving in the azimuthal direction, and thus performs twisting motions [151]. We note that some phenomena, like the drift of the LSC due to the Coriolis force, see Ref. [154], can be analyzed using the LSC orientation based on the polynomial and cosine method, because in this case only the long term drift of the LSC is important.

More remarkably is the presence of a specific frequency of approximately $25\tau_f$ in the signal $\phi^{w}_{m,c} - \phi^{w}_{m,p}$, see figure 5.7. This specific frequency seems to be related

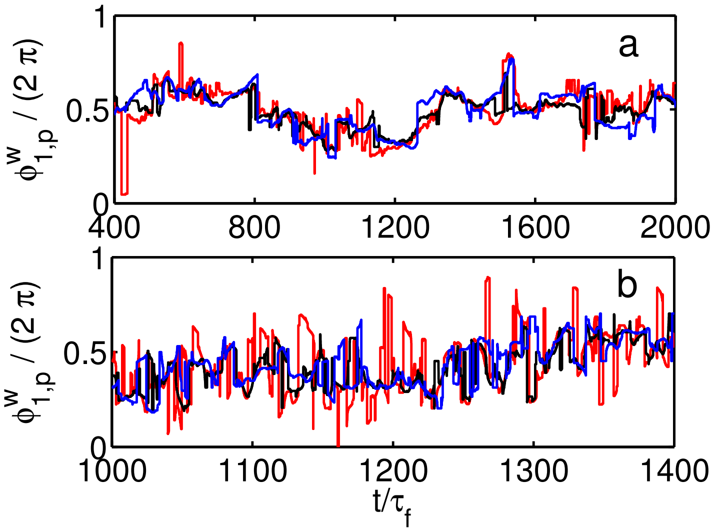

Figure 5.5: The red, black, and blue lines indicate $\phi^w_{b,p}$, $\phi^w_{m,p}$, and $\phi^w_{t,p}$, respectively, for $Ra = 1 \times 10^8$, $Pr = 6.4$, and $\Gamma = 1$ on the $257 \times 129 \times 257$ grid. Panel a and b show $\phi^w_{1,p}$ based on the azimuthal profiles of the vertical velocity averaged over $50\tau_f$ and $4\tau_f$, respectively. The difference between the LSC orientation at the different levels is due to plumes and the torsional motion of the LSC. Here the data of all 64 azimuthally equally spaced probes per horizontal level have been used.

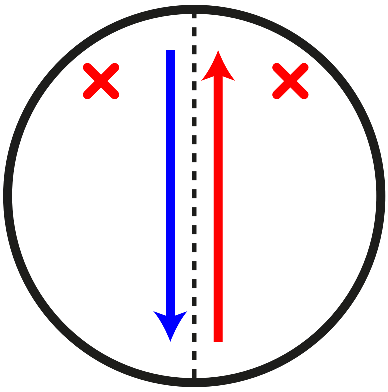

Figure 5.6: Sketch of the top view on the RB sample. The dotted line indicates the orientation of the LSC based on the cosine fit and the red (up-pointing) and blue (down-pointing) arrows indicated the flow direction close to the bottom and top plate, respectively. Strong plumes are detected alternatingly on the left and right side of the LSC, see crosses, with a specific frequency, see also figure 5.2.

to the frequency in which plumes are passing the horizontal midplain [172], which in our case shows up in the frequency in which plumes are detected on the left and right hand side of the LSC orientation based on the cosine fit, see figure 5.6. This frequency might also be related to the low frequency mode found already in Ref. [173] or to the off-center oscillation of the LSC [174].

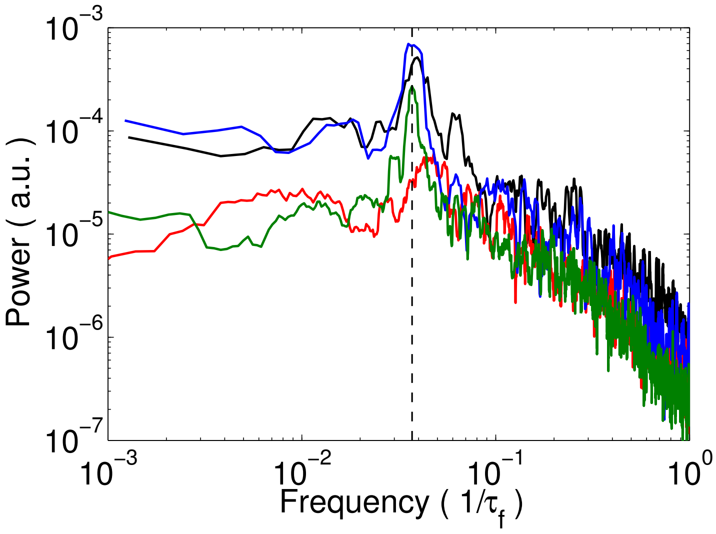

Figure 5.7: The power spectra of $\phi^w_{m,c} - \phi^w_{m,p}$ shows a maximum around $25\tau_f$, which is indicated by the vertical dashed line. This frequency is caused by plumes that pass the LSC orientation based on the cosine fit on the left and right side . The different spectra are obtained from simulations for $Pr = 6.4$ in a $\Gamma = 1$ sample for different Ra and resolution, i.e. $Ra = 1 \times 10^8$ on a $257 \times 129 \times 257$ (red) and on a $385 \times 193 \times 385$ grid (black), and $Ra = 5 \times 10^8$ on a $257 \times 129 \times 257$ (green) and a $385 \times 193 \times 385$ (blue) grid.

We find this frequency in our simulations for $Pr = 6.4$ in a $\Gamma = 1$ sample. We note that we also find this frequency when we do not apply any time averaging on the data before we determine the LSC orientation. Actually one can already see this phenomenon in figure 5.2d where $\phi^w_{m,p}$ fluctuates around $\phi^w_{m,c}$ with a typical period of about $25\tau_f$. Further confirmation is obtained when the temporal behavior of the data obtained from the 64 probes at midheight is shown in a movie, see the supplementary material [115]. The movie is based on the data obtained from the simulation on the $385 \times 193 \times 385$ grid at $Ra = 5 \times 10^8$ with $Pr = 6.4$ in a $\Gamma = 1$ sample. The movie shows a passing plume at t ≈ 2412, see the snapshot of the movie in figure 5.8b, which is indicated by the two peak structure around the maximum position obtained by the cosine fit. When this plume is passed the double peak structure disappears. Subsequently, the LSC orientation based on the polynomial fit method is smoothly passing the LSC orientation based on the cosine fit. Thus showing an off-center motion of the LSC. We note that having a large number of probes is essential to confirm these plume events. To show this we made a movie of the same time interval, see the supplementary material [115] and the snapshot in figure 5.8a, with the data of only 8 probes. From these movies and figure 5.8a we conclude that it is impossible to see the double peak structure when the data of only 8 probes is used and therefore we cannot distinguish the off-center motion of the LSC from passing plumes, when

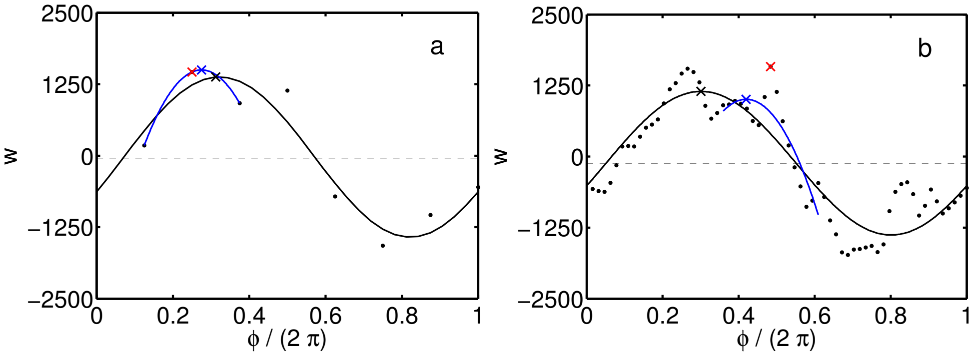

Figure 5.8: Snapshot of the azimuthal vertical velocity profile averaged over $4\tau_f$ for $Pr = 6.4$ in a $\Gamma = 1$ sample at $Ra = 5 \times 10^8$. The symbols have the same meaning as indicated in figure 5.1. Panel a indicates the obtained profile using the data of 8 probes and panel b the profile as it is obtained from the data of 64 probes. The accompanying movies can be found in the supplementary material [115].

the plumes stretches over two rows of thermistors.

In summary, in a $\Gamma = 1$ sample the obtained LSC orientation using a cosine and polynomial fit is the same when the data of only 8 or all 64 azimuthally equally spaced probes per horizontal level are used. Because the azimuthal temperature profile is only an indirect measure of the LSC orientation we find that the LSC orientation can be determined with more precision from the azimuthal vertical velocity profile. In addition, we find that many of its interesting phenomena like azimuthal meandering, reversals, cessations, and the sloshing mode of the LSC look the same when the data of only 8 or all 64 azimuthally equally spaced probes per horizontal level are considered. However, only with the data of 64 equally spaced probes per horizontal level the effect of passing plumes on the azimuthal temperature and azimuthal vertical velocity profiles can be identified.

5.5 Results for $\Gamma = 1/2$

We now come to the $\Gamma = 1/2$ case. For this geometry Verzicco and Camussi [109] have used the data accessibility provided by direct numerical simulations to show that the large scale circulation can be either in a single-roll state (SRS) or in a double-roll state (DRS). Subsequently, a model introduced by Stringano and Verzicco [164] found that the switching between the DRS and the SRS can influence the Nusselt number, and can thus be a possible reason for the bimodal behavior of Nusselt found in some experiments, see e.g. [43, 61].

The first extensive experimental study on the transition between the SRS and the DRS was performed by Xi and Xia [160]. They studied flow mode transition in samples of aspect ratio 1, 1/2 and 1/3. Figure 10 of their paper [160] shows the

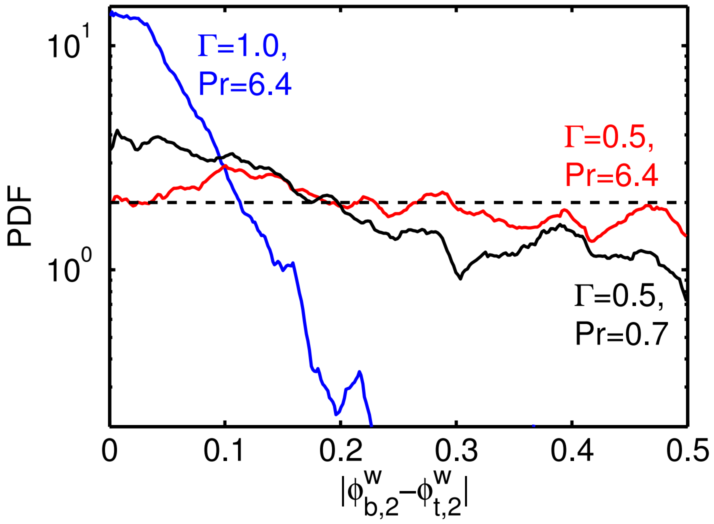

Figure 5.9: The PDF of $|\phi^w_{b,c} - \phi^w_{t,c}|$ for $Ra = 1 \times 10^8$. The PDF for $Pr = 6.4$ and $\Gamma = 1$ is given in blue. The red and black line give the PDF for $Pr = 6.4$ and $Pr = 0.7$ in the $\Gamma = 1/2$ geometry, respectively.

percentages of the time the flow spends in either the SRS or the DRS. In addition, they showed that the heat transfer in the SRS is higher than in the DRS. Recently, Weiss & Ahlers [170] have also experimentally investigated the switching between the SRS and the DRS, but now over a much larger range of Ra than Xi and Xia [160]. The conclusion of this work is summarized in figure 11 of Ref. [170]. That figure shows that the SRS is more dominant at higher Ra and smaller Pr. They note that they find a good agreement with the results of Xi and Xia in the Ra number range in which both experiments overlap. In addition, the work of Xi and Xia [160] and Weiss and Ahlers [170] showed that the flow state can not always be defined as SRS or DRS. This is particularly important for $Ra \lesssim 3 \times 10^9$. E.g., for $Ra = 1 \times 10^8$ and $Pr = 4.38$ the flow state is undefined for about 50% of the time according to Weiss and Ahlers [170].

In this chapter we will qualitatively confirm these findings experimental and numerical findings. We will restrict ourselves to this relatively low Ra number regime, namely to $Ra = 1 \times 10^8$: First, in order to directly compare with the $\Gamma = 1$ case of the previous section, second, because current high Ra number simulations, see chapter 2 and chapter 3 of this thesis, are too limited in the number of turnover times to obtain sufficient statistics on the different flow states.

Our simulations confirm Weiss & Ahlers's [170] finding that there is more disorder in a $\Gamma = 1/2$ sample than in a $\Gamma = 1$ sample. We find that in this low Ra number regime it is important to have a large number of probes to accurately represent the azimuthal temperature and azimuthal vertical velocity profiles to analyze the flow.

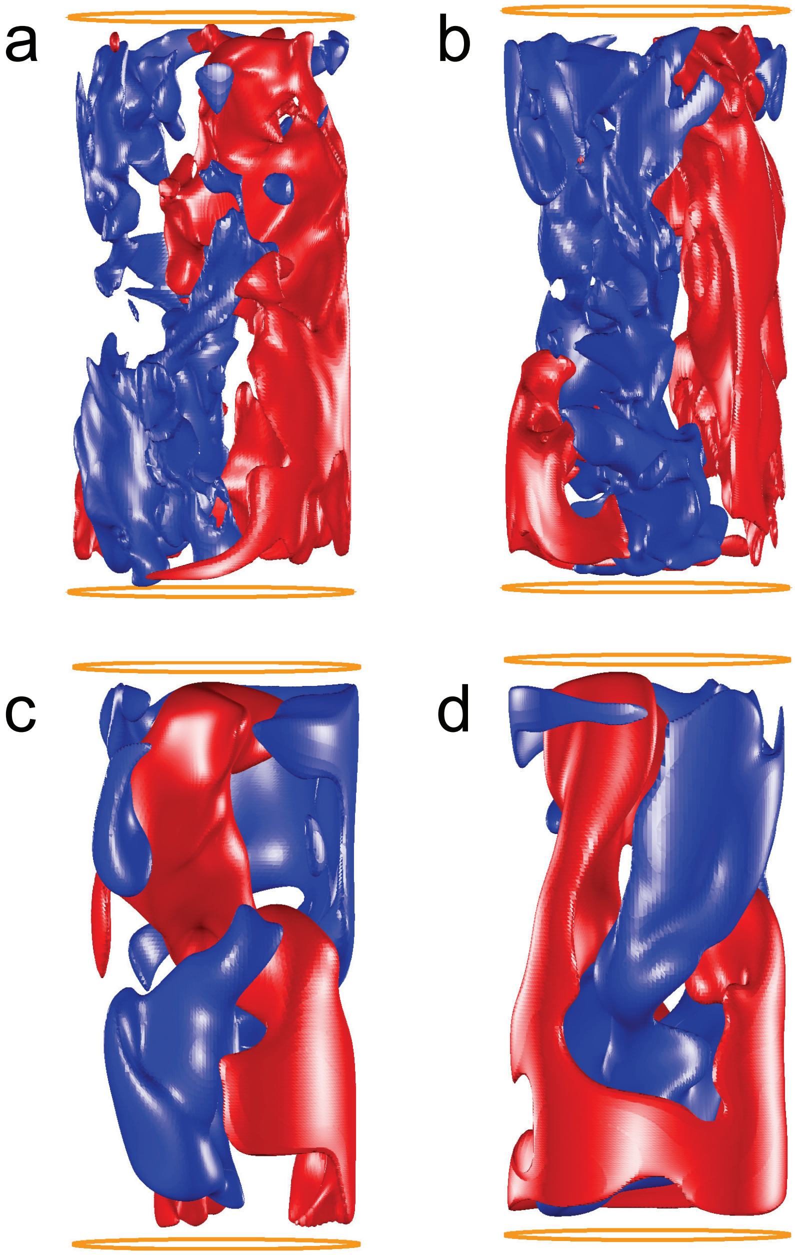

Figure 5.10: Snapshot of the regions with the strongest, i.e. $w \geqq 0.35 w_{max}$, up (red) and down-flow (blue) for $Ra = 1 \times 10^8$ and $\Gamma = 1/2$. a) $Pr = 0.7$, SRS, b) $Pr = 0.7$, very strong corner flows, c) $Pr = 6.4$, DRS, d) $Pr = 6.4$, strong plume/torsional motion. Supplementary movies that offer a full three dimensional view are provided in the supplementary material [115].

In this regime we see that deflection of plumes due to corner rolls and other plumes happens more often than in a $\Gamma = 1$ sample. These effects can be observed in the supplementary movies for $\Gamma = 1/2$ at $Ra = 1 \times 10^8$ and $Pr = 0.7$ and $Pr = 6.4$ [115]. In the movies that show horizontal cuts at the heights $0.25L$, $0.50L$, and $0.75L$ one can see that the hot and cold regions interchange more often in a $\Gamma = 1/2$ sample than in a $\Gamma = 1$ sample.

In order to determine whether there is a SRS or a DRS in this geometry we determined the probability density function (PDF) of the quantity $|\phi^w_{b,c} - \phi^w_{t,c}|$. When this PDF peaks around zero it means that the fluid is flowing straight up, and this indicates the presence of a SRS. When there is a DRS the PDF should peak around π. Figure 5.9 shows that for $Pr = 6.4$ in a $\Gamma = 1$ sample the PDF peaks around zero and this confirms the dominance of the SRS in this geometry. For $Pr = 0.7$ in a $\Gamma = 1/2$ sample the figure shows that there is a small peak around zero, but it is much less pronounced than for the $\Gamma = 1$ case. For $Pr = 6.4$ in a $\Gamma = 1/2$ sample the figure shows that the PDF is nearly uniform, which would suggest that neither the SRS or the DRS is dominant. This agrees with the results of Weiss & Ahlers [170], since they find that for $Pr = 4.38$ and $Ra \lesssim 3 \times 10^9$ the flow state is poorly defined and no state dominates. Figure 5.10 reveals the origin of these nearly uniform PDFs in the $\Gamma = 1/2$ sample by showing three-dimensional visualizations of the regions where the vertical velocities are strongest. An analysis of these (and similar figures) revealed that the uniform PDF is due to the possibility of different flow states, i.e. the SRS (figure 5.10a) with $|\phi^w_{b,c} - \phi^w_{t,c}| \approx 0$, the DRS (figure 5.10c) with $|\phi^w_{b,c} - \phi^w_{t,c}| \approx \pi$, strong corner flows (figure 5.10b) which can have any $|\phi^w_{b,c} - \phi^w_{t,c}|$, and strong plume and/or torsional motions (figure 5.10d) which also can have any $|\phi^w_{b,c} - \phi^w_{t,c}|$.

To better compare our results with the results of Weiss & Ahlers [170] we also determined the PDF of the quantity $\phi^w_{b/t,c} - \phi^w_{m,c}$, see figure 5.11. Here $\phi^w_{b/t,c}$ means that both $\phi^w_{b,c}$ and $\phi^w_{t,c}$ are compared with $\phi^w_{m,c}$ to construct the PDF. A similar PDF for higher *Ra*, based on experimental data, can be found in figure 21 of Weiss & Ahlers [170]. Figure 5.11 shows this PDF based on the data of only 8 and all 64 equally spaced probes per horizontal level for the cases of figure 5.9. First of all, figure 5.11 shows that the DRS is much more pronounced for $Pr = 6.4$ than for $Pr = 0.7$, which is in agreement with the results of Weiss and Ahlers [170] and the results shown in figure 5.9. a comparison of the PDFs in figure 5.11 reveals that the PDFs based on the data of 8 and all 64 equally spaced probes are almost identical. The largest difference is visible for $Pr = 6.4$ in a $\Gamma = 1$ sample. Here the PDF based on the data of 64 equally spaced probes is more confined in the SRS region than the one based on 8 equally spaced probes, because the larger number of probes reduces 'random' fluctuations in the obtained LSC orientation.

Furthermore, and this is the main issue here, for this relatively low Ra sometimes the data of three rows of 8 thermistors can give misleading hints for the actual flow

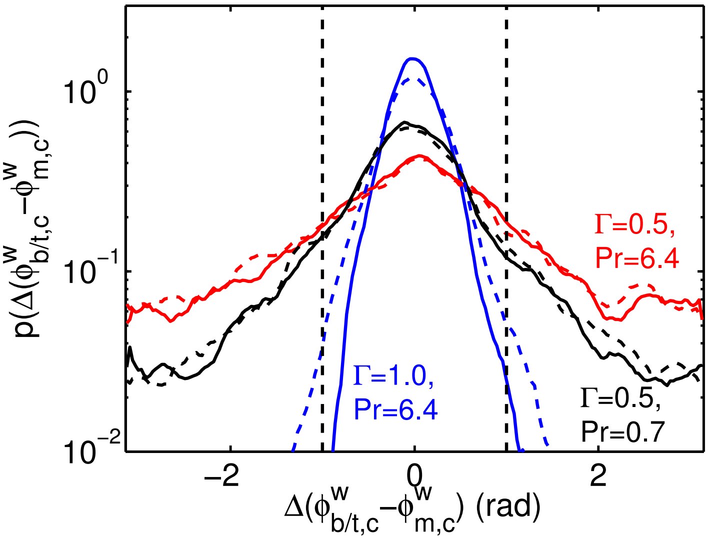

Figure 5.11: The PDF of $\phi^w_{b/t,c} - \phi^w_{m,c}$ for $Ra = 1 \times 10^8$, see text for details. The dashed and solid lines indicate the PDF based on the data of only 8 or all 64 probes equally spaced probes per horizontal level, respectively. The vertical dashed lines indicate the definition of the SRS according to Xi and Xia [160] and Weiss & Ahlers [170].

state of the system due to the effect of passing plumes and corner rolls on the azimuthal profiles. The importance of these effects is shown in figure 5.12. This figure shows that based on the data of 8 azimuthally equally spaced probes at each horizontal level the flow structure shown in figure 5.10b, which is a SRS with a strong corner flow, would be identified as a DRS. In addition, the figure shows that the full azimuthal temperature profiles reveal that a higher azimuthal resolution (e.g., 64 instead of only 8 probes) could resolve the double peak structure (originating from the coexistence of the SRS with some corner flow), which makes it possible to distinguish this state from a real DRS.

We note that the experiments of Weiss & Ahlers [170] show that for $Pr = 4.38$ and $Ra \lesssim 3 \times 10^9$ the flow state is undefined for about 50% of the time. In the experiments the SRS only establishes itself for higher Ra, where the flow state is much better defined, as the area of the corner flow becomes smaller and smaller (14). It is therefore likely that the examples presented here are primarily important in the low Ra number regime investigated here and are much less common in the higher Ra number regime considered in most experiments. We stress however that one does not know a priori whether one is in a difficult case or in a case where the method works fine. Therefore we feel that it is important to realize that there are some limitations in the methods to determine the flow state from three rows of 8 equally spaced thermistors. An example of such a difficult case is the breakdown of the LSC when a strong rotation is applied around the cylinder axis, see part II of this thesis.

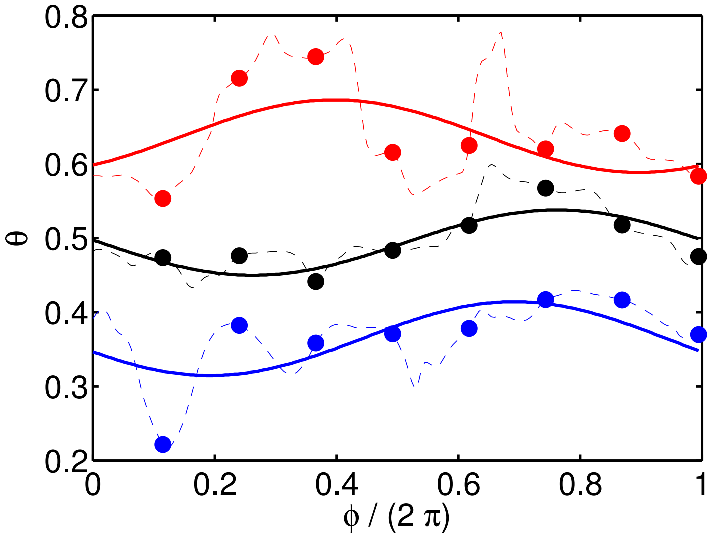

Figure 5.12: Red (top), black (middle), and blue (bottom) data indicate the azimuthal temperature profile at the heights $0.25L$, $0.50L$, and $0.75L$, respectively, for the flow state indicated in figure 5.10b. The dots indicate the data of 8 azimuthally equally spaced probes per horizontal plane. Based on the cosine fits (solid lines) obtained from this probe data this state would be identified as a DRS, while figure 5.10b shows that it is in fact a SRS with a strong corner flow. The dashed lines show that a higher azimuthal resolution can resolve the double peak structure of the corner flow and the main flow. The temperatures at $0.25L$ ($0.75L$) have been raised (lowered) by 0.1 for clarity.

5.6 The relative LSC strength

The instantaneous temperature profiles in figure 5.12 show that the LSC is not always clearly present, meaning that the cosine fit becomes poor. In order to study this in more detail, we introduce the concept of the relative LSC strength, which we define as the strength of the LSC, i.e. the cosine mode, with respect to the strength of the plumes and turbulent fluctuations, i.e. the fluctuations around the cosine fit.

A convenient way to define a relative LSC strength that is independent of the number of probes is to determine the energy in the different Fourier modes of the azimuthal temperature or the azimuthal vertical velocity profile. In order to obtain relative LSC strength $\bar{S}_k$ with a number between 0 and 1 we normalize the energy in the first Fourier mode, i.e. the cosine mode, as follows:

$$\bar{S}_k = \mathrm{Max}\left(\left(\frac{\sum_{t_b}^{t_e} E_1}{\sum_{t_b}^{t_e} E_{tot}} - \frac{1}{N}\right) / \left(1 - \frac{1}{N}\right), 0\right). \tag{5.2}$$

Here $\sum_{t_b}^{t_e} E_1$ indicates the sum of the energy in the first Fourier mode over time, i.e. from the beginning of the simulation $t = t_b$ to the end of the simulation $t = t_e$, $\sum_{t_b}^{t_e} E_{tot}$ the sum of the total energy in all Fourier modes over time, and N the total number of Fourier modes that can be determined. Note that the factor $1/N$ is only used to subtract the part of energy coming from the equi-distribution among all the modes. The number of Fourier modes N that can be determined is $n_p/2$, where $n_p = 2^i$ is the number of probes and i is an integer. The subscript k $(= b, m, t)$ indicates the height level in the sample at which the relative LSC strength is determined. Here we will only determine $\bar{S}_k$ for the middle row of thermistors, thus only $\bar{S}_m$. We note that the LSC amplitude δ_m and the phase ϕ_m of the first Fourier mode are identical to the ones determined when using the least square fit in equation (5.1). We moreover note that the quantity $\bar{S}_k$ is *not* time resolved and thus does not allow to study the switching between the SRS and DRS [170]. Results on time-resolved relative LSC strengths will be presented in the next section.

The normalization in eq. (5.2) has been chosen such that the relative LSC strength $\bar{S}_m$ always has a value between 0 and 1: The value 1 indicates that the azimuthal profile is a pure cosine profile, which is a signature of the LSC according to [98], and the value 0 indicates that the magnitude of the cosine mode is equal to (or weaker than) the value expected from a random noise signal. $\bar{S}_m \gg 0.5$ indicates that the cosine fit on average is a reasonable approximation of the data, as then most energy in the signal is in the first Fourier mode, i.e. the cosine mode. In contrast, $\bar{S}_m \ll 0.5$ indicates that most energy is in the higher Fourier modes, meaning that the application of a cosine fit to the data becomes questionable. Somehow arbitrary, we define the SRS as dominant once $\bar{S}_m > 0.5$.

To further demonstrate these properties of $\bar{S}_k$, we analyze the test function

$$\theta_i(j) = A_{cos}\cos(\phi_i + j/100) + f(j). \tag{5.3}$$

Here $\phi_i = 2i\pi/n_p$ and $f(j)$ is a set of Gaussian distributed random numbers with a certain standard deviation $\langle f^2 \rangle^{1/2}$, the "time" j is varied between 1 and 125000, and the noise is supposed to model the effect of turbulent fluctuations around the cosine fit. The result for the relative strength $\bar{S}_k$ of the LSC as function of the noise level is shown in figure 5.13a. Indeed, $1 \geq \bar{S}_k \geq 0$ and $\bar{S}_k > 0.5$ only if the noise is smaller than the amplitude, $\left\langle f^2 \right\rangle^{1/2}/A_{cos} \ll 1$.

We now come back to the numerical data of our simulations. For each simulation we calculated the relative LSC strength $\bar{S}_m$ based on the instantaneous azimuthal vertical velocity profiles at midheight based on the data of either only 8 or all 64 probes at the horizontal midplane. We show the results for two aspect ratios, two Rayleigh numbers, and two Prandtl numbers in table 5.1. For $\Gamma = 1$ the flow is clearly in the SRS, as indicated by $\bar{S}_m \geq 0.65$. For $\Gamma = 1/2$ the SRS is less dominant, in particular for the large Prandtl number case $Pr = 6.4$, where the SRS hardly occurs. This confirms our conclusions of the previous section where we stated that the SRS is not always present in the $\Gamma = 1/2$ sample.

Another method used in the literature [98, 170] to identify the flow pattern is to average the azimuthal profile with respect to the LSC orientation. This method

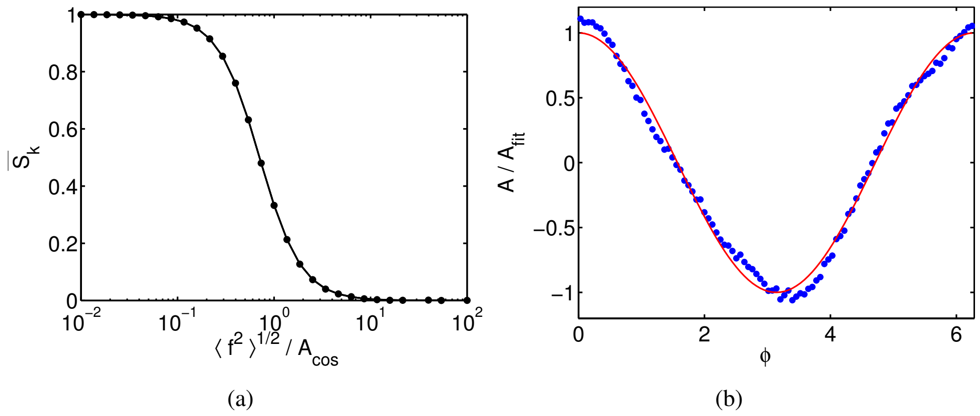

(a) (b)

Figure 5.13: a) The relative strength of the LSC $\bar{S}_k$ versus the relative noise level $\langle f^2 \rangle^{1/2}/A_{cos}$, calculated from the stochastic model (equation (5.3)). For strong noise $\bar{S}_k < 0.5$ and the SRS is defined to break down. b) The azimuthal vertical velocity profile after averaging with respect to the orientation of the LSC, which was obtained using a cosine fit, is indicated by the dots. The method has been applied to the data of all 64 probes in the horizontal midplane obtained in the simulation at $Pr = 6.4$, $Ra = 1 \times 10^8$, and $\Gamma = 1/2$. The solid line indicates a pure cosine profile.

assumes that the deviations from the cosine fit are due to turbulent fluctuations. It will work for cases for which $\bar{S}_m$ is large. However, when $\bar{S}_m$ is low, this method gives misleading results as is shown in figure 5.13b where we apply it to above discussed data for $Pr = 6.4$ in the $\Gamma = 1/2$ sample, where the relative LSC strength using the data of all 64 probes in the horizontal level is $\bar{S}_m = 0.27$ (see table 5.1): The average profile obtained with the method of refs. [98, 170] cannot be distinguished from the ones obtained from the cases where $\bar{S}_m$ is larger and therefore the method cannot be used to claim the dominance of the SRS.

5.7 Time resolved relative LSC strength

The relative LSC strength can also be calculated on instantaneous azimuthal temperature and vertical velocity profiles. We demonstrate this by constructing the PDF of the relative LSC strength at midheight $S_m(t)$ for instantaneous azimuthal temperature and vertical velocity profiles using the definition

$$S_m(t) = \left(\frac{E_1(t)}{E_{tot}(t)} - \frac{1}{N} \right) / \left(1 - \frac{1}{N} \right). \tag{5.4}$$

The only difference with respect to equation (5.2) is that $E_1(t)$ and $E_{tot}(t)$ and thus $S_m(t)$ are time dependent and that we have dropped the criterion that the minimal value should be 0. The reason for the latter is that we want to prevent strange jumps in the PDFs of S_m at 0. For $N = 8$ probes we have $-\frac{1}{3} \leq S_m(t) \leq 1$ and for $N = 64$ probes

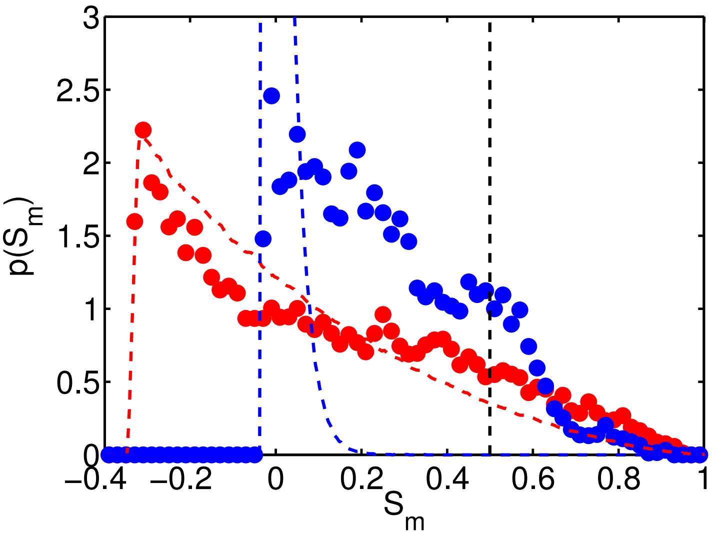

Figure 5.14: PDFs of the relative LSC strength at midheight for $Ra = 1 \times 10^8$, $Pr = 6.4$, and $\Gamma = 0.5$. The red ($-\frac{1}{3} \leq S_m(t) \leq 1$) and blue ($-\frac{1}{31} \leq S_m(t) \leq 1$) data points indicate the PDF based on the azimuthal vertical velocity profile sampled with only 8 and all 64 probes, respectively. The colored dashed lines give the corresponding PDFs based on a purely random signal. The vertical dashed lines at $S_m = 0.5$ indicates the region $0.5 \leq S_m \leq 1.0$ where the first Fourier modes contains at least 50% of the energy of the azimuthal vertical velocity profile.

we have $-\frac{1}{31} \leq S_m(t) \leq 1$. Note that these intervals follow directly from equation 5.4 by filling in the limiting cases, i.e. $E_1(t)/E_{tot}(t) = 0$ and $E_1(t)/E_{tot}(t) = 1$, and by using the relation $N = n_p/2$, where n_p is the number of probes, see previous section.

Figure 5.14 shows the PDFs for S_m based on the measurement of the vertical velocity by only 8 or all 64 equally spaced probes at midheight in the simulation with $Ra = 1 \times 10^8$, $Pr = 6.4$, and in the $\Gamma = 0.5$ sample. In addition, for both cases we determined the distribution of $S_m(t)$ for a random signal. When we compare the PDFs based on the simulation data with the distributions obtained for random signals, we see that the difference is relatively small when the data of only 8 probes is considered, whereas a much larger difference is obtained when the data of all 64 probes is taken into account. Figure 5.14 thus clearly shows that it can be beneficial to use more than 8 azimuthally equally spaced probes, since it becomes much easier to show that certain events are statistically relevant.

5.8 Conclusions

We studied the LSC dynamics in DNS simulations by investigating the azimuthal temperature and vertical velocity profiles obtained from 64 equally spaced numerical probes at three different heights. For $Pr = 6.4$ in a $\Gamma = 1$ sample we find that the azimuthal profile is well presented with the data of 8 numerical probes, a number normally used in experiments, as the LSC orientation obtained by a cosine fit is the same when the data of 8 and 64 probes is considered. We find that the improved azimuthal resolution (64 instead of 8 probes in the sidewall at one height) can reveal the effect of the plumes.

In agreement with the findings of Xi and Xia [160] and Weiss and Ahlers [170] we find that there is more disorder present in the $\Gamma = 1/2$ sample than in the $\Gamma = 1$ sample. For the $\Gamma = 1/2$ case we also show that when the azimuthal temperature profile is only determined from 8 probes per horizontal level a SRS can erroneously be identified as a DRS, because the azimuthal resolution is too small to distinguish between the structure of the corner flow and the main roll. Here we again stress that this result is obtained in the relatively low *Ra* number regime. The experimental results of Weiss & Ahlers [170] show that for the low *Ra* number regime the flow state is undefined for about 50% of the time. For $\Gamma = 1/2$ the SRS only establishes itself for higher *Ra*, where the flow state is much better defined [170]. It is therefore likely that the examples presented here are primarily important in this low *Ra* number regime investigated here and are much less common in the higher *Ra* number regime.

We quantified the LSC strength relative to the turbulent fluctuations by determining the ratio between the energy in the first Fourier mode and the energy in all Fourier modes of the azimuthal temperature and azimuthal vertical velocity profiles. We find that the relative LSC strength at $Ra = 1 \times 10^8$ is considerably lower in the $\Gamma = 1/2$ sample than in the $\Gamma = 1$ sample, i.e. that the SRS is much less pronounced in the $\Gamma = 1/2$ sample than in the $\Gamma = 1$ sample. This determination of the relative LSC strength can be applied directly to available experimental data to determine whether the SRS is present in high Ra number thermal convection and in rotating RB convection.

Part II

Rotating Rayleigh-Bénard convection

6

Prandtl-, Rayleigh-, and Rossby-number dependence of heat transport * †

Experimental and numerical data for the heat transfer as a function of the Rayleigh-, Prandtl-, and Rossby numbers in turbulent rotating Rayleigh-Bénard convection are presented. For relatively small Ra $\approx 10^8$ *and large Pr modest rotation can enhance the heat transfer by up to 30%. At larger Ra there is less heat-transfer enhancement, and at small Pr* $\lesssim 0.7$ *there is no heat-transfer enhancement at all. We suggest that the small-Pr behavior is due to the breakdown of the heat-transfer-enhancing Ekman pumping because of larger thermal diffusion.*

6.1 Introduction

In the present chapter we determine systematically as a function of the Rayleigh number *Ra*, Prandtl number *Pr*, and Rossby number *Ro* where the heat-flux enhancement occurs in rotating RB. We present both experimental measurements and results from direct numerical simulation (DNS). They cover different but overlapping parameter ranges and thus complement each other. Where they overlap they agree very well. We find that in certain regimes the heat-flux enhancement can be as large as 30%;

---

[*] Based on: J.Q. Zhong, R.J.A.M. Stevens, H.J.H. Clercx, R. Verzicco, D. Lohse, and G. Ahlers, Prandtl-, Rayleigh-, and Rossby-Number Dependence of Heat Transport in Turbulent Rotating Rayleigh-Bénard Convection, Phys. Rev. Lett. 102, 044502 (2009).

[†] The experiments discussed in this chapter were performed by J.Q. Zhong and G. Ahlers in Santa Barbara.

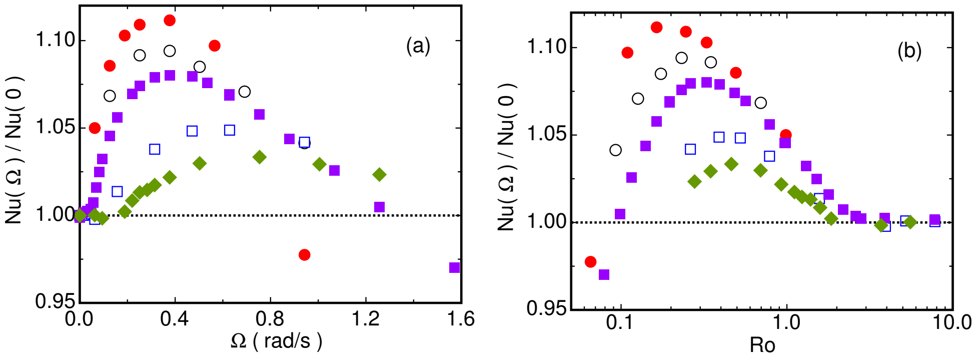

Figure 6.1: The ratio of the Nusselt number $Nu(\Omega)$ in the presence of rotation to $Nu(\Omega = 0)$ for $Pr = 4.38$ ($T_m = 40.00°\mathrm{C}$). (a): Results as a function of the rotation rate in rad/sec. (b): The same results as a function of the Rossby number Ro on a logarithmic scale. Red solid circles: $Ra = 5.6 \times 10^8$ ($\Delta = 1.00$ K). Black open circles: $Ra = 1.2 \times 10^9$ ($\Delta = 2.00$ K). Purple solid squares: $Ra = 2.2 \times 10^9$ ($\Delta = 4.00$ K). Blue open squares: $Ra = 8.9 \times 10^9$ ($\Delta = 16.00$ K). Green solid diamonds: $Ra = 1.8 \times 10^{10}$ ($\Delta = 32.00$ K)

this raises the possibility of relevance in industrial processes. Even more remarkably, we observe a heretofore unanticipated strong dependence of this enhancement on Pr as well as on Ra.

6.2 Experimental measurements

The convection apparatus was described in detail as the "medium sample" in Ref. [175]. Since the previous measurements [176] it had been completely dis- and re-assembled. It had copper top and bottom plates, and a new plexiglas side wall of thickness 0.32 cm was installed for the current project. The sample had a diameter $D = 24.8$ cm and a height $L = 24.8$ cm, yielding $\Gamma = 1.00$. The apparatus was mounted on a rotating table. We used rotation rates up to 0.3 Hz. Thus the Froude number $Fr = \Omega^2(L/2)/g$ did not exceed 0.05, indicating that centrifugal effects were small. Cooling water for the top plate and electrical leads were brought into and out of the rotating frame using Dynamic Sealing Technologies feed-throughs mounted on the rotation axis above the apparatus. All measurements were made at constant imposed Δ and Ω, and fluid properties were evaluated at $T_m = (T_t + T_b)/2$. Data were taken at 60.00°C ($Pr = 3.05$, $t_v = L^2/\nu = 1.27 \times 10^5$ sec), 40.00°C ($Pr = 4.38$, $t_v = 9.19 \times 10^4$ sec), 24.00°C ($Pr = 6.26$, $t_v = 6.69 \times 10^4$ sec) and 23.00°C ($Pr = 6.41$, $t_v = 6.56 \times 10^4$ sec). In a typical run the system was allowed to equilibrate for three or four hours, and temperatures and heat currents were then averaged over an additional three or four hours and used to calculate Ra and the Nusselt number $Nu = QL/(\lambda\Delta)$ (Q is the heat-current density).

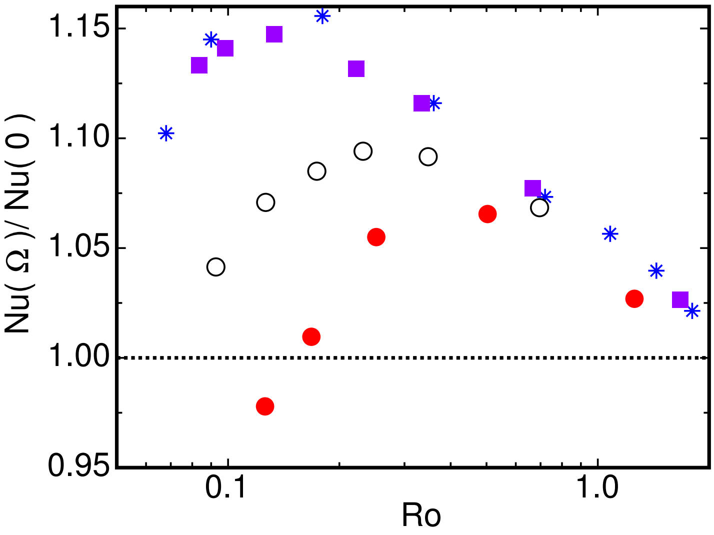

Figure 6.2: The ratio $Nu(\Omega)/Nu(\Omega = 0)$ for $Ra = 1.2 \times 10^9$ as function of Ro on a logarithmic scale. Red solid circles: $Pr = 3.05$ ($T_m = 60.00$°C). Black open circles: $Pr = 4.38$ ($T_m = 40.00$°C). Purple solid squares: $Pr = 6.41$ ($T_m = 23.00$°C). Blue stars: Numerical simulation for $Ra = 1.0 \times 10^9$ and $Pr = 6.4$ from Ref. [75].

Measurements of the Nusselt number without rotation, $Nu(\Omega = 0)$, over the range $5 \times 10^8 \lesssim Ra \lesssim 10^{10}$ ($1 \lesssim \Delta \lesssim 20$K) agreed within estimated systematic errors of about 1% with previous results [176] obtained in the same apparatus. The ratio $Nu(\Omega)/Nu(\Omega = 0)$ is shown in Fig. 6.1a as a function of the rotation rate Ω. Those results are for $T_m = 40.00$°C, where $Pr = 4.38$. The enhancement of Nu due to modest rotation is clearly seen at all Ra. It is larger at the smaller Ra.

In Fig. 6.1b we show the same data as a function of the Rossby number Ro. At large Ro (small Ω) the data must approach unity, and indeed they do. As Ro decreases, Nu is first enhanced, but then reaches a maximum and decreases as expected. The maximum of $Nu(\Omega)/Nu(\Omega = 0)$ occurs at larger Ro for larger Ra, and the value of this ratio at the maximum diminishes with increasing Ra.

In Fig. 6.2 the results at constant Ra are shown as a function of Ro for several values of Pr. Also shown are the DNS results from Ref. [75]; these data agree rather well with the experimental data at nearly the same Pr and Ra. One sees that the enhancement of Nu at large Ro is nearly independent of Pr; but as Ro decreases below unity a strong Pr dependence manifests itself. As Ro decreases, the depression of Nu sets in earlier for smaller Pr, and the maximal relative heat transfer enhancement is smaller.

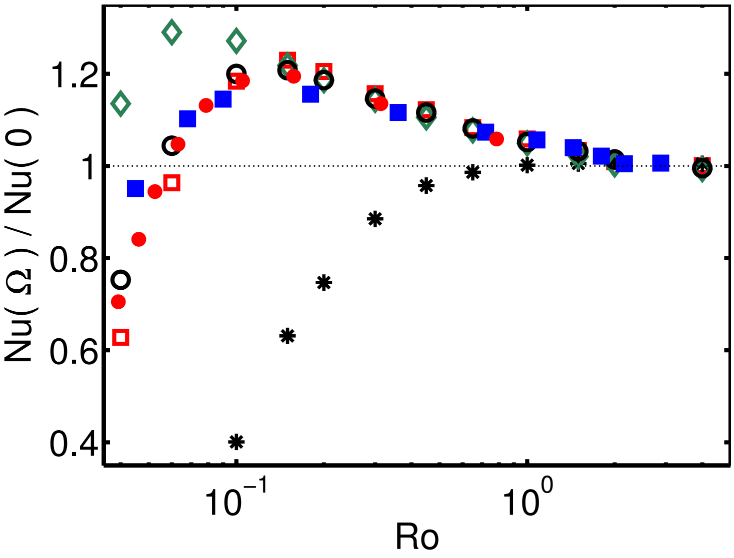

Figure 6.3: The ratio $Nu(\Omega)/Nu(\Omega=0)$ as function of Ro on a logarithmic scale. Red solid circles: $Ra = 2.73\times10^8$ and $Pr = 6.26$ (experiment). Black open circles: $Ra = 2.73\times10^8$ and $Pr = 6.26$ (DNS). Blue solid squares: $Ra = 1\times10^9$ and $Pr = 6.4$ (DNS) [75]. Red open squares: $Ra = 1\times10^8$ and $Pr = 6.4$ (DNS). Green open diamonds: $Ra = 1\times10^8$ and $Pr = 20$ (DNS). Black stars: $Ra = 1\times10^8$ and $Pr = 0.7$ (DNS).

6.3 Numerical simulations

In the DNS we solved the three-dimensional Navier-Stokes equations within the Boussinesq approximation,

$$\frac{D\mathbf{u}}{Dt} = -\nabla P + \left(\frac{Pr}{Ra}\right)^{1/2}\nabla^2\mathbf{u} + \theta\widehat{z} - \frac{1}{Ro}\widehat{z}\times\mathbf{u}, \qquad (6.1)$$

$$\frac{D\theta}{Dt} = \frac{1}{(PrRa)^{1/2}}\nabla^2\theta, \qquad (6.2)$$

with $\nabla\cdot\mathbf{u} = 0$. Here $\widehat{z}$ is the unit vector pointing in the opposite direction to gravity, $\mathbf{u}$ the velocity vector, and θ the non-dimensional temperature, $0 \leq \theta \leq 1$. Finally, P is the reduced pressure (separated from its hydrostatic contribution, but containing the centripetal contributions): $P = p - r^2/(8Ro^2)$, with r the distance to the rotation axis. The equations have been made non-dimensional by using, next to L and Δ, the free-fall velocity $U = \sqrt{\beta g\Delta L}$. The simulations presented in this chapter were performed on a grid of $257\times129\times257$ nodes, respectively, in the azimuthal, radial, and vertical directions, allowing for a sufficient resolution of the small scales both inside the bulk of turbulence and in the BLs (where the grid-point density has been enhanced) for the parameters employed here [75, 90]. Nu is calculated as in chapter 2 and its statistical convergence has been verified.

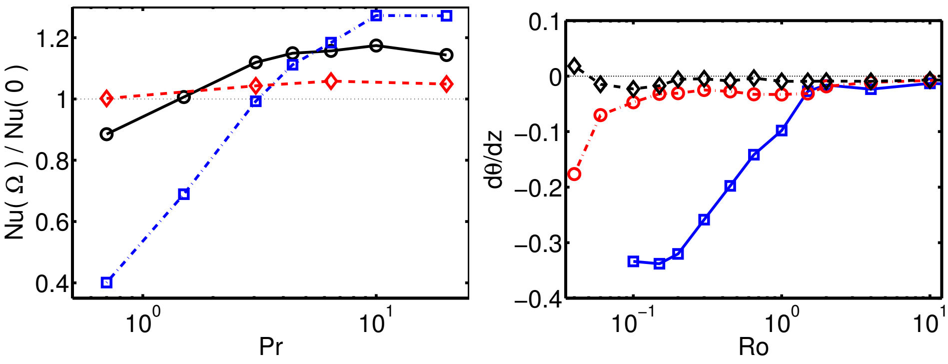

(a) (b)

Figure 6.4: (a) Numerical result for the ratio $Nu(\Omega)/Nu(0)$ as function of Pr for $Ra = 10^8$ and $Ro = 1.0$ (red open diamonds), $Ro = 0.3$ (black open circles), and $Ro = 0.1$ (blue open squares). (b) The horizontally averaged vertical temperature gradient $d\theta/dz$ at the sample mid-plane as a function of Ro for $Ra = 1 \times 10^8$. Blue open squares: $Pr = 0.7$. Red open circles: $Pr = 6.4$. Black open diamonds: $Pr = 20$.

The numerical results for Nu as function of Ro for several Ra and Pr are shown in Fig. 6.3. For $Ra = 2.73 \times 10^8$ and $Pr = 6.26$ experimental data (not previously shown in Figs. 6.1 and 6.2) are plotted as well, showing near-perfect agreement with the numerical results. This gives us confidence that the partial neglect of centrifugal effects in the simulations [namely, neglecting the density dependence of the centripetal forces, which in the Boussinesq equations show up as $-2\mathrm{Fr}\, r\theta\hat{r}$ [177] (with the radial unit vector $\hat{r}$)] is justified, as already found in Refs. [75, 85], because $\mathrm{Fr} \ll 1$. Thus neither do the experimentally unavoidable finite conductivity of the top and bottom plates [175, 178] and the side-wall conductivity [60, 179] seem to matter in this regime of parameter space, as already explained in Ref. [20] for the non-rotating case.

6.4 Simulation results

As was seen for the experimental data in Figs. 6.1 and 6.2, the numerical results in Fig. 6.3 also reveal a drastic dependence of the Nusselt-number enhancement on Pr. For large $Pr \gtrsim 6$ the enhancement can be as large as 30% for $Ra \approx 10^8$ and $Ro \approx 0.1$. However, there is no enhancement at all for small $Pr \lesssim 0.7$. This trend is further elucidated in Fig. 6.4a, where we show the Nusselt-number enhancement as function of Pr for three different Ro and $Ra = 10^8$.

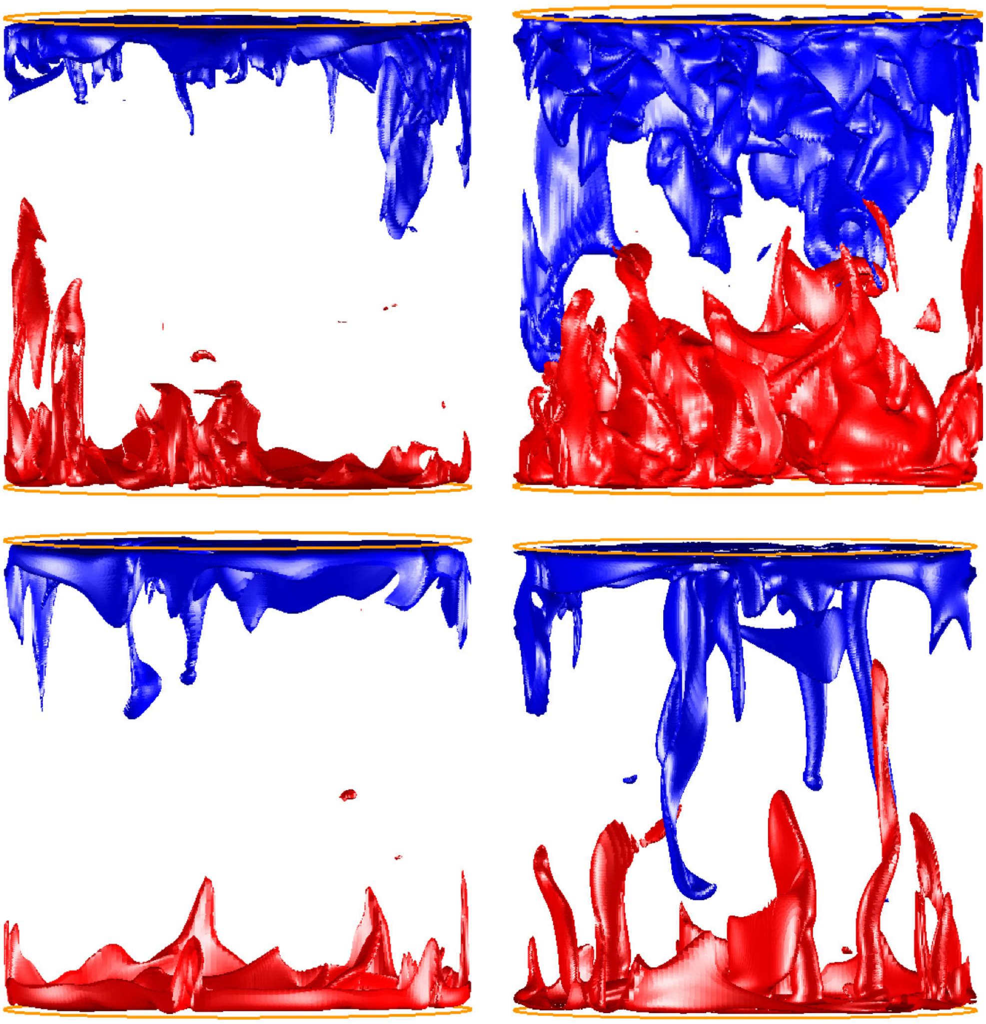

Figure 6.5: 3D visualization of the temperature isosurfaces at 0.65Δ (red) and 0.35Δ (blue), respectively, for $Pr = 0.7$ (upper plot) and $Pr = 6.4$ (lower plot) for $Ra = 10^8$ and $Ro = \infty$ (left) $Ro = 0.30$ (right).

6.5 Influence of Rayleigh and Prandtl

Why does the heat-transfer enhancement through Ekman pumping at modest rotation rates break down as Ro decreases below a Pr-dependent typical value, as seen in Figs. 6.1 to 6.3? To obtain a hint, we visualized (see Fig. 6.5) the three-dimensional temperature iso-surfaces for $Pr = 0.7$ and for $Pr = 6.4$ at both $Ro = 0.30$ and $Ro = \infty$, at $Ra = 10^8$. While for the larger $Pr = 6.4$ case the temperature iso-surfaces organize to reveal long vertical vortices as suggested by the Ekman-pumping picture, these structures are much shorter and broadened for the low $Pr = 0.7$ case, due to the larger thermal diffusion which makes the Ekman pumping ineffective. This would imply enhanced horizontal heat transport which should also lead to a steeper gradient of the mean temperature in the bulk. Indeed, in the DNS, we find that when Ro becomes small enough, the bulk of the fluid displays an increasingly destabilizing mean temperature gradient (see Fig. 6.4b), which of course must be accompanied by a reduction of the mean temperature drop over the thermal BLs and thus a Nusselt-number reduction. The first manifestation of the enhancement of the mean destabilizing vertical temperature gradient agrees with the onset of relative heat-transfer reduction in figure 6.3, and thus supports this explanation.

Along the same line of arguments one may also expect that the Ra dependence of the reduction of Nu at small Ro seen in Fig. 6.1 is attributable to relatively less effective Ekman pumping at higher Ra: The enhanced turbulence may lead to a larger eddy thermal diffusivity, promoting a homogeneous mean temperature in the bulk. Again this would make Ekman pumping relatively less effective and reduce the peak in the relative Nusselt number.

6.6 Conclusions

Another interesting aspect of our data is that within our experimental or numerical resolution there is no heat-flux enhancement for $Ro \gtrsim 2$ for any Ra or Pr. As already noticeable from the data of Ref. [75], the heat-flux enhancement first becomes resolved as Ro decreases below about two. This will be discussed in more detail in chapters 8 and 9, where we show that with increasing rotation and large enough Ra a supercritical bifurcation from a turbulent state with nearly rotation independent heat transfer to another with enhanced heat transfer is observed. In the next chapter we will first discuss the influence of the Pr number on the heat transfer enhancement in more detail.

7

Optimal Prandtl number for heat transfer enhancement [*]

Numerical data for the heat transfer as a function of the Prandtl (Pr) and Rossby (Ro) numbers in turbulent rotating Rayleigh-Bénard convection are presented for Rayleigh number $Ra = 10^8$. When Ro is fixed the heat transfer enhancement with respect to the non-rotating value shows a maximum as function of Pr. This maximum is due to the reduced effect of Ekman pumping when Pr becomes too small or too large. When Pr becomes small, i.e. for large thermal diffusivity, the heat that is carried by the vertical vortices spreads out in the middle of the cell, and Ekman pumping thus becomes less effective. For higher Pr the thermal boundary layers (BLs) are thinner than the kinetic BLs and therefore the Ekman vortices do not reach the thermal BL. This means that the fluid that is sucked into the vertical vortices is colder than for lower Pr which limits the upwards heat transfer.

7.1 Introduction

In the previous chapter it was shown that no heat-transfer enhancement is observed at small $Pr \lesssim 0.7$. This was explained by the larger thermal diffusivity at lower Pr due to which the heat that is carried by the vertical vortices created by Ekman pumping spreads out in the middle of the cell. This leads to a larger destabilizing tempera-

---

[*] Based on: R.J.A.M. Stevens, H.J.H. Clercx, and D. Lohse Optimal Prandtl number for heat transfer enhancement in rotating turbulent Rayleigh-Bénard convection, New J. Phys. 12, 075005 (2010).

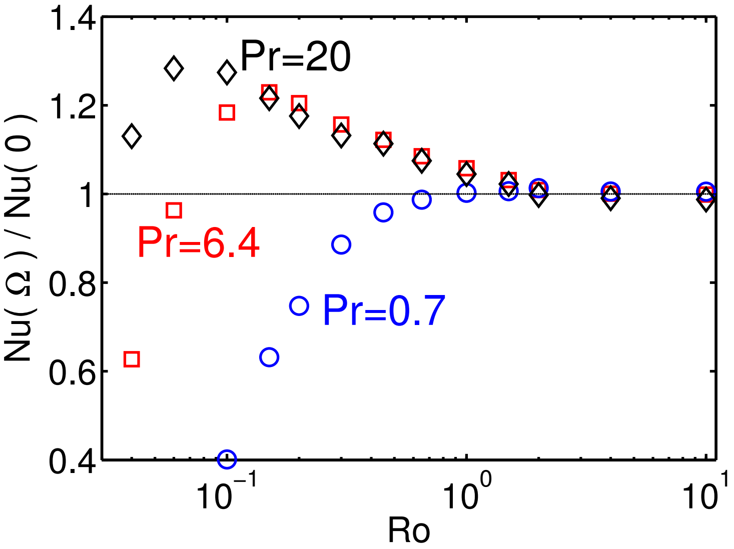

Figure 7.1: The ratio $Nu(\Omega)/Nu(\Omega = 0)$ as function of Ro on a logarithmic scale for $Ra = 1 \times 10^8$ and different Pr. Blue open circles: $Pr = 0.7$, red open squares: $Pr = 6.4$, and black open diamonds: $Pr = 20$.

ture gradient in the bulk and a lower heat transfer. Furthermore, Ekman pumping turned out to become less effective at higher Ra numbers where a larger eddy thermal diffusivity limits the effect of Ekman pumping. In this chapter we systematically determine the heat-transfer enhancement with respect to the non rotating value as function of the Pr number by using DNS.

7.2 Numerical method

In the DNS we solved the three-dimensional Navier-Stokes equations within the Boussinesq approximation. The numerical scheme was already described in Refs. [107–109] and chapter 6. The numerical details concerning rotating RB convection are described in detail in chapter 6. Most simulations were performed on a grid of $257 \times 129 \times 257$ nodes, respectively, in the azimuthal, radial, and vertical directions, allowing for a sufficient resolution of the small scales both inside the bulk of turbulence and in the BLs (where the grid-point density has been enhanced) for the parameters employed here, see chapter 6. Nu is calculated in several ways as described in detail in chapter 2 and its statistical convergence has been checked. A grid of $385 \times 193 \times 385$ nodes has been used for the simulations at the highest Pr number and to verify the results for $Pr = 6.4$ obtained on the coarser grid. Furthermore, for the higher Pr number cases the flow is simulated for a very long time (400 dimensionless time units to reach the statistically stationary state followed by 800 time units

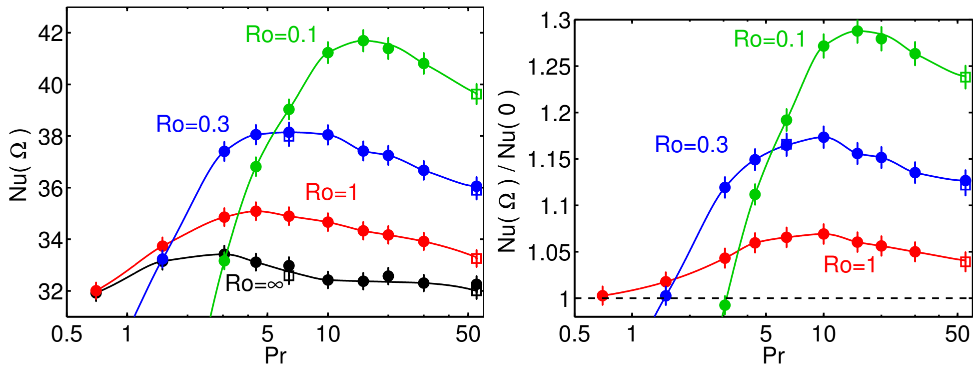

Figure 7.2: The heat transfer as function of Pr on a logarithmic scale for $Ra = 1 \times 10^8$. Black, red, blue, and green indicate the results for $Ro = \infty$, $Ro = 1.0$, $Ro = 0.3$, and $Ro = 0.1$, respectively. The data obtained on the $385 \times 193 \times 385$ (open squares) and the $257 \times 129 \times 257$ grid (solid circles) are in very good agreement.

for averaging) to assure statistical convergence. In chapter 6 we already showed that our DNS results agree very well with experimental results in this Ra number regime.

7.3 Two competing mechanisms

The numerical results for $Nu(\Omega)/Nu(0)$ as function of Ro for several Pr are shown in figure 7.1. The figure shows that the heat transport enhancement caused by Ekman pumping can be as large as 30% for $Pr = 20$. However, no heat transport enhancement is found for $Pr = 0.7$ which is due to the larger thermal diffusivity which makes Ekman pumping less effective, see chapter 6. In figure 7.1 one can already see that the heat transfer enhancement reaches a maximum at a certain Pr when the Ro number is fixed. Indeed figure 7.2 confirms that the heat transfer enhancement as function of Pr reaches a maximum. Its location depends on Ro; namely the stronger the rotation rate the higher the Pr number for which the maximum heat transfer enhancement is found. This trend is even more pronounced when the heat transfer $Nu(Ro)$ itself is considered.

The observation that there is a Pr number for which the heat transfer enhancement is largest suggests that there should be at least two competing effects, which strongly depend on the Pr number, that control the effect of Ekman pumping. One wonders why Ekman pumping becomes less effective for higher Pr numbers. Clearly, it must have a different origin than the reduced effect of Ekman pumping at lower Pr. Indeed, there is an important difference between the high and the low Pr number regime, namely the relation between the thickness of the thermal and the kinetic boundary layers (BL). For the low Pr number regime the kinetic BL is thinner than the thermal BL and therefore the fluid that is sucked into the vertical vortices is very hot. When

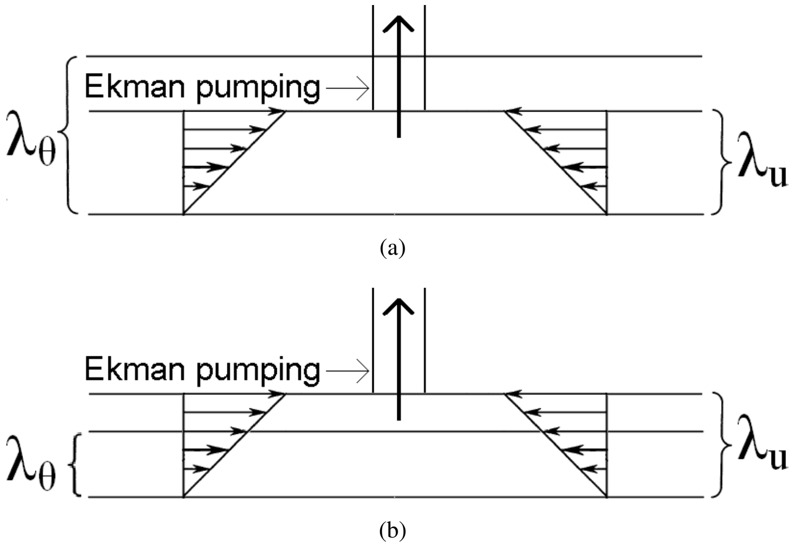

(a)

(b)

Figure 7.3: a) Sketch for the low *Pr* number regime where the Ekman vortices reach the thermal BL. b) Sketch for the high *Pr* number regime where the Ekman vortices do not reach the thermal BL.

the *Pr* number is too low this heat will spread out in the middle of the cell due to the large thermal diffusivity. For somewhat higher *Pr* number the fluid that is sucked out of the thermal BL is still sufficiently hot and due to the smaller thermal diffusivity the heat can travel very far from the plate in the vertical vortices. In this way Ekman pumping can increase the heat transfer for moderate *Pr*. In the high *Pr* number regime the kinetic BL is much thicker than the thermal BL. Therefore the Ekman vortices forming in the bulk do not reach the thermal BL and hence the temperature of the fluid that enters the vertical vortices is much lower. This is schematically shown in figure 7.3.

An investigation of the temperature isosurfaces in the previous chapter revealed long vertical vortices as suggested by Ekman-pumping at $Pr = 6.4$, while these structures are much shorter and broadened for the $Pr = 0.7$ case due to the larger thermal diffusivity at lower *Pr* (chapter 6). In figure 7.4 we show the temperature isosurfaces at $Ro = 0.30$ for several *Pr* to identify the difference between the high and moderate *Pr* number cases. The figure reveals that the vertical transport of hot (cold) fluid away from the bottom (top) plate through the vertical vortex tubes is strongly reduced in the high-Pr number regime compared to the case with $Pr = 6.4$. This is illustrated in figure 7.4 where the threshold for the temperature isosurfaces is taken constant for all cases. Indeed, a closer investigation shows that the vortical structures for the higher *Pr* are approximately as long as for the $Pr = 6.4$ case. This confirms the view that the temperature of the fluid that is sucked into the Ekman vortices decreases with increasing *Pr*.

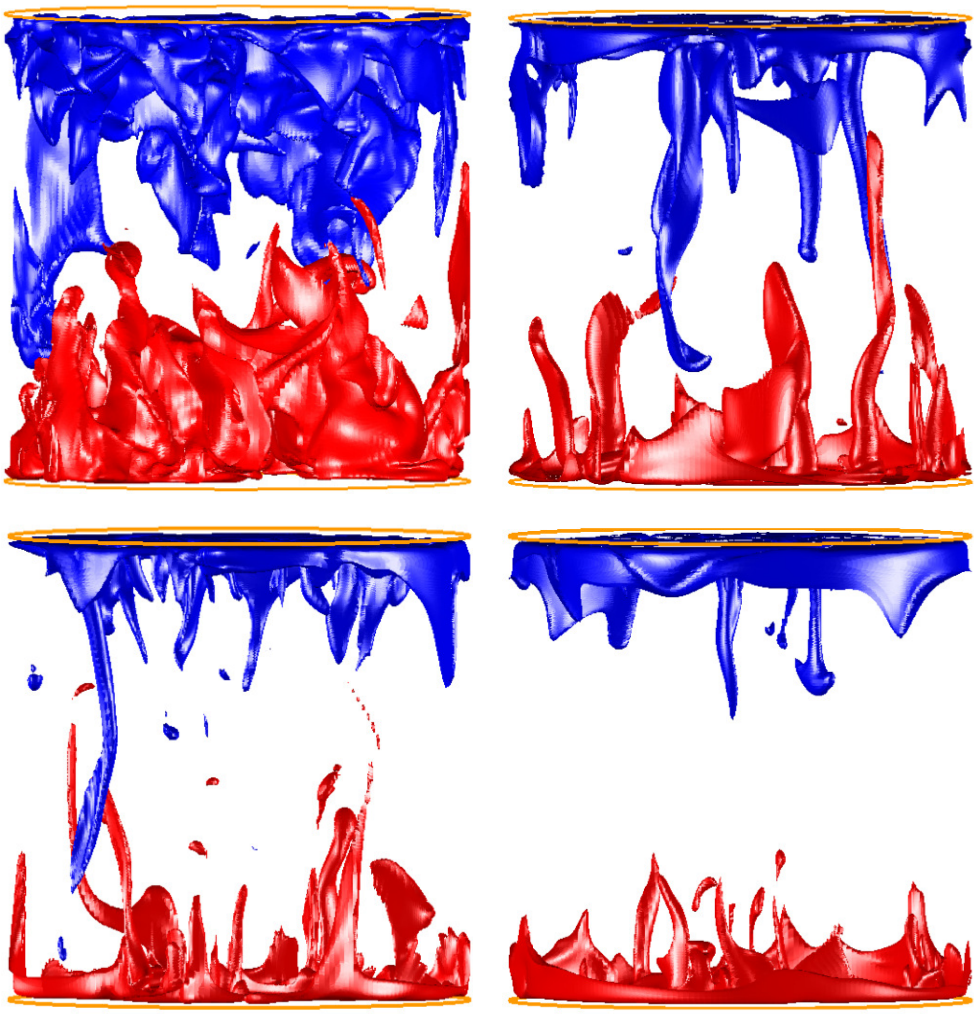

Figure 7.4: 3D visualization of the temperature isosurfaces in the cylindrical sample of $\Gamma = 1$ at 0.65Δ (red) and 0.35Δ (blue), respectively, for $Pr = 0.7$ (left upper plot) and $Pr = 6.4$ (right upper plot), $Pr = 20$ (left lower plot), and $Pr = 55$ (right lower plot) for $Ra = 10^8$ and $Ro = 0.30$. The snapshots were taken in the respective statistically stationary regimes.

To further verify the above explanation we determined the horizontally averaged temperature at the kinetic BL height, defined as two times the height where $\varepsilon_u^{"} := \mathbf{u} \cdot \nabla^2 \mathbf{u}$, see chapter 2 and 11 for details. This height is chosen as it indicates the position where effects of Ekman pumping are dominant. Furthermore, we also determined the horizontally averaged temperature at the edge of the radially dependent thermal BL thickness, i.e. $\lambda_\theta^{sl}(r)$. We determined $\lambda_\theta^{sl}(r)$ by finding the intersection point between the linear extrapolation of the temperature gradient at the plate with

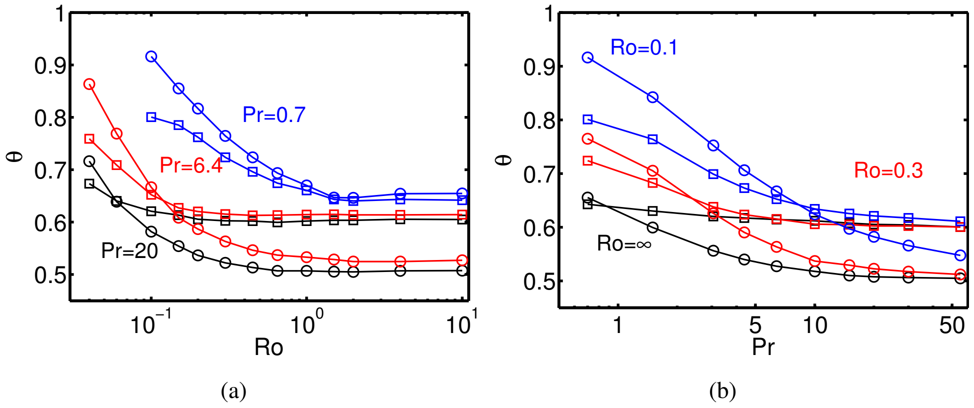

(a) (b)

Figure 7.5: The horizontally averaged temperature at the edge of the kinetic BL (circles) and at the edge of the thermal BL (squares) for $Ra = 1 \times 10^8$. a) Blue, Red, and black indicates the results for $Pr = 0.7$, $Pr = 6.4$ and $Pr = 20$, respectively. b) Black, red, and blue indicate the results for $Ro = \infty$, $Ro = 0.3$, and $Ro = 0.1$, respectively. The results for $Ro = 1$ (not shown) are almost identical to the data obtained for $Ro = \infty$.

the behavior found in the bulk, see chapter 11. Indeed, figure 7.5 shows that the average temperature at the edge of the kinetic BL decreases with increasing Pr. Thus the temperature of the fluid that enters the vertical vortices decreases with increasing Pr and this limits the effect of Ekman pumping at higher Pr. Furthermore, the temperature difference with respect to the bottom plate shows that for the non-rotating case the kinetic BL is thinner than the thermal BL when $Pr < 1$ and thicker than the thermal BL when $Pr > 1$. The figure shows that this transition point shifts towards higher Pr when the rotation rate is increased. We note that in chapter 11 we find that the kinetic BL thickness scales with $Ro^{1/2}$, i.e. Ekman BL scaling, when $Ro \lesssim 1$. Therefore the cases for $Ro = 0.1$ and $Ro = 0.3$, which are shown in figure 7.5, are in the strong rotating regime where the kinetic BL thickness is approximately equal to the Ekman BL thickness.

Another way to identify the effect of Ekman pumping is to look at the horizontally averaged $Re_{z,rms}$ (dimensionless root mean square velocity of the axial velocity fluctuations) value at the height $\lambda_\theta^{sl}(r)$, see chapter 8. An increase in the value of $Re_{z,rms}$ shows that Ekman pumping becomes important. In figure 7.6b it is shown that Ekman pumping is strongest for moderate Pr, because $Re_{z,rms}$ has a maximum around $Pr = 10$. Note that the strength of the Ekman pumping measured in this way reflects the measured Nu number enhancement. One can also deduce from figure 7.5 that the kinetic BL becomes thinner with respect to the thermal BL when the rotation rate is increased, because the temperature difference with the plate becomes smaller. Therefore more hot fluid is sucked into the vertical vortices and this further supports the Ekman pumping effect for moderate rotation rates where the strongest

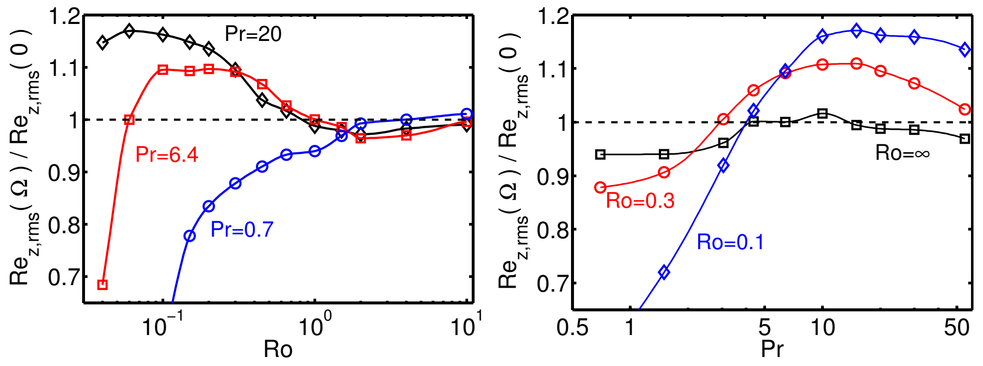

(a) (b)

Figure 7.6: The normalized horizontally averaged rms vertical velocities fluctuation $Re_{z,rms}$ at the edge of the thermal BL for $Ra = 1 \times 10^8$. a) Blue circles, red squares, and black diamonds indicate the data for $Pr = 0.7$, $Pr = 6.4$, and $Pr = 20$, respectively. b) Black squares, red circles, and blue diamonds indicate the data for $Ro = \infty$, $Ro = 0.3$, and $Ro = 0.1$, respectively.

heat transfer enhancement is observed. Furthermore, the maximum in the heat transfer enhancement as shown in figure 7.1 occurs at lower *Ro*, i.e. stronger rotation, for higher *Pr*. The breakdown of *Nu* at low *Ro* is an effect of the suppression of vertical velocity fluctuations through the strong rotation, which is seen in figure 7.6a. Moreover, in figure 7.6a it is shown that the vertical velocity fluctuations are suppressed at higher *Ro*, i.e. lower rotation rate, when *Pr* is lower. Furthermore, at low *Ro* there is experimental [74, 77] and numerical [91] evidence that the vertical component of the vorticity at mid height becomes more symmetric. Near the plates it is positively skewed for $Ro \gtrsim 0.5$, which points at the input of positive vorticity by Ekman pumping. For $Ro \lesssim 0.3$ there is a discrepancy between experimental and numerical measurements of the skewness near the plates, i.e. experiments [74] show that the vorticity distribution becomes more symmetric, while numerical results [91] show a further increase of the positive skewness when *Ro* is decreased.

7.4 Conclusions

To summarize, we studied the *Pr* number dependence of the heat transport enhancement in rotating RB convection and showed that at a fixed *Ro* number there is a *Pr* number for which the heat transfer enhancement reaches a maximum. This is because Ekman pumping, which is responsible for the heat transfer enhancement, becomes less effective when the *Pr* number becomes too small or too large. At small *Pr* numbers the effect of Ekman pumping is limited due to the large thermal diffusivity due to which the heat that is sucked out of the BLs rapidly spreads out in the bulk. At high *Pr* numbers the temperature of the fluid that is sucked into the vertical vortices near the bottom plate is much lower, because the thermal BL is much thinner than the kinetic BL, and therefore the effect of Ekman pumping is lower. Furthermore, the rotation rate for which the heat transfer enhancement reaches its maximum increases with increasing Pr, because the suppression of vertical velocity fluctuations only becomes important at larger rotation rates for higher Pr.

8

Transitions between turbulent states * †

Weakly-rotating turbulent Rayleigh-Bénard convection was studied experimentally and numerically. With increasing rotation and large enough Rayleigh number a supercritical bifurcation from a turbulent state with nearly rotation-independent heat transport to another with enhanced heat transfer is observed at a critical inverse Rossby number $1/Ro_c \simeq 0.4$. *The strength of the large-scale convection-roll is either enhanced or essentially unmodified depending on parameters for* $1/Ro < 1/Ro_c$, *but the strength increasingly diminishes beyond* $1/Ro_c$ *where it competes with Ekman vortices that cause vertical fluid transport and thus heat-transfer enhancement.*

8.1 Introduction

Turbulence evolves either through a sequence of bifurcations, possibly passing through periodic and chaotic states [180] as in Rayleigh-Bénard (RB) convection [4] when the Rayleigh number *Ra* is increased, or through subcritical bifurcations [181] as in pipe or Couette flow. Once the flow is turbulent, it usually is characterized by large random fluctuations in space and time and by a loss of temporal and spatial coherence. For the turbulent state common wisdom is that the large fluctuations assure that the phase-space is always fully explored by the dynamics, and that transitions between

---

[*] Based on: R.J.A.M. Stevens, J.Q. Zhong, H.J.H. Clercx, G. Ahlers, and D. Lohse, Transitions between Turbulent States in Rotating Rayleigh-Bénard Convection, Phys. Rev. Lett. 103, 024503 (2009).

[†] The experiments discussed in this chapter were performed by J.Q. Zhong and G, Ahlers in Santa Barbara.

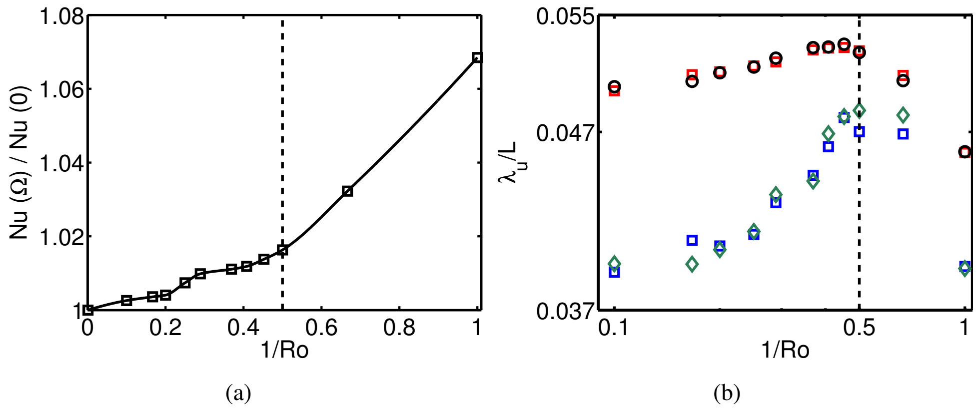

(a) (b)

Figure 8.1: a) The ratio $Nu(\Omega)/Nu(\Omega = 0)$ as function of $1/Ro$ for $Ra = 4 \times 10^7$ and $Pr = 6.26$. Open black squares indicate the numerical results. The numerical error is approximately 0.2% which is indicated by the size of the symbols. b) The thickness of the kinematic top and bottom BLs based on the maximum rms azimuthal (upper symbols: black open circles (red open squares) for top (bottom) BL) and radial (lower symbols: green open diamonds (blue open squares) for top (bottom) BL) velocity fluctuations. The vertical dashed lines in both graphs represent $1/Ro_c$ and indicates the transition in boundary-layer character from Prandtl-Blasius (left) to Ekman (right) behavior.

potentially different states that might be explored as a control parameter is changed are washed out.

Contrary to the above, we show that *sharp* transitions between distinct turbulent states can occur in rotating RB convection. At relatively small *Ra* where the turbulence is not yet fully developed, we find that the system evolves smoothly as $1/Ro$ is increased. However, when *Ra* is larger and the turbulent state of the non-rotating system is well established [‡] , we find that sharp transitions between different turbulent states occur, with different heat-transfer properties and different flow organizations. Sharp transitions between different states were reported also for turbulent flows in liquid sodium [182, 183], where the increase of the magnetic Reynolds number beyond a certain threshold leads to bifurcations between different turbulent states of the magnetic field. Sharp transitions between turbulent states are found also in the rotating von Karman experiment [184]. The transitions in RB convection are related to boundary layer (BL) dynamics, whereas it is not known whether the transitions *e.g.* in the dynamo experiment are affected by boundaries. The influence of a possible transition between different states on the heat transport in RB convection is discussed in the context of a theoretical model in Ref. [185]. We note that in our case we have supercritical bifurcations, whereas all other cases are subcritical.

We present both experimental measurements and direct numerical simulations (DNS) for a sample with diameter *D* equal to *L*. They cover different but overlapping

---

[‡] $Ra/Ra_c \gtrsim 10^3$ for all of our data (Ra_c is the critical *Ra* number given by Ref. [1].

parameter ranges and thus complement each other. Where they overlap they agree very well. Without or with only weak rotation, it is known for this system that there are thermal BLs just below the top and above the bottom plate, with a temperature drop approximately equal to $\Delta/2$ across each. The bulk of the system contains vigorous fluctuations, and in the time average a large-scale circulation (LSC) that consists of a single convection roll with up-flow and down-flow opposite each other and near the side wall.

8.2 Experimental and numerical method

The numerical scheme was already described in refs. [75, 90, 107] and chapter 6. The apparatus also is well documented, see (Ref. [175] and chapter 6) and here we give only a few relevant details. The sample cell had $D = L = 24.8$ cm, with plexiglas side walls of thickness 0.32 cm and copper top and bottom plates kept at temperatures T_t and T_b, respectively. The fluid was water. Eight thermistors, labeled $k = 0,\ldots,7$, were imbedded in small holes drilled horizontally from the outside into but not penetrating the side wall [186]. They were equally spaced around the circumference at the horizontal mid-plane ($z = 0$). A second and third set were located at $z = -L/4$ and $z = L/4$. Since the LSC carried warm (cold) fluid from the bottom (top) plate up (down) the side wall, these thermistors detected the location of the upflow (downflow) of the LSC by indicating a relatively high (low) temperature. To determine the orientation and strength of the LSC, we fit the function

$$T_{f,k}(z=0) = T_{w,0} + \delta_0 \cos(k\pi/4 - \theta_0); \;\; k = 0,\ldots,7 \tag{8.1}$$

separately at each time step, to the eight temperature readings $T_k(z = 0)$ obtained from the thermistors at $z = 0$. Similarly we obtained θ_t, δ_t, and $T_{w,t}$ for the top level at $z = L/4$. At $z = -L/4$ only the mean temperature $T_{w,b}$ was used in the current work.

In chapter 6 we explored Nu as a function of Ra, Pr, and Ro in a large parameter regime, ranging towards strong rotation ($1/Ro \gg 1$) and from small to large Pr. Here we focus on $Pr \approx 4-7$ (typical of water) and weak rotation ($Ro \gtrsim 1$) to study the transition from the non-rotating state at $1/Ro = 0$ towards the rotating case for different Ra.

8.3 Results

We start with numerical results for the relatively small $Ra = 4 \times 10^7$ which is not accessible with the current experimental apparatus because L is too large. Those simulations where done on a grid of $193 \times 65 \times 129$ nodes in the azimuthal,radial, and vertical directions, respectively, allowing for a sufficient resolution of the small scales both inside the bulk of turbulence and in the BLs adjacent to the bottom and top plates where the grid-point density was enhanced [75, 90]. The small Ra allowed for very long runs of 4000 dimensionless time units and thus excellent statistics. Fig. 8.1 shows the ratio of $Nu(\Omega)$ in the presence of rotation to $Nu(\Omega = 0)$ as function of $1/Ro$. This ratio increases rather *smoothly* with increasing rotation. For the larger $Ra = 2.73 \times 10^8$ and $Pr = 6.26$ where the turbulence of the non-rotating system is well developed, both numerical and experimental findings are very different. In Fig. 8.2 one sees that now there is a critical inverse Rossby number $1/Ro_c \approx 0.38$ at which the heat-transfer enhancement *suddenly* sets in. For weaker rotation the data are consistent with no heat-transfer modification as compared to the non-rotating case. The experimental and numerical data (now based on a resolution of $257 \times 129 \times 257$, see chapter 6) agree extremely well. In Ref. [75] data from DNS were reported on the relative Nusselt number for $Ra = 1 \times 10^9$ and $Pr = 6.4$, which show a similar transition also at $1/Ro_c \approx 0.4$.

The increase in Nusselt is thought to be due to the formation of the Ekman vortices which align vertically and suck up (down) hot (cold) fluid from the lower (upper) BLs (Ekman pumping) [68, 72, 74, 75, 77, 96] and chapter 6. This is supported by the change in character of the kinetic BL near the bottom and top walls based on the maximum root-mean-square (rms) velocity fluctuations in the azimuthal (and radial) direction. For $1/Ro \lesssim 1/Ro_c$ the BL thickness (based on the rms azimuthal velocity fluctuations) is roughly constant or even slightly increases. In contrast, for $1/Ro \gtrsim 1/Ro_c$ it behaves according to Ekman's theory and decreases with increasing rotation rate, see Fig. 8.1b ($1/Ro_c \approx 0.5$), and Fig. 8.2b ($1/Ro_c \approx 0.38$), and see data for $Ra = 1 \times 10^9$ and $Pr = 6.4$ in Ref. [187]. The scaling with rotation rate is in agreement with Ekman BL theory $\lambda_u/L \sim Ro^{1/2}$, whereas the constant BL thickness is consistent with the presence of the LSC and the Prandtl-Blasius BL. Furthermore, the numerical results in chapter 9 confirm the presence of Ekman vortices at the edge of the thermal BL above onset which are not present below onset. Furthermore, particle image velocimetry (PIV) measurements have also shown that vortices are present close to the plates when rotation is applied [74, 96]. In addition these measurements show that the number of vortices increases with the rotation rate.

To further characterize the flow field, we numerically calculated the rms velocity fluctuations averaged over horizontal planes and over the entire volume, respectively. For $1/Ro > 1/Ro_c$ the normalized (by the value without rotation) volume-averaged vertical velocity fluctuations w_{rms} strongly decrease, indicating that the LSC becomes weaker, see Fig. 8.3. The decrease in normalized *volume averaged* vertical velocity fluctuations coincides with a significant increase of the *horizontal average* at the edge of the thermal BLs, indicating enhanced Ekman transport (see also Figs. 8.1b and 8.2b). These averages provide additional support for the mechanism of the sud-

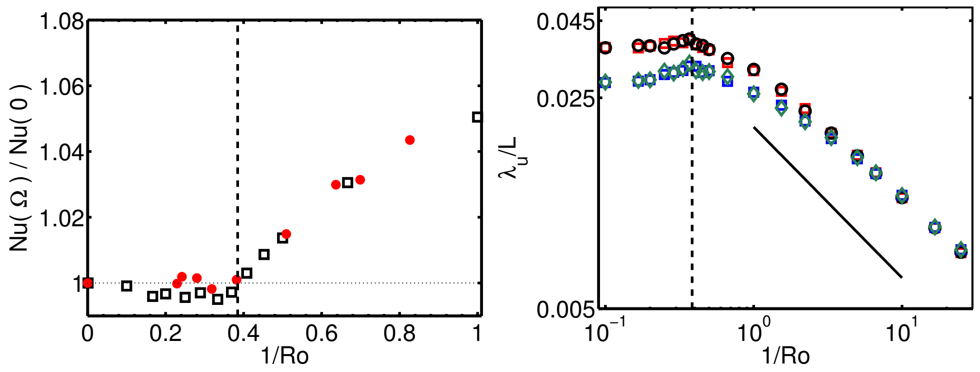

(a) (b)

Figure 8.2: a) $Nu(\Omega)/Nu(\Omega=0)$ for $Ra = 2.73\times10^8$ and $Pr = 6.26$. Red solid circles: experimental data ($T_m = 24°\mathrm{C}$ and $\Delta = 1.00\mathrm{K}$). Open black squares: numerical results. The experimental error coincides approximately with the symbol size and the numerical error is approximately 0.5%. b) The thickness of the kinematic top and bottom BLs based on the maximum rms azimuthal (upper symbols: black open circles (red open squares) for top (bottom) BL) and radial (lower symbols: green open diamonds (blue open squares) for top (bottom) BL) velocity fluctuations. For dashed vertical lines: see Fig. 8.1.

den transition seen in Nu and indicate an abrupt change from a LSC-dominated flow structure for $1/Ro < 1/Ro_c$ to a regime where Ekman pumping plays a progressively important role as $1/Ro$ increases.

Our interpretation for the two regimes is as follows: Once the vertical vortices organize so that Ekman pumping sucks in the detaching plumes from the BLs, those plumes are no longer available to feed the LSC which consequently diminishes in intensity. A transition between the two regimes should occur once the buoyancy force, causing the LSC, and the Coriolis force, causing Ekman pumping, balance. The ratio of the respective velocity scales is the Rossby number. For $Ro \gg 1$ the buoyancy-driven LSC is dominant, whereas for $Ro \ll 1$ the Coriolis force and thus Ekman pumping is stronger. The transition between the two regimes should occur at $Ro = \mathcal{O}(1)$, consistent with the observed $Ro_c \approx 2.6$.

One wonders of course why the transition between the two regimes is sudden (in Nu) for $Ra = 2.73\times10^8$ and less abrupt for the smaller $Ra = 4\times10^7$ shown in Fig. 8.1. We do not know the answer. We speculate that below onset at the lower Ra the main effect is the thinning of the thermal BL through the rotation which is less pronounced at larger Ra, as there the BL is already thinner anyhow, thanks to the stronger LSC. The Nu vs. Ra scaling at a fixed Ro number changes due to the transition, because $Nu(\Omega)/Nu(\Omega=0)$ decreases with increasing Ra as is shown in chapter 6.

At even higher $Ra = 9.0\times10^9$ (where Δ is larger and temperature amplitudes

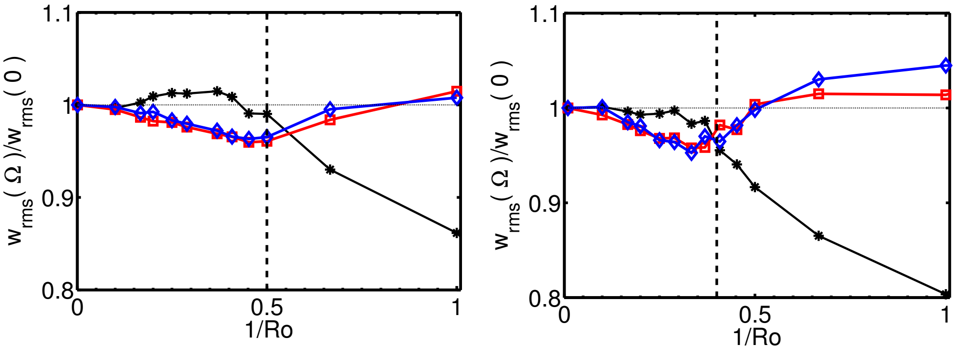

Figure 8.3: The normalized averaged rms vertical velocities fluctuations w_{rms} for $Ra = 4 \times 10^7$ (left) and $Ra = 2.73 \times 10^8$ (right) as function of $1/Ro$. The black stars indicates the normalized *volume averaged* value of w_{rms}. The red open squares and the blue open diamonds indicate the normalized *horizontally averaged* w_{rms} at the edge of the thermal BL based on the slope at respectively the lower and upper plate. The vertical dashed lines again indicate the position of $1/Ro_c$.

can thus more easily be measured) and $Pr = 4.38$ an even more complex situation is revealed, as seen in Fig. 8.4 (here DNS is not available because it would be too time consuming). We find that now $Nu(\Omega)/Nu(\Omega = 0)$ (Fig. 8.4a), after a slight increase, first decreases, but these changes are only a small fraction of a percent. Then Nu undergoes a sharp transition at $1/Ro_{c,2} = 0.415$ (vertical dotted line in Fig. 8.4a) and beyond it increases due to Ekman pumping. Comparison with Figs. 8.1 and 8.2 shows that the transition of Nu is not strictly at a constant $1/Ro_c$, but that Ro_c depends weakly on Ra and/or Pr.

The LSC amplitudes δ_0 and δ_t determined from fits of Eq. (8.1) to the sidewall-thermometer readings are shown in Fig. 8.4b as solid symbols. Consistent with the results reported in Ref. [186], $\delta_t < \delta_0$ when there is no rotation ($1/Ro = 0$). This inequality disappears as $1/Ro$ increases. Both amplitudes first increase by nearly a factor of two. At $1/Ro_{c,1} \simeq 0.337$, where the two amplitudes have just become equal to each other, they begin to decrease quite suddenly and remain equal to each other up to the largest $1/Ro$. The transition at $1/Ro_{c,1}$ is indicated by the leftmost vertical dotted line in Figs. 8.4b and c. At that point there also is a transition revealed by the vertical temperature difference $\Delta T_w = 2 \times [T_{w,b} - T_{w,t}]$ along the side wall as seen in Fig. 8.4c which shows $\Delta T_w/\Delta$ as a function of $1/Ro$. Consistent with the initially enhanced LSC amplitudes δ_0 and δ_t, these results first show a reduction of the thermal gradient as the LSC becomes more vigorous, but then reveal an increase due to enhanced plume and/or vortex activity above $1/Ro_{c,1}$.

Also of interest are the rms fluctuations $\delta T/\Delta = \langle [T_k(z=0) - T_{f,k}(z=0)]^2 \rangle^{1/2}/\Delta$ about the fit of Eq. (8.1) to the temperature measurements at the horizontal midplane ($z = 0$), and similarly at $z = L/4$. They are shown as open symbols in Fig. 8.4b. These fluctuations begin to rise at $1/Ro_{c,2}$ rather than at $1/Ro_{c,1}$. Then they soon become

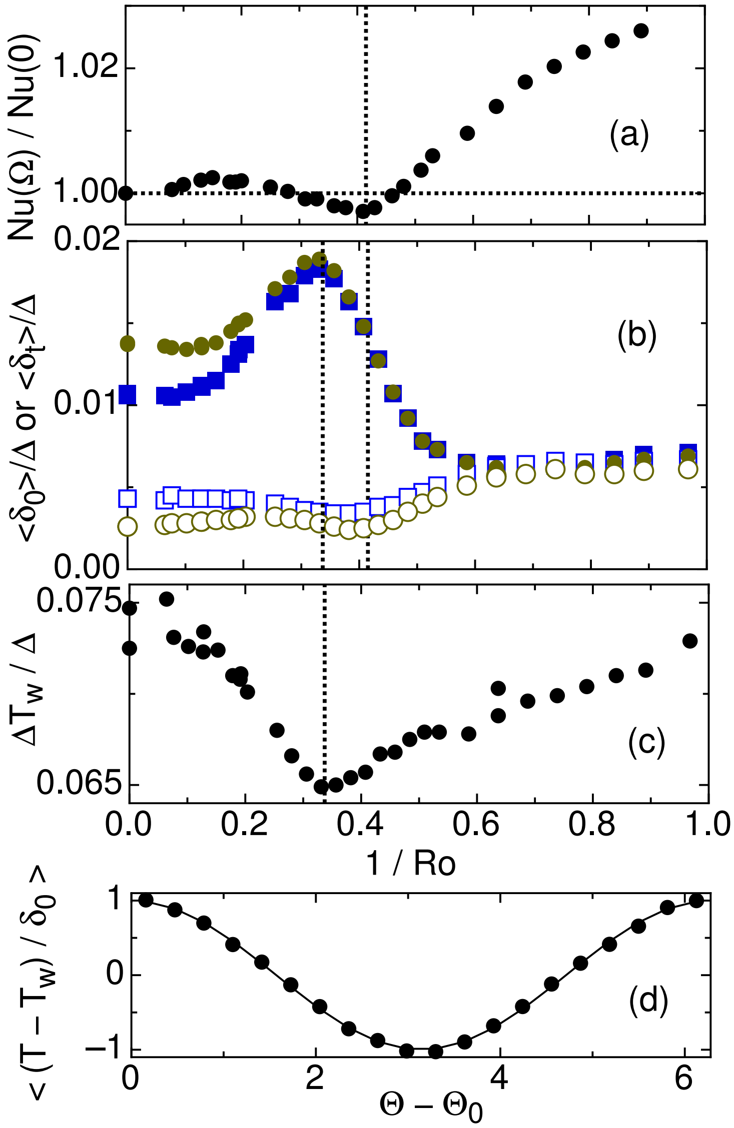

Figure 8.4: Results for $Ra = 9.0 \times 10^9$ and $Pr = 4.38$ ($T_m = 40.00$°C, $\Delta = 16.00$ K). (a): $Nu(\Omega)/Nu(\Omega = 0)$ vs. $1/Ro$. The error bar is smaller than the size of the symbols. (b): Solid symbols: time-averaged LSC amplitudes $\langle \delta_0 \rangle/\Delta$ ($z = 0$, circles) and $\langle \delta_t \rangle/\Delta$ ($z = L/4$, squares) as a function of $1/Ro$. Open symbols: rms fluctuations about the cosine fit (Eq. 8.1) to the temperature data. (c): Vertical temperature variation $\Delta T_w/\Delta$ along the sidewall. (d): Circles: time-averaged normalized sidewall-temperature profile $\langle [T(\theta) - T_w]/\delta_0 \rangle$ at the horizontal midplane for $1/Ro = 1$ determined as in [186]. Solid line: $\cos(\Theta - \Theta_0)$.

comparable to δ_0 and δ_t, suggesting that the LSC becomes more and more hidden in a fluctuating environment. Nonetheless, remnants of the LSC survive and can be found when the fluctuations are averaged away, as shown in Fig. 8.4d. There we see that even for $1/Ro = 1.0$ the time average $\langle (T_k(z=0) - T_{w,0})/\delta_0 \rangle$ of the deviation from the mean temperature $T_{w,0}$ retains a near-perfect cosine shape.

8.4 Conclusions

From these measurements we infer that the establishment of the Ekman-pumping mechanism is a three-stage process. First, up to $1/Ro_{c,1}$, the time-averaged LSC amplitudes, such as $\langle \delta_0 \rangle / \Delta$, nearly double in value (see Fig. 8.4b) and thereby reduce the vertical thermal gradient along the wall (see Fig. 8.4c). Beyond $1/Ro_{c,1}$ there is an enhanced accumulation of plumes and vortices, which coincides with an increase of the BL thickness near onset as shown by the simulations at lower Ra (see insets in Figs. 8.1 and 8.2). This accumulation detracts from the driving of the LSC but the flow is not yet organized into effective Ekman vortices. This organization sets in at $1/Ro_{c,2}$, leads to Ekman pumping, and enhances Nu and reduces the strength of the LSC as supported by the volume-average of w_{rms}, see Fig. 8.3 (for lower Ra). This sequence of events is altered as Ra (and presumably also Pr) is changed, but it is remarkable that for fully developed turbulent RB convection sharp supercritical bifurcations occur. In the next chapter we will show that this bifurcation is caused by the limited horizontal extend of the system and that the rotation tay at which heat transfer enhancement first sets in depends strongly on the aspect ratio of the system.

9

Finite-size effects lead to supercritical bifurcations [*] [†]

In turbulent thermal convection in cylindrical samples of aspect ratio $\Gamma \equiv D/L$ *(D is the diameter and L the height) the Nusselt number Nu is enhanced when the sample is rotated about its vertical axis, because of the formation of Ekman vortices that extract additional fluid out of thermal boundary layers at the top and bottom. We show from experiments and direct numerical simulations that the enhancement occurs only above a bifurcation point at a critical inverse Rossby number* $1/Ro_c$*, with* $1/Ro_c \propto 1/\Gamma$*. We present a Ginzburg-Landau like model that explains the existence of a bifurcation at finite* $1/Ro_c$ *as a finite-size effect. The model yields the proportionality between* $1/Ro_c$ *and* $1/\Gamma$ *and is consistent with several other measured or computed system properties.*

9.1 Introduction

Turbulence, by virtue of its vigorous fluctuations, is expected to sample all of phase space over wide parameter ranges. This viewpoint implies that there should not be any bifurcations between different turbulent states. Contrary to this, several cases

---

[*] Based on: S. Weiss, R.J.A.M. Stevens, J.-Q. Zhong, H.J.H. Clercx, D. Lohse, and G. Ahlers, Finite-size effects lead to supercritical bifurcations in turbulent rotating Rayleigh-Bénard convection, Phys. Rev. Lett. 105, 224501 (2010).

[†] The experimental results from Santa Barbara and the Ginzburg-Landau model discussed in this chapter are from S. Weiss, J.-Q. Zhong, and G. Ahlers.

of discontinuous transitions have been observed recently in turbulent systems [182–184]. When they occur, they are likely to be provoked either by changes in boundary conditions or boundary-layer structures, or by discontinuous changes in the large-scale structures, as a parameter is varied.

In chapters 6-8 we discussed the effect of rotation on the heat transfer in Rayleigh-Bénard convection. For a cylindrical sample of aspect ratio $\Gamma \equiv D/L = 1.00$ (D is the diameter and L the height) a supercritical bifurcation was found, both from experiments and from direct numerical simulation (DNS) of the Boussinesq equations of motion. At a *finite* Ω, as expressed by the inverse Rossby number $1/Ro \propto \Omega$, there was a *sharp* transition from a state of nearly rotation-independent heat transport to one in which Nu was enhanced by an amount $\delta Nu(1/Ro)$. This is illustrated by the data shown in Fig. 9.1. The increase of Nu was attributed to Ekman pumping, see Refs. [68, 72, 74, 76, 81, 85] and chapters 6-8, i.e. to the formation of (cyclonic) vertical vortex tubes ("Ekman vortices"), which extract and vertically transport additional fluid from the boundary layers (BLs) and thereby enhance the heat transport. The bifurcation was located at a critical value $1/Ro_c \simeq 0.40$ (chapter 8). The reason for the existence of the bifurcation at $1/Ro_c > 0$ hitherto had not been understood. While such bifurcations are common near the onset of RBC in the domain of pattern formation [4], their existence in the turbulent regime implies a paradigm shift.

In this chapter we report on further experiments for samples with $\Gamma = 2.00$, 1.00, and 0.50 which (i) all show bifurcations between different turbulent states and (ii) reveal that $1/Ro_c$ varies approximately in proportion to $1/\Gamma$. We offer an explanation of these and other phenomena in terms of a phenomenological Ginzburg-Landau like description which predicts a finite-size effect upon the vortex density A.

We assumed that the relative Nusselt enhancement $\delta Nu(1/Ro)/Nu(0)$ is proportional to the average $\bar{A}$ of A over a horizontal cross section of the sample near the BLs. Consistent with the DNS that we report here, we assumed that A vanishes at the sample side wall. For the infinite system the model predicts that A, and thus $\delta Nu/Nu(0)$, increases linearly from zero starting at $1/Ro = 0$. For the finite system the model gives a threshold shift proportional to $1/\Gamma$ as found in the experiment and by DNS. The shift is predicted to be followed by a linear increase of $\bar{A}$ in proportion to $(1/Ro) - (1/Ro_c)$ which yields $\delta Nu/Nu(0) = S_1(\Gamma)(1/Ro - 1/Ro_c)$. The model gives an initial slope $S_1(\Gamma)$ that decrease with decreasing Γ, again consistent with DNS and measurements. From DNS we show that A decreases to zero near the side wall over a length that is consistent with an estimate of a healing-length ξ based on the model. Thus, we found consistency between the model predictions and all properties that we were able to either measure or compute from DNS.

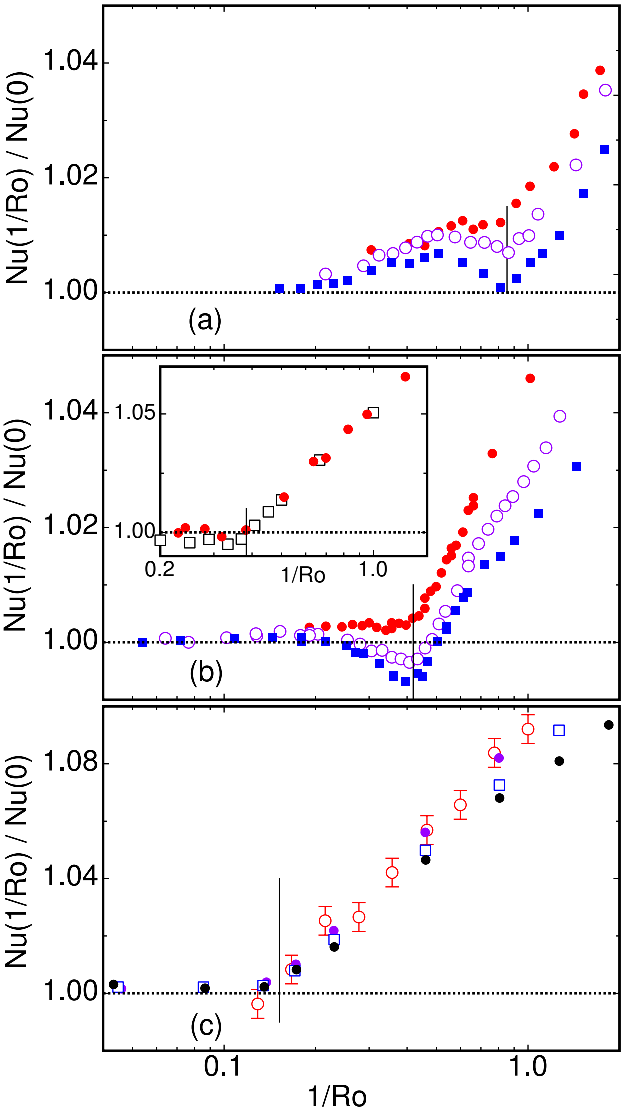

Figure 9.1: The Nusselt number $Nu(1/Ro)$, normalized by $Nu(0)$ without rotation, as a function of the inverse Rossby number $1/Ro$. Data are from experiments unless mentioned otherwise. (a): $\Gamma = 0.50$ and $Pr = 4.38$; Rayleigh numbers $Ra = 9.0 \times 10^9$ (solid red circles), 1.8×10^{10} (open circles), and 3.6×10^{10} (solid squares). (b): $\Gamma = 1.00$. Main figure: $Pr = 4.38$, $Ra = 2.25 \times 10^9$ (solid circles), 8.97×10^9 (open circles), and 1.79×10^{10} (solid squares). Inset: $Pr = 6.26$ and $Ra = 2.73 \times 10^8$. DNS: open squares. Experiment: solid circles. (c): $\Gamma = 2.00$ and $Pr = 4.38$; the data are for $Ra = 2.91 \times 10^8$ (open circles, DNS; solid circles, experiment), 5.80×10^8 (open squares), and 1.16×10^9 (solid squares). Note the different vertical scale for (c) compared to (a) and (b). The small vertical lines indicate the locations of the bifurcation points.

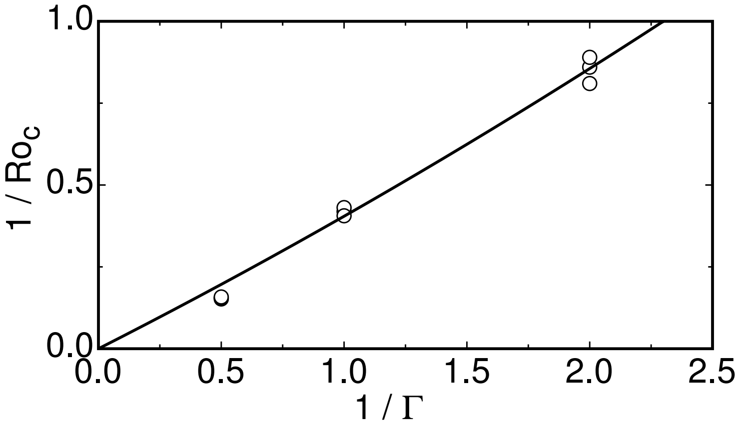

Figure 9.2: The critical inverse Rossby number $1/Ro_c$ as a function of the inverse aspect ratio $1/\Gamma$ for $Pr = 4.38$ and different Ra (see Fig. 9.1). The line is a fit of a quadratic equation with the constant coefficient set to zero.

9.2 Finite size effects

In Fig. 9.1 we show experimental and numerical data [‡] for $Nu(1/Ro)/Nu(0)$ as a function of $1/Ro$ for several values of Ra. From top to bottom the three panels are for $\Gamma = 0.50$, 1.00, and 2.00, respectively [§]. One sees that there is considerable structure even below the bifurcation, particularly at the larger Ra. To our knowledge the origin of this structure is not known in detail. One sees that there are clear breaks in the curves, *e.g.* for $\Gamma = 1.00$ (Fig. 9.1b) at $1/Ro \simeq 0.4$, indicating the bifurcation to a different state. The location of this transition is within our resolution independent of Ra.

In Fig. 9.2 we plotted all available data for $1/Ro_c$ for $Pr = 4.38$ (and different Ra) as a function of $1/\Gamma$. The line shown there is a fit of

$$\frac{1}{Ro_c} = \frac{a}{\Gamma}\left(1 + \frac{b}{\Gamma}\right) \tag{9.1}$$

to the data. Its coefficients are $a = 0.381$ and $b = 0.061$. One sees that the data are consistent with an initial linear increase from zero of $1/Ro_c$ with $1/\Gamma$, with a small quadratic contribution becoming noticeable as $1/\Gamma$ becomes larger.

In order to understand the Γ dependence of $1/Ro_c$, we studied the vortex statistics using data obtained from DNS. We used the so-called Q-criterion [74, 91, 96, 188] to determine the percentage $\bar{A}$ of the horizontal area that was covered by vortices. Using this criterion, implies that the quantity Q_{2D}, see Ref. [189] and section B, which is a quadratic form of various velocity gradients, was calculated in a plane of

---

[‡] The numerical details of the simulations presented here are discussed in chapter 10

[§] Some of the data for $\Gamma = 1.00$ are already shown in chapter 6 and 8

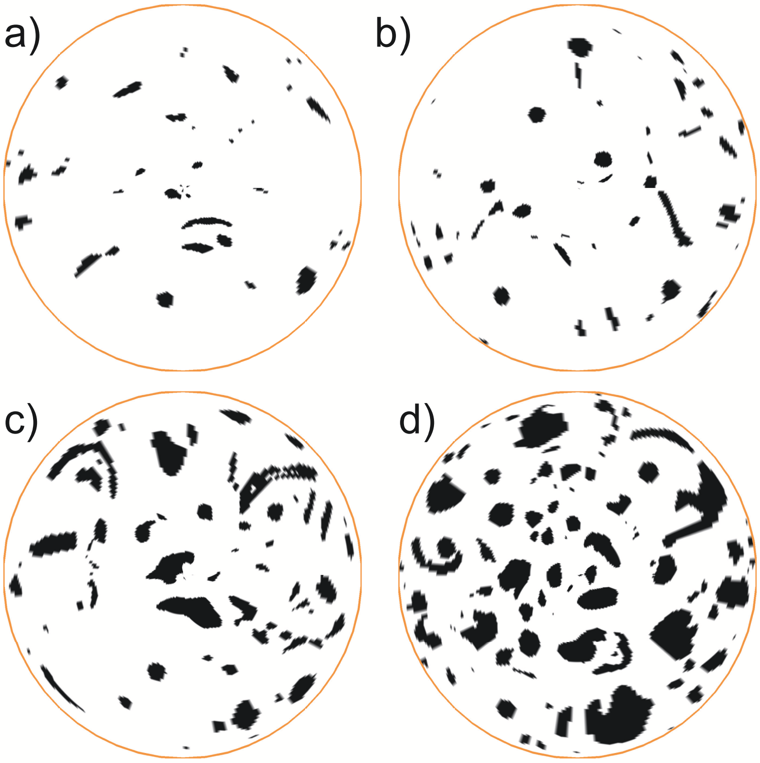

Figure 9.3: The vortices as identified by the Q_{2D} criterion, see Ref. [189] and section B, for $Ra = 2.73 \times 10^8$, $Pr = 6.26$, and $\Gamma = 1$. a) $1/Ro = 2/3$, b) $1/Ro = 1$, c) $1/Ro = 1.54$, and d) $1/Ro = 3.33$. The vortex area increases with increasing $1/Ro$. This trend is quantified in Fig. 9.4a.

fixed height. An area is then identified as “vortex” when $Q_{2D} < -0.1\langle|Q_{2D}|\rangle_v$, were $\langle|Q_{2D}|\rangle_v$ is the volume-averaged value of the absolute values of Q_{2D}, see appendix B. The result of this procedure is shown for different $1/Ro$ in Fig. 9.3 for $Pr = 6.26$. In Fig. 9.4 we plot $\bar{A}$ as a function of $1/Ro$ at the edge of the kinetic BL (which depends on Ro, see chapter 11) and at the fixed distance $0.023L$ (the kinetic BL thickness without rotation) from the plates. Although there is quite a bit of scatter, the data are consistent with a linear increase of $\bar{A}$ for $1/Ro > 1/Ro_c$, with a small constant background $\bar{A} = A_0$ below $1/Ro_c$. The azimuthally averaged vortex density $\langle A\rangle_\phi$ is given in Fig. 9.4b. It shows that the Ekman vortices are inhomogeneously distributed: While in the bulk their fraction is roughly constant there are almost no vortices at all close to the side wall, signaling a strong boundary effect.

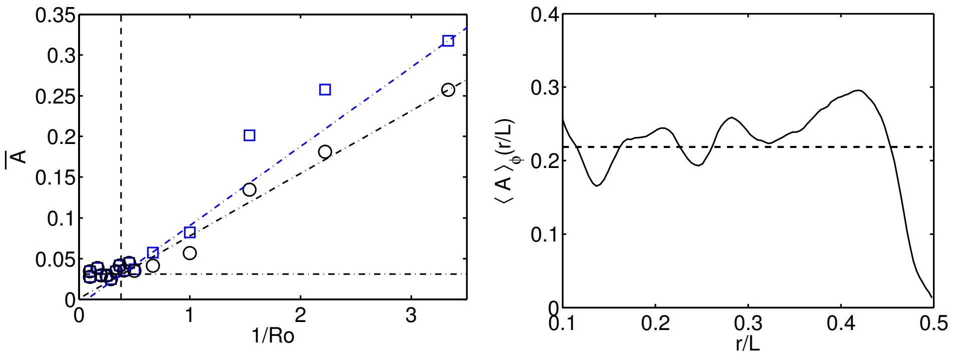

(a) (b)

Figure 9.4: Vortex statistics for $Ra = 2.73 \times 10^8$, $Pr = 6.26$, $\Gamma = 1$, and different Ro. a) Fraction $\bar{A}$ of a horizontal slice covered with vortices at the edge of the kinetic BL (circles) and at a distance $0.023L$ (the kinetic BL thickness without rotation, squares) from the plates as a function of $1/Ro$ for. The vertical dashed line indicates the bifurcation point at $1/Ro_c$ and the horizontal dash-dotted line is a background vorticity level $\bar{A}_0$ present even below $1/Ro_c$. b) Azimuthal average $\langle A \rangle_\phi(r/L)$ of the vortex density A for $2.22 < 1/Ro < 3.33$. In total, the statistics is based on 8 snapshots. The dashed line is the uniform case. The density approaches zero close to the side wall.

9.3 Ginzburg-Landau model

In an effort to understand the existence of a finite onset (see Fig. 9.1) of the Ekman-vortex formation and the dependence of the critical inverse Rossby number on Γ (see Fig. 9.2), to elucidate the linear rise and initial slope of $Nu(1/Ro)$ above onset (see Fig. 9.1), and to explain the rapid decrease of $\langle A \rangle_\phi(r/L)$ near the wall (see Fig. 9.4b), we propose a phenomenological Ginzburg-Landau like model for the local vortex density

$$\dot{A} = (1/Ro^2)A - gA^3 + \xi_0^2 \nabla^2 A \; . \tag{9.2}$$

Here $\dot{A}$ is the time derivative of A. We chose the coefficient of the linear term as $1/Ro^2$ because for the time independent infinitely extended spatially uniform system it yields a stable solution $A = g^{-1/2}(1/Ro)$ which implies a vortex density proportional to the rotation rate. The term with $\nabla^2 A$ represents the lowest-order term of a gradient expansion since terms proportional to ∇A would lead to an unphysical propagating mode.

When spatial variations are allowed, the ground state $A = 0$ can be shown to be stable (i.e. to have a growth rate $\sigma < 0$) to disturbances with wave vector k when $1/Ro$ falls below a neutral curve given by

$$1/Ro_0(k) = \xi_0 k \; . \tag{9.3}$$

For the finite system it is necessary to introduce appropriate boundary conditions. Here we shall consider a one-dimensional system over the range $-\Gamma/2 \le x \le \Gamma/2$

for simplicity and illustrative purposes. The two-dimensional system with circular boundaries and no azimuthal variation was treated in detail in Ref. [190] and yields the same result for $1/Ro_c$. Since there can be no vortices at the side wall of the sample (see Fig. 9.4b where we verified this based on the numerical data), we chose $A(-\Gamma/2) = A(\Gamma/2) = 0$. For the wave number k_0 of the lowest mode this yields $k_0 = \pi/\Gamma$. This in turn gives

$$\frac{1}{Ro_c} \equiv \frac{1}{Ro_0(k_0)} = \frac{\pi\xi_0}{\Gamma}. \tag{9.4}$$

Thus, consistent with the data in Fig. 9.2, the model yields the proportionality between $1/Ro_c$ and $1/\Gamma$. We note that the curvature indicated by the quadratic contribution to the fit Eq. 9.1 can be accommodated easily by higher-order gradient terms in Eq. 9.2. Comparison with experiment (see Eq. 9.1) gives $\xi_0 = a/\pi = 0.121$.

To elucidate the rapid decrease of $\langle A\rangle_\phi(r/L)$ in Fig. 9.4b near $r/L = 0.5$, we consider Eq. 9.2 for a semi-infinite system over the range $-\infty < x \leq 0.5$ with the boundary condition $A(x = 0.5) = 0$. It yields the solution

$$A(x) = (Ro^2 g)^{-1/2} \tanh\left((0.5 - x)/\xi\right) \tag{9.5}$$

with

$$\xi = \sqrt{2}\xi_0 Ro. \tag{9.6}$$

Thus, near the boundaries, the model predicts that the amplitude $A(x)$ of the one-dimensional model, and thus to a good approximation also the azimuthal average $\langle A\rangle_\phi(r/L)$ in Fig. 9.4b, should "heal" to its bulk value over a length ξ. Using a representative $Ro \simeq 0.4$ for Fig. 9.4b, we estimate from Eq. 9.6 that $\xi \simeq 0.07$. This is roughly consistent with the rapid variation of $\langle A\rangle_\phi(r/L)$ near $r/L = 0.5$ seen in Fig. 9.4b.

Above the bifurcation the model yields [190]

$$\bar{A} = \tilde{g}^{-1/2}\left(\frac{1}{Ro} - \frac{1}{Ro_c}\right). \tag{9.7}$$

Thus

$$\frac{\delta Nu}{Nu(0)} = S_1(\Gamma)\left(\frac{1}{Ro} - \frac{1}{Ro_c}\right) \tag{9.8}$$

which is consistent with the data in Fig. 9.1. Numerical solutions of the amplitude equation of Ref. [190] have shown that the re-normalized coefficient $\tilde{g}$ in Eq. 9.7 is larger than g in Eq. 9.2. Thus, the initial slope of $\bar{A}$ above $1/Ro_c$ and $S_1(\Gamma)$ in Eq. 9.8 are reduced by the finite size of the system. The decrease of $S_1(\Gamma)$ with decreasing Γ that can be seen in Fig. 9.1 is also consistent with the model.

At constant Γ, S_1 depends slightly on the Prandtl number. This suggests that the nonlinear coefficient g in Eq. 9.2, and thus $\tilde{g}$ in Eq. 9.7, is dependent on Pr. Similarly, the bifurcation point $1/Ro_c$ depends slightly on Pr. This is accommodated in the model Eq. 9.2 by a slightly Prandtl-dependent length scale ξ_0.

9.4 Conclusions

It remains to be seen whether the phenomena reported and explained here in terms of a finite-size effect have analogies in bifurcations between turbulent states in other systems [182–184]. The more general lesson which is learned is that the Ginzburg-Landau approach, which has been so versatile to understand the spatio-temporal dynamics of patterns, can also be useful in understanding the remarkable bifurcations between turbulent states.

10

Effect of aspect-ratio on vortex distribution and heat transfer in rotating Rayleigh-Bénard [*] [†]

Numerical and experimental data for the heat transfer as function of the Rossby number Ro in turbulent rotating Rayleigh-Bénard convection are presented for Prandtl number $Pr = 4.38$ *and Rayleigh number* $Ra = 2.91 \times 10^8$ *up to* $Ra = 4.52 \times 10^9$*. The aspect ratio* $\Gamma \equiv D/L$*, where L is the height and D the diameter of the sample, is varied between* $\Gamma = 0.5$ *and* $\Gamma = 2.0$*. Without rotation, where the aspect ratio influences the global large scale circulation, we see a small aspect-ratio dependence in the Nusselt number for* $Ra = 2.91 \times 10^8$*. However, for stronger rotation, i.e.* $1/Ro \gg 1/Ro_c$*, the heat transport becomes independent of the aspect-ratio. We interpret this finding as follows: In the rotating regime the heat is mainly transported by vertically-aligned vortices. Since the vertically-aligned vortices are local, the aspect ratio has a negligible effect on the heat transport in the rotating regime. Indeed, a detailed analysis of vortex statistics shows that the fraction of the horizontal area that is covered by vortices is independent of the aspect ratio when* $1/Ro \gg 1/Ro_c$*. In agreement with the results of Weiss* et al. *(Phys. Rev. Lett., vol 105, 224501 (2010)) we find a vortex-depleted area close to the sidewall. Here, we in addition show that there is also an*

---

[*] Based on: R.J.A.M. Stevens, J. Overkamp, D. Lohse, H.J.H. Clercx, Disappearance of aspect-ratio dependence of heat transport with increasing rotation rate in turbulent Rayleigh-Bénard convection, submitted to Phys. Rev. E (2011).

[†] A part of the experimental measurements discussed in this chapter are performed by J. Overkamp.

area with enhanced vortex concentration next to the vortex-depleted edge region and that the absolute widths of both regions are independent of the aspect ratio.

10.1 Introduction

As is shown by Refs. [80, 91, 93] and in chapters 6-9, three different regimes can be identified in rotating RB convection. As function of increasing rotation rate one first finds a regime without any heat transport enhancement at all in which the large scale circulation (LSC) is still present (regime I). Zhong and Ahlers [80] showed that – though the Nusselt number is unchanged in this regime – nonetheless various properties of the LSC do change with increasing rotation in this regime. Here we mention the increase in the temperature amplitude of the LSC, the LSC precession (also observed by Hart et al. [100] and Kunnen et al. [75]), the decrease of the temperature gradient along the sidewall, and the increased frequency of cessations. The start of regime II (moderate rotation) is indicated by the onset of heat transport enhancement due to Ekman pumping as is discussed in chapters 8 and 9. When the rotation rate is increased in regime II the heat transfer increases further until one arrives at regime III (strong rotation), where the heat transfer starts to decrease. This decrease of the heat transfer in regime III is due to the suppression of the vertical velocity fluctuations, see Ref. [80]) and chapters 6 and 7.

Several experimental, see Refs. [72, 76, 78–80] and chapters 6,8,9, and numerical, see Refs. [75–77, 87–91], and chapters 6- 9, studies on rotating RB convection have shown that in regime II the heat transport with respect to the non-rotating case increases due to rotation. A detailed overview of the parameter ranges covered in the different experiments can be found in the $Ra-Pr-Ro$ phase diagram shown in figure 1 of chapter 11 and the $Ra-Ro-\Gamma$ phase diagram shown in figure 10.1. The heat transport enhancement in regime II is caused by Ekman pumping ([68, 72, 74–77, 80] and chapters 6- 9).

In chapters 6 and 7 we used results from experiments and direct numerical simulations (DNS) in a $\Gamma = 1$ sample to study the influence of Ra and Pr on the effect of Ekman pumping. It was found that at fixed Ro the effect of Ekman pumping is largest, and thus the observed heat transport enhancement with respect to the non-rotating case highest, at an *intermediate* Prandtl number. At lower Pr the effect of Ekman pumping is reduced as more hot fluid that enters the vortices at the base spreads out in the middle of the sample due to the large thermal diffusivity of the fluid. At higher Pr the thermal BL becomes thinner with respect to the kinetic BL, where the base of the vortices is formed, and hence the temperature of the fluid that enters the vortices becomes lower. In addition, it was found that the effect of Ekman pumping is reduced for increasing Ra. This is because the turbulent viscosity increases with increasing Ra, which means that more heat spreads out in the middle

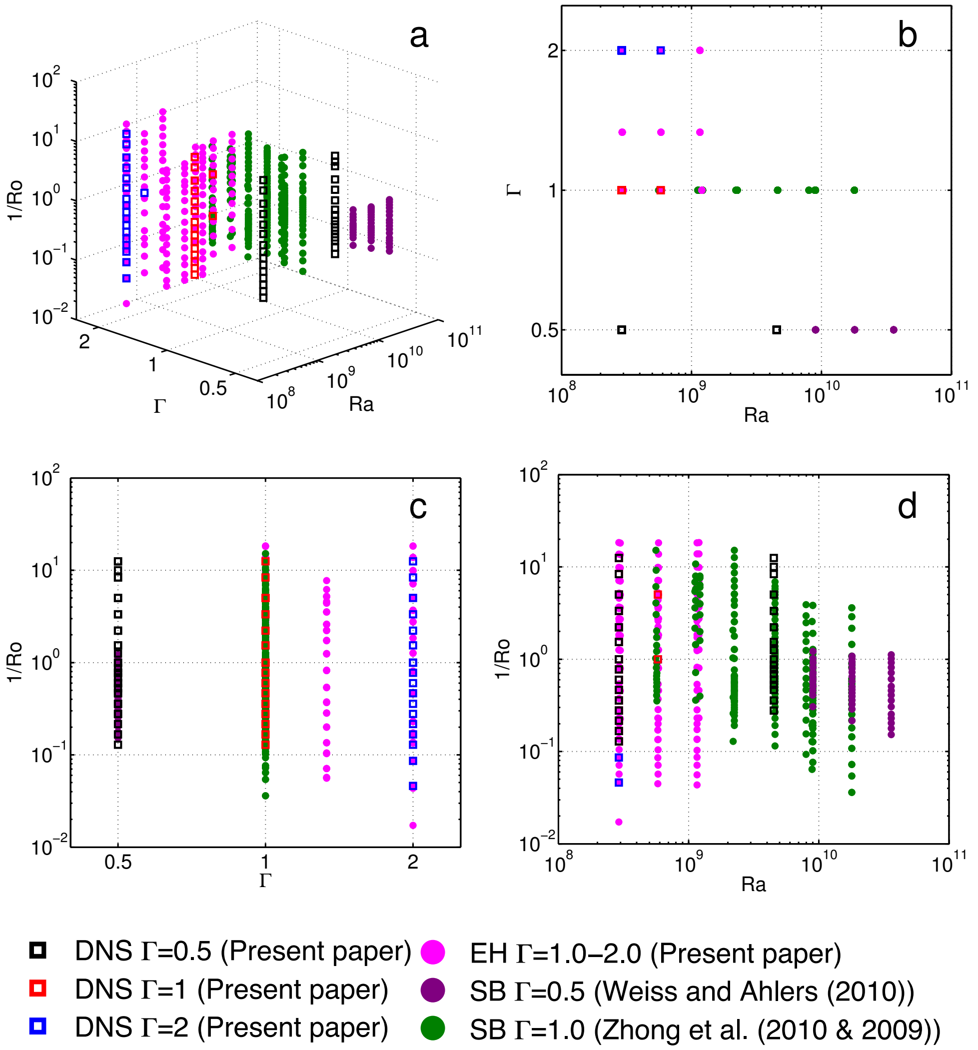

Figure 10.1: Phase diagram in $Ra - Ro - \Gamma$ space for rotating RB convection with $Pr = 4.38$. The data points indicate where Nu has been experimentally measured or numerically calculated in a cylindrical sample with no-slip boundary conditions. The DNS data and the Eindhoven (EH) experiments are from this chapter. The experimental results from Santa Barbara (SB) are from chapter 9 and Zhong and Ahlers [80] for the $\Gamma = 0.5$ and $\Gamma = 1.0$, respectively. The EH experimental data focus on $\Gamma > 1$, but for one case we also give the result for $\Gamma = 1$ for benchmarking with the earlier SB data. a) A three dimensional view on the phase space (see also the movie 10.1 in the supplementary material [115]), b) Projection on $\Gamma - Ra$ phase space, c) Projection on $1/Ro - \Gamma$ phase space and, d) Projection on $1/Ro - Ra$ phase space. We also refer to figure 1 of chapter 11 for a full representation of the $Ra - Pr - Ro$ phase space of rotating RB convection.

of the sample. This explains why for the high Ra-number of Niemela et al. [81] no heat transfer enhancement was found in the rotating case.

In chapter 9 we showed that the rotation rate at which the onset of heat transport enhancement sets in ($1/Ro_c$) increases with decreasing aspect ratio due to finite size effect. This means that the aspect ratio is an important parameter in rotating RB convection. In this chapter we report on a systematic study of the influence of the aspect ratio on heat transfer (enhancement) for moderate and strong rotation rates, i.e., for $1/Ro \gg 1/Ro_c$.

This chapter is organized as follows. The experimental setup that has been built at the Fluid Dynamics Laboratory at Eindhoven University of Technology is discussed in section 10.2. The design of this setup is closely based on the Santa Barbara design [175]. Subsequently we will discuss the numerical procedures that have been followed. Where the experimental and simulation results overlap an excellent agreement is found. Based on the numerical data we will show that for $1/Ro \gg 1/Ro_c$ the Nusselt number is independent of the aspect ratio, while there are some visible differences for the non-rotating case. The reason for this is that in the non-rotating case there is a global flow organization, which can be influenced by the aspect ratio. In the rotating regime vertically aligned vortices, in which most of the heat transport takes place [101, 102], form the dominant feature of the flow. As this is a local effect the heat transport in this regime does not depend on the aspect ratio. In the last part of the chapter we will analyze the vortex statistics for the different aspect ratios to support that the vortices are indeed a local phenomenon.

10.2 Experimental setup

Based on the setup described by Brown et al. [175] we have built a new RB setup in Eindhoven, which is suitable for high precision heat transport measurements. The convection cell has a diameter D of 250 mm. The modular design of the setup provides the ability to adjust the height of the convection cell. Here we will present measurements for $\Gamma = 1$, $\Gamma = 4/3$, and $\Gamma = 2$ During rotating experiments the RB cell is placed on the Eindhoven Rotating Table Facility (RTF) (for details, see Ref. [191]). A rotating connection is available for coolant fluid, with separated in and out flow tubes. The rotation rate Ω of the RTF can be controlled from 0 to 10 rad/s with a resolution of 0.001 rad/s and a relative accuracy of 0.5%. The rotation rates were kept below $\Omega = 1.57$ rad/s, yielding Froude numbers $Fr = \Omega^2(D/2)/g$ less than 0.03 for all runs and much smaller for most. This means that the effect of centrifugal forces can be considered negligible.

A schematic diagram of the RB cell is shown in figure 10.2. From bottom to top, we first find the support plate A (400 x 400 mm aluminium), used to mount the setup on the RTF and to align the rotational axes of the table and the convection cell so that

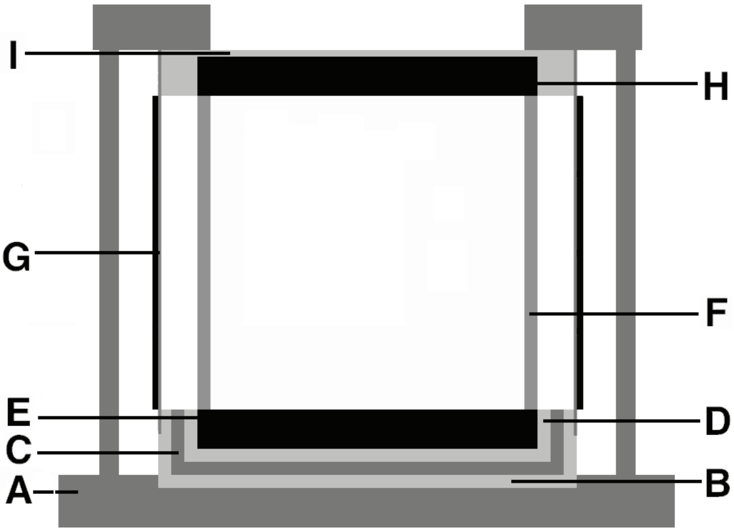

Figure 10.2: Schematic diagram (not to scale) of the Eindhoven RB apparatus. From bottom to top the figure shows the support plate (A), an insulation layer (B), the bottom adiabatic shield (C), an insulation layer (D), the bottom copper plate (E), the Plexiglas sidewall (F), the adiabatic side shield (G), the top copper plate (H), and the Plexiglas top plate (I). See further details in the text.

the offset of the cylinder axis and the rotation axis is less than 0.1 mm. Next, part *B* is a 10 mm insulation layer to prevent heat loss of the bottom adiabatic shield *C* (310 mm outer diameter, 10 mm thick aluminium) to the support plate. The shield is fitted with a 250 W heater to actively control its temperature. Inside this adiabatic shield, part *D* is another 10 mm insulation layer, followed by the copper bottom plate *E* (270 mm outer diameter, 30 mm thick) of the convection cell. The back of the bottom plate is covered uniformly with two double spiral grooves of 2 mm depth, 2 mm width and 6 mm spacing. Two 4 m, 12.3 Ω resistance wires are epoxied into these grooves. From the back of the plate, five small holes (one at the centre, two at a radius of 98 mm and two at 100 mm, i.e. in the space that is available between the heater wires that are placed inside the plate) are drilled to within 0.7 mm of its top surface and thermistors are mounted in these holes.

On top of the bottom plate, the Plexiglas sidewall *F* with an inner diameter of 250 mm is placed. The thickness of the Plexiglas sidewall is 10 mm to provide enough strength in strongly rotating RB experiments. A rubber O-ring seals the interface between the bottom plate and the sidewall and prevents any leakage of fluid. The sidewall contains a fluid inlet near the bottom plate and, at opposite angular position, an outlet adjacent to the top plate. Care has been taken to avoid the entrapment of air in the convection cell, both when filling the cell and when heating the fluid. The sidewall is surrounded by an adiabatic side shield *G* made of two 3 mm thick aluminium plates. The shield is actively temperature controlled, ensuring that its temperature is always close to the mean temperature of the system. Additional insulation is present between the Plexiglas side wall and the aluminium side shield.

The top of the convection cell is formed by the copper top plate H, which has similar dimensions as the bottom plate. The top plate contains a double spiral water channel of 8 mm width, 26 mm depth and 25 mm spacing. The water, coming from a refrigerated circulator (Thermo Scientific HAAKE DC50-K41) at 12.5 L/min, cools the top plate down to the desired temperature. From the top of the plate, five small holes (one at the centre, four at a radius of 100 mm) were drilled to within 0.7 mm of the copper-fluid interface and thermistors are mounted in these holes. The top plate is covered by a Plexiglas top I and the water channel is sealed with a rubber ring. The visual access provides a way to check the proper operation of the cooling system. An aluminium construction ring is connected to the upper side of the top plate. It is supported by 6 stainless steel support poles. With these poles, the RB cell can be fixed to achieve a fully watertight connection between the plates and the sidewall. To decrease the effects of air convection near the convection cell, the entire construction is placed in a wooden box covered with a 40 mm insulating layer on the inside.

The apparatus contains 40 thermistors, which were calibrated simultaneously in a separate apparatus against a laboratory standard. During the calibration procedure all thermistors and the laboratory standard are placed in an extremely well temperature-controlled batch (temperature differences less than 0.002 K) to determine the resistance at a set of known temperatures. From this calibration data fits were made with 5-th order logarithmic polynomials to calculate temperature values from 3-wire resistance measurements. Deviations from these fits are generally less than 0.001 K. During the calibration procedure all thermistors are connected to the same software and hardware as in the real experiments. 24 of these thermistors are placed in the sidewall, forming 3 rings of 8 equally spaced sensors at heights $0.25L$, $0.5L$ and $0.75L$. Both the top and bottom plate contain 5 sensors to monitor the temperature of the plate. The remaining sensors are used to control the temperature of the bottom adiabatic shield and of the insulation around the Plexiglas sidewall. Readings of all thermometer resistances and of the bottom plate heater current and heater voltage were taken every second. The top (bottom) temperature T_t (T_b) was set equal to the area average of the five thermometers embedded in the top (bottom) plate. For any given data point, measurements over typically the first four hours were discarded to avoid transients, and data taken over an additional period of at least another eight hours were averaged to get the heat-current density Q, and the temperatures T_b and T_t. Because of the imperfect temperature uniformity of the bottom shield there was a small parasitic heat loss from the bottom plate of about 0.1 W, which was determined by measuring the required power to keep the bottom and top plate at $40°C$, a measurement which takes two days. For each measurement this parasitic heat loss was subtracted from the measured power.

In addition various heat transport measurements on rotating RB convection were performed in the group of Guenter Ahlers in Santa Barbara, see also chapter 6 and 8. These measurements were done in an aspect ratio $\Gamma = 1$ sample and cover the Ra number range $3 \times 10^8 \lesssim Ra \lesssim 2 \times 10^{10}$, the Pr number range $3.0 \lesssim Pr \lesssim 6.4$, and the $1/Ro$ number range $0 \lesssim 1/Ro \lesssim 20$. These data points are shown in the $Ra - Ro - \Gamma$ phase diagram for rotating RB shown in figure 10.1. The experimental procedure that has been used in these experiments is described in detail by Zhong and Ahlers [80]. All the Nusselt number measurements of Zhong and Ahlers [80] were documented in the accompanying supplementary material of that paper, and we use those data in our figures here. Recently, Weiss & Ahlers [192] did similar measurements in an aspect ratio $\Gamma = 0.5$ sample. As these measurement data are not yet available in the open literature we do not include a comparison with their data.

Zhong and Ahlers [80] restricted themselves to aspect ratio $\Gamma = 1$. In this chapter we present new heat transport measurements from the Eindhoven RB setup, which is based on the Santa Barbara design [80, 175], for aspect ratio $\Gamma = 4/3$ and $\Gamma = 2.0$. We also present some $\Gamma = 1.0$ measurements from the Eindhoven setup, (i) because this particular Ra number was not available in the Santa Barbara (SB) data set of Zhong and Ahlers [80] and we wanted to compare the results with those for $\Gamma = 4/3$ and $\Gamma = 2$ at the same Ra, (ii) because we want to compare with the simulation results which are restricted to small Ra, and (iii) because we wanted to benchmark the results of our new setup against those of the SB setup. Recently, Weiss & Ahlers [192] did similar measurements in an aspect ratio $\Gamma = 0.5$ sample. As these measurement data are not yet available in the open literature we do not include a comparison with their data.

The Eindhoven measurements have been verified against the experiments of Funfschilling et al. [176] and the SB measurements presented in chapter 6 and 8. For the present measurements the difference is in the order of 1%, well within the differences observed between different RB setups [20]. In figure 10.3 we show the heat transfer enhancement $Nu(\Omega)/Nu(0)$ as function of the rotation rate $1/Ro$ for $Ra = 2.99 \times 10^8$, $Ra = 5.88 \times 10^8$ and $Ra = 1.16 \times 10^9$ at $Pr = 4.38$, which corresponds with a mean temperature of the fluid of 40.00°C, and compare them with the SB heat transport measurements reported in chapter 6 and 8. Perfect agreement between the two datasets is found.

Presently, the Eindhoven experiments can only be performed with one type of plate material (copper) and not with more as done in Santa Barbara. For this reason we can not apply the plate corrections to obtain the absolute Nusselt number without making some assumptions that cannot be verified at the moment. Therefore for the experimental results we restrict ourself to relative Nusselt numbers $Nu(1/Ro)/Nu(0)$.

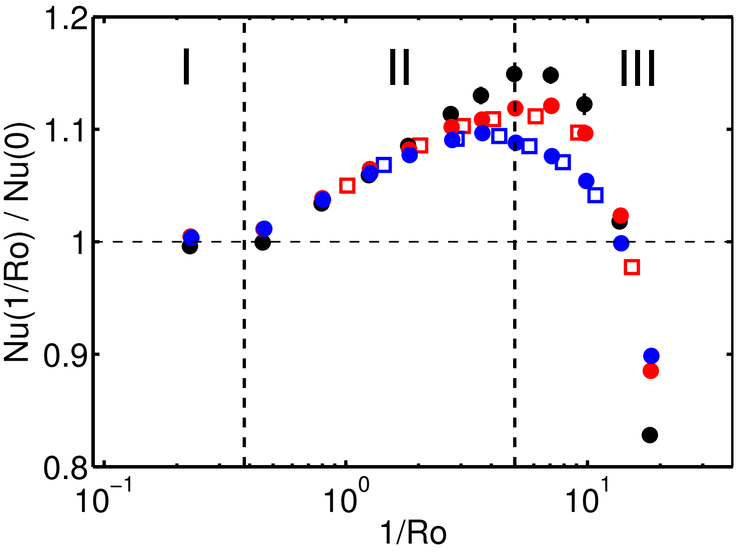

Figure 10.3: The ratio of the Nusselt number $Nu(1/Ro)$ in the presence of rotation to $Nu(0)$ for $Pr = 4.38$ ($T_m = 40.00°\mathrm{C}$) and $\Gamma = 1$. The solid circles are the data obtained in the Eindhoven RB setup and the open squares are the corresponding data obtained in Santa Barbara, see also chapter 6 and 8. Black solid circles: $Ra = 2.99 \times 10^8$ ($\Delta = 0.50$ K). Red solid circles: $Ra = 5.88 \times 10^8$ ($\Delta = 1.00$ K). Blue solid circles: $Ra = 1.16 \times 10^9$ ($\Delta = 2.00$ K). Red open squares: $Ra = 5.6 \times 10^8$ ($\Delta = 1.00$ K, run E4 in Zhong &Ahlers [80]). Blue open squares: $Ra = 1.2 \times 10^9$ ($\Delta = 2.00$ K, run E5 in Zhong &Ahlers [80]).

10.3 Numerical procedure

In the simulations the flow characteristics of rotating RB convection for $Ra = 2.91 \times 10^8 - 4.52 \times 10^9$, $Pr = 4.38$, $0 < 1/Ro < 12.5$, and $0.5 < \Gamma < 2.0$, see also table 10.1 and figure 10.1, are obtained from solving the three-dimensional Navier-Stokes equations within the Boussinesq approximation. Details about the numerical procedure can be found in Refs. [107–109] and in chapter 6.

The resolutions used for the simulations are summarized in table 10.1. These grids allow for a very good resolution of the small scales both inside the bulk of turbulence and in the BLs where the grid-point density has been enhanced. We checked this by calculating the convergence of the volume averaged kinetic ε_u and thermal ε_θ dissipation rates as is proposed in chapter 2. We find that these quantities always converge within a 5% margin at most. A comparison with the results of chapter 2 shows that this convergence rate is clearly sufficient to reliably calculate the heat transfer. As argued in chapter 4 it is especially important to properly resolve the BLs. According to equation (42) of that chapter the minimal number of nodes that should be placed in the thermal BL is $N_{BL} = 4.7$ ($N_{BL} = 7.1$) when $Ra = 2.91 \times 10^8$ ($Ra = 4.52 \times 10^9$) and $Pr = 4.38$. In the simulations at $Ra = 2.91 \times 10^8$ ($Ra = 4.52 \times 10^9$) we placed $N_{BL} = 14$ ($N_{BL} = 22$) points in the thermal BL, which is on the safe side.

Table 10.1: Simulations performed in this study. The columns from left to right indicate the following: the Rayleigh number Ra, the aspect ratio Γ, the inverse Rossby number $1/Ro$, the number of Ro cases that is simulated (n_{Ro}), and the number of grid points in the azimuthal, radial, and axial directions ($N_\theta \times N_r \times N_z$)

Ra	Γ	$1/Ro$	n_{Ro}	$N_\theta \times N_r \times N_z$
2.91×10^8	0.5	$0-12.5$	16	$257 \times 97 \times 289$
4.52×10^9	0.5	$0-12.5$	18	$641 \times 161 \times 641$
2.91×10^8	1.0	$0-12.5$	16	$385 \times 193 \times 289$
5.80×10^8	1.0	$0-5.0$	3	$641 \times 193 \times 385$
2.91×10^8	2.0	$0-12.5$	18	$769 \times 385 \times 289$
5.80×10^8	2.0	$0-5.0$	2	$1281 \times 385 \times 385$

For the non-rotating case similar numbers are obtained for the grid point resolution in the kinetic BL. When rotation is applied the kinetic BL becomes thinner. This effect only becomes significant for the highest $1/Ro$ number cases considered here, and we emphasize that for all cases the number of points in the kinetic BL is above the criterion put forward in chapter 4. Furthermore, it is also very important to make sure that the results are statistically converged. Again we use the methods introduced in chapter 2 to check this. For all cases the convergence is in the order of 1% and it is much better for most. For the simulations at $Ra = 2.91 \times 10^8$ in the aspect ratios $\Gamma = 0.5$, $\Gamma = 1.0$, and $\Gamma = 2.0$ the average statistical uncertainty is only about 0.5%.

As last check we compare the numerical results with experimental data. For this we use the data of the group of Guenter Ahlers, who did high precision heat transport measurements in $\Gamma = 0.5$ [170], $\Gamma = 1.0$ [176], and $\Gamma = 2.0$ [176] samples. For all cases we find that the numerical results are within 1% of these experimental data. For some cases the numerical data of the present simulations are even slightly below the experimental data. This is reassuring with respect to numerical resolution issues, as normally the heat transport in underresolved simulation is *larger* than the actual heat transport, see chapter 2.

In the simulations we partially neglect centrifugal forces, namely the density dependence of the centripetal forces, which in the Boussinesq equations show up as $-2Fr\ r\theta\hat{r}$, with the radial unit vector $\hat{r}$ [177]. It is shown in chapter 6 and by Refs. [75, 85] that this is justified for small Fr numbers. For all experiments in the $\Gamma = 1$ sample, where the Fr number is below 0.03 for all cases, this condition is fulfilled. For the experiments in the $\Gamma = 2$ sample the Froude number is below 0.05 for all experiments up to $1/Ro = 5$. For higher $1/Ro$ the Froude number quickly increases up to 0.12 for $Ra = 2.91 \times 10^8$ and up to 0.49 for $Ra = 1.16 \times 10^9$. For the experiments at $Ra = 2.91 \times 10^8$, for which the highest Fr number is 0.12, this does not influence the results as we find a perfect agreement between the experimental and numerical results, see figure 2c. The experimental results for higher Ra in the $\Gamma = 2$ sample, where the Froude numbers are higher for the highest $1/Ro$ case, do not suggest a strong influence of this effect on the heat transport measurements. However, at the moment we can not rule it out completely either.

We note that the simulations presented here are very CPU time intensive; about 1.5 million standard DEISA CPU hours have been used, due to the large aspect ratios, the relatively high *Ra* numbers that are resolved with high resolution, the number of different *Ro* number cases, and the long averaging times that are needed to get sufficient statistical convergence. This puts this numerical study in the top three of largest numerical RB studies, next to the high Rayleigh number studies presented in chapters 2 and 3.

10.4 Results

In figure 10.4 the heat transport enhancement with respect to the non-rotating case is shown for $\Gamma = 0.5$, $\Gamma = 1$, $\Gamma = 4/3$, and $\Gamma = 2$ and different *Ra*. Here we find an excellent agreement between experimental and numerical results. The figure shows that there is a strong heat transport enhancement due to Ekman pumping when $1/Ro > 1/Ro_c$, where $1/Ro_c$ indicates the position of the onset of heat transport enhancement (see chapters 8 and 9). The figure also shows that the heat transport enhancement decreases with increasing *Ra*. This is because the eddy thermal diffusivity is larger at higher *Ra* and this causes the warm (cold) fluid that enters the base of the vortices to spread out more quickly in the middle of the sample. This makes the effect of Ekman pumping smaller and this results in a lower heat transport enhancement. The breakdown of Nu at high $1/Ro$ is an effect of the suppression of vertical velocity fluctuations through the strong rotation.

When the results for $\Gamma = 0.5$, $\Gamma = 1$, $\Gamma = 4/3$ and $\Gamma = 2$ are compared, they look pretty similar on first sight, i.e. a strong heat transport enhancement when $1/Ro > 1/Ro_c$ and a heat transport reduction for very strong rotation rates. However, when we look more closely we see that there are several important differences. First of all $1/Ro_c$, the rotation rate needed to get heat transport enhancement, increases with decreasing aspect ratio. In chapter 9 we already observed this and explained it by finite size effects. In addition a close comparison between the $\Gamma = 1$ and $\Gamma = 2$ data in figure 10.4 shows that the heat transport enhancement is slightly larger in a $\Gamma = 2$ sample than in a $\Gamma = 1$ sample. This can be observed in more detail in figure 10.5, where the relative heat transport enhancement at fixed *Ra* is compared for several aspect ratios.

The absolute heat transfer shown in figure 10.6 is available only for the numerical case, (as explained in section 2). From that figure we conclude that the heat transport becomes independent of the aspect ratio once $1/Ro \gg 1/Ro_c$, while there are some visible differences for the non-rotating case. Also for $Ra = 5.80 \times 10^8$ and $1/Ro = 5$ we find that the difference in the heat transport between the $\Gamma = 1$ and the $\Gamma = 2$ case

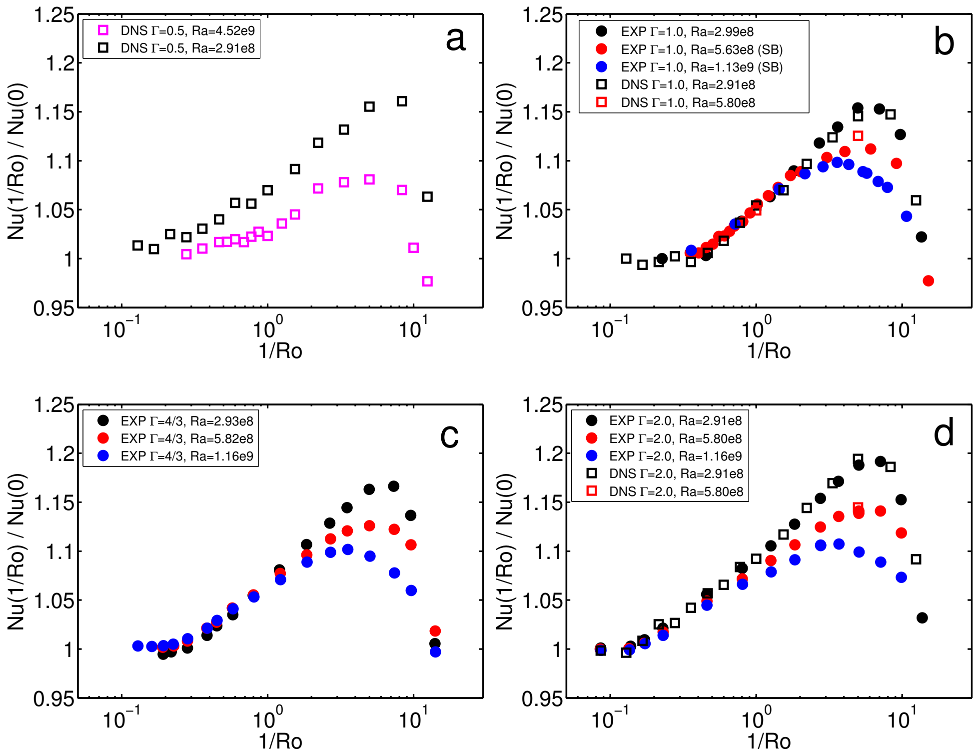

Figure 10.4: The ratio $Nu(1/Ro)/Nu(0)$ as function of $1/Ro$ for different Ra for a) $\Gamma = 0.5$, b) $\Gamma = 1$, c) $\Gamma = 4/3$, and d) $\Gamma = 2$. a) The results from the DNS at $Ra = 2.91 \times 10^8$, and $Ra = 4.52 \times 10^9$ are indicated by the black and magenta open squares, respectively. b) The experimental results for $Ra = 2.99 \times 10^8$, $Ra = 5.63 \times 10^8$ (run E4 of Zhong & Ahlers [80]), and $Ra = 1.13 \times 10^9$ (run E5 of Zhong & Ahlers [80]) are indicated in black, red, and blue solid circles, respectively. The DNS results for $Ra = 2.91 \times 10^8$, and $Ra = 5.80 \times 10^8$ are indicated by black and red open squares, respectively. c) The experimental results for $Ra = 2.93 \times 10^8$, $Ra = 5.82 \times 10^8$, and $Ra = 1.16 \times 10^9$ are indicated in black, red, and blue solid circles, respectively. d) The experimental results for $Ra = 2.91 \times 10^8$, $Ra = 5.80 \times 10^8$, and $Ra = 1.16 \times 10^9$ are indicated in black, red, and blue solid circles, respectively. The DNS results for $Ra = 2.91 \times 10^8$, and $Ra = 5.80 \times 10^8$ are indicated by black and red open squares, respectively. All presented data in this figure are for $Pr = 4.38$.

is smaller than for the non-rotating case. These small differences in the heat transport for different aspect ratios were also found in the numerical study of Bailon-Cuba et al. [171] and in experiments of Funfschilling et al. [176] and Sun et al. [152]. However, the experimental and numerical results seem to suggest that this effect decreases with increasing Ra.

For the non-rotating case the flow organizes globally in the large scale convection roll. Because this global flow structure can depend on the aspect ratio, there can be small variations in the Nusselt number as function of the aspect ratio. For strong enough rotation, i.e. $1/Ro \gg 1/Ro_c$, the global LSC is replaced by vertically-aligned

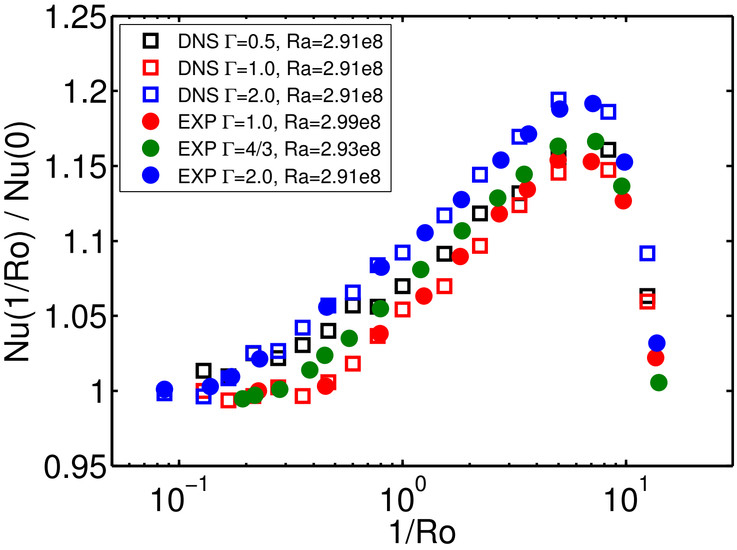

Figure 10.5: The ratio $Nu(1/Ro)/Nu(0)$ as function of $1/Ro$ for $Ra \approx 3 \times 10^8$ and different Γ. The experimental results for $\Gamma = 1$, $\Gamma = 4/3$, and $\Gamma = 2$ are indicated in red, dark green, and blue solid circles, respectively. The DNS results for $\Gamma = 0.5$, $\Gamma = 1$, and $\Gamma = 2$ are indicated by black, red and blue open squares, respectively. All presented data are for $Pr = 4.38$.

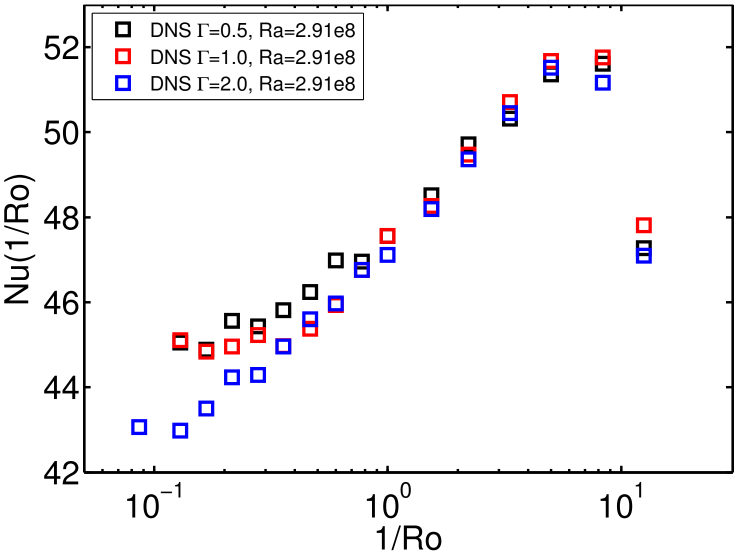

Figure 10.6: The absolute Nusselt number of the simulation data presented in figure 10.5. The results for $\Gamma = 0.5$, $\Gamma = 1$, and $\Gamma = 2$ are indicated by black, red and blue open squares, respectively. All presented data are for $Pr = 4.38$.

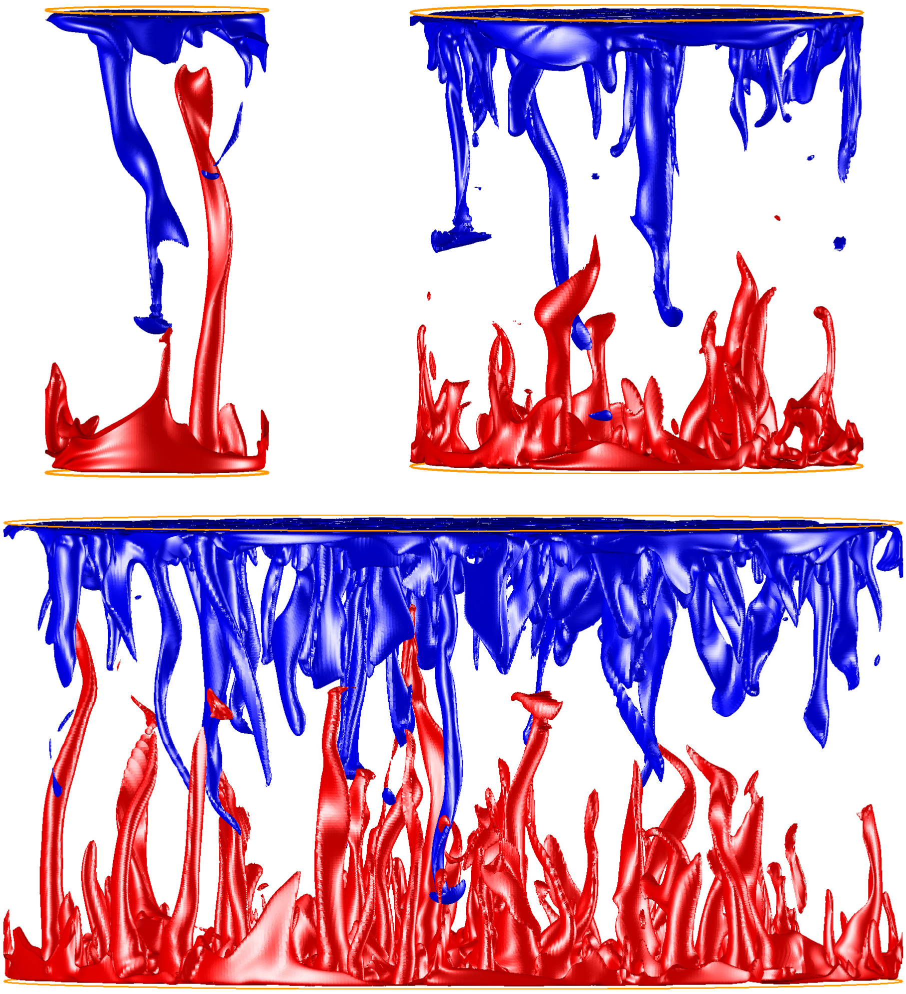

Figure 10.7: 3D visualization of the temperature isosurfaces in the cylindrical sample at 0.65Δ (red) and 0.35Δ (blue), respectively for $Ra = 2.91 \times 10^8$, $Pr = 4.38$, $1/Ro = 3.33$ and $\Gamma = 0.5$ (left upper plot), $\Gamma = 1.0$ (right upper plot), and $\Gamma = 2.0$ (lower plot).

vortices as the dominant feature of the flow, see Refs. [85, 91] and chapters 6-9). In this regime most of the heat transport takes place in vertically-aligned vortices [101, 102]. Because the vortices are a local effect the influence of the aspect ratio on the heat transport in the system should be negligible. This assumption is used in several models [84, 101, 102], which consider a horizontally periodic domain, that are developed to understand the heat transport in rotating turbulent convection.

To investigate this idea we made three-dimensional visualizations of the temperature isosurfaces at $Ra = 2.91 \times 10^8$, $Pr = 4.38$, and $1/Ro = 3.33$, for the different as-

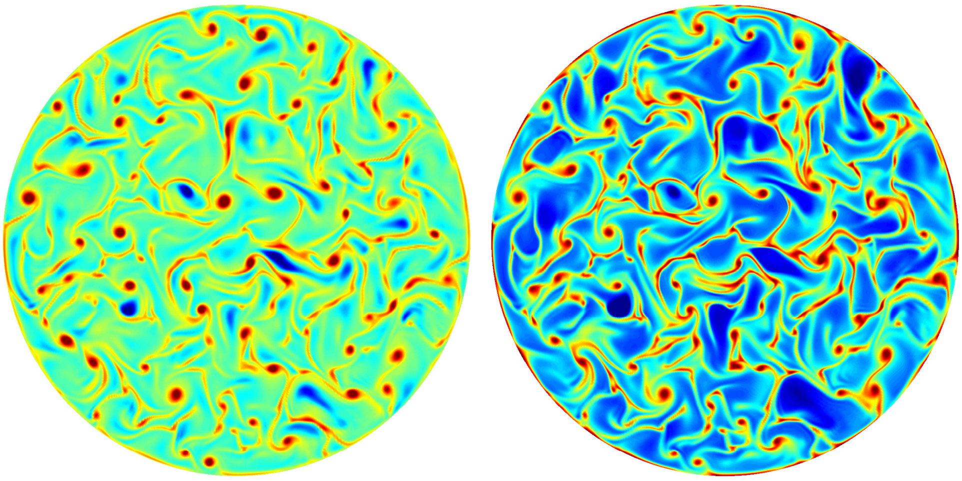

Figure 10.8: Visualization of the vertical velocity (left plot) and temperature (right plot) fields at the kinetic BL height for $Ra = 2.91 \times 10^8$, $\mathrm{Pr} = 4.38$, $1/Ro = 3.33$, and $\Gamma = 2$. Note that there is a strong correlation between the areas where the strongest vertical velocity and highest temperatures are found, namely in the vortices. Red and blue indicate upflowing (warm) and downflowing (cold) fluid in the left (right) panel.

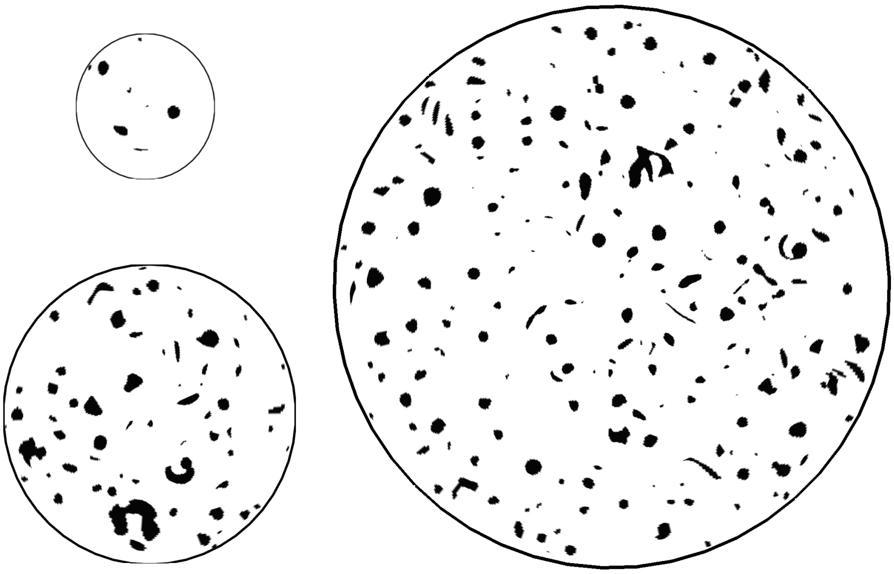

Figure 10.9: The vortices at the edge of the kinetic BL as identified by the Q_{2D} criterion for $Ra = 2.91 \times 10^8$, $\mathrm{Pr} = 4.38$, $1/Ro = 3.33$ and $\Gamma = 0.5$ (upper left plot), $\Gamma = 1.0$ (lower left plot), and $\Gamma = 2.0$ (right plot).

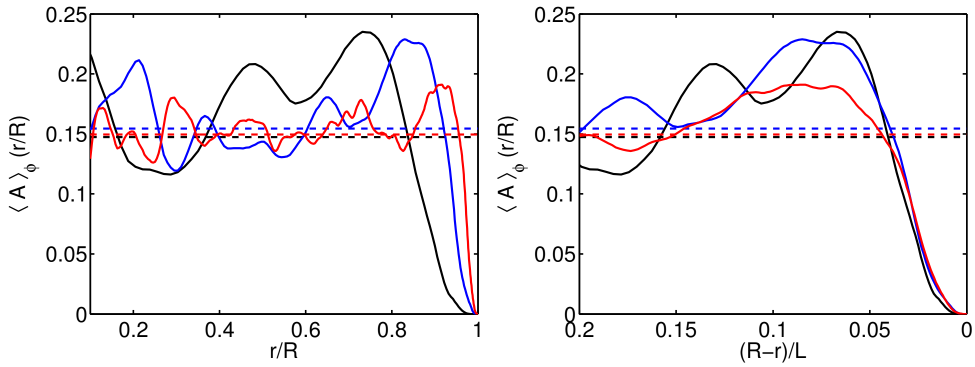

(a) (b)

Figure 10.10: Azimuthal average $\langle A\rangle_{r/R}$ of the vortex density A for $Ra = 2.91\times10^8$, $Pr = 4.38$, $3.33 < 1/Ro < 8.33$ as function of r/R (panel a) and $(R-r)/L$ (panel b) for different aspect ratios. The solid black, blue, and red lines indicated the distribution for $\Gamma = 0.5$, $\Gamma = 1.0$, and $\Gamma = 2.0$. The dashed lines indicate the average horizontal area covered by vortices. The data for each aspect ratio are based on 12 snapshots.

pect ratios, see figure 10.7. Indeed the figures confirm that vertically-aligned vortices are formed in all aspect-ratio samples. Furthermore, the figure reveals that a larger number of vortices is formed in the $\Gamma = 1$ and $\Gamma = 2$ samples than in the $\Gamma = 0.5$ sample. This is expected, since these samples have a larger horizontal extension.

In order to reveal the structure of the flow in more detail we show the temperature and vertical velocity fields at the kinetic BL height near the bottom plate for $Ra = 2.91\times10^8$, $Pr = 4.38$, $1/Ro = 3.33$, and $\Gamma = 2$ in figure 10.8 . This figure clearly shows that hot fluid is captured in the up-going vortices. Similar plots (not shown) revealed that cold fluid near the top plate is captured in down going vortices. In order to study the vortex statistics one needs to have a clear criterion of what exactly constitutes a vortex. For this we use the so-called Q-criterion, see Refs. [74, 92, 96, 188], chapter 9 and appendix B. This criterion requires that the quantity Q_{2D} [193, 194], which is a quadratic form of various velocity gradients, is calculated in a plane of fixed height. Here we always take the kinetic BL height. Following chapter 9 an area is identified as "vortex" when $Q_{2D} < -\langle|Q_{2D}|\rangle_v$, were $\langle|Q_{2D}|\rangle_v$ is the volume-averaged value of the absolute values of Q_{2D}. Here we have set the threshold for the vortex detection more restrictive than in chapter 9 to make sure that only the strong upgoing (downgoing) vortices are detected. However, we note that similar results are obtained when a less restrictive threshold is used.

The result of this procedure for $Ra = 2.91\times10^8$, $1/Ro = 3.33$, and $\Gamma = 0.5-2.0$ is shown in figure 10.9. The figure shows that the vortices (both up and down going) are in general randomly distributed. However, note that no vortices are formed close to the sidewall. To quantify this we determined the radial distribution of the vortices from the plots shown in figure 10.9 and similar plots. The result is shown in figure 10.10. Figure 10.10a confirms that no vortices are formed close to the sidewall, while in the bulk their fraction is roughly constant. Figure 10.10b shows that the size of the region close to the sidewall where no vortices are formed is roughly independent of the aspect ratio.

This is in agreement with the predication of Weiss & Ahlers [192] that is derived from a phenomenological Ginzburg-Landau model. As detailed information about the flow field is needed to determine the vortex distribution it is very hard to obtain this data from experimental measurements [92]. In figure 10.10b one can see that the vortex density in the region $(R-r)/L \lesssim 0.015$ decreases faster to zero than for $(R-r)/L \gtrsim 0.015$, which is due to the vortex detection method employed in this study. More specifically, we detect only the core of the vortex. As the vortex core is always formed some distance away from the wall this causes an (artificial) enhanced decrease in the vortex density in the direct vicinity of the wall. The origin of the peaks in the distribution function is similar to the origin of the peaks observed in pair correlation functions of the distribution of hard disks.

However, and this is the main point here, one can see in figure 10.10 that the fraction of the horizontal area that is covered by vortices, see the dashed lines in the figure, is independent of the aspect ratio. This means that the vortices are indeed a local effect. This observation supports our finding that the heat transport is independent of the aspect ratio in the rotating regime. Based on the observation that less vortices are formed close to the sidewalls, one would have expected that the vortex density averaged over the whole area is higher for larger aspect ratio. The reason is that for larger aspect ratio samples this vortex-depleted sidewall region is relatively smaller than for smaller aspect ratio ones. However, just next to the vortex depletion region we find a region where the vortex density is enhanced. As is shown in figure 10.10b, the absolute width of this region seems to be rather independent of the aspect ratio of the sample, too. Hence the effect of the vortex depletion and the vortex enhancement region on the horizontally averaged vortex density cancel out in first order.

10.5 Conclusions

In summary, we investigate the effect of the aspect ratio on the heat transport in turbulent rotating Rayleigh-Bénard convection by results obtained from experiments and direct numerical simulations. We find that the heat transport in the rotating regime is independent of the aspect ratio, although there are some visible differences in the heat transport for the different aspect ratios in the non-rotating regime at $Ra = 2.91 \times 10^8$. This is because in the non-rotating regime the aspect ratio can influence the global flow structure. However, in the rotating regime most heat transport takes place in vertically-aligned vortices, which are a local effect. Based on the simulation results we find that the fraction of the horizontal area that is covered by the vortices is independent of the aspect ratio, which confirms that the vertically-aligned vortices are indeed a local effect. This supports the simulation results, which show that the heat transport becomes independent of the aspect ratio in the rotating regime. In addition, it confirms the main assumption that is used in most models, which consider a horizontally periodic domain [84, 101, 102], that are developed to understand the heat transport in rotating turbulent convection. The analysis of the vortex statistics also revealed that the vortex concentration is reduced close to the sidewall, while the distribution is nearly uniform in the center. In between these two regions, there is a region of enhanced vortex concentration. The widths of both that region and the vortex-depleted region close to the sidewall are independent of the aspect ratio. This analysis highlights the value of numerical simulations in turbulence research: The determination of the vortex distribution requires detailed knowledge of the flow field and therefore it would have been very difficult to obtain this finding purely from experimental measurements.

11

Boundary layers in rotating weakly turbulent Rayleigh-Bénard *

The effect of rotation on the boundary layers (BLs) in a Rayleigh-Bénard (RB) system at a relatively low Rayleigh number, i.e. $Ra = 4 \times 10^7$*, is studied for different Pr by direct numerical simulations and the results are compared with laminar BL theory. In this regime we find a smooth onset of the heat transfer enhancement as function of increasing rotation rate. We study this regime in detail and introduce a model based on the Grossmann-Lohse theory to describe the heat transfer enhancement as function of the rotation rate for this relatively low Ra number regime and weak background rotation* $Ro \gtrsim 1$*. The smooth onset of heat transfer enhancement observed here is in contrast to the sharp onset observed at larger* $Ra \gtrsim 10^8$ *in chapter 8 and 9, although only a small shift in the* $Ra - Ro - Pr$ *phase space is involved.*

11.1 Introduction

Normally the transition between different turbulent states is smooth, because the large random fluctuations that characterize the turbulent flow make sure that the entire phase space is explored and therefore the transitions between different states, that are explored as a control parameter is changed, are washed out. For non-rotating RB system the heat transport can satisfactory be described by the Grossmann-Lohse (GL)

---

[*] Based on: R.J.A.M. Stevens, H.J.H. Clercx, and D. Lohse, Boundary layers in rotating weakly turbulent Rayleigh-Bénard convection, Phys. Fluids, 22, 085103 (2010).

theory [20, 25–28] and shows that RB convection has different turbulent regimes in the $Ra - Pr$ phase space (see Fig. 3 of Ref. [20]). The dynamics of rotating RB convection are determined by three control parameters, i.e. Ra, Pr, and Ro, and this leads to a huge $Ra - Pr - Ro$ phase space, see Fig. 11.1.

In this chapter we will discuss the results of Direct Numerical Simulations (DNS) that show that this heat transfer enhancement as function of the Ro number is smooth for relatively low Ra number, here $Ra = 4 \times 10^7$ (see Fig. 11.2a), while experimental and numerical data for $Ra = 2.73 \times 10^8$ and $Pr = 6.26$ show a sharp onset for the heat transport enhancement, see Fig. 11.2b. This difference is remarkable since only a small shift in the $Ra - Pr - Ro$ phase space is involved (see Fig. 11.1). We will first describe the flow characteristics found in the simulations. We will show that there is a smooth transition from one turbulent regime to another for the relatively low Ra number regime whereas a sharp transition is found for higher Ra. In section 11.2 we will discuss the properties of the BLs found in the DNS in detail. Subsequently the laminar BL theory for flow over an infinitely large rotating disk will be discussed in section 11.3 in order to explain the BL properties found in the DNS. The derived scaling laws from this theory will be used in a model based on the GL theory to describe the heat transfer enhancement as function of Ro for the relatively low Ra number regime with weak background rotation, see section 11.4.

11.2 Boundary layers in rotating RB convection

The flow characteristics of rotating RB convection for $Ra = 4 \times 10^7$, $1 < Ro < \infty$, $0.2 < Pr < 20$, and aspect ratio $\Gamma = 1$, are obtained from solving the three-dimensional Navier-Stokes equations within the Boussinesq approximation. The numerical method is already described in detail in chapter 6 and Refs. [107–109].

The first set of simulations is used to study the Ro number dependence of the following quantities: the normalized heat transfer, the thickness of the thermal BL, and the normalized averaged root mean square (rms) vertical velocity fluctuations. Here we have simulated rotating RB convection at several Ro numbers for three different Pr numbers ($Pr = 0.7$, $Pr = 6.4$, and $Pr = 20$). All these simulations are performed on a grid with $193 \times 65 \times 129$ nodes, respectively, in the azimuthal, radial, and vertical directions, allowing for sufficient resolution in the bulk and the BL according the resolution criteria set in chapter 2. The Nusselt number is calculated in several ways as is discussed in detail in chapter 2 and its statistical convergence has been verified. Some data for $Pr = 6.4$ are already shown in chapter 8. There the average was over 4000 dimensionless time units. The new results for $Pr = 0.7$ and $Pr = 20$ are averaged over 2500 dimensionless time units. Note that we simulated the flow for a large number of eddy turnover times to reduce the statistical error in the obtained Nusselt number results and to prevent the influence of transient effects. This is necessary to

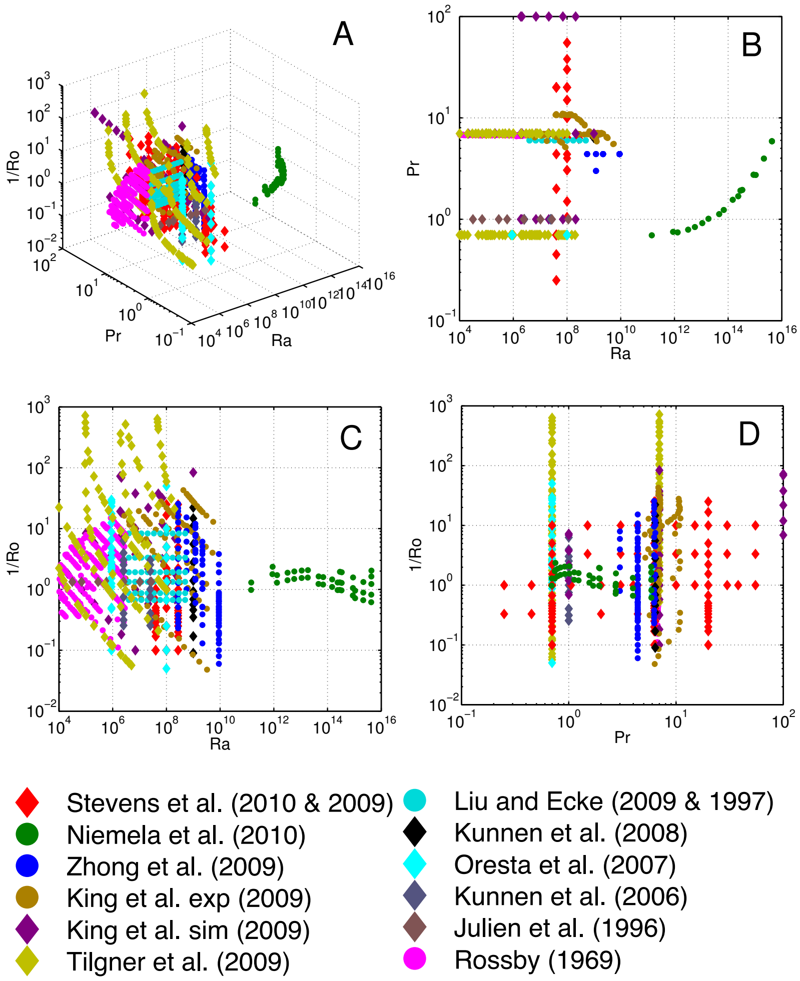

Figure 11.1: Phase diagram in Ra-Pr-Ro space for rotating RB convection. The data points indicate where *Nu* has been measured or numerically calculated. The data are obtained in a cylindrical cell with aspect ratio $\Gamma = 1$ with no slip boundary conditions, unless mentioned otherwise. The data from direct numerical simulations and experiments are indicated by diamonds and dots, respectively. The data sets, which are ordered chronologically in panel e, are from: Stevens et al. (2010 & 2009) (see chapters 6-8) and the simulations of this chapter; Niemela et al. (2010) [81] ($\Gamma = 0.5$); Zhong and Ahlers (2009) (see chapter 6 and 8); King et al. (2009) [76]; Schmitz and Tilgner (2009) [88] (free slip boundary conditions and horizontally periodic); Liu and Ecke (2009 & 1997) [78, 79] (square with $\Gamma = 0.78$); Kunnen et al. (2008) [75]; Oresta et al. (2007) [90] ($\Gamma = 0.5$); Kunnen et al. (2006) [85] ($\Gamma = 2$, horizontally periodic); Julien et al. (1996) [77] ($\Gamma = 2$, horizontally periodic); Rossby (1969) (varying aspect ratio). Panel a shows a three dimensional view on the phase space (see also movie 11.1 in the supplementary material [115]), b) projection on the Ra-Pr phase space, c) projection on the Ra-Ro phase space, d) projection on the Pr-Ro phase space.

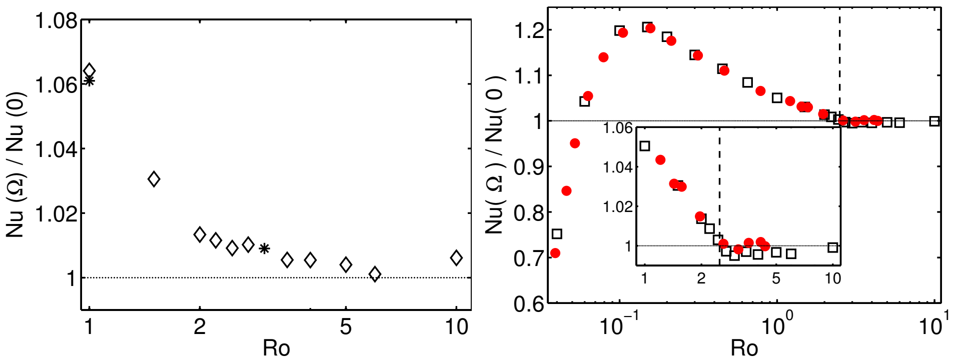

(a) (b)

Figure 11.2: Normalized heat transfer as a function of the Rossby number. a) Numerical results for $Ra = 4 \times 10^7$ and $Pr = 6.4$. The diamonds and stars indicate the results obtained on the $193 \times 65 \times 129$ and $257 \times 97 \times 193$ grid, respectively. b) $Ra = 2.73 \times 10^8$ and $Pr = 6.26$. Solid circles: experimental data of chapter 6 and 8. Open squares: numerical results of chapter 6 and 8. The vertical dashed line indicates the position of the onset.

accurately resolve the transition regime where the heat transfer starts to increase and to accurately determine the flow statistics. Furthermore, we note that all simulations are started from a new flow field in order to rule out hysteresis effects.

The second set of simulations is used to study the Pr number dependence of the same set of quantities. Here we simulated rotating RB for several Pr numbers and three different Ro numbers ($Ro = \infty$, $Ro = 3$, and $Ro = 1$). The simulations for $Pr \geqq 0.70$ are performed on a $257 \times 97 \times 193$ and the simulations at $Pr = 0.25$ and $Pr = 0.45$ are performed on a $385 \times 129 \times 257$ grid. The finer resolution is needed here as the structure of the flow changes and the Reynolds number based on the LSC increases for lower Pr. For most cases the flow is simulated for 400 dimensionless time units and 200 dimensionless time units were simulated before data are collected to prevent any influence of transient effects. For $Pr = 2$ and $Pr = 4.4$ we averaged over 1200 dimensionless time units in order to obtain more accurate statistics on the velocity field. Note that the second set of simulations is partially overlapping with the first set of simulations. We find that results obtained on the different grids, are very similar, i.e. the difference is generally between 0.5% and 1%, see Figs. 11.2a, 11.5a and 11.7a. Again all simulations are started from a new flow field in order to rule out any hysteresis effects.

Fig. 11.3 shows the azimuthally averaged temperature profile at the cylinder axis for different system parameters. In previous numerical studies concerning (rotating) RB convection the thermal BL thickness is usually defined by either looking at the maximum rms value of the temperature fluctuations or by considering the BL thickness based on the slope of the mean temperature profile. In the latter case it is usually

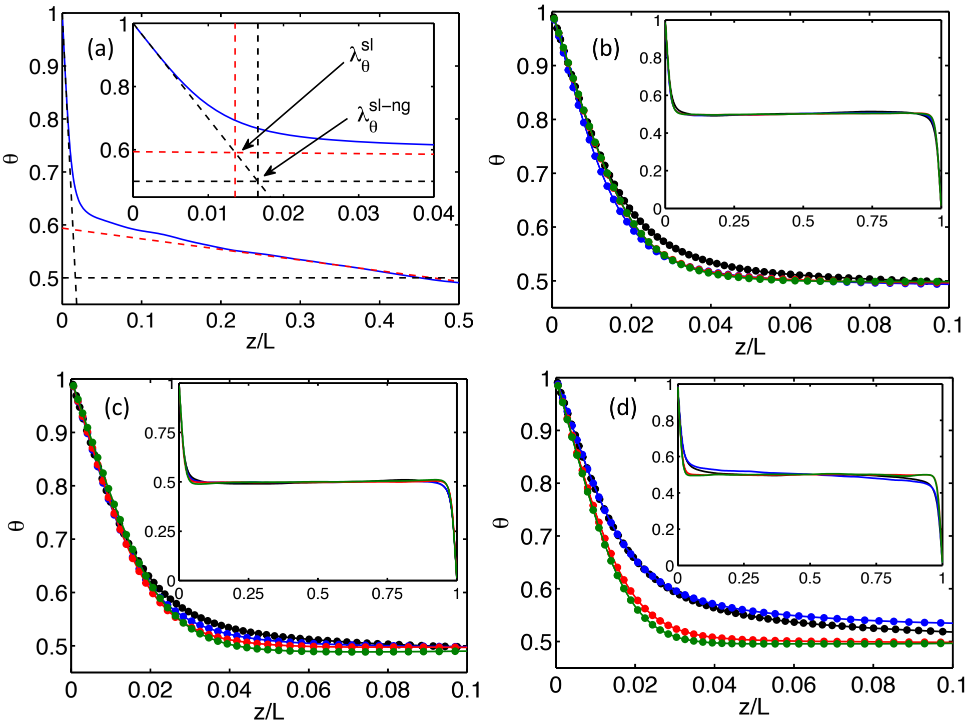

Figure 11.3: a) Visualization of the definitions of the thermal BL thicknesses λ_θ^{sl} and λ_θ^{sl-ng} (assuming zero gradient in the bulk). b-d) Azimuthally averaged temperature profiles for $Ra = 4 \times 10^7$ and different Pr and Ro numbers at the cylinder axis $r = 0$ for b) $Ro = \infty$, c) $Ro = 3$, and d) $Ro = 1$. Black, blue, red, and dark green indicate the profiles for $Pr = 0.25$, $Pr = 0.7$, $Pr = 6.4$, and $Pr = 20$, respectively. The dots indicate the data points obtained from the simulations. The insets show the profile over the full cell.

assumed that no mean temperature gradient exists in the bulk (the BL thickness according to this assumption is denoted by λ_θ^{sl-ng}). The temperature gradient in the bulk is, however, strongly influenced by rotation, see Ref. [86] and chapter 6, and when rotation is present also by Pr, see Fig. 11.4. We define the thermal BL thickness λ_θ^{sl} as the intersection point between the linear extrapolation of the temperature gradient at the plate with the linear fit to the temperature profile in the bulk region ($0.25L < z < 0.75L$), see Fig. 11.3a. From now on this definition of the thermal BL thickness will be used.

For the relatively low Ra number regime, here $Ra = 4 \times 10^7$, the heat transfer enhancement as function of Ro is smooth, see Fig. 11.5a. Note that although the behaviour of λ_θ^{sl} (see fig. 11.5b), i.e. the horizontally averaged value of the radially dependent thermal BL thickness ($\lambda_\theta^{sl}(r)$), as function of Ro is similar for all Pr the behaviour of Nu is very different. This is due to the influence of Pr on the effect of Ekman pumping, see see chapter 6 and 7. At low Pr the larger thermal diffusivity

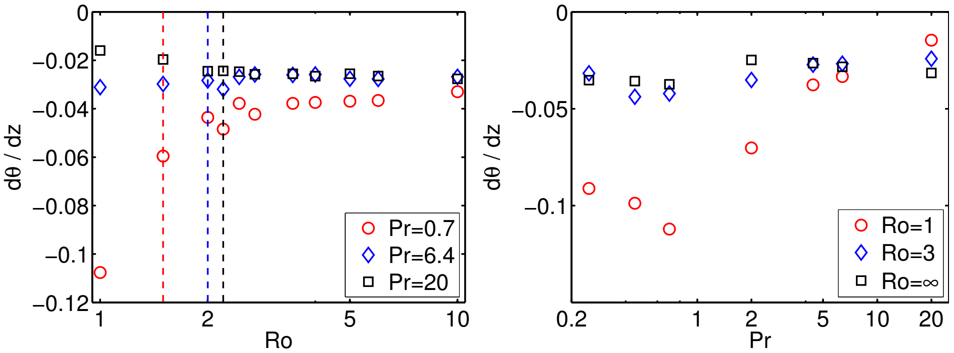

(a) (b)

Figure 11.4: a) Horizontally averaged temperature gradient at midheight as a function of Ro for $Ra = 4 \times 10^7$ and different Pr. The circles, diamonds, and squares indicate the data for $Pr = 0.7$, $Pr = 6.4$, and $Pr = 20$, respectively. b) Temperature gradient at midheight as function of Pr for $Ra = 4 \times 10^7$ and different Ro. The circles, diamonds, and squares are the data for $Ro = 1$, $Ro = 3$, and $Ro = \infty$, respectively. The vertical dashed lines (from left to right for $Pr = 0.7$, $Pr = 6.4$ and $Pr = 20$) in Fig. 11.4a indicate the position of the onset, see Fig. 11.6.

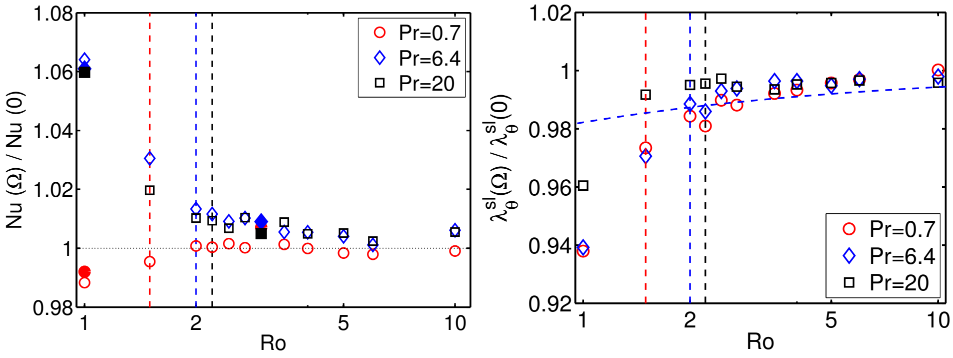

(a) (b)

Figure 11.5: a) Normalized heat transfer as a function of Ro for $Ra = 4 \times 10^7$ and different Pr. The circles, diamonds, and squares are the data for $Pr = 0.7$, $Pr = 6.4$, and $Pr = 20$, respectively. The dash-dotted line is the fit obtained by the model Eq. 11.20, with $\alpha = 55$. The filled symbols indicate the results from the grid refinement check (see text). b) Horizontally averaged thickness of the thermal BL λ_θ^{sl} as function of Ro. Symbols as in Fig. 11.5a and the dash-dotted line indicates the same model fit as in Fig. 11.5a. The vertical dashed lines (from left to right for $Pr = 0.7$, $Pr = 6.4$ and $Pr = 20$) in both graphs represent the point at which the LSC strength starts to decrease, see Fig. 11.6.

limits the effect of Ekman pumping and causes a larger destabilizing temperature gradient in the bulk, see chapter 6 and 7, see Fig. 11.4. Due to the limited effect of Ekman pumping there is no heat transport enhancement for low Pr, see Fig. 11.5.

Fig. 11.6 shows that the volume averaged $Re_{z,rms}$ (dimensionless rms velocity

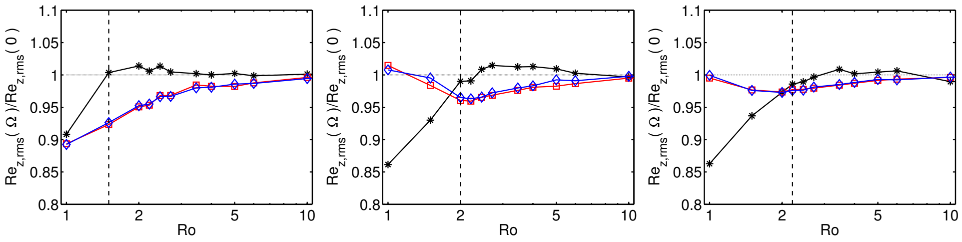

(a) (b) (c)

Figure 11.6: The normalized averaged rms vertical velocity fluctuations $Re_{z,rms}$ for $Ra = 4 \times 10^7$ and different Pr as function of Ro. The stars indicate the volume averaged value of $Re_{z,rms}$. The squares and diamonds indicate the horizontally averaged values of the $Re_{z,rms}$ at a distance $\lambda_\theta^{sl}(r)$ from the lower and upper plate, respectively. The vertical dashed lines again indicate the position where the LSC strength starts to decrease. a) $Pr = 0.7$, b) $Pr = 6.4$, c) $Pr = 20$.

of the axial velocity fluctuations), which is a measure for the strength of the LSC, decreases strongly for strong enough rotation. The vertical dashed lines in Fig. 11.6 indicate the position where $Re_{z,rms}(\Omega)/Re_{z,rms}(0)$ becomes smaller than 1, which we use to indicate the point at which the LSC strength starts to decrease. This value is determined by extrapolating the behaviour observed at low Ro numbers to reduce the effect of the uncertainty in single data points. In figure 8.3 we also used this method to indicate the position of the onset of the heat transfer enhancement in the high Ra number regime. However, for this lower Ra number we do not find any evidence for a sudden onset around this point, see Fig. 11.5 where the vertical lines are plotted at the same positions as in Fig. 11.6. In contrast to the decrease in the volume averaged value of $Re_{z,rms}$ the horizontally averaged value of $Re_{z,rms}$ at the edge of the thermal BL (thus at the distance $\lambda_\theta^{sl}(r)$ from either the top or bottom boundary) increases. This indicates that Ekman pumping, which is responsible for the increase in Nu, sets in and no sign of Ekman pumping prior to the decrease in LSC strength is found. Fig. 11.6 thus shows that the flow makes a transition between two different turbulent states, i.e. a transition from a LSC dominated regime to an Ekman pumping dominated regime as is discussed in detail in chapter 8 and 9. Fig. 11.6a shows no increase in the horizontally averaged value of $Re_{z,rms}$ at the edge of the thermal BL for $Pr = 0.7$, because the flow is suppressed for higher Ro, i.e. lower rotation rate, when Pr is lower, see also the discussion in chapter 7.

The Pr number dependence of the Nu number and the thickness of the thermal BL is shown in Fig. 11.7. From Fig. 11.7a we can conclude that hardly any Pr number dependence on the Nu number exists in the weak rotating regime ($Ro = 3$). However, a strong Pr number effect appears for stronger rotation rates, where Ekman pumping is the dominant effect (chapter 6). Fig. 11.7b shows that the effect of weak background rotation on the thermal BL thickness is largest for $Pr \approx 2$. The Pr number dependence of $Re_{z,rms}$ is shown in Fig. 11.8. The difference between the data points

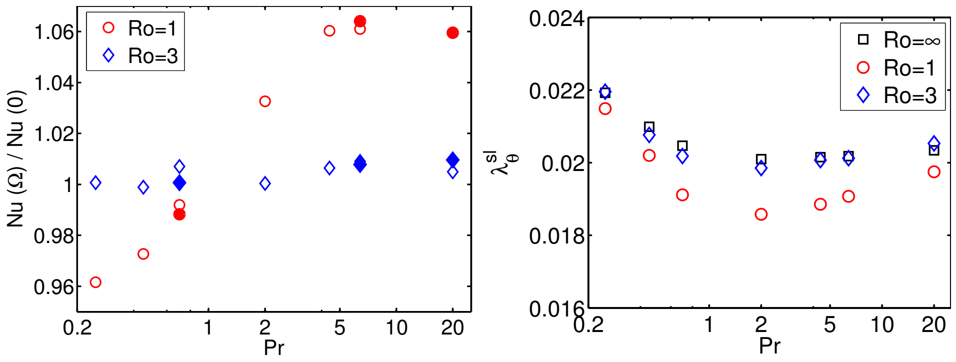

(a) (b)

Figure 11.7: a) Normalized heat transfer as a function of Pr number for $Ra = 4\times10^7$ and different Ro. The circles and diamonds indicate the data for $Ro = 1$, and $Ro = 3$, respectively. The open and filled symbols indicate the results obtained on the $257\times97\times193$ and the $193\times65\times129$ grid, respectively. b) Horizontally averaged thermal BL thickness λ_θ^{sl} as function of Pr. Symbols as in a) and squares for $Ro = \infty$.

obtained for the bottom and top BL in Fig. 11.8 indicate the uncertainty in the results. Increasing the averaging time, which we checked for $Pr = 2$ and $Pr = 4.4$, reduces the differences for the data points obtained for the bottom and top BL. Furthermore, we note that it is important to take the radial thermal BL dependence ($\lambda_\theta^{sl}(r)$) into account for lower Pr, where the radial BL dependence is strongest, and we excluded the region close to the sidewall ($0.45 < r < 0.5$) from the horizontal averaging in order to eliminate the effect of the sidewall.

The computation of the kinetic BL thickness can be either based on the position of the maximum rms value of the azimuthal velocity fluctuations, see Ref. [91] and chapter 8, or on the position of the maximum value of $\varepsilon_u'' := \mathbf{u}\cdot\nabla^2\mathbf{u}$, i.e. two times the height at which this quantity is highest, as shown in chapter 2. In chapter 4 we compared the result of this empirical method with theoretical results and show that it is indeed a suitable method to define the kinetic BL thickness. Here we first average ε_u'' horizontally in the range $0.05 \le r \le 0.45$ before we determine the position of the maximum. This r range has been taken to exclude the region close to the sidewall, where ε_u'' misrepresents the kinetic BL thickness due to the rising plumes, and the region close to the cylinder axis, since there it is numerically very difficult to reliably calculate ε_u'', due to the singularity in the coordinate system. When the radially dependent kinetic BL thickness ($\lambda_u^{\varepsilon_u''}(r)$) is horizontally averaged a small difference, depending on the averaging time, is observed between the bottom and top because of the specific orientation of the LSC. We note that the same quantity ε_u'' is used in chapter 2, where it is shown that the kinetic BL thickness based on ε_u'' represents the BL thickness better than the one considering the maximum rms

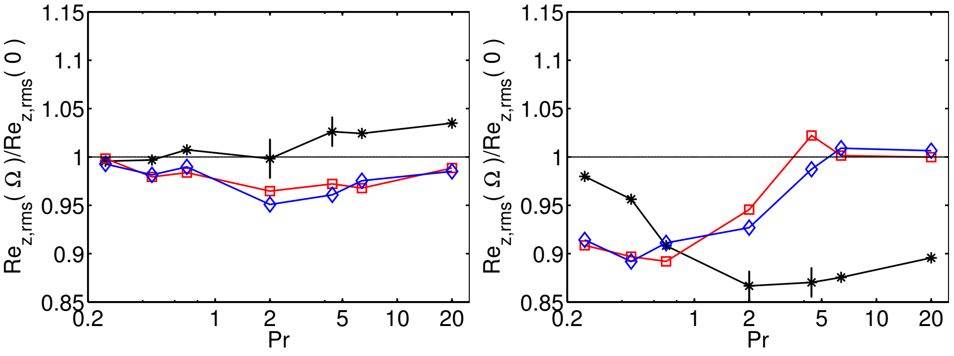

(a) (b)

Figure 11.8: The normalized averaged rms vertical velocity fluctuations $Re_{z,rms}$ for $Ra = 4 \times 10^7$ and different Ro as function of Pr. The stars indicate the volume averaged value of $Re_{z,rms}$. The vertical error bars at $Pr = 2$ and $Pr = 4.4$ indicate the difference in the volume averaged value obtained after 1200 dimensionless time units (data point) and 400 dimensionless time units. The squares and the diamonds indicate the horizontally averaged $Re_{z,rms}$ at a distance $\lambda_\theta^{sl}(r)$ from the lower and upper plate, respectively. a) $Ro = 3$, b) $Ro = 1$.

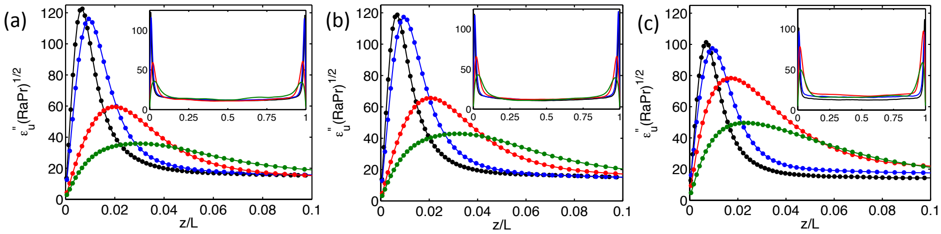

Figure 11.9: Azimuthally averaged profile of $\varepsilon_u''(RaPr)^{1/2}$ for $Ra = 4 \times 10^7$ and different Pr and Ro at the radial position $r = 0.25L$. The figures, from left to right, are for $Ro = \infty$, $Ro = 3$, and $Ro = 1$. Black, blue, red, and green indicate the profiles for $Pr = 0.25$, $Pr = 0.7$, $Pr = 6.4$, and $Pr = 20$, respectively. The dots indicate the data points obtained from the simulations. The insets shows the profile over the whole domain.

velocity fluctuations, which is normally used in the literature. The volume averaged value of ε_u'' is the same as the volume averaged kinetic energy dissipation rate ε_u (although it differs locally), which can be derived using Gauss's theorem [20]. Fig. 11.9 shows the azimuthally averaged profiles for $\varepsilon_u''(RaPr)^{1/2}$ at $r = 0.25L$. The normalization factor $(RaPr)^{1/2}$ is used to get Nu number values for all profiles, see Ref. [109]. In Fig. 11.10 the kinetic BL thickness based on the position of the maximum kinetic dissipation rate is shown as function of Ro and Pr. To compare the relative changes in the kinetic BL thicknesses the values are normalized by values for the non-rotating case. For all Pr numbers there is a change in the BL behaviour at the point where the LSC decreases in strength (vertical dashed lines in Fig. 11.10a).

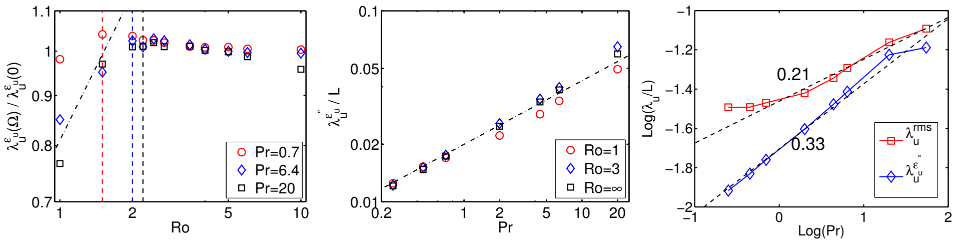

(a) (b) (c)

Figure 11.10: a) The thickness of the kinetic BL, average of bottom and top BL, based on the position of the maximum value of ε_u'' for $Ra = 4 \times 10^7$ and different Pr. The circles, diamonds, and squares are the data for $Pr = 0.7$, $Pr = 6.4$, and $Pr = 20$, respectively. The dash-dotted line indicates $Ro^{1/2}$ scaling. The vertical dashed lines (from left to right for $Pr = 0.7$, $Pr = 6.4$ and $Pr = 20$) represent the point at which the LSC strength starts to decrease. b) As in a), but now for different Ro. The circles, diamonds, and squares are the data for $Ro = 1$, $Ro = 3$, and $Ro = \infty$, respectively. The dash-dotted line indicates $Pr^{1/3}$ scaling. c) The kinetic BL thickness based on the position of the maximum value of ε_u'' and based on the position of the maximum rms velocity fluctuations are indicated by diamonds and squares, respectively.

We see no clear change in the thickness of the kinetic BL thickness before the onset. This could be caused by the method we use to define the kinetic BL thickness, i.e. the data close to the sidewall and the cylinder axis were excluded since the method based on the maximum position of ε_u'' misrepresents the kinetic BL thickness in these regions.

Figure 11.10c shows that when the kinetic BL thickness is based on the position of the maximum value of ε_u'' its thickness increases with $Pr^{1/3}$, which is in agreement with the GL model. Namely, since $\lambda_u = aH/\sqrt{Re}$ and the simulations are mostly in regime II_u where $Re \sim Pr^{-2/3}$ this gives a scaling of $Pr^{1/3}$ scaling for the kinetic BL thickness. In non-rotating measurements in a cylindrical geometry Lam et al. [195] used the position of the maximum velocity to determine the kinetic BL thickness and they found the exponent to be 0.24 over a wide range of Pr. When we base the kinetic BL thickness on the position of the maximum rms velocity fluctuations, which is closely related to the position of the maximum velocity, we get an exponent of 0.21, see figure 11.10c. This is in excellent agreement with the experimental measurements, since the higher Pr numbers used in the experiments go more towards regimes I_u and IV_u of the GL theory than the numerical data and in these regimes a slightly higher exponent is expected.

We conclude this section with a brief summary of the results obtained for the high Ra number regime presented in chapters 6-9. For $Ra \gtrsim 1 \times 10^8$ a sudden onset at $Ro = Ro_c$ in the heat transport enhancement occurs, see Fig. 11.2b, where we find a smooth transition at lower Ra, see Fig. 11.2a. Fig. 11.11a shows the volume averaged ratio $Re_{z,rms}(\Omega)/Re_{z,rms}(0)$. The behaviour is similar to the one observed at lower Ra,

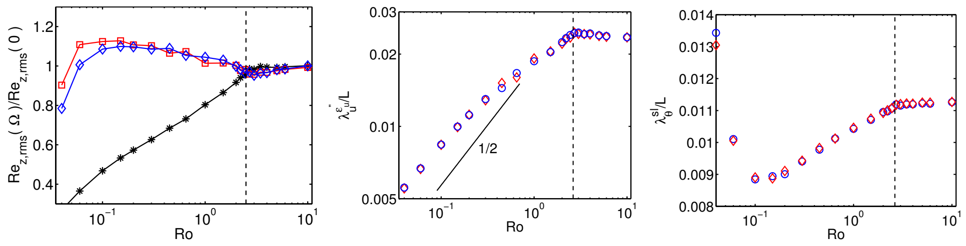

(a) (b) (c)

Figure 11.11: a) The averaged rms vertical velocities $Re_{z,rms}$ as function of Ro. The stars indicate the volume averaged value of $Re_{z,rms}$. The squares and diamonds, respectively, indicate the horizontally averaged $Re_{z,rms}$ at the distance $\lambda_\theta^{sl}(r)$ from the bottom and top plate. b) The thickness of the kinetic top and bottom BLs based on the position of the maximum $\varepsilon_u^{''}$, diamonds (circles) for top (bottom) BL. The vertical dashed lines in panel a and b indicate the position of Ro_c. Here the BL behaviour changes from Prandtl-Blasius (right) to Ekman (left) (chapter 8). c) The circles (diamonds) indicate λ_θ^{sl} for the bottom (top) plate.

see Fig. 11.6. For the high Ra number regime the onset at Ro_c is defined as the point where the ratio $Re_{z,rms}(\Omega)/Re_{z,rms}(0)$ becomes smaller than 1. For the low Ra number this point indicates the position where the LSC strength starts to decrease and just as for the relatively low Ra number regime, Ekman pumping in the high Ra number regime is indicated by an increase of the horizontally averaged $Re_{z,rms}$ value at the edge of the thermal BL. Although the two cases, i.e. the relatively low Ra number regime and the high Ra number regime both, show a transition between two different turbulent states the important difference between the two is that the transition is sharp in the high Ra number regime and smooth in the relatively low Ra number regime. The onset in the high Ra number regime is also observed in the behaviour of the BLs. Fig. 11.11b shows that the kinetic BL thickness does not change below onset ($Ro > Ro_c$) and above onset the BL behaviour is dominated by rotational effects and thus Ekman scaling (proportional to $Ro^{1/2}$) is observed. This scaling factor is also found in the laminar BL theory, which will be discussed in the next section. Finally, fig. 11.11c shows the thermal BL thickness λ_θ^{sl}.

11.3 Boundary layer theory for weak background rotation

In the previous section we observed that there is a smooth increase in the heat transfer as function of the Ro number when the Ra number is relatively low. In this section we set out to account for the increase in the heat transfer as function of the rotation rate within a model, which extends the ideas of the GL-theory to the rotating case. In the GL theory the Prandtl-Blasius BL theory for laminar flow over an infinitely large plate was employed in order to estimate the thicknesses of the kinetic and thermal BLs, and the kinetic and thermal dissipation rates. These results were then connected with the *Ra* and *Pr* number dependence of the Nusselt number. In perfect analogy, in the present chapter we apply laminar BL theory for the flow over an infinitely large rotating plate to study the effect of rotation on the scaling laws. We stress that employing the results of laminar BL theory over an infinite rotating disk to the rotating RB case in a closed cylinder is fully analogous to employing Prandtl-Blasius BL theory for flow over an infinite plate to the standard RB case without rotation, where the method was very successful [20, 25–28].

In both cases the equations used to derive the scaling laws are time independent and therefore the resulting solutions are associated with laminar flow. However, evidently, high Rayleigh number thermal convection is time dependent. Therefore one wonders whether the derived scaling laws still hold for time-dependent flow over an infinite rotating disk. We will show that the *Ro* and *Pr* scaling that is derived is not changed when temporal changes are included. This is again in perfect analogy to the Prandtl-Blasius BL case where the scaling laws also hold for time dependent flow provided that the viscous BL does not break down [28]. Indeed, recent experiments [33, 34] and numerical simulations presented in chapter 13 have shown that in non-rotating RB the BLs scaling wise behave as in laminar flow and therefore we feel confident to assume the same for the weakly rotating case. The basic idea of the model we introduce is to combine the effect of the LSC roll, which is implemented in the GL theory by the use of laminar Prandtl-Blasius BL theory over an infinitely large plate, and the influence of the rotation on the thermal BL.

The system we are analyzing to study the influence of rotation on the thermal BL thickness above a heated plate is schematically shown in Fig. 11.12a. It is the laminar flow of fluid over an infinite rotating disk. The disk rotates with an angular velocity Ω_D and the fluid at infinity with angular velocity $\Omega_F = s\Omega_D$, with $s < 1$. Fig. 11.12b shows that a positive radial velocity is created due to the action of the centrifugal force. Because of continuity there is a negative axial velocity, i.e. fluid is flowing towards the disk. The system has been analyzed before in the literature, e.g. Refs. [29, 30, 196–198]. Here we will briefly summarize the procedure.

The system is analyzed by using the Navier-Stokes equations in cylindrical coordinates and assuming a steady stationary, axial symmetric solution. To reduce the Navier-Stokes equations to a set of ordinary differential equations (ODE) we employ self-similarity. The first step is to determine the dimensionless height in the system just as in the Prandtl-Blasius approach, in which the BL thickness scales as [24] $\delta \sim \sqrt{\nu x/U}$. For the case of a large rotating disk in a fluid rotating around an axis perpendicular to the disk, the thickness of the BL can be estimated by replacing U by $\Omega_D x$ [24]. The thickness then scales as $\delta \sim \sqrt{\nu/\Omega_D}$. The similarity variable in the system is the dimensionless height

$$\zeta = z\sqrt{\frac{\Omega_D}{\nu}}. \qquad (11.1)$$

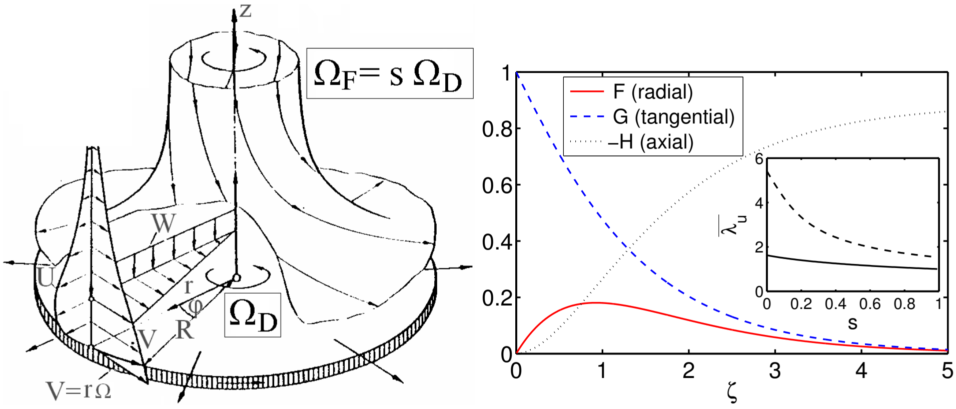

(a) (b)

Figure 11.12: a) Flow near a disk rotating with an angular velocity Ω_D when the fluid at infinity is rotating with $\Omega_F = s\Omega_D$. Adapted from [30]. b) Velocity components in the von Kármán case: inset shows $\overline{\lambda}_u^{sl}$ (solid line) and $\overline{\lambda}_u^{99\%}$ (dashed line).

According to von Kármán, the following self-similarity ansatz for the velocity components and the pressure can be taken [29, 30, 196–198]

$$u = r\Omega_D F(\zeta), \tag{11.2}$$

$$v = r\Omega_D G(\zeta), \tag{11.3}$$

$$w = \sqrt{\nu\Omega_D} H(\zeta), \tag{11.4}$$

$$p = \rho\nu\Omega_D P(\zeta) + \frac{1}{2}\rho s^2 \Omega_D^2 r^2. \tag{11.5}$$

After substitution into the Navier-Stokes equations one obtains a system of four coupled ODEs,

$$F^2 + F^{'}H - G^2 - F^{''} + s^2 = 0, \tag{11.6}$$

$$2FG + HG^{'} - G^{''} = 0, \tag{11.7}$$

$$P^{'} + HH^{'} - H^{''} = 0, \tag{11.8}$$

$$2F + H^{'} = 0, \tag{11.9}$$

where the prime indicates differentiation with respect to ζ. This set of ODEs must be supplemented by the boundary conditions

$$u = 0, \quad v = r\Omega_D \quad , \quad w = 0 \qquad \text{for } z = 0, \tag{11.10}$$

$$u = 0, \quad v = sr\Omega_D \qquad \text{for } z = \infty. \tag{11.11}$$

When substituting the self similarity ansatz (11.2) - (11.5) into these boundary conditions one obtains

$$F = 0, \quad G = 1 \quad , \quad H = 0 \qquad \text{for } \zeta = 0, \tag{11.12}$$

$$F = 0, \quad G = s \qquad \text{for } \zeta = \infty. \tag{11.13}$$

Note that the boundary condition at infinity together with the continuity equation (11.9) gives $H^{'}(\zeta \to \infty) = 0$. One can further simplify the set of ODEs by realizing that the ODE for the pressure (11.8) is decoupled from the ODEs determining the velocity profiles by using the continuity equation (11.9) in (11.8) and subsequently integrating this relation. The velocity profiles, for the von Kármán case ($s = 0$), are shown in Fig. 11.12b. The inset shows that the dimensionless kinetic BL thickness $\overline{\lambda}_u \equiv \lambda_u/\delta$ decreases with increasing relative rotation rate s of the fluid at infinity. This is due to the decreasing effect of the centrifugal force. We determined $\overline{\lambda}_u^{99\%}$, the dimensionless kinetic BL thickness at which the velocity has achieved 99% of the outer flow velocity, using the tangential velocity profile, i.e. when $G(\zeta) = s + 0.01(1-s)$. Additionally, we calculated $\overline{\lambda}_u^{sl}$, the dimensionless kinetic BL thickness based on the slope of the tangential velocity at the disk. The scaling of the kinetic BL predicted by the above rotating BL theory, i.e. $Ro^{1/2}$, is the classical Ekman scaling. In the simulations of rotating RB we find the same scaling of the kinetic BL once the flow is dominated by rotational effect, i.e. $Ro \lesssim Ro_c$, see Fig. 11.11b.

The GL theory heavily builds on laminar Prandtl-Blasius BL theory, which describes the laminar flow over an infinite plate. In the Prandtl-Blasius theory the temperature field is assumed to be passive to derive the Pr number scaling. As we want to extend the GL theory to the rotating case we keep this analysis analogous to the Prandtl-Blasius theory. Therefore, we assume the temperature field to be passive in order to derive the scaling laws as function of the Pr number. We non-dimensionalize the temperature by

$$\widetilde{\theta}(\zeta) = \frac{\theta - \theta_\infty}{\theta_b - \theta_\infty}, \tag{11.14}$$

where θ_b is the temperature of the bottom disk, and $\theta_\infty < \theta_b$ is the ambient temperature. Then one obtains the following ODE describing the temperature field [199–201]

$$\widetilde{\theta}'' = PrH(\zeta)\widetilde{\theta}', \tag{11.15}$$

where the prime indicates a differentiation with respect to ζ. The boundary conditions are

$$\widetilde{\theta} = 1 \quad \text{for} \quad \zeta = 0, \tag{11.16}$$

$$\widetilde{\theta} = 0 \quad \text{for} \quad \zeta = \infty. \tag{11.17}$$

The resulting system of ODEs subjected to the boundary conditions, is solved numerically with a fourth order Runge-Kutta method using a Newton-Raphson root finding method to find the initial conditions. One can take the analytic solution for the Ekman case ($s \approx 1$), see appendix C, or the known solution for the Bödewadt case, see for example [30, 196], as one of the starting cases to determine the solutions over the whole parameter range in s and Pr.

In this way we obtain the full temperature profile for all s and Pr. For the heat transfer the most relevant quantity is the thermal BL thickness λ_θ, which we non-dimensionalized by δ, thus $\overline{\lambda}_\theta \equiv \lambda_\theta/\delta$. One can distinguish between $\overline{\lambda}_\theta^{sl}$ and $\overline{\lambda}_\theta^{99\%}$, the dimensionless BL thickness based on the 99% criterion, thus when $\widetilde{\theta}(\zeta) = 0.01$. Fig. 11.13a shows that the asymptotic scaling of $\overline{\lambda}_\theta^{99\%}$ and $\overline{\lambda}_\theta^{sl}$ is the same. Furthermore, the figure shows that rotation does not influence the scaling of the thermal BL thickness in the high Pr regime, because the same scaling, namely proportional to $Pr^{-1/3}$, is found as for the Prandtl-Blasius case. However, the rotation does influence the scaling in the low Pr regime, where now $\overline{\lambda}_\theta \propto Pr^{-1}$ instead of $\overline{\lambda}_\theta \propto Pr^{-1/2}$ as found in the Prandtl-Blasius case. Notice that $\overline{\lambda}_\theta^{99\%} > \overline{\lambda}_\theta^{sl}$, which is due to the decreasing temperature gradient with increasing height. Note that the thermal BL thickness as given in figure 11.13a does not directly represent the heat transfer in rotating RB convection. For weakly rotating RB convection one should account for the effect of the LSC, which we will discuss in detail in the next section. And for strongly rotating RB convection the relation $Nu = L/(2\lambda_\theta)$ no longer holds, as part of the mean temperature drop is across the bulk, see Fig 11.4. This temperature gradient in the bulk is affected by the leaking of plumes out of the Ekman vortices, see chapter 6.

In Fig. 11.13b we show the effective power-law exponent $\gamma = (d \log \overline{\lambda}_\theta)/(d \log Pr)$ of an assumed effective power law $\overline{\lambda}_\theta \sim Pr^\gamma$. It confirms that the effective scaling in the high Pr regime is the same for the Prandtl-Blasius (no rotation) and the von Kármán case ($s = 0$), but already at $Pr = 1$ a significant difference is observed.

The temperature advection equation (11.15) directly suggests the following relation between the scaling of the thermal BL thickness $\overline{\lambda}_\theta^{sl}$ and the scaling of the axial velocity at the edge of the thermal BL, $H_{BL} \sim 1/Pr\overline{\lambda}_\theta^{sl}$. This immediately implies for the low Pr regime, with $\overline{\lambda}_\theta^{sl} \sim Pr^{-1}$, that H_{BL} is independent of Pr. For the high Pr regime, with $\overline{\lambda}_\theta^{sl} \sim Pr^{-1/3}$, it gives $H_{BL}(Pr) \sim Pr^{-2/3}$. The scaling of the thermal BL thickness in the low Pr regime can be understood on physical grounds. In this regime $\overline{\lambda}_\theta \gg \overline{\lambda}_u$ and, the kinetic BL is fully submerged in the thermal BL. The axial velocity at the edge of the kinetic BL (11.13) is $H_{BL} = H(\zeta \to \infty)$, as can be shown by applying mass conservation expressed by Eq. (11.9). As a consequence, in the low Pr regime the axial velocity is constant in almost the whole thermal BL. Then Eq. (11.15) can trivially be integrated and immediately gives $\overline{\lambda}_\theta^{sl} \sim Pr^{-1}$. This derivation

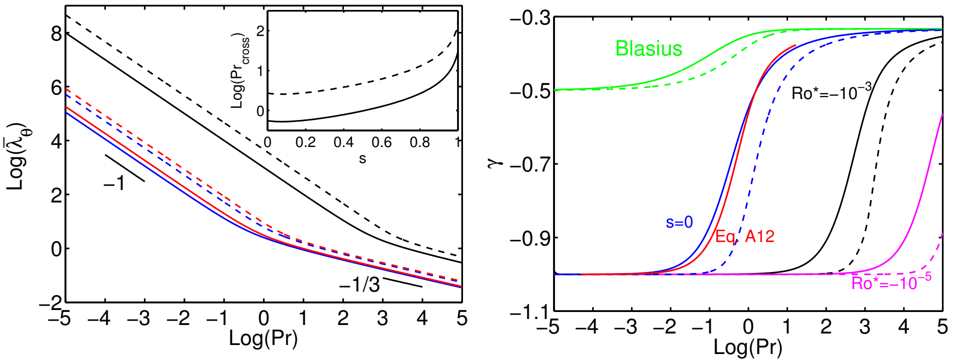

(a) (b)

Figure 11.13: a) The thermal BL thickness $\overline{\lambda}_\theta \equiv \lambda_\theta/\delta$ as function of Pr. The solid lines from bottom to top indicate $\overline{\lambda}_\theta^{sl}$ for the von Kármán case ($s = 0$), for $s = 0.5$, and for the Ekman case ($s \approx 1, Ro^* = 10^{-3}$, see definition Eq. (C.2) in appendix C), respectively. The dashed lines from bottom to top indicate $\overline{\lambda}_\theta^{99\%}$ for $s = 0$, $s = 0.5$, and $s \approx 1, Ro^* = 10^{-3}$, respectively. Note that the scaling for the thermal BL thickness goes asymptotically to $Pr^{-1/3}$ in the high Pr regime and to Pr^{-1} in the low Pr regime. The inset shows Pr_{cross}, the transition between the high and the low Pr regime as function of s based on the behaviour $\overline{\lambda}_\theta^{sl}$ (solid line) and $\lambda_\theta^{99\%}$ (dashed line). Note that the low Pr regime is more favored for higher s. b) The solid lines indicate the effective scaling γ in $\overline{\lambda}_\theta \sim Pr^\gamma$ as function of Pr for $\overline{\lambda}_\theta^{sl}$ for the Blasius case (no rotation), the von Karman case ($s = 0$), and the Ekman case ($s \approx 1$) for two Rossby numbers. The corresponding dashed lines indicate the effective scaling for $\overline{\lambda}_\theta^{99\%}$. Also the analytic prediction, see Eq. (C.12) in appendix C, for the von Kármán case is indicated in the figure.

is valid for all s, i.e. the scaling in the low Pr regime does not depend on the rotation of the fluid at infinity. The scaling in the high Pr regime is also independent of the rotation of the fluid at infinity. In the Ekman case $s \approx 1$, see appendix C, this $1/3$ scaling regime shifts towards very large Pr.

The equations (11.6)-(11.9) are time independent and therefore the resulting solutions are understood to describe laminar flow. Temporal changes can be included by adding $\partial_{\tilde{t}}\tilde{u}_\theta$, $\partial_{\tilde{t}}\tilde{u}_r$, and $\partial_{\tilde{t}}\tilde{u}_z$ where $\tilde{t} = t\Omega_D$ without changing the Ro and Pr scaling discussed above, i.e. the derived scaling laws above still hold for time dependent flow provided that the viscous BL does not break down. This is in perfect analogy to the Prandtl-Blasius BL case where the scaling laws also hold for time dependent flow [28]. Recently Zhou and Xia [34] have developed a method of expressing velocity profiles in the time-dependent BL frame and found that the re-scaled profiles agree perfectly with the theoretical Prandtl-Blasius profile. This method could possibly reveal the effect of weak rotation on the BL profiles. However, since the LSC orientation is not known a priori in three-dimensional RB convection it is impossible to sample the BL statistics at the position of the LSC without slightly tilting the sample. Since only very small differences between the BL statistics for non-rotating and weakly rotating RB ($Ro \gtrsim 2$) are observed the effect of tilting could significantly influence this comparison. Therefore such an analysis is beyond the scope of this thesis.

To investigate the crossover between the high and the low Pr regime we define Pr_{cross} as the crossover point. Pr_{cross} is calculated by determining the intersection between the asymptotic behaviour of the high and the low Pr regime. To calculate Pr_{cross} we considered $\overline{\lambda}_{\theta}^{sl}(Pr)$ and $\overline{\lambda}_{\theta}^{99\%}(Pr)$. The inset of Fig. 11.13a shows that the low Pr regime becomes more favored when the rotation of the fluid at infinity becomes stronger. Then the kinetic BL thickness becomes thinner and the axial velocity decreases, i.e. the thermal BL thickness increases. Because the thermal BL thickness decreases with increasing Pr the crossover shifts towards higher Pr as is shown in the inset of Fig. 11.13a. This effect is visible in rotating RB as shown in figure 7.5. Here it is shown that for the non-rotating case $\lambda_u < \lambda_{\theta}^{sl}$ when $Pr \lesssim 1$. When the rotation rate is increased, i.e. Ro is lowered, this transition shifts towards higher Pr and for $Ro = 0.1$ $\lambda_u < \lambda_{\theta}^{sl}$ when $Pr \lesssim 9$.

In summary, the laminar rotating BL theory explains the $Ro^{1/2}$ scaling of the kinetic BL thickness in rotating RB convection and the shift of the position where $\lambda_u = \lambda_{\theta}$ towards higher Pr when the flow is dominated by rotational effects.

11.4 Model for smooth onset in rotating RB convection

In this section we will introduce a model in the spirit of the GL approach in order to describe the smooth increase in the heat transfer as a function of Ro that is observed for relatively low Ra and weak background rotation. Since the GL theory assumes smooth transitions between different turbulent states the model is limited to the relatively low Ra number regime, since a sharp onset as function of Ro is found for $Ra \gtrsim 1 \times 10^8$. Furthermore, we assume that then the LSC, a basic ingredient of the GL model, is still present. In this simple model we neglect the influence of Ekman pumping, because it is a local effect that is rather insignificant at weak background rotation. This is supported by the results in Fig. 11.6 and the results presented in chapter 8 and 9, where we find no evidence for Ekman pumping at weak background rotation. When strong rotation is applied Ekman pumping is the dominant effect and the validity regime of our model is thus restricted to weak background rotation. The basic idea of the model is to combine the effect of the LSC roll, which is implemented in the GL theory by the use of the laminar Prandtl-Blasius theory over an infinitely large plate, and the influence of rotation on the thermal BL.

Applying laminar BL theory requires that the viscous BL above the flat rotating plate does not brake down. This assumption will now be verified. The stability for the von Kármán flow has been studied theoretically and experimentally by Lingwood [202–204], showing that instability occurs at $Re \approx 510$ where Re is defined as

$Re = r\sqrt{\Omega/\nu}$ (with r the distance to the rotation axis). Lingwood also pointed out that other experimental studies show the same transition point within a very narrow Reynolds number range $Re = 513 \pm 15$, see [202] and references therein. More recent experiments show similar results [205, 206]. For the Ekman case the instability occurs at $Re \approx 200$, see [204]. For the case under consideration it can be shown that $Re \lesssim 55$ (with $r = 12.5$ cm, $\Omega \approx 0.20$ rad/s, and $\nu = 1 \times 10^6$ m^2/s), see chapter 6. It can safely be conjectured that laminar BL theory can be applied as the estimated Reynolds number is an order of magnitude smaller than the critical Reynolds number. For further discussion on the stability of the rotational flow we refer to the classic Refs. [1, 207].

We introduce $\lambda_{\theta R} = \overline{\lambda}_\theta^{sl}(Pr)\sqrt{\nu/\Omega}$, see $\overline{\lambda}_\theta^{sl}(Pr)$ in Fig. 11.13a, as the thermal BL thickness based on the background rotation and $\lambda_{\theta C}$ as the BL thickness based on the LSC roll. Furthermore, Γ is the diameter-to-height aspect ratio of the RB cell and we set the radial length $r = (\Gamma L)/2$. Note that this is analogous to the length L which is introduced in the GL theory for the length of the plate. Thus the Reynolds number based on the background rotation is

$$Re_R = \frac{\Omega L^2 \Gamma^2}{4\nu} \propto \frac{1}{Ro} \,. \tag{11.18}$$

To calculate $\lambda_{\theta R}$ we used $\nu = 1 \times 10^{-6} m^2/s$ (water) and $\Gamma = 1$ and we set $\lambda_{\theta R} = \lambda_{\theta C}$ at $Ro = \infty$. The strength of the LSC roll is taken constant and $\lambda_{\theta C}$ is known from $\lambda_{\theta C}/L = (2Nu)^{-1}$.

We model the increase of Nu as a crossover between a convection role dominated BL and a rotation dominated BL. Thus without rotation the BL thickness is determined by the LSC roll, i.e. $\lambda_\theta = \lambda_{\theta C}$, and when rotation becomes dominant the BL thickness is determined by the rotating BL thickness, i.e. $\lambda_\theta = \lambda_{\theta R}$. We now model the crossover between these two limiting cases as

$$\frac{\lambda_\theta}{L} = \frac{\sqrt{Re_R}\lambda_{\theta R} + \alpha^* \sqrt{Re_C}\lambda_{\theta C}}{(\sqrt{Re_R} + \alpha^* \sqrt{Re_C})L}. \tag{11.19}$$

Here the square root of Reynolds has been chosen since the dimensionless BL thicknesses scale with $1/\sqrt{Re}$. We rewrite the above equation in terms of Ro, using $Re_R \propto Re_C/Ro$,

$$\frac{\lambda_\theta}{L} = \frac{\frac{1}{\alpha\sqrt{Ro}}\lambda_{\theta R} + \lambda_{\theta_C}}{\left(\frac{1}{\alpha\sqrt{Ro}} + 1\right)L} \tag{11.20}$$

and we use the free parameter α to fit the model with the numerical data shown in Fig. 11.5. It can be concluded that the presented model, based on the approach of the GL theory, indeed reflects the increase of Nu (as compared to the case without rotation) observed at relatively low Ra number ($Ra = 4 \times 10^7$) when the LSC is still present. Furthermore, the thickness of the thermal BLs is also reflected correctly by the model. Note that the large value of the parameter $\alpha = 55$ indicates that the influence of the rotation is rather weak before Ekman pumping sets in and it also explains that for higher *Ra* ($Ra \gtrsim 1 \times 10^8$) no heat transfer enhancement is observed below onset. The sudden (instead of smooth) transition is then fully determined by the rotation rate where Ekman pumping sets in. This may be because at higher *Ra* the thermal BL is already much thinner due to the stronger LSC and therefore the effect of weak rotation is not sufficient to result in a significant thinner thermal BL. When $Ro < Ro_c$ the model cannot be used, since Ekman pumping is dominant in this regime which is responsible for the strong increase observed in *Nu* when $Ro < Ro_c$.

11.5 Conclusions

To summarize, we have studied the effect of rotation on the RB system at relatively low *Ra* number, i.e. $Ra = 4 \times 10^7$ by using DNS. We find a smooth increase of the heat transfer as function of the rotation rate when weak rotation is applied. To describe this heat transfer enhancement we have extended the GL theory to the rotating case by studying the influence of rotation on the scaling of the thermal BL thickness. It is based on a similar approach as in the laminar Prantl-Blasius BL theory over an infinitely large plate, as we analyzed the flow over an infinitely large rotating disk where the fluid at infinity is allowed to rotate. Just as in the Prantdl-Blasius BL theory we used a passive temperature field to calculate the characteristics of the thermal BL. It turns out that weak background rotation does not influence the scaling of the BL thickness in the high *Pr* regime, because again $Pr^{-1/3}$ scaling is found. However, rotation does influence the scaling in the low *Pr* regime where we find a scaling of Pr^{-1} instead of $Pr^{-1/2}$ found in the Prandtl-Blasius BL theory. With our model for the thermal BL thickness, see Eq. (11.20), we can explain the increased heat transfer observed in the relatively low *Ra* number regime before the strength of the LSC decreases. The model neglects the effect of Ekman pumping as this effect is rather insignificant before the strength of the LSC decreases, i.e. the regime to which the model is applied. This means that the model cannot predict the heat transfer enhancement that is observed at moderate rotation rates where Ekman pumping is the dominant mechanism. The contrast between the smooth onset at $Ra = 4 \times 10^7$ and the sharp onset at $Ra \gtrsim 1 \times 10^8$ is remarkable since only a small shift in the $Ra - Pr - Ro$ phase space is involved.

12

The role of Stewartson and Ekman boundary layers [*] [†]

When the classical RB system is rotated about its vertical axis roughly three regimes can be identified. In regime I (weak rotation) the large scale circulation (LSC) is the dominant feature of the flow. In regime II (moderate rotation) the LSC is replaced by vertically aligned vortices. Regime III (strong rotation) is characterized by suppression of the vertical velocity fluctuations. Using results from experiments and direct numerical simulations of RB convection for a cell with a diameter-to-height aspect ratio equal to one at $Ra \sim 10^8 - 10^9$ *(*$Pr = 4-6$*) and* $0 \lesssim 1/Ro \lesssim 25$ *we identified the characteristics of the azimuthal temperature profiles at the sidewall in the different regimes. In regime I the azimuthal wall temperature profile shows a cosine shape and a vertical temperature gradient due to plumes that travel with the LSC close to the sidewall. In regime II and III this cosine profile disappears, but the vertical wall temperature gradient is still observed. It turns out that the vertical wall temperature gradient in regimes II and III has a different origin than that observed in regime I. It is caused by boundary layer dynamics characteristic for rotating flows, which drives a secondary flow that transports hot fluid up the sidewall in the lower part of the container and cold fluid downwards along the sidewall in the top part.*

---

[*] Based on: R.P.J. Kunnen, R.J.A.M. Stevens, J. Overkamp, C.Sun, G.J.F. van Heijst, H.J.H. Clercx, The role of Stewartson and Ekman layers in turbulent rotating Rayleigh-Bénard convection, submitted to J. Fluid Mech. (2011).

[†] The experimental measurements discussed in this chapter are performed by J. Overkamp and the discussion presented in section 12.4 is based on the PhD thesis of R.P.J. Kunnen.

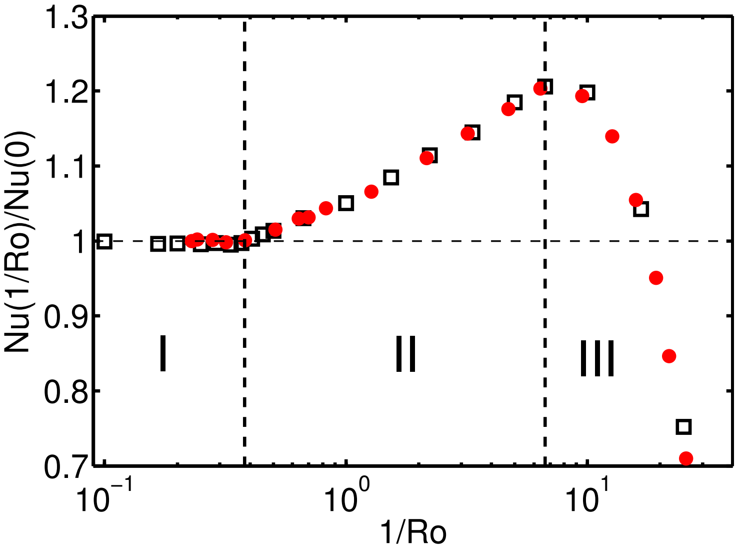

Figure 12.1: The scaled heat transfer $Nu(1/Ro)/Nu(0)$ as function of $1/Ro$ on a logarithmic scale. Experimental and numerical data for $Ra = 2.73 \times 10^8$ and $Pr = 6.26$ are indicated by red dots and open squares, respectively. Data taken from chapter 6 and 8 and are called run E2 in Zhong & Ahlers [80]. The transition between the different regimes, see text, is indicated by the vertical dashed lines.

12.1 Introduction

In figure 12.1 we show a typical measurement of the heat transport enhancement with respect to the non-rotating case as function of the rotation rate, see also chapters 6 and 8. The figure shows that, depending on the rotation rate, three different regimes can be identified. Regime I (weak rotation), where no heat transport enhancement is observed, regime II (moderate rotation), where a strong heat transport enhancement is found, and regime III (strong rotation), where the heat transport starts to decrease. We note that the division between regime I and regime II is obvious as there is a bifurcation as is discussed in chapter 8 and 9. Furthermore, we note that the log plot in figure 12.1 makes the transition from regime II to regime III look more sudden than it actually is. Flow visualization experiments [91, 93] and the analysis of the flow structures obtained in numerical simulations, see Kunnen et al. [91] and chapter 8, have confirmed that this division of regimes coincides with changes observed in the flow patterns and flow characteristics.

In regime I ($1/Ro \lesssim 0.5$) the large scale circulation (LSC), typical for non-rotating RB convection, is still present, because the Coriolis force is too weak to overcome the buoyancy force that causes the LSC. In chapter 8 and 9 we showed that there is a sharp transition to the regime where rotational effects become important, while at the same time the strength of the LSC is decreasing [75]. Zhong & Ahlers [80] experimentally found that the time-averaged LSC amplitudes decrease strongly at the transition from regime I to regime II, see figure 13 of their paper. In regime II ($0.5 \lesssim 1/Ro \lesssim 6.67$) the LSC is replaced by predominantly vertically oriented vortical columns as the dominant flow structures and a large increase in the heat transport is observed. When the rotation rate is increased further a large decrease in the heat transport is observed, because the vertical velocity fluctuations are suppressed due to the rotation [91, 97]. We will call this regime III.

In this chapter we address the question of how these different regimes can be identified from measurements of the azimuthal wall temperature distribution and the vertical temperature gradient along the sidewall, with probes that are embedded in the sidewall of a RB convection cell. This method of sidewall temperature measurements has been introduced by Brown et al. [148] and a validation of this method is described in the second paragraph of Section 2 of the paper by Brown & Ahlers [98]. Recently, Zhong & Ahlers [80] have extensively studied the properties of the LSC in rotating RB convection in aspect ratio $\Gamma = 1$ experiments using this method. These measurements covered the Ra number range $3 \times 10^8 \lesssim Ra \lesssim 2 \times 10^{10}$, the Pr number range $3.0 \lesssim Pr \lesssim 6.4$, and the $1/Ro$ number range $0 \lesssim 1/Ro \lesssim 20$. In these measurements detailed statistics about the thermal LSC amplitude (i.e. the amplitude of the cosine fit to the azimuthal temperature profile at the sidewall), the LSC orientation over time, the temperature gradient along the sidewall, the retrograde rotation of the LSC, the frequency of cessations, etc., over this wide parameter range were determined.

In this chapter is organized as follows. In section 12.2 we will present some experimental results on the properties of the azimuthal temperature profiles, which were obtained with the Eindhoven RB setup discussed in section 10.2. For a much more detailed set of experimental results on the properties of the azimuthal temperature profiles we refer to the paper of Zhong & Ahlers [80]. In section 12.3 we compare the experimental data with the azimuthal temperature and vertical-velocity profiles close to the sidewall found in direct numerical simulations (DNS). In order to explain the sidewall temperature measurements we study the azimuthally averaged flow profiles obtained from DNS. The analysis presented in section 12.4 reveals that the sidewall temperature measurements, particularly the presence of the vertical wall temperature gradients in regimes II and III [80], can be explained by the presence of Stewartson layers that are formed along the sidewall.

12.2 Experimental sidewall measurements

In RB experiments it is common to determine the flow properties by analyzing the azimuthal wall temperature profile obtained by thermistors that are embedded in the sidewall [20] and in our setup we do the same. Following section 5.6 we define the relative LSC strength at midheight ($\bar{S}_m$), based on the energy in the different modes of the azimuthal temperature profile, as

$$\bar{S}_m = \text{Max}\left(\left(\frac{\sum_{t_b}^{t_e} E_1}{\sum_{t_b}^{t_e} E_{tot}} - \frac{1}{N}\right) / \left(1 - \frac{1}{N}\right), 0\right). \tag{12.1}$$

Here $\sum_{t_b}^{t_e} E_1$ indicates the sum of the energy in the first Fourier mode over time, i.e. from the beginning of the simulation $t = t_b$ to the end of the simulation $t = t_e$, $\sum_{t_b}^{t_e} E_{tot}$ the sum of the total energy in all Fourier modes over time, and N the total number of Fourier modes that can be determined. The relative LSC strength $\bar{S}_m$ always has a value between 0 and 1; here 1 indicates that the azimuthal profile is a pure cosine profile, which is a signature of the LSC according to Brown & Ahlers [98], and 0 indicates that the magnitude of the cosine mode is equal to (or weaker than) the value expected from a random noise signal. Hence $\bar{S}_m \gg 0.5$ indicates that a cosine fit on average is a reasonable approximation of the data, as then most energy in the signal resides in the first Fourier mode. In contrast, $\bar{S}_m \ll 0.5$ indicates that most energy resides in the higher Fourier modes. Hence, we consider the LSC as dominant once $\bar{S}_m \gg 0.5$ at midheight. A small value of $\bar{S}_m$ indicates that no single LSC is found, implying the existence of either multiple rolls or, in the case of rotating Rayleigh-Bénard convection, vertically aligned vortices.

Figure 12.2a shows the magnitude of the different Fourier modes of the azimuthal wall temperature profile for the experiments at $Ra = 1.16 \times 10^9$ with $Pr = 4.38$ based on the data of eight equally spaced thermistors placed inside the sidewall (located at $z = 0.5L$). The corresponding relative LSC strength is given in panel b. The figure clearly shows that the relative LSC strength is large in regime I, which indicates the presence of a LSC. However, for higher rotation rates, i.e. regime II, the relative LSC strength decreases because vertically aligned vortices become the dominant feature of the flow. For this flow one expects a random azimuthal temperature profile at midheight, which is confirmed by the low relative LSC strength S_m in regime II and III, see figure 12.2b.

Extensive sidewall temperature gradient measurements for non-rotating RB convection were done by Brown & Ahlers [156] and for rotating RB convection by Zhong & Ahlers [80], see their figures 10 and 11. When the LSC is the dominant feature of the flow the vertical temperature gradient at the sidewall is mainly due to plumes that travel close to the sidewall with the LSC. Thus one would expect that the temperature gradient along the sidewall should decrease in regime II as the LSC disappears there. However figure 10 of Zhong & Ahlers [80] shows that the temperature gradient along the sidewall even increases in regime II and III. This nonzero temperature gradient along the sidewall in regime II and III is caused by the secondary flow that will be discussed in section 12.4.

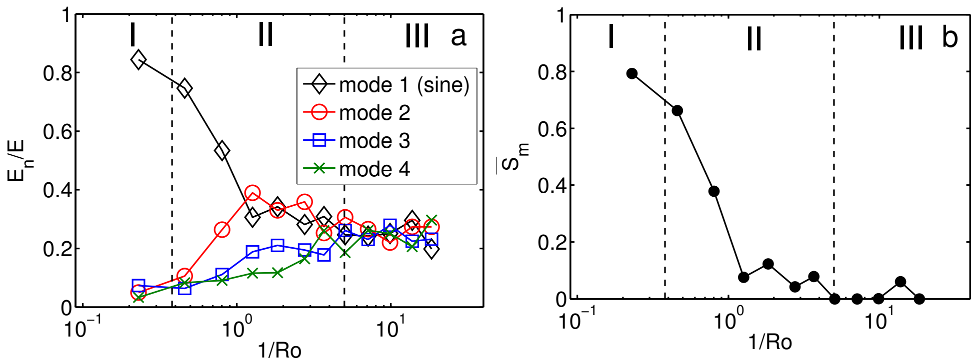

Figure 12.2: Experimental results on the magnitude of the different Fourier modes and S_m for $Ra = 1.16 \times 10^9$ and $Pr = 4.38$ based on the data of 8 azimuthally equally spaced probes at $z = 0.50L$. a) The energy in the different Fourier modes of the azimuthal wall temperature profile normalized by the energy present in all Fourier modes as function of $1/Ro$. b) The corresponding relative LSC strength S_m. The two dashed vertical lines in both panels indicate the transitions between regimes I and II, and between II and III, respectively.

12.3 Numerical sidewall measurements

In order to verify the experimental results we analyze the data of DNS simulations of rotating RB convection performed at varying Ro-values for $Ra = 2.73 \times 10^8$ and $Pr = 6.26$ (see details in chapter 6) and for $Ra = 1.00 \times 10^9$ and $Pr = 6.4$ (see details in Kunnen et al. [91]). In the simulations we solved the three-dimensional Navier-Stokes equations within the Boussinesq approximation in a cylindrical cell with $\Gamma = 1$ with no-slip boundary conditions at all walls, a uniform temperature at the horizontal plates, and an adiabatic sidewall. For further details about the numerical code we refer to Refs. [107, 109, 124]. In all simulations we calculate the azimuthal averages of the three velocity components and the temperature. Furthermore, in the simulations at $Ra = 2.73 \times 10^8$ we placed 32 azimuthally equally spaced numerical probes that provide simultaneous point-wise measurements of the temperature and the three velocity components u_r, u_ϕ, u_z in the radial, azimuthal, and vertical directions r, ϕ and z, respectively, at the heights $0.25L$, $0.50L$, and $0.75L$ and a distances $0.45L$ from the cylinder axis. The azimuthal temperature and vertical-velocity profiles measured by the probes are analyzed in the same way as the experimental data.

Figure 12.3 shows the magnitude of the different Fourier modes of the azimuthal vertical-velocity profiles for $Ra = 2.73 \times 10^8$ and $Pr = 6.26$ based on the data of 8, 16, and 32 equally spaced probes. The result in panel (a) agrees well with the result obtained by Kunnen et al. [75]. Furthermore, a comparison of the relative energy in the different Fourier modes based on the data of 8, 16, and 32 probes, see figure 12.3, reveals that 8 probes are insufficient to capture all flow characteristics. Since the results based on the data of 16 and 32 probes are very similar, we assume that 16

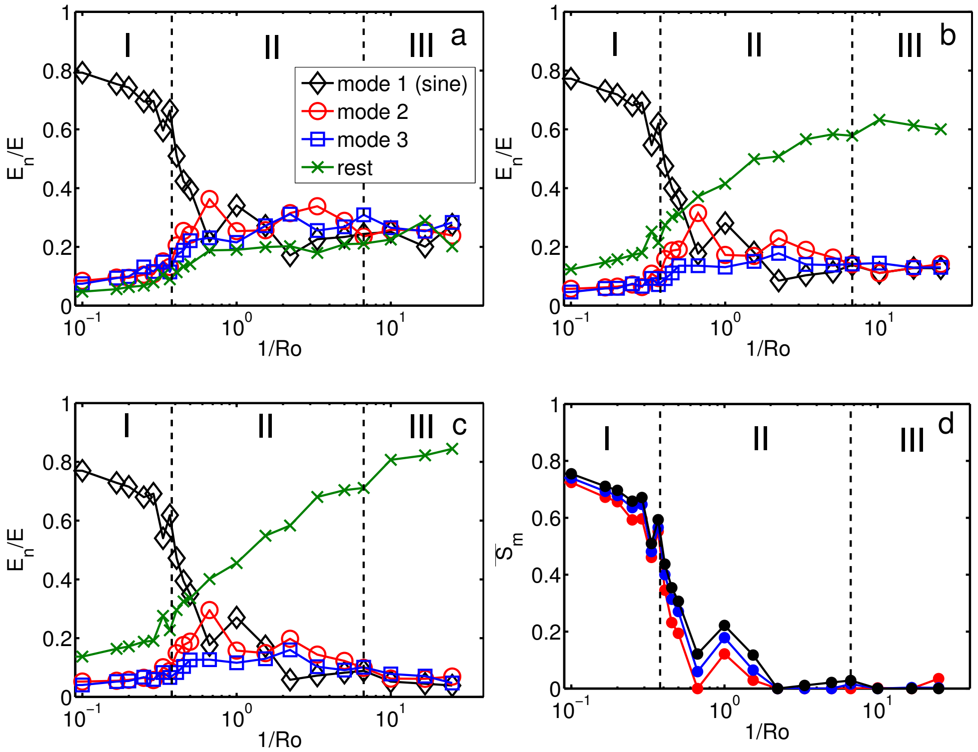

Figure 12.3: Results from DNS on the magnitude of the different Fourier modes and S_m for $Ra = 2.73 \times 10^8$ and $Pr = 6.26$ based on the data of the numerical probes at $z = 0.50L$. Panels (a), (b), and (c) show the energy in the different Fourier modes of the azimuthal temperature profile normalized by the energy present in all Fourier modes based on the data of 8, 16, and 32 equally spaced probes, respectively. The black, red, blue, and dark green lines indicate the energy in the first, second, third, and the additional modes, respectively. Note that when the data of 8 probes are used a lot of information about the higher modes is lost. Panel d shows the corresponding relative LSC strength based on the data of 8 (red), 16 (blue), and 32 (black) equally spaced probes. The two dashed vertical lines indicate the transitions between regimes I and II, and between II and III, respectively.

probes should be sufficient to capture all relevant features of the azimuthal profiles.

Fortunately, the data of 8 equally spaced thermistors are already sufficient to reliably calculate S_m for non-rotating RB convection, see chapter 11. To confirm this observation for the rotating RB case (and validate the experimental results with 8 probes discussed in section 12.2) we therefore calculate S_m based on the data of 8, 16, and 32 equally spaced probes. The result is given in figure 12.3d, which shows that the curves for the relative LSC strength almost collapse for the three cases. Moreover, the numerical data are in good agreement with the experimental result shown in figure 12.2, including the large decrease of S_m at the transition between regimes I and II. The small value of the relative LSC strength ($S_m \ll 0.5$) suggests the absence of the LSC and that the azimuthal temperature profile at midheight becomes random in regime II and III. This is confirmed by a three-dimensional visualization of the flow, see e.g. figure 6.5, where it is shown that in regime II vertically aligned vortices are the dominant feature of the flow.

12.4 The role of Stewartson and Ekman boundary layers

In this section we will first discuss the flow characteristics for regimes I and II and sketch the influence of background rotation on the mean flow in general terms, and the role of the Ekman and Stewartson boundary layers is emphasized. Subsequently, we provide physical explanations for the structure of the mean flow as observed for regime II. Finally, we discuss the implications for the mean temperature gradient at the sidewall of the convection cell.

12.4.1 Description of the flow characteristics

In figure 12.5 we show the azimuthally averaged temperature and velocity components u_z, u_ϕ and u_r for three typical rotation regimes: (the top row) $1/Ro = 0$ (no rotation, regime I), (the middle row) $1/Ro = 0.35$ (weak rotation, regime I) and (the bottom row) $1/Ro = 2.78$ (moderate rotation, regime II) at $Ra = 1 \times 10^9$ and $Pr = 6.4$. The left hand side of each picture ($r = 0$) represents the position of the cylinder axis (dash-dotted line), while the right-hand side ($r/L = 0.5$) corresponds with the sidewall. A close-up of the thermal and flow structure in the bottom corner of the tank for the case $1/Ro = 2.78$ (see figure 12.5c) is shown in figure 12.6. We note that the azimuthally averaged profiles for lower Ra values are similar to the ones presented in figure 12.5.

For the non-rotating case ($1/Ro = 0$), shown in 12.5a, we observe the signature of the LSC. The cell has an elliptic shape, with its major axis oriented at some angle with the cylinder axis (see the sketch in figure 12.4, and also in Qiu & Tong [208]). It is due to this mean tilt of the elliptic LSC, combined with the rotation sense as shown in figure 12.4, that the azimuthal average of this flow is not zero; especially upward and downward motions are separated in these azimuthally averaged plots. In the top half upward motion (positive u_z) is found near the cylinder axis, while the downward flow (negative u_z) is strongest near the sidewall. The opposite situation is found for u_z in the bottom half. The azimuthal velocity u_ϕ does not show a well-defined mean profile, just some small fluctuations. The averaged radial velocity u_r has maximal values near the intersections of the horizontal plates with the sidewall, consistent with the averaged vertical velocity u_z near these regions. Note also the weak radially inward flow near the sidewall around midheight.

When a small rotation is introduced [$1/Ro = 0.35$, figure 12.5b], a first observation is that the mean velocities become smaller (except the averaged azimuthal velocity u_ϕ which grows due to organization of the azimuthal flow). The vertical velocity u_z still has the dominant structuring due to the LSC, but especially near the cylinder axis some disturbances appear. For the azimuthal velocity a well-defined structure emerges due to the azimuthal averaging. The Coriolis force, deviating the parts of the LSC with mean horizontal velocity to the right with respect to the local direction of the (mean) horizontal flow, is driving the organization of an average azimuthal flow. The blue regions near the corners in the plot of the azimuthal velocity u_ϕ represent the anticyclonic motion induced by the mean horizontal outward flow of the LSC (near the bottom and top plates, see figure 12.4). The sketch of the LSC motion shows that the up (down) going plumes are first traveling straight up (down), before the radial inward flow of the LSC sets in. The cyclonic motion that is observed in the central sidewall region of the azimuthally averaged azimuthal velocity is due to the radial inward flow of the LSC in the top (bottom) half of the cell for the upward (downward) branch of the LSC, see figure 12.4. This radial inward flow of the LSC results in a spin-up, i.e. in cyclonic azimuthal motion, by the action of the Coriolis force. This mechanism is equivalent to conservation of angular momentum: radial inward motion ($u_r < 0$) of fluid parcels results in an increase of u_ϕ, i.e. in cyclonic motion. Because this radial inward flow is in the top (bottom) part of the sample for the up (down) going plumes this results, after azimuthal averaging, in one central sidewall region in which a cyclonic motion is found. This means that this particular snapshot, cannot be used for interpretation of the movement of individual plumes traveling from bottom to top and the other way around. However, in this very schematic picture it does seem to be consistent with experimental measurements of the anticyclonic motion of the LSC, see Refs. [75, 80, 100, 154], as both upgoing and downgoing plumes get anticyclonic deflection by the mean anticyclonic azimuthal flow near the plates and any effect of mean cyclonic flow becomes effective only for $z \gtrsim 2/3H$ (for upgoing plumes) and $z \lesssim H/3$ (for downgoing plumes).

At much higher rotation rates, i.e. for larger $1/Ro$-values, the LSC no longer exists, and the secondary circulation takes a different appearance. It is obvious from the velocity plots that relatively large velocities occur in thin regions near the solid container walls. A division of the domain into several regions is appropriate, being the bulk interior domain, the Ekman layers at the horizontal plates, and the Stewartson layer at the sidewall. The Ekman layers have a (non-dimensional) thickness $\delta_E = Ek^{1/2}$ (with the Ekman number defined according to $Ek = \nu/(\Omega L^2)$, representing an inverse Reynolds number based on the length scale L and velocity scale $L\Omega$). The Stewartson layer at the sidewall has a sandwich structure consisting of a thicker outer layer of (non-dimensional) thickness $\delta_{S,1/4} = Ek^{1/4}$ and a thinner inner layer of (non-dimensional) thickness $\delta_{S,1/3} = Ek^{1/3}$ (see e.g. [209–214]). The dashed lines in

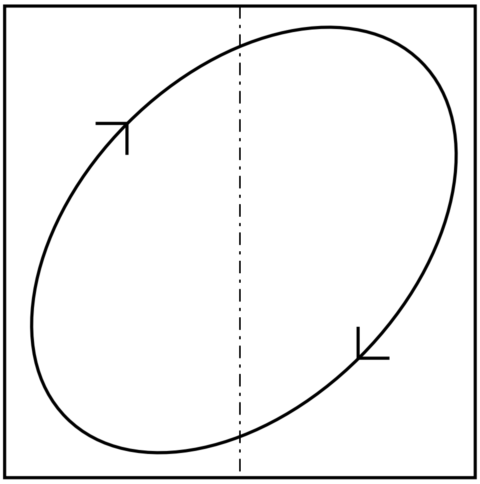

Figure 12.4: Schematic side view of the tilted LSC in the cylinder in the non-rotating or weakly rotating (regime I) case. The dash-dotted line is the axis of the cylinder.

figure 12.5c and figure 12.6 indicate the typical layer thicknesses. In figure 12.6 the bottom right-hand corner is magnified for the temperature (top panel) and each of the velocity components, so that the various boundary layers are more easily recognized. Note that since the secondary circulation associated with the Ekman and Stewartson layers is weak, the mean velocities u_r and u_z in the bulk are very small and therefore hardly noticeable, as is confirmed by the simulation results. It should be emphasized that the secondary circulation found here is considerably different from that suggested by Hart & Olsen [215], based on a linear mean temperature gradient, or that of Homsy & Hudson [177] enacted by centrifugal buoyancy. In both these works there is no up-down symmetry, which is still fulfilled here. It must also be stated that the aforementioned circulation is only of secondary magnitude. The still-turbulent field of the vortical plumes is dominant.

The most remarkable change is observed in the distribution of the azimuthal velocity u_ϕ: in the bulk of the domain an anticyclonic flow ($u_\phi < 0$, indicated by blue in figure 12.5c) is present, while a thin band of cyclonic flow ($u_\phi > 0$, indicated by red) is visible only close to the sidewall. Simulations for the parameter range $0.35 \lesssim 1/Ro \lesssim 2.78$ (not shown here) revealed that for increasing rotation rates (increasing $1/Ro$-values) the cyclonic flow region becomes confined to a region near the sidewall of increasingly smaller size. These observations suggest that in this Ro-regime the Ekman and Stewartson layers play an essential role in the mean secondary circulation, even though this circulation is relatively weak and even continuously disturbed by the non-steady thermally driven turbulent plumes that are present throughout the flow domain.

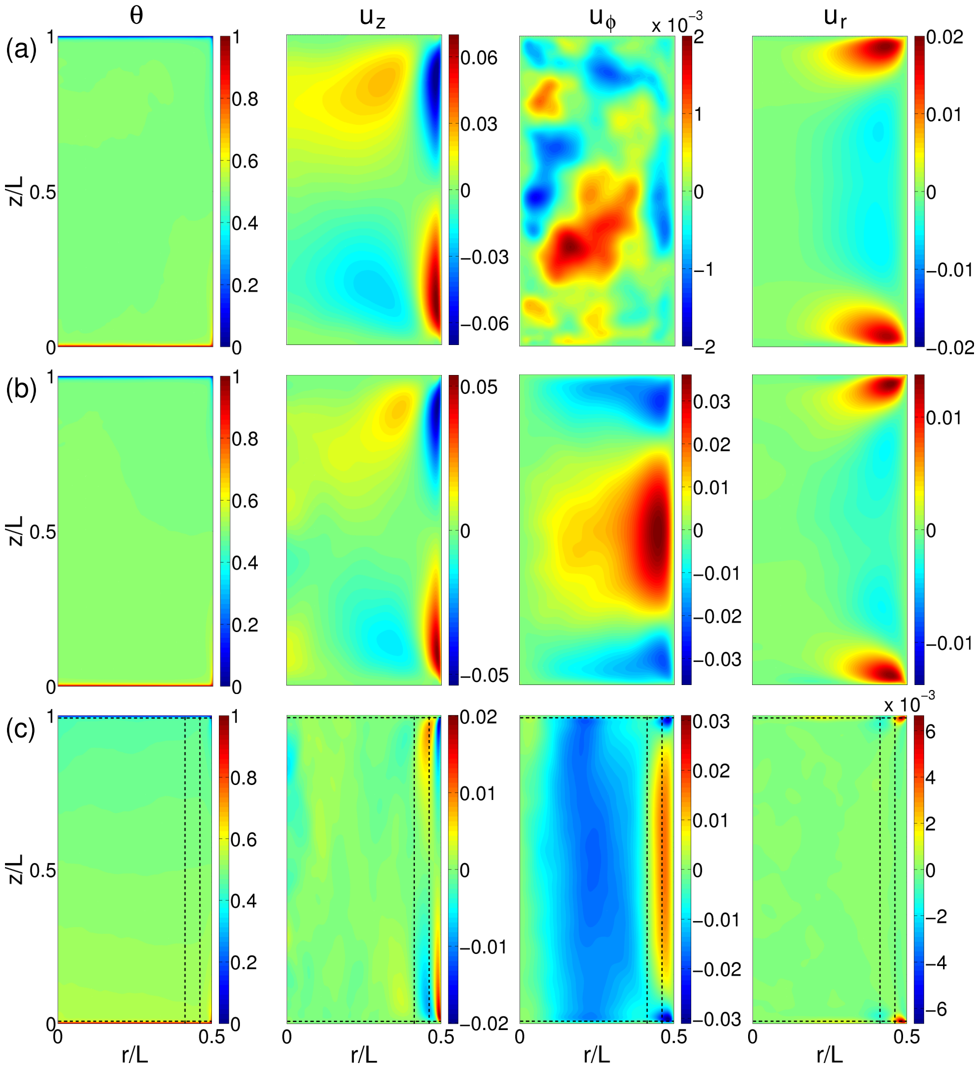

Figure 12.5: The figures from left to right indicate the azimuthally averaged temperature, and the velocity components u_z, u_ϕ, and u_r, respectively, for $Ra = 1.00 \times 10^9$ and $Pr = 6.4$. The rows from top to bottom indicate the results for (a) $1/Ro = 0$, (b) $1/Ro = 0.35$, and (c) $1/Ro = 2.78$, respectively. The left-hand side of each picture is the cylinder axis $r = 0$; the right-hand side corresponds to the sidewall $r/L = 0.5$. The dashed lines in the pictures of the bottom row indicate typical boundary-layer thicknesses: $\delta_E = Ek^{1/2}$ near the bottom and top plates, and $\delta_{S,1/3} = Ek^{1/3}$ and $\delta_{S,1/4} = Ek^{1/4}$ near the sidewall ($\delta_{S,1/3}$ is closest to the sidewall). Note that the azimuthally averaged azimuthal velocity for $1/Ro = 0$ (a) is much smaller than for $1/Ro = 0.35$ (b) and $1/Ro = 2.78$ (c).

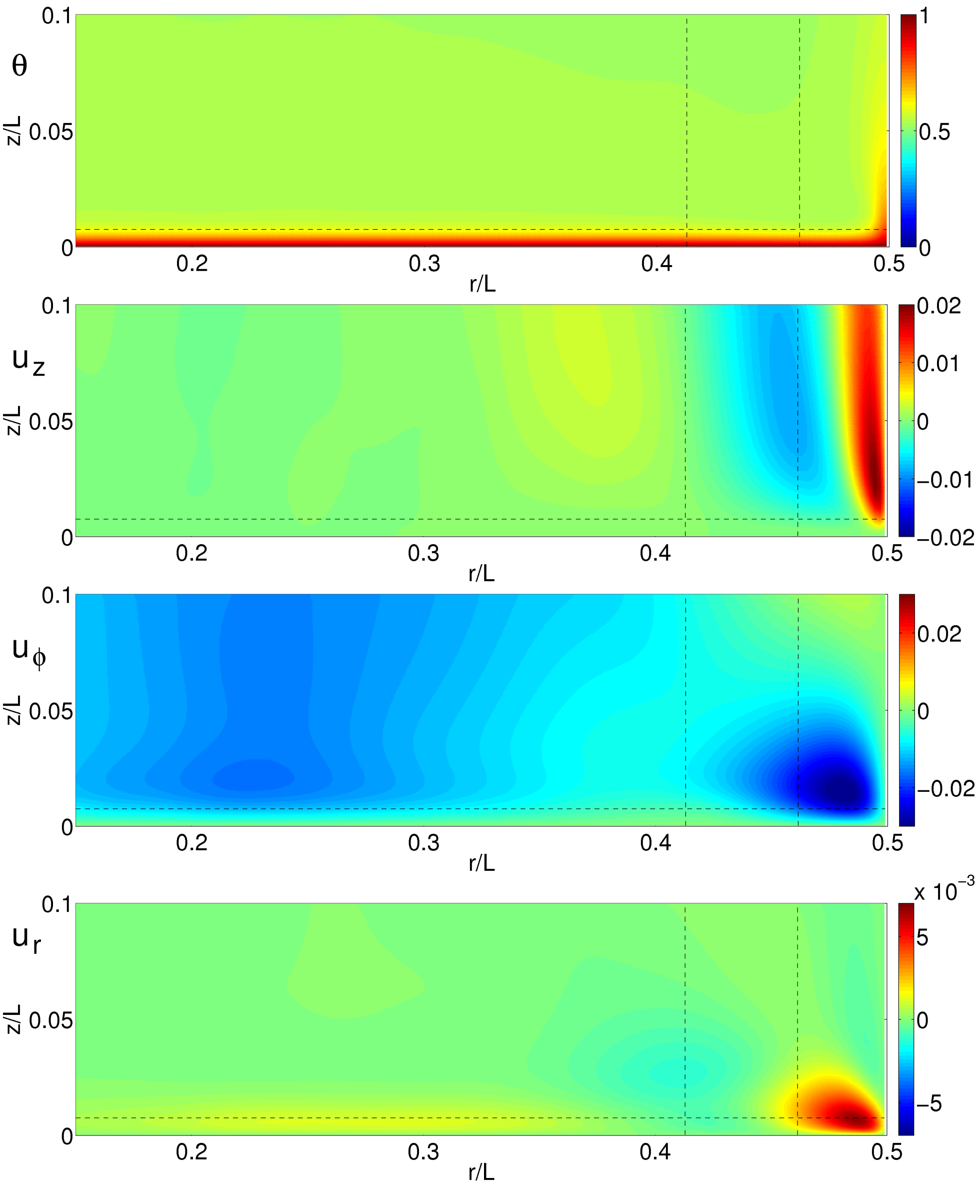

Figure 12.6: Close-up of the bottom-right corner of the figures shown in figure 12.5c ($1/Ro = 2.78$). The area displayed is $0.15 < r/L < 0.5$; $0 < z/L < 0.1$. Color coding and dashed lines as in figure 12.5c. The panels from top to bottom indicate the azimuthally averaged temperature, and the velocity components u_z, u_ϕ, and u_r, respectively.

12.4.2 Analysis secondary circulation regime II

The remarkable feature of the weak anticyclonic swirl flow in the bulk of the domain in combination with a region of cyclonic swirling motion near the cylinder wall (the u_ϕ-plot in figure 12.5c) can be explained as follows. The heated fluid rising upward from the bottom plate and the cooled fluid flowing downward from the top plate result in a radially outward mean flow in the bulk of the domain. Although this radial motion is relatively weak, conservation of angular momentum ($\sim rV$, with $V = \Omega r + u_\phi$ the absolute azimuthal velocity) implies that the absolute swirl velocity of fluid parcels will decrease, i.e. in the co-rotating frame this fluid will acquire an anticyclonic azimuthal motion ($u_\phi < 0$). This radial outflow in the bulk of the domain should be compensated by a radial inflow through the thin Ekman boundary layers at the bottom and the top plates. The structure of this thermally driven secondary flow in the r,z-plane is sketched in figure 12.7a.

This picture of the flow is not complete, however, because a competing mechanism is active simultaneously, tending to counteract the anticyclonic swirl motion ($u_\phi < 0$) in the bulk of the domain: the spin-up process. This counteracting adjustment process is essentially driven by the Ekman layers: the bottom Ekman layer imposes a suction velocity on the interior given by $u_z = \frac{1}{2}Ek\omega_I$ (in dimensionless form), with ω_I the vertical component of the rotation of the relative interior flow. A similar suction velocity is imposed on the interior flow by the upper Ekman layer. As implied by conservation of mass, this differential suction drives a flow as depicted schematically in figure 12.7b: a radial inflow is thus generated in the bulk of the domain, while radial outflow takes place in both Ekman layers. The radial outflux of the heated (cooled) fluid in the bottom (top) Ekman layer is returned through the Stewartson layer at the cylinder wall, radially inwards into the interior. Again, according to the principle of conservation of angular momentum rV, with $V = \Omega r + u_\phi$, the radial motion in the bulk implies a change in the swirl velocity, now leading to an increase in u_ϕ (spin-up), as is observed in figure 12.5c.

As stated before, both mechanisms are acting simultaneously: the thermal forcing leads to anticyclonic motion in the bulk (figure 12.7a), while the spin-up mechanism tends to counteract this negative swirl (see figure 12.7b). Signatures of the latter mechanism can be seen in the enlarged u_r-graph in figure 12.6: although weak, a radial outflow is observed in the bottom boundary layer, while the u_ϕ-graph shows a well-defined anticyclonic flow in the bulk.

Figure 12.8a shows the azimuthally averaged velocity profiles $u_r(r)$, $u_\phi(r)$, and $u_z(r)$ at $z = 0.25L$ according to a numerical simulation for $1/Ro = 2.78$. The radial u_ϕ-distribution clearly shows the presence of anticyclonic swirl in the interior domain, while significant positive swirl exists in the region close to the cylinder wall. Also, the velocity components u_r and u_z show significant non-zero values near and in this wall region.

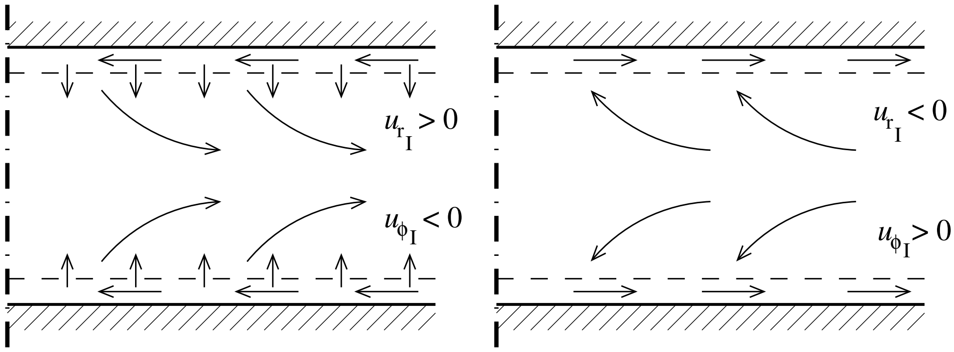

(a) (b)

Figure 12.7: a) Fluid motion due to thermal forcing. The heated (cooled) fluid rising upward (flowing downwards) from the bottom (top) plate result in a radially outward mean flow in the bulk of the domain. This is compensated by a radial inflow through the thin Ekman boundary layers at the bottom and the top plates. b) Fluid motion due to spin up. The Ekman layers impose suction towards the plates. Due to mass conservation this leads to a radial inflow in the bulk domain and a radial outflow in the Ekman layers. The dash dotted line in both panels indicates the center of the cell (which coincides with the rotation axis).

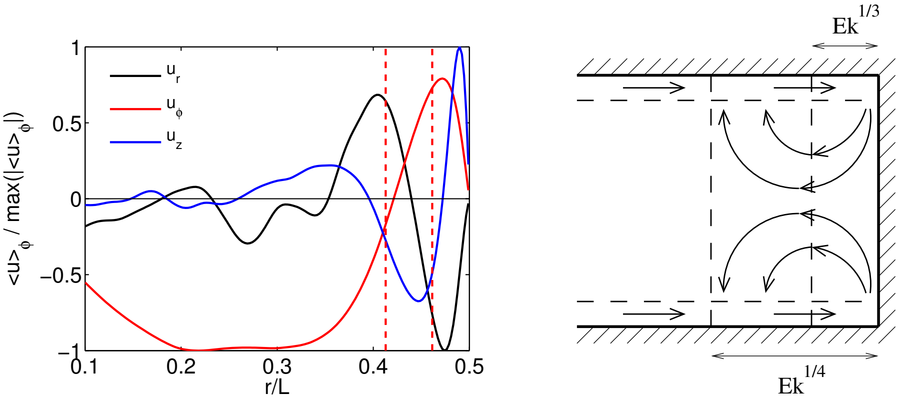

(a) (b)

Figure 12.8: a) The azimuthally averaged velocity profiles at $z = 0.25L$ for $Ra = 1.00 \cdot 10^9$ and $Pr = 6.4$ for $1/Ro = 2.78$. The azimuthal, radial, and axial velocity components are indicated in red, black, and blue, respectively. (b) Sketch of the secondary circulation in the Ekman and Stewartson layers. Note the singular eruption of the Ekman flux into the $Ek^{1/3}$-layer in the bottom an top right corners, see details in the text.

The matching of the azimuthal velocity component $u_\phi(r = 0.5L)$ to the sidewall requires a Stewartson $Ek^{1/4}$-layer, in which this velocity is given by $u_\phi = -\frac{1}{L}u_\phi(r = 0.5L)\exp(\xi\sqrt{2/L})$, with L the height of the cylinder, and $\xi = (r - 0.5L)Ek^{-1/4}$ the stretched radial boundary-layer coordinate. When referring to this principal velocity component as being $\mathcal{O}(1)$, the vertical and radial velocity components in this layer are much smaller, viz. $\mathcal{O}(Ek^{1/4})$ and $\mathcal{O}(Ek^{1/2})$, respectively (in non-dimensional terms). Matching of these velocities to the cylinder wall requires the presence of a thinner $Ek^{1/3}$-layer. The radial matching and the mass flux requirements imply a principal solution with a vertical velocity $u_z \sim \mathcal{O}(Ek^{1/6})$ and a radial velocity $u_r \sim \mathcal{O}(Ek^{1/2})$ within this layer (see, e.g. [212, 214]).

Where the Stewartson $Ek^{1/3}$-layer meets the Ekman layers, the vertical velocity has a singular structure: $u_z \sim \pm\delta(\eta)$ at $z = 0$ and L, with $\eta = (r - 0.5L)Ek^{-1/3}$ the stretched radial coordinate in this Stewartson layer, and δ the Dirac delta function. Signs of these singular eruptions of the Ekman layer fluxes at $z = 0$ and $z = L$ into the thinner Stewartson layer are clearly visible in the u_z-plot in figure 12.5c, and for the case of the bottom corner in figure 12.6. Note that these vertical fluxes are positive and negative near the bottom and top Ekman layers, respectively. Weaker vertical velocities of opposite signs are observed in the thicker $Ek^{1/4}$-layer, see figure 12.5c. The velocity profile $u_z(r)$ at $z = 0.25L$, see figure 12.8a, also shows this peaked structure close to the cylinder wall, indicating the singular eruption of the Ekman flux into the $Ek^{1/3}$-layer. The oppositely signed vertical velocity next to the peak corresponds with the vertical motion in the thicker $Ek^{1/4}$-layer. The secondary circulation in the Ekman and Stewartson layers is schematically shown in figure 12.8b. Additional evidence that the mean velocity profiles close to the sidewall are indeed governed by Stewartson boundary layer dynamics is provided in figure 12.9, where it is shown that the thickness of the sidewall boundary layers observed in the simulations follows the theoretical predictions, see Kunnen et al. [91].

The matching of the regions of anticyclonic ($u_\phi < 0$) and cyclonic ($u_\phi > 0$) flow in the interior will also be carried out in a shear layer, in this case in the form of a detached Stewartson layer, also having a sandwich structure consisting of a thinner $Ek^{1/3}$-layer embedded within a thicker $Ek^{1/4}$-layer. The presence of this detached shear layer is visible in the shape of the u_r and u_z profiles in figure 12.8a, around the radius at which the sign-change in u_ϕ occurs. This picture may be less clear, however, because the detached Stewartson layer and the Stewartson layer attached to the cylinder wall are overlapping to some extent. The detailed structure of the velocity fields and the associated transport characteristics will be analyzed in a separate study.

The role of Ekman and Stewartson boundary layer dynamics on the average mean flow is here illustrated with numerical simulations with $Ra = 1 \times 10^9$ and $Pr = 6.4$, see details in Kunnen et al. [91]. Separate sets of simulations with $Ra = 2.73 \times 10^8$ with $Pr = 6.26$ and $Ra = 1 \times 10^8$ with $Pr = 6.4$ essentially revealed the same picture. The explanation provided in this section is therefore applicable to a range of Rayleigh numbers. Further studies are needed to explore the regime with $Ra \gtrsim 1 \times 10^9$ and the role of the Prandtl number. We have also explored the role of the Rossby number,

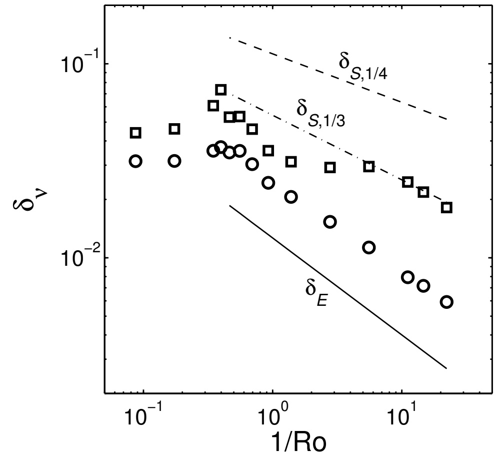

Figure 12.9: Boundary layer thicknesses for $Ra = 1.00 \times 10^9$ and $Pr = 6.4$. The dimensionless viscous boundary layer thickness near the plates is indicated by the circles. The dimensionless boundary layer thickness of the viscous boundary layers near the sidewall, i.e. the Stewartson layers, is indicated by the squares and follows the scaling of the inner Stewartson boundary layer thickness, i.e. $\delta_{S,1/3}$. Adapted from Kunnen et al. [91].

in particular by increasing the value of $1/Ro$ such that the flow is dominated by strong rotation (close to and even in regime III). The vertical vortex plumes become then stronger and data from azimuthally averaged components of velocity reveal an increasing number of alternating, vertically almost homogeneous regions of $u_\phi < 0$ and $u_\phi > 0$.

12.4.3 Influence of the secondary circulation on sidewall temperature measurements

The above observations of the flow structure enable us to explain the sidewall temperature measurements. In figure 12.10 we have plotted radial distributions of the azimuthally averaged temperature and vertical velocity at $z = 0.25L$. Three main observations from the data extracted at this particular level are: a strong vertical mean flow near the sidewall (and for the highest rotation rate clearly within the $Ek^{1/3}$-layer), an increase of the mean temperature in the bulk with the rotation rate, and an increased mean temperature near the sidewall compared to the bulk, regardless of the existence of the LSC. We start with the latter observation. In regime I (weak rotation) where the LSC is the dominant feature of the flow, the temperature gradient at the sidewall is caused by the LSC, which carries warm fluid upwards along the sidewall and cold fluid down in the middle; and vice versa in the top half of the cylindrical domain. In regime II (moderate rotation) the LSC has disappeared and vertical vortices form the dominant feature of the flow. In this regime the secondary circulation described above causes a flow directed vertically away from the

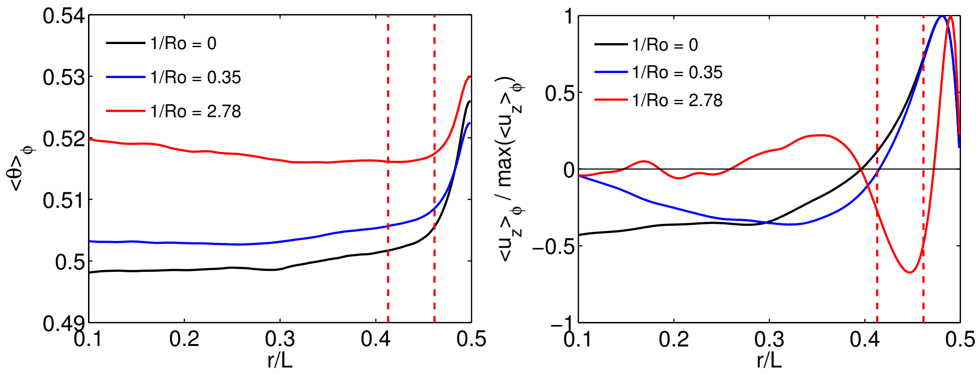

(a) (b)

Figure 12.10: (a) Azimutally averaged temperature and (b) vertical velocity profiles as function of the radial position at the height $z = 0.25L$ for $Ra = 1.00 \times 10^9$ and $Pr = 6.4$. Black, blue, and red indicate the data for $1/Ro = 0$, $1/Ro = 0.35$, and $1/Ro = 2.78$, respectively. The dashed lines indicate typical Stewartson boundary layer thicknesses ($\delta_{S,1/3} = Ek^{1/3}$ and $\delta_{S,1/4} = Ek^{1/4}$ near the sidewall for $1/Ro = 2.78$ ($\delta_{S,1/3}$ is closest to the sidewall). Note that for $1/Ro = 2.78$ there is a strong up flow of fluid in the inner Stewartson $Ek^{1/3}$-layer, which causes a vertical temperature gradient at the sidewall. In panel (a) the increasing mean temperature in the bulk with increasing rotation rate indicates that the vertical temperature gradient in the bulk increases with increasing $1/Ro$. The temperature gradient in the bulk for this case is shown in figure 15 of Kunnen et al. [91].

plate close to the sidewall, i.e. in the $Ek^{1/3}$-layer, see figure 12.10b. This means that in regime II the secondary circulation carries warm fluid upwards along the sidewall in the lower half of the cylinder and cold fluid downwards along the sidewall in the top half. The enhanced mean temperature in the bulk with increasing rotation rate indicates that the vertical temperature gradient in the bulk increases with increasing $1/Ro$, see for example figure 15 of Kunnen et al. [91]. This temperature gradient is caused by the merger of vertical plumes (see, e.g., [68, 77, 83, 84, 87, 87, 188, 216]), i.e. the enhanced horizontal mixing of the temperature anomaly of the plumes results in a mean temperature gradient. In regime III this temperature gradient in the bulk becomes stronger than in regime II and eventually becomes equal to the temperature gradient at the sidewall.

12.5 Conclusions

Based on the experimental data and results obtained from DNS we studied the characteristics of the azimuthal temperature profiles at the sidewall. We find that in regime I (weak rotation) the LSC is the dominant feature of the flow. In the sidewall temperature measurements this is identified by the strong presence of the first Fourier mode in the signal. When the rotation is increased a sudden onset in the heat transport enhancement is found that indicates the beginning of regime II, the moderate rotation regime. In this regime the LSC is replaced by vertically aligned vortices and due to their random position the magnitude of the first Fourier mode is very weak, which confirms that the LSC has disappeared. This feature is also observed in regime III, where the heat transfer decreases, because the vertical velocity fluctuations are suppressed by the rotation.

When the LSC is the dominant feature of the flow the vertical temperature gradient at the sidewall is mainly due to plumes that travel close to the sidewall because they travel with the LSC. However, also in regime II and III, in which the LSC is absent, there is a strong temperature gradient at the sidewall. In these regimes, where the vertical vortices are the dominant feature of the flow, the observed vertical temperature gradient along the sidewall is mainly due to the secondary flow that transports hot fluid radially outwards via the Ekman layer and then upwards along the sidewall through the Stewartson boundary layer in the bottom part of the cell and mutatis mutandis in the top part.

It is remarkable that the secondary flow in turbulent RB convection, which is observed after time-averaging of the flow field, is so well described by linear Ekman and Stewartson BL theory. This namely means that the laminar flow profiles are hidden under the highly turbulent flow. Thus the knowledge about laminar flow dynamics can still be highly relevant in the study of turbulent flows. We note that recently more of these remarkable cases have been discovered. For example, in chapter 13 we used the methods introduced by Zhou & Xia [34] to show that the laminar PB profile is hidden under the turbulent fluctuations. In addition several examples of sharp transitions between different turbulent regimes, which were previously mainly found around onset, were discovered. In this context we also mention the sharp transitions found in rotating RB convection found in chapter 8 and 9, the rotating von Karman experiment [129, 184], and in turbulent flows with liquid sodium [182, 183], where the increase of the magnetic Reynolds number beyond a certain threshold leads to bifurcations between different turbulent states of the magnetic field. These transitions can be partially understood by insight in laminar profiles. For example in rotating RB the transition between the two turbulent regimes is triggered by the transition from Prandtl-Blasius BL to Ekman BL at the bottom and top plate. We also observed sharp transitions between different turbulent states in rotating thermal convection as is described in chapter 8 and 9.

Part III

Two-dimensional Rayleigh-Bénard convection

13

Prandtl-Blasius temperature and velocity boundary layer profiles * †

The shapes of the velocity and temperature profiles near the horizontal conducting plates' center regions in turbulent Rayleigh-Bénard convection are studied numerically and experimentally over the Rayleigh number range $10^8 \lesssim Ra \lesssim 3 \times 10^{11}$ *and the Prandtl number range* $0.7 \lesssim Pr \lesssim 5.4$. *The results show that both the temperature and velocity profiles well agree with the classical Prandtl-Blasius laminar boundary-layer profiles, if they are re-sampled in the respective dynamical reference frames that fluctuate with the instantaneous thermal and velocity boundary-layer thicknesses. The study further shows that the Prandtl-Blasius boundary layer in turbulent thermal convection not only holds in a time-averaged sense, but is most of the time also valid in an instantaneous sense.*

13.1 Introduction

In thermal convective turbulent flow two types of boundary layers (BL) exist near the top and bottom plates, both of which are generated and stabilized by the viscous shear of the large-scale mean flow: One is the kinematic boundary layer and the other is the thermal boundary layer. The two layers are not isolated but are coupled dynam-

---

[*] Based on: Q. Zhou, R. J. A. M. Stevens, K. Sugiyama, S. Grossmann, D. Lohse, K.Q. Xia, Prandtl-Blasius temperature and velocity boundary layer profiles in turbulent Rayleigh-Bénard convection, J. Fluid Mech. 664, 297312 (2010).

[†] The analysis of the numerical data has been performed by Q. Zhou and K.Q. Xia.

ically to each other. They both play an essential role in turbulent thermal convection, especially for the global heat flux across the fluid layer. The relation between the shear rate and the heat flux depends crucially on the shape of the temperature profile, see e.g. Ching [217]. Furthermore, almost all theories proposed to predict the relation between *Nu* and the control parameters *Ra* and *Pr* are based on some kind of assumptions for the BLs, such as the stability assumption of the thermal BL from the early marginal stability theory [218], the turbulent-BL assumption from the theories of Shraiman & Siggia [113] and Siggia [143] and of Dubrulle [185, 219], and the Prandtl-Blasius laminar-BL assumption of the Grossmann & Lohse (GL) theory [25–28]. Because of the complicated nature of the problem, different theories based on different assumptions for the BL may yield the same predictions for the global quantities, such as the *Nu*-*Ra* scaling relation [113, 173]. Therefore, direct characterization of the BL properties is essential for the differences between and the testing of the various theoretical models and will also provide insight into the physical nature of turbulent heat transfer in the RB system.

In the GL theory, the kinetic energy and thermal dissipation rates have been decomposed into boundary layer and bulk contributions. Scaling-wise and in a time averaged sense a laminar Prandtl-Blasius boundary layer has been assumed. This theory can successfully describe and predict the Nusselt and the Reynolds number dependences on *Ra* and *Pr* (see e.g. the recent review in [20]. As the Prandtl-Blasius laminar BL is a key ingredient of the GL theory, it is important to make direct experimental verification of it. We note that also the (experimentally verified) calculation of the mean temperature in the bulk in both liquid and gaseous non-Oberbeck-Boussinesq RB flows [105, 136, 220] is based on the Prandtl-Blasius theory.

In a recent high-resolution measurement of the properties of the velocity boundary layer, Sun, Cheung & Xia [33] have found that, despite the intermittent emission of plumes, the Prandtl-Blasius-type laminar boundary layer description is indeed a good approximation, in a time-averaged sense, both in terms of its scaling and its various dynamical properties. However, because of the intermittent emissions of thermal plumes from the BLs, the detailed dynamics of both kinematic and thermal BLs in turbulent RB flow are much more complicated. On the one hand, direct comparison of experimental velocity [221] and numerical temperature [137] profiles with theoretical predictions has shown that both the classical Prandtl-Blasius laminar BL profile and the empirical turbulent logarithmic profile are not good approximations for the time-averaged velocity and temperature profiles. Furthermore, two-dimensional (2D) ([106]) and three-dimensional (3D) (see chapter 2) numerical simulations found that the deviation of the BL profile from the Prandtl-Blasius profile increases from the plate's center towards the sidewalls, due to the rising (falling) plumes near the sidewalls. On the other hand, Qiu & Xia [127] have found near the sidewall and Sun et al. [33] near the bottom plate that the velocity BL obeys the scaling law of the Prandtl-

Blasius laminar BL, i.e., its width scales as $\lambda_v/H \sim Re^{-0.5}$, where λ_v is the kinematic BL thickness, defined as the distance from the wall at which the extrapolation of the linear part of the local mean horizontal velocity profile $u(z) = \langle u_x(z,t)\rangle$, with z being the vertical distance from the bottom plate and $\langle\cdots\rangle$ being the time average at the plate center, meets the horizontal line passing through the maximum horizontal velocity $[u(z)]_{max}$, and and $Re = [u(z)]_{max}H/\nu$ is the Reynolds number based on $[u(z)]_{max}$. These papers highlight the need to study the nature of the BL profiles, both velocity and temperature, in turbulent thermal RB convection.

Considerable progress on this issue has recently been achieved by Zhou & Xia [34] who have experimentally studied the velocity BL for water ($Pr = 4.3$) with particle image velocimetry (PIV). They found that, since the dynamics above and below the range of the boundary layer is different, a time-average at a fixed height z above the plate with respect to the laboratory (or container) frame will sample a mixed dynamics, one pertaining to the BL range and the other one pertaining to the bulk, because the measurement position will be sometimes inside and sometime outside of the fluctuating width of the boundary layer. To make a clean separation between the two types of dynamics, Zhou & Xia [34] studied the BL quantities in a *time-dependent frame* that fluctuates with the instantaneous BL thickness itself. Within this dynamical frame, they found that the mean velocity profile well agrees with the theoretical Prandtl-Blasius laminar BL profile. In figure 13.1 we show the essence of the results, again for the velocity boundary layer but for somewhat larger Pr, now $Pr = 5.4$. (For details of the experiment and the apparatus used, please see Refs. [34, 150]). It is seen here that the method of using the time dependent frame works equally well as for the $Pr = 4.3$ case of Zhou & Xia [34]. While at the large $Ra = 1.8\times10^{11}$ the time and space averaged velocity profile (triangles) already considerably deviates from the Prandtl-Blasius profile (solid line), the dynamically rescaled profile (circles) perfectly agrees with the Prandtl-Blasius profile. Thus a dynamical algorithm has been established to directly characterize the BL properties in turbulent RB systems, which is mathematically well-defined and requires no adjustable parameters.

The questions which immediately arise are: (i) Does this dynamical rescaling method also work for the temperature field, giving good agreement with the (Prandtl number dependent) Prandtl-Blasius temperature profile? (ii) And does the method also work for lower Pr, where the velocity field is more turbulent? Both these questions cannot be answered with the current Hong Kong experiments, as PIV only provides the velocity field and not the temperature field, and as PIV has not yet been established in gaseous RB, i.e., at low Pr number Rayleigh-Bénard flows.

In the present chapter we will answer these two questions with the help of direct numerical simulations (DNS). To avoid the complications of oscillations and rotations of the large scale convection roll plane and as the Prandtl-Blasius theory is a 2D theory anyhow we will restrict ourselves to the 2D simulations of Sugiyama et

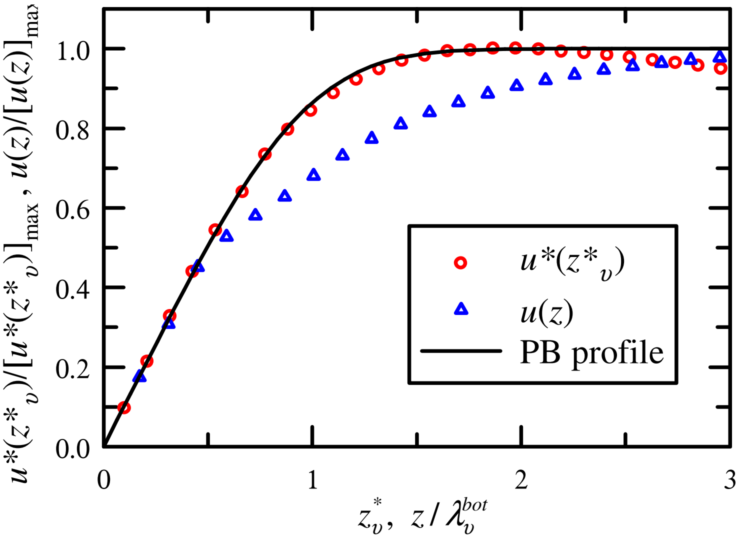

Figure 13.1: Comparison between the spatial x-interval and time averaged velocity profiles $u(z)$ (triangles), the dynamically rescaled velocity profile $u^*(z^*_v)$ (circles – for the notation we refer to section 13.3), and the Prandtl-Blasius velocity profile (solid line) near the bottom plate obtained experimentally at $Ra = 1.8 \times 10^{11}$ and $Pr = 5.4$ (working fluid water).

al. [106]. Our results will show that Zhou & Xia's idea [34] of using time-dependent coordinates to disentangle the mixed dynamics of BL and bulk works excellently also for the temperature field and also for low Pr flow. I.e., if dynamically rescaled, both velocity and temperature BL profiles can be brought into excellent agreement with the theoretical Prandtl-Blasius BL predictions, for both larger and lower Pr.

13.2 DNS of the 2D Oberbeck-Boussinesq equations

The numerical method has been explained in detail in Sugiyama et al. [106]. In a nutshell, the Oberbeck-Boussinesq equations with no-slip velocity boundary conditions at all four walls are solved for a 2D RB cell with a fourth-order finite-difference scheme. The aspect ratio is $\Gamma \equiv D/H = 1.0$. Four sets of data are presented here, their Rayleigh number Ra, Prandtl number Pr and the corresponding Reynolds number Re are (10^8, 0.7, 5.4×10^3); (10^9, 0.7, 1.9×10^4); (10^8, 4.3, 8.3×10^2); and (10^9, 4.3, 3.2×10^3), respectively. In all the computations, the kinematic viscosity, thermal expansion coefficient, and the temperature difference were fixed at $\nu = 6.6945 \cdot 10^{-7}$ m^2/s, $\alpha = 3.8343 \cdot 10^{-4}$ /K and $\Delta = 40$ K, respectively. The cell height was $H = 7.524$ cm for $Ra = 10^8$ and $Pr = 0.7$, $H = 4.108$ cm for $Ra = 10^8$ and $Pr = 4.3$, $H = 16.21$ cm for $Ra = 10^9$ and $Pr = 0.7$, and $H = 8.851$ cm for $Ra = 10^9$ and $Pr = 4.3$. Sugiyama et al. [106] have provided a detailed code validation.

As the governing equations are strictly Oberbeck-Boussinesq, there exists a top-

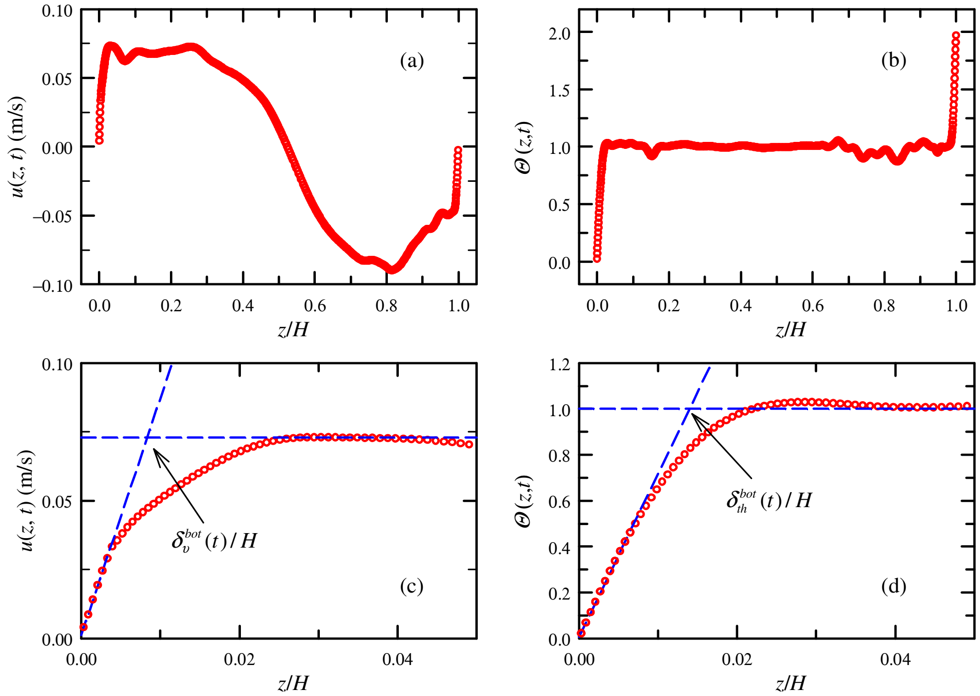

Figure 13.2: Examples of (a) an instantaneous horizontal velocity profile $u(z,t)$ and (b) a normalized instantaneous temperature profile $\Theta(z,t)$, averaged over $0.475 < x/D < 0.525$. The DNS data are obtained at $Ra = 10^9$ and $Pr = 0.7$. (c) and (d) show enlarged portions of the velocity and temperature profiles near the bottom plate, respectively. The two tilted dashed lines are linear fits to the linear parts of the velocity and temperature profiles near the plate and the two horizontal dashed lines mark the instantaneous maximum horizontal velocity and the bulk temperature $\Theta = 1$, respectively. The distances of the crossing points from the plate define the instantaneous BL thicknesses $\delta_{v,th}^{bot}(t)$. The instantaneous profiles are not top-down symmetric, the time averaged ones are. Within our present statistical error our data are consistent with zero thermal gradient in the bulk.

bottom symmetry. We therefore discuss only the velocity and temperature profiles near the bottom plate. For the temperature profiles, we introduce the non-dimensional temperature $\Theta(z,t)$, defined as

$$\Theta(z,t) = \frac{\theta^{bot} - \theta(z,t)}{\Delta/2}, \tag{13.1}$$

where θ^{bot} is the temperature of the bottom plate. In this definition, $\Theta(H) = 2$ and $\Theta(0) = 0$ are the temperatures for the top and bottom plates, respectively, and $\Theta(H/2) = 1$ is the mean bulk temperature.

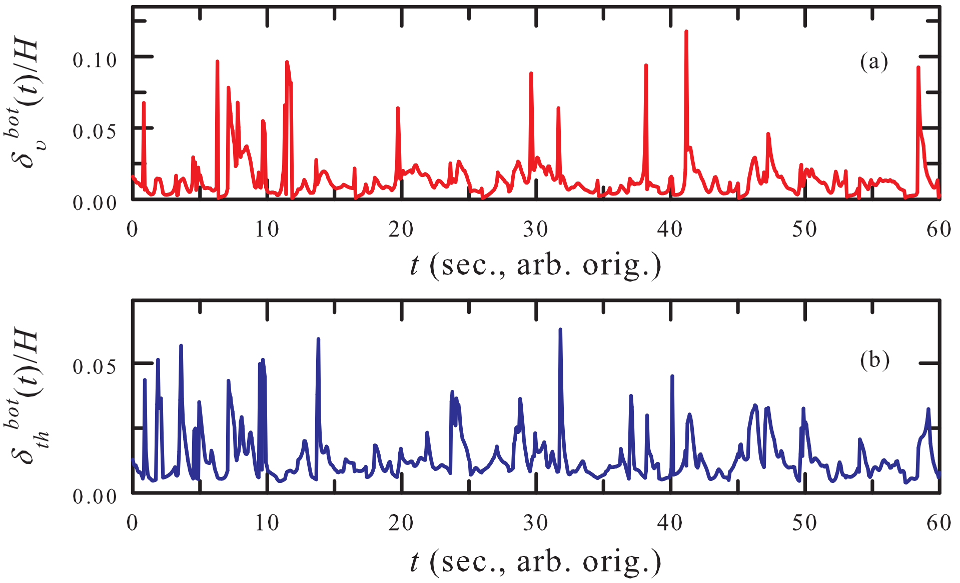

Figure 13.3: Sample time traces of (a) instantaneous kinematic BL thickness, $\delta_v^{bot}(t)$, and (b) instantaneous thermal BL thickness, $\delta_{th}^{bot}(t)$, normalized by the cell height. The data were obtained above the center of the bottom plate at $Ra = 1.0 \times 10^9$ and $Pr = 0.7$.

13.3 Dynamical boundary layer rescaling

The idea of the Zhou & Xia method [34] is to construct a dynamical frame that fluctuates with the local instantaneous BL thickness. To do this, first the instantaneous kinematic and thermal BL thicknesses are determined using the algorithm introduced by [34] [34]. To reduce data scatter, the horizontal velocity and temperature profiles at each discrete time t, $u(z,t)$ and $\Theta(z,t)$, are obtained by averaging the velocity and temperature fields along the x-direction (horizontal) over the range $0.475 < x/D < 0.525$. Figures 13.2(a) and (b) show examples of $u(z,t)$ and $\Theta(z,t)$ versus the normalized height z/H, respectively, of the DNS data obtained at $Ra = 10^9$ and $Pr = 0.7$. Both $u(z,t)$ and $\Theta(z,t)$ rise very quickly from 0 to either the instantaneous maximum velocity or to the bulk temperature within very thin layers above the bottom plate. While after reaching its maximum value, $u(z,t)$ slowly decreases in the bulk region of the closed convection cell, $\Theta(z,t)$ reaches and stays nearly constant at the bulk temperature $\Theta = 1$. To examine the velocity and the temperature in the vicinity of plates in more detail, we plot the enlarged near-plate parts of the $u(z,t)$ and $\Theta(z,t)$ profiles in figures 13.2 (c) and (d). One observes that both profiles are linear near the plate. The instantaneous velocity BL thickness $\delta_v(t)$ is then defined as the distance from the plate at which the extrapolation of the linear part of the velocity

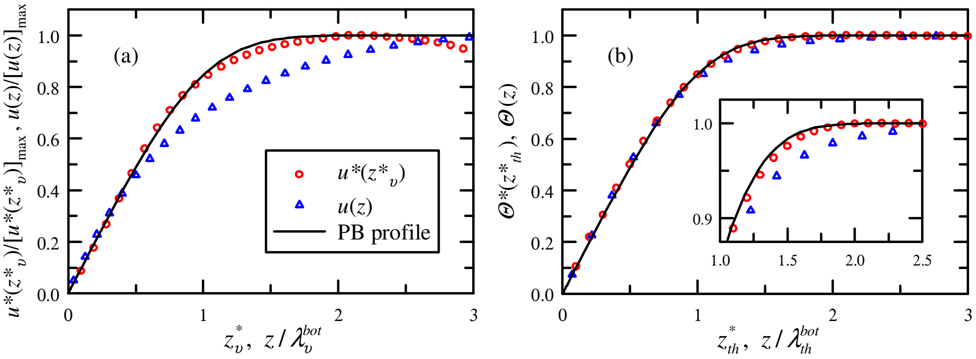

Figure 13.4: Comparison among (a) velocity profiles: dynamical frame based $u^*(z_v^*)$ (circles), laboratory frame based $u(z)$ (triangles), and the Prandtl-Blasius velocity profile (solid line), and (b) the corresponding temperature profiles: $\Theta^*(z_{th}^*)$ (circles), $\Theta(z)$ (triangles), and the Prandtl-Blasius temperature profile (solid line) near the bottom plate. All results obtained numerically at $Ra = 10^8$ and $Pr = 4.3$. The inset of (b) shows enlarged portions of the profiles around the thermal boundary layers' mergers to the bulk.

profile meets the horizontal line passing through the instantaneous maximum horizontal velocity, and the instantaneous thermal BL thickness $\delta_{th}(t)$ is obtained as the distance from the plate at which the extrapolation of the linear part of the temperature profile crosses the horizontal line passing through the bulk temperature. The arrows in figures 13.2(c) and (d) illustrate how to determine $\delta_v(t)$ and $\delta_{th}(t)$ as the crossing point distances and figure 13.3 (a) and (b) show 60-second time traces of $\delta_v^{bot}(t)/H$ and $\delta_{th}^{bot}(t)/H$, respectively.

With these measured $\delta_v(t)$ and $\delta_{th}(t)$, we can now construct the local dynamical BL frames at the plate's center. The time-dependent rescaled distances $z_v^*(t)$ and $z_{th}^*(t)$ from the plate in terms of $\delta_v(t)$ and $\delta_{th}(t)$, respectively, are defined as

$$z_v^*(t) \equiv z/\delta_v(t) \quad \text{and} \quad z_{th}^*(t) \equiv z/\delta_{th}(t). \tag{13.2}$$

The dynamically time averaged mean velocity and temperature profiles $u^*(z_v^*)$ and $\Theta^*(z_{th}^*)$ in the dynamical BL frames are then obtained by averaging over all values of $u(z,t)$ and $\Theta(z,t)$ that were measured at different discrete times t but at the same relative positions z_v^* and z_{th}^*, respectively, i.e.,

$$u^*(z_v^*) \equiv \langle u(z,t)|z = z_v^*\delta_v(t)\rangle \quad \text{and} \quad \Theta^*(z_{th}^*) \equiv \langle \Theta(z,t)|z = z_{th}^*\delta_{th}(t)\rangle. \tag{13.3}$$

We first discuss our results from the simulation performed at $Pr = 4.3$, the Prandtl number corresponding to water at 40 °C. Figure 13.4(a) shows the $u^*(z_v^*)$ profile (circles), normalized by its maximum value $[u^*(z_v^*)]_{max}$, obtained at $Ra = 10^8$. For comparison, we also plot in the figure the time-averaged horizontal velocity profile $u(z)$ ($= \langle u(z,t)\rangle$) (triangles), obtained from the same simulation. The solid line represents the Prandtl-Blasius velocity BL profile, the initial slope of which is matched to that of

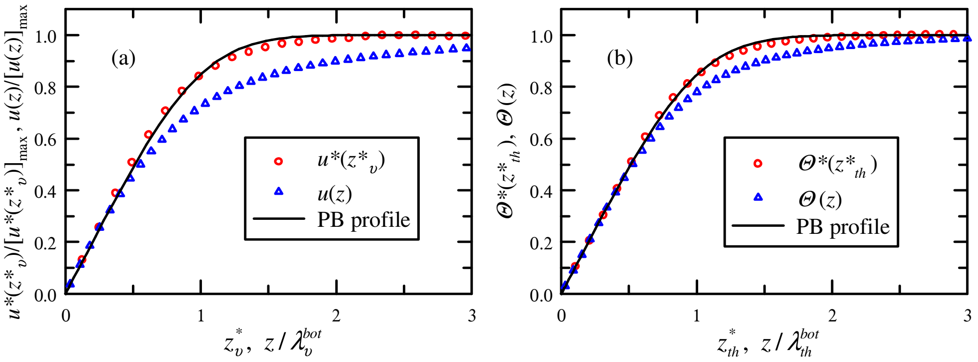

Figure 13.5: Comparison between (a) velocity profiles: dynamical $u^*(z_v^*)$ (circles), laboratory $u(z)$ (triangles), and the Prandtl-Blasius laminar velocity profile (solid line), and (b) temperature profiles: dynamical $\Theta^*(z_{th}^*)$ (circles), laboratory $\Theta(z)$ (triangles), and the Prandtl-Blasius laminar temperature profile (solid line) near the bottom plate, all obtained numerically at $Ra = 10^9$ and $Pr = 0.7$, representative for gases.

the measured profiles (Ahlers et al. [136]). For the range $z_v^* \lesssim 2$ the $u^*(z_v^*)$ profile obtained in the dynamical frame agrees well with the Prandtl-Blasius profile, while the time-averaged $u(z)$ profile obtained in the laboratory frame obviously is much lower than the Prandtl-Blasius profile in the region around a few kinematic BL widths. – Note that for $z_v^* \gtrsim 2$ the $u^*(z_v^*)$ profile deviates gradually from the Prandtl-Blasius profile because $u^*(z_v^*)$ decreases in the bulk region of the closed convection system down to 0 in the center and then changes sign. The Prandtl-Blasius profile, instead, describes the situation of an asymptotically constant, nonzero flow velocity. – These DNS results are similar to those found experimentally in a rectangular cell [34].

Figure 13.4(b) shows a direct comparison among the temperature profiles obtained from the same simulation: the dynamical frame based $\Theta^*(z_{th}^*)$ (circles), the laboratory frame time-averaged temperature profile $\Theta(z)$ $(= \langle\Theta(z,t)\rangle)$ (triangles), and the Prandtl-Blasius temperature profile. At first glance both the $\Theta^*(z_{th}^*)$ and $\Theta(z)$ profiles are consistent with the Prandtl-Blasius thermal profile. However, looking more carefully at the region around the thermal BL to bulk merger (the inset of figure 13.4(b)), one notes that the $\Theta^*(z_{th}^*)$ profile obtained in the dynamical frame is significantly closer to the Prandtl-Blasius profile than the time-averaged $\Theta(z)$ profile obtained in the laboratory frame, indicating that the dynamical frame idea of Zhou & Xia [34] works also for the thermal BL. Taken together, figures 13.4(a) and (b) illustrate that both the kinematic and the thermal BLs in turbulent RB convection are of Prandtl-Blasius type, which is a key assumption of the GL theory [25–28], and the dynamical frame idea of Zhou & Xia [34] can achieve a clean separation for both temperature and velocity fields between their BL and bulk dynamics.

We next turn to the simulation performed at $Pr = 0.7$, a Prandtl number typical for gases, which is relevant in all atmospheric processes and many technical applications. Figures 13.5(a) and (b) show direct comparison between the temperature and velocity profiles, respectively, at $Ra = 10^9$. Again, around the BL-bulk merger range the laboratory frame time-averaged profiles are found to be obviously lower than the Prandtl-Blasius profile. This once more indicates that the time-averaged BL quantities obtained in the laboratory frame are contaminated by the mixed dynamics inside and outside the fluctuating BLs. On the other hand, within the dynamical frame, both $u^*(z_v^*)$ and $\Theta^*(z_{th}^*)$ are found to agree pretty well with the Prandtl-Blasius laminar BL profiles, indicating that the dynamical frame idea works also for the turbulent RB system with working fluids whose Prandtl numbers are of the same order as those for gases.

13.4 Shape factors of velocity and temperature profiles

Let us now quantitatively compare the differences between the Prandtl-Blasius profile and the profiles obtained from both simulations and experiments for various Ra and Pr. The shapes of the velocity and temperature (thermal) profiles, labeled by $i = v$ or $i = th$, can be characterized quantitatively by their shape factors H_i, defined as [222],

$$H_i = \frac{\lambda_i^d}{\lambda_i^m}\,, \quad i = v, th. \tag{13.4}$$

λ_i^d and λ_i^m denote, respectively, the displacement and the momentum thicknesses of the profile, namely,

$$\lambda_i^d = \int_0^\infty \left[1 - \frac{Y(z)}{[Y(z)]_{max}}\right] dz \text{ and } \lambda_i^m = \int_0^\infty \left[1 - \frac{Y(z)}{[Y(z)]_{max}}\right] \frac{Y(z)}{[Y(z)]_{max}} dz. \tag{13.5}$$

Here $Y(z) = u(z)$ is the velocity profile if $i = v$ and $Y(z) = \Theta(z)$ the thermal profile if $i = th$. The deviation of these profiles from the Prandtl-Blasius profile is then measured by

$$\delta H_i = H_i - H_i^{PB}, \tag{13.6}$$

where H_i^{PB} is the shape factor for the respective Prandtl-Blasius laminar BL profile. If a given profile exactly matches the Prandtl-Blasius profile, δH_i is zero. Note that the Prandtl-Blasius velocity profile shape factor $H_v^{PB} = 2.59$ is independent of Pr, while the thermal Prandtl-Blasius BL profile shape factor H_{th}^{PB} varies with Pr.

Figure 13.6(a) shows the shape factors $H_i(Pr)$ of the thermal and the velocity Prandtl-Blasius BL profiles as functions of Pr and figure 13.6(b) shows the corresponding thermal profiles as functions of z_{th}^* for three different Pr. Note that the Prandtl-Blasius velocity BL profile is identical to the thermal one for $Pr = 1$. The two figures show that the thermal shape factor H_{th}^{PB} decreases with decreasing Pr. We attribute this to the decrease of the temperature profiles in the BL range and the

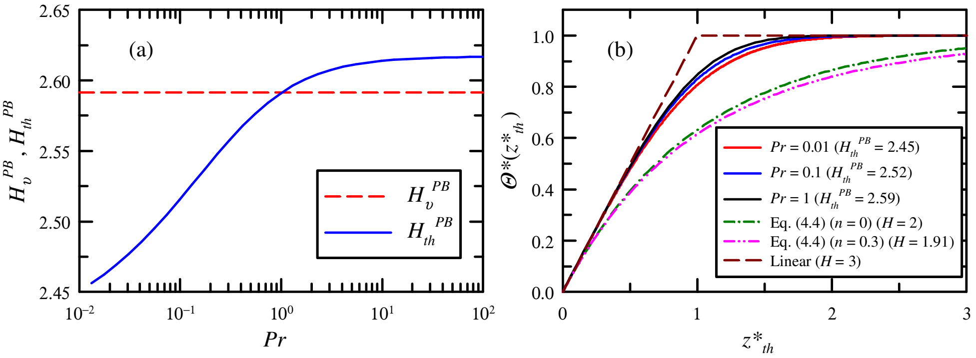

Figure 13.6: (a) The shape factors for the thermal (solid line) and velocity (dashed line) Prandtl-Blasius BL profiles as function of Pr. The asymptotic value $H_{th}^{PB}(Pr \gg 1)$ is 2.61676... and $H_v^{PB} = 2.59$. Both Prandtl-Blasius BL profiles for the velocity and for the temperature coincide for $Pr = 1$. (b) The thermal Prandtl-Blasius BL profiles for three (four) Pr numbers and the reference linear and exponential profiles, see (13.7); in the figure's resolution the thermal profile for $Pr = 100$ is indistinguishable from that of $Pr = 1$. Note that the shape factor of the thermal Prandtl-Blasius BL profile decreases with decreasing Pr due to the slower approach to its asymptotic level 1.

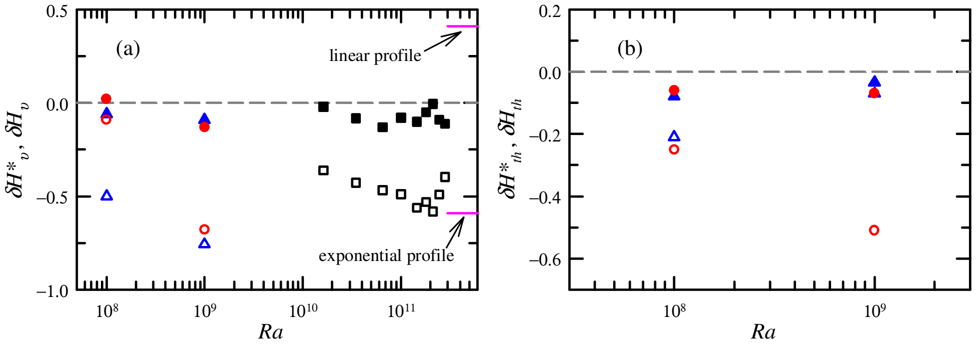

Figure 13.7: The Ra-dependence of the deviations of the profile shape factors from the respective Prandtl-Blasius shape factors. (a) Laboratory frame δH_v (open symbols) and dynamical frame δH_v^* (solid symbols); (b) laboratory frame δH_{th} (open symbols) and dynamical frame δH_{th}^* (solid symbols); all from simulations performed at $Pr = 0.7$ (circles), $Pr = 4.3$ (triangles), and from experiments at $Pr = 5.4$ (squares).

corresponding increase of the tails for lower Pr. Thus we expect that the slower approach to the asymptotic height 1 of the thermal profiles in the laboratory frame in figures 13.4 and 13.5 should lead to a negative deviation of their H_{th}'s from the respective Prandtl-Blasius values, cf. figure 13.7. In contrast, a positive δH_i is obtained if the profile runs to its asymptotic level faster than the Prandtl-Blasius profile. To see this more clearly, we have plotted in figure 13.6(b) also two extreme cases, the linear and the exponential profiles. Using (13.5) one calculates the shape factor 3 for the linear profile $\Theta^*(z^*_{th}) = \min(1, z^*_{th})$ and the shape factor 2 for the exponential one $\Theta^*(z^*_{th}) = 1 - \exp(-z^*_{th})$. The H-decreasing effect by lowering the profile can also be demonstrated by analyzing some profiles analytically. Using a combination of exponential profiles,

$$\Theta^*(z^*_{th}) = 0.5(1-\exp(-(1-n)(z^*_{th})) + 0.5(1-\exp(-(1+n)z^*_{th})), \qquad (13.7)$$

with $0 \leq n < 1$ one can evaluate, using (13.5), that the shape factor for small n is

$$H(n) \approx H(n=0) - n^2 = 2 - n^2. \qquad (13.8)$$

As is shown in figure 13.6(b) the profile for $n > 0$ is below the profile for $n = 0$. This analytical example again reflects what we found as the characteristic difference between the laboratory frame profiles as compared to the dynamical frame profiles.

Figure 13.7(a) shows the velocity shape factor deviations δH_v (open symbols) and δH^*_v (solid symbols) as obtained from simulations at $Pr = 0.7$ (circles) and $Pr = 4.3$ (triangles) as well as from experiments at $Pr = 5.4$ (squares). Here, δH_v is calculated with the time averaged profile $u(z)$ in the laboratory frame, while δH^*_v is calculated with the dynamical, time-dependent frame profile $u^*(z^*_v)$. The laboratoty frame based deviations turn out to be definitely smaller than zero. In contrast, the shape factor deviations δH^*_v for the dynamical frame profiles obviously are much closer to zero. A similar result is found for the thermal BLs: Figure 13.7(b) shows δH_{th} (open symbols) and δH^*_{th} (solid symbols), versus Ra, for the same Pr number simulations. Again δH^*_{th} is nearly zero, whereas δH_{th} is significantly off. Thus these quantitative deviation measures again indicate that the algorithm using the dynamical coordinates can effectively disentangle the mixed dynamics inside and outside the fluctuating BLs.

13.5 Shape of instantaneous velocity and temperature profiles

To further understand the results of our dynamical rescaling method, we study the instantaneous velocity and temperature profiles. Figures 13.8, 13.9, and 13.10 show examples of instantaneous velocity and temperature profiles, where the distance from the plate, z, has been normalized by the instantaneous BL thickness corresponding to that moment and the velocity has been normalized by the instantaneous maximum horizontal velocity. In these figures we also plot the Prandtl-Blasius profiles for comparison and give the instantaneous shape factors. It is seen that most of the time both the velocity and temperature BL profiles are of Prandtl-Blasius type; instantaneous deviations are associated with plume detachments. We note that averaging all these *rescaled* profiles corresponds to the averaging of Eq. (3.2). On the other hand, a simple average of the *unscaled* profiles will distort the shape of the profiles from that of Prandtl-Blasius because of the mixing between BL and bulk dynamics, owing

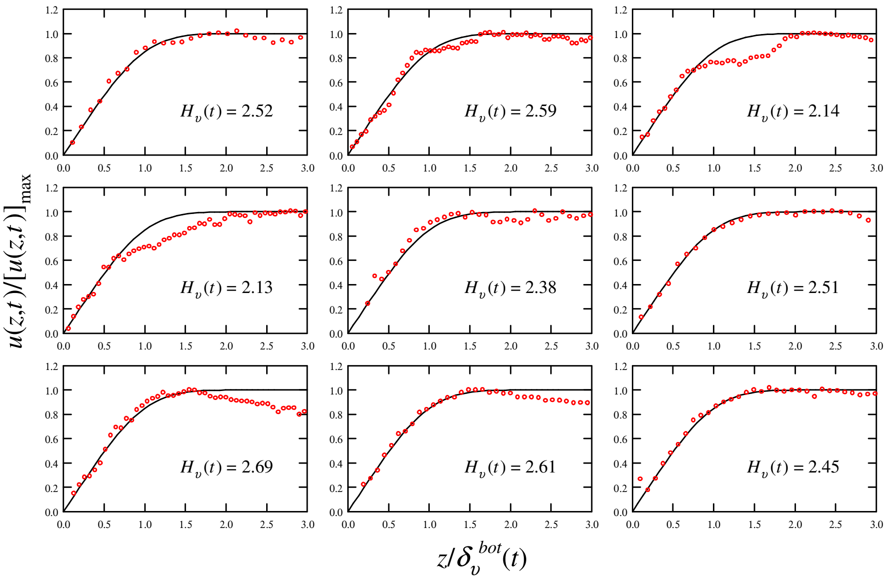

Figure 13.8: Examples of experimental instantaneous horizontal velocity profiles measured at $Ra = 1.8 \times 10^{11}$ and $Pr = 5.4$, and rescaled by the instantaneous kinematic boundary layer thickness and maximum velocity. Here the time average $[u(z)]_{max}$ is 2.2 cm/s and δ_v has a most probable value of $0.004H$. We also give the instanteous shape factors. The solid curves are the Prandtl-Blasius velocity profiles. These examples (and those in figures 13.9 and 13.10) are chosen to show various shapes of profiles observed: the majority have excellent agreement with the PB profile.

to the fluctuations of the BL thickness. This also explains why our method works, i.e., averages of the normalized instantaneous profiles will naturally separate the BL and bulk dynamics, as they are all expressed in the intrinsic BL length scale, which in this case is time-dependent. The properties of the instantaneous profiles can be quantified by their *time-dependent* shape factor $H_i(t)$ ($i = v$ or th). Again, we examine the shape factor difference $\delta H_i(t) = H_i(t) - H_i^{PB}$ for the respective instantaneous profiles and that of the Prandtl-Blasius profile H_i^{PB}. Figures 13.11(a) and 13.11(b) show the probability density functions (PDF) of $\delta H_i(t)$ for the experimental and numerical velocity profiles, respectively. Overall, these PDFs are all peaked close zero, showing that most of the time the velocity profiles are indeed of Prandtl-Blasius type. For the experimental results, the distributions are exactly peaked at zero, except that for the highest $Ra = 2.5 \times 10^{11}$, for which the maximum is slightly off. In addition, comparing to DNS data, the experimental data have broader distributions, which is presumably due to their larger values of Ra (hence greater fluctuations). This is consistent with our analysis in section 13.5 that a more turbulent profile should approach its asymptotic value slower than the PB profile and thus give rise to a negative value of δH_v. The peaks for the numerical data are a bit off zero. These data may also suggest that the PDFs of the shape factors are slightly dependent on Pr. Note that there is

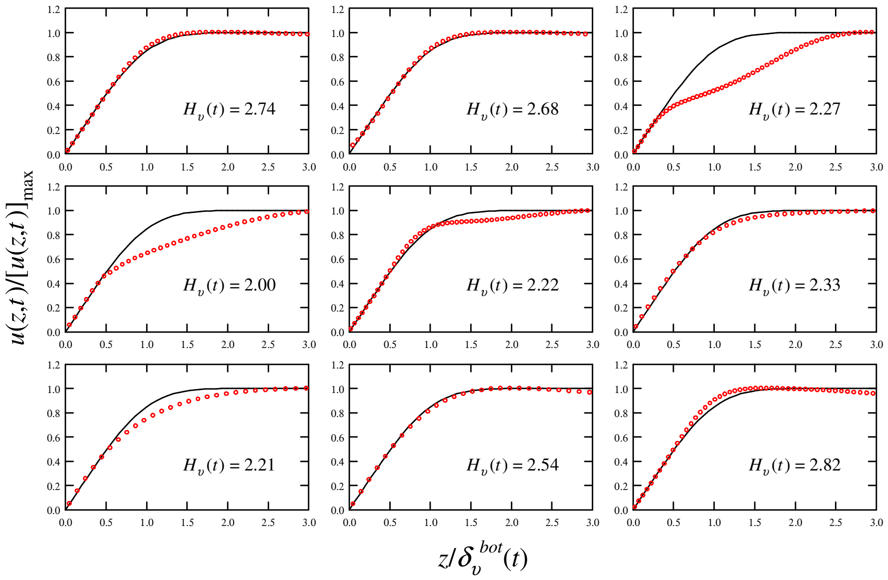

Figure 13.9: Examples of rescaled instantaneous horizontal velocity profiles obtained numerically at $Ra = 10^9$ and $Pr = 0.7$. The mean $[u(z)]_{max}$ is 8.0 cm/s (corresponding to a Reynolds number of $[u(z)]_{max}H/\nu \approx 19\,100$) and δ_v has a most probable value of $0.01H$. The solid curves are the Prandtl-Blasius velocity profiles.

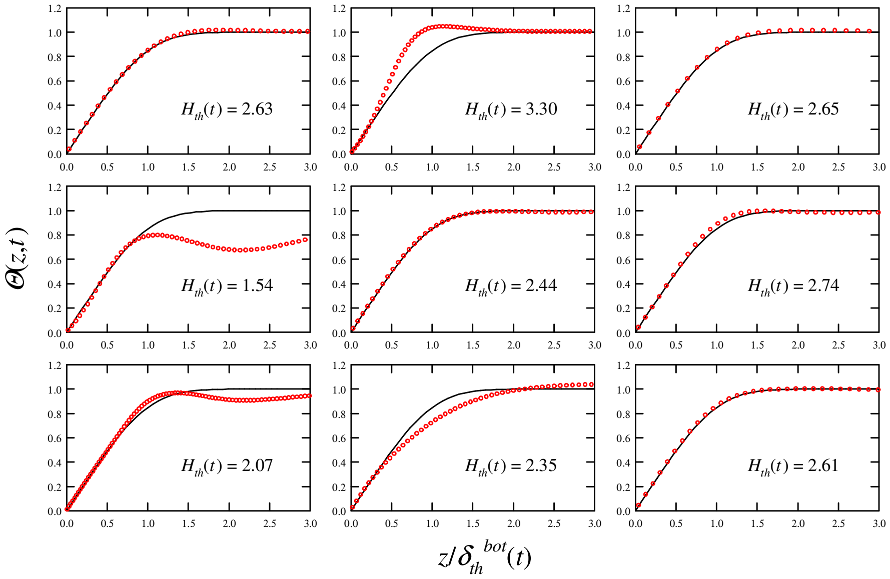

Figure 13.10: Examples of rescaled instantaneous temperature profiles obtained numerically at $Ra = 10^9$ and $Pr = 0.7$. The solid curves are the Prandtl-Blasius temperature profiles. Here δ_{th} fluctuates about its most probable value of $0.012H$.

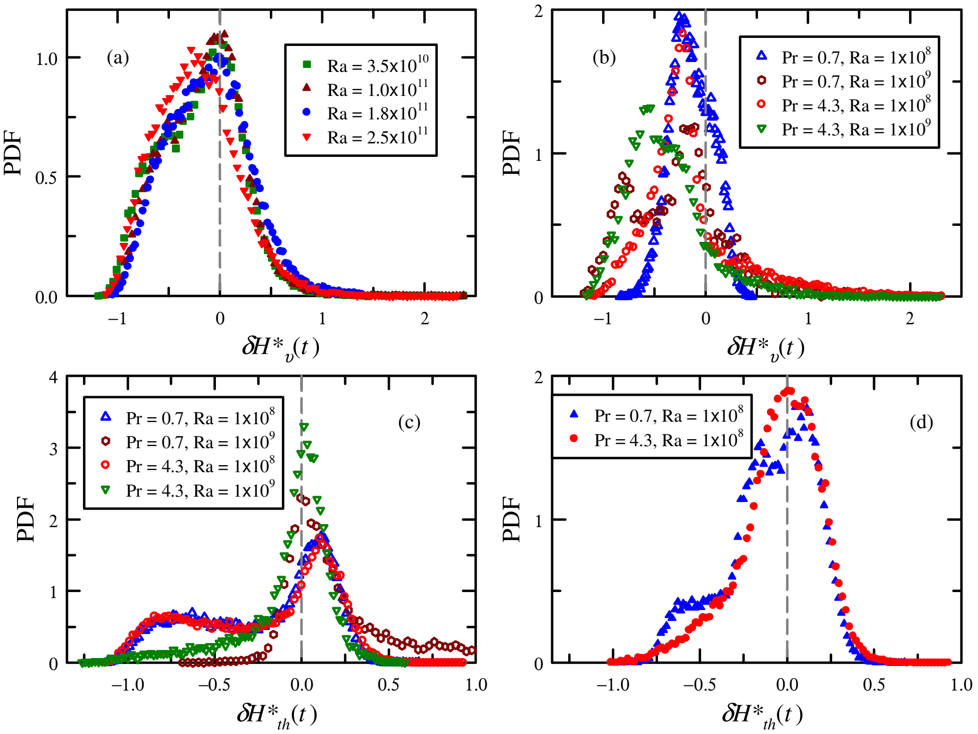

Figure 13.11: PDFs of the shape factor difference between those of the rescaled instantaneous profiles and those of the corresponding Prandtl-Blasius profiles. (a) Experimental velocity data. (b) DNS velocity data. (c) DNS temperature data (profiles saturate at bulk temperature). (d) DNS temperature data (profiles saturate at first maximum). See text for explanation

a minor peak located at $\delta H_v(t) \simeq -0.8$ for the data set $Ra = 10^9$ and $Pr = 0.7$. While we do not know why only this set exhibits this behavior, it is interesting to note that the instantaneous profile shown in figure 13.2(c) has a shape factor $H_v = 1.8$ which corresponds to exactly the shape factor of the minor peak here.

In figure 13.11(c) we show the PDFs for $\delta H_{th}(t)$ from the DNS temperature data. In the examined regime, these PDFs are independent of Pr, but show a certain Ra-dependence. While the high Ra data are peaked exactly at zero, the low Ra data show a minor peak or hump at a negative value. This suggests that there are temperature profiles that have a much slower approach to the asymptotic value. Take, for example, the middle figure in the left panel of figure 13.10: In that plot one can observe that at the position around the BL thickness, $\Theta \simeq 0.8$, i.e., the temperature at the edge of the BL only reaches about 80% of the asymptotic value. This distortion of the BL profile is probably caused by a plume emission that thins the BL thickness corresponding to that instant, while the temperature adjacent to the BL is not able to instantly relax back to the bulk value. Recall that the instantaneous thermal boundary layer thickness is defined through the asymptotic value of Θ (see figure13.2(d)). If we, however,

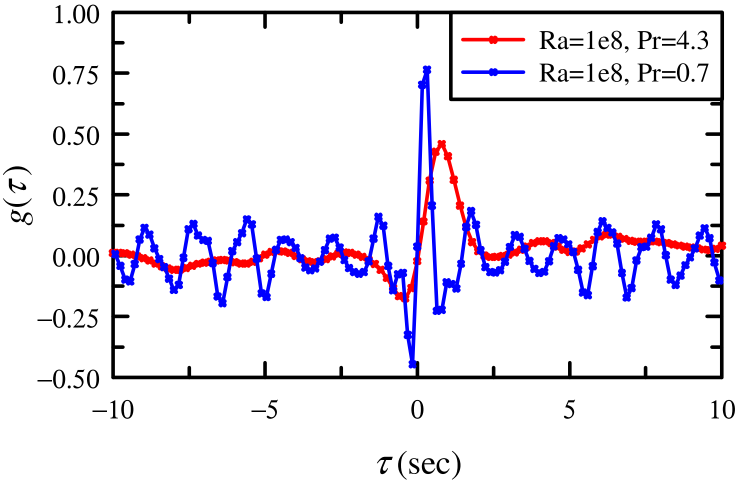

Figure 13.12: Cross-correlation function $g(\tau)$ between $\delta_v(t)$ and $\delta_{th}(t)$.

define the BL thickness as the intersection between the extrapolations of the linear part of the profile and its *first maximum*, the rescaled instantaneous profile looks quite different. Indeed, following this procedure, we can obtain temperature profiles that are much closer to the Prandtl-Blasius type. Figure 13.11(d) shows the PDFs of the shape factor difference for instantaneous rescaled temperature profiles obtain this way. The figure shows that the PDFs for the data sets $Ra = 10^8$, $Pr = 0.7$ and 4.3 now peak at zero and the minor peak seen in figure 13.11(c) is either gone or significantly reduced. We stress, however, that here we use the first maximum instead of the asymptotic value of the temperature profile in the determination of the thermal boundary layer thickness only for the purpose of gaining a better understanding. In order to have a consistent and uniform procedure, all the BL thicknesses presented in this chapter are obtained using the more “traditional” definitions, i.e., those shown in figure 13.2.

13.6 Relationship between $\delta_v(t)$ and $\delta_{th}(t)$

The relation between $\delta_v(t)$ and the external large-scale velocity field has been discussed in detail in Zhou & Xia [34]. Here, we further study the relation between the measured instantaneous kinematic and thermal BL thicknesses. We calculate the cross-correlation function between $\delta_v(t)$ and $\delta_{th}(t)$, i.e., $g(\tau) = \langle[\delta_v(t) - \langle\delta_v(t)\rangle][\delta_{th}(t) - \langle\delta_{th}(t)\rangle]\rangle/\sigma_v\sigma_{th}$, where $\sigma_v = \sqrt{\langle[\delta_v(t) - \langle\delta_v(t)\rangle]^2\rangle}$ and $\sigma_{th} = \sqrt{\langle[\delta_{th}(t) - \langle\delta_{th}(t)\rangle]^2\rangle}$. Figure 13.12 shows two examples of $g(\tau)$ measured at $Pr = 4.3$ and 0.7, respectively. Two features are worthy to note: (i) There is a strong positive correlation between $\delta_v(t)$ and $\delta_{th}(t)$, i.e. a thicker kinematic BL leads to a thicker thermal BL and vice versa; (ii) The positive peak is located at a positive time lag τ_0, indicating that the variations of $\delta_v(t)$ lead the variations of $\delta_{th}(t)$. One can also see that τ_0 for $Pr = 4.3$ is larger than τ_0 for $Pr = 0.7$. The reason for this behavior is that the kinematic boundary layer is thicker than the thermal one at $Pr = 4.3$ and hence a longer time lag is needed for the influence of the kinematic BL to propagate to the thermal BL via momentum diffusion, while the two layers are of the same order at $Pr = 0.7$. This result provides a direct evidence for the interplay between the kinematic BL and the thermal BL.

We also notice oscillations in the cross-correlation functions, which are rather robust for the lower Pr data. The timescale of this oscillation is of the order of 1.5 seconds (3 seconds) for $Pr = 0.7$ ($Pr = 4.3$). This is comparable to $H/[u(z)]_{max}$, which equals 1.58 seconds (3.02 seconds). This immediately suggests a connection to the periodic plume emission model of Villermaux [172]. However, from watching movies of the respective flows, we conclude that the flow organization is more complicated than suggested in that model: Next to the large scale convection roll, corner-flow develop, see chapter 14. Plumes emitted from the BL are first collected by the corner-flow and then partly emitted again. These plumes then hit the thermal BL from the top, leading to further plume emission. This periodic process is more pronounced and more stable at $Pr = 0.7$, leading to stronger long-time correlations. On the other hand, in a 3D system, Xi et al. [149] and Zhou et al. [162] have shown experimentally that thermal plumes are emitted neither periodically nor alternately, but randomly and continuously, from the top and bottom plates. We note that Villermaux's model is 2D and the present numerical simulation is also 2D. Oscillations observed here might then be a major difference between the 2D and 3D systems. Further work beyond the scope of the present thesis will be required to fully settle this issue.

13.7 Conclusions

In summary, we have studied the velocity and temperature BL profiles in turbulent RB convection both numerically and experimentally. We extended previous results to different Prandtl numbers and in particular to thermal BLs. The results show that both the velocity and the temperature BLs (at least in the plates' center region) are of laminar Prandtl-Blasius type in the co-moving dynamical frame in turbulent thermal convection for the parameter ranges studied. However, the fluctuations of the BL widths, induced by the fluctuations of the large-scale mean flow and the emissions of thermal plumes, cause measuring probes at fixed heights above the plate to sample a mixed dynamics, one pertaining to the BL range and the other one pertaining to the bulk. This is the reason why the time-averaged velocity and temperature profiles measured in previous work in fixed laboratory (RB cell) frames deviate from the Prandtl-Blasius profiles. To disentangle that mixed dynamics, we constructed a dynamical BL frame that fluctuates with the instantaneous BL thicknesses. Within this dynamical frame, both velocity and temperature profiles are very well consistent with the classical Prandtl-Blasius laminar BL profiles, both for lower and larger *Pr* (from 0.7 to 5.4). Furthermore, when the instantaneous velocity and temperature are rescaled by their respective instantaneous boundary layer thicknesses, we find that the Prandtl-Blasius profiles not only hold in a time-averaged sense, but most of the time is also true in an instantaneous sense. We have thus extended the time-independent Blasius boundary layer equation or the Prandtl-Blasius boundary layer to the time-dependent case, in the sense that it holds at every instant in the frame that fluctuates with the instantaneous BL thickness.

To conclude, we have validated the idea and algorithm of using dynamical coordinates over a range of *Pr* and *Ra* for both kinematic and thermal BLs and have shown that the Prandtl-Blasius laminar BL profile is a valid description for the BLs of both velocity and temperature in turbulent thermal convection. Laminar Prandtl-Blasius BL theory in turbulent RB thermal convection has thus turned out to indeed be valid not only in terms of the scaling properties, but also in terms of BL profiles as seen from the dynamical frame, co-moving with the local, instantaneous BL widths.

14

Flow reversals in thermally driven turbulence

∗ †

We analyze the reversals of the large scale flow in Rayleigh-Bénard convection both through particle image velocimetry flow visualization and direct numerical simulations (DNS) of the underlying Boussinesq equations in a (quasi) two-dimensional, rectangular geometry of aspect ratio 1. For medium Prandtl number there is a diagonal large scale convection roll and two smaller secondary rolls in the two remaining corners diagonally opposing each other. These corner flow rolls play a crucial role for the large scale wind reversal: They grow in kinetic energy and thus also in size thanks to plume detachments from the boundary layers up to the time that they take over the main, large scale diagonal flow, thus leading to reversal. Based on this mechanism we identify a typical time scale for the reversals. We map out the Rayleigh number vs Prandtl number phase space and find that the occurrence of reversals very sensitively depends on these parameters.

[∗] Based on: K. Sugiyama, R. Ni, R.J.A.M. Stevens, T.S. Chan, S.-Q. Zhou, H.-D Xi, C. Sun, S. Grossmann, K.-Q. Xia, D. Lohse, Flow reversals in thermally driven turbulence, Phys. Rev. Lett. 105, 034503 (2010).

[†] The experiments have been performed in Hong Kong by R. Ni, T.S. Chan, S.-Q. Zhou, H.-D. Xi, C. Sun, and K.-Q. Xia.

14.1 Introduction

Spontaneous flow reversals occur in various buoyancy driven fluid dynamical systems, including large scale flows in the ocean, the atmosphere, or the inner core of stars or the earth, where such reversals are associated with the reversal of the magnetic field. In RB convection flow reversals have been detected and statistically analyzed, mainly through measurements of the temperature at one [166] or several points [98, 156] in the flow or at the walls and more recently through flow visualization with particle image velocimetry (PIV) [155, 161]. Various models have been developed to account for the reversals, either of stochastic nature [157, 167] or based on simplifying (nonlinear) dynamical equations [168, 169], which show chaotic deterministic behavior. Most of the experimental studies have so far been done in a cylindrical cell, where the complicated three-dimensional dynamics of the convection role (see e.g. [149, 163] and section VIII of [20]) complicates the identification of the reversal process.

In the present chapter, we restrict ourselves to the study of flow reversals in (quasi) two-dimensional (2D) rectangular geometry: experimentally to RB convection in a flat cell and numerically to DNS of the two-dimensional Oberbeck-Boussinesq equations, for which reversals have been observed already in [223]. This approach offers three advantages: (i) The flow reversal in quasi-2D is less complicated than in 3D (and therefore of course may be different); (ii) the visualization of the full flow is possible; and (iii) a study of a considerable fraction of the Rayleigh number Ra vs Prandtl number Pr phase space becomes numerically feasible.

14.2 Experimental and numerical method

The experiments were made in rectangular, quasi-2D cells [150]. To extend the range of Ra, two cells of nearly identical geometry are used. The larger (smaller) cell has a horizontal cross section of 24.8×7.5 (12.6×3.8) cm^2, and the heights of the larger (smaller) cell is $H = 25.4$ cm ($H = 12.6$ cm), giving an aspect ratio $\Gamma \approx 1$ in the plane of the main flow (and an aspect ratio of about 0.3 in the direction perpendicular to it). The fluid is water with a mean temperature of 28^oC, corresponding to Pr=5.7. For direct visualization of flow reversals, PIV is used for a few selected Ra. The PIV measurement in this system has also been described previously [150]. To study the statistical properties of the reversals over long time periods, we measure the temperature contrast δT between two thermal probes embedded respectively in the left and right sides of either the top or the bottom plates. Reversals of the upward going hot plumes and downward going cold plumes correspond to the switching between the right and left sides of the system, δT therefore is indicative of reversals.

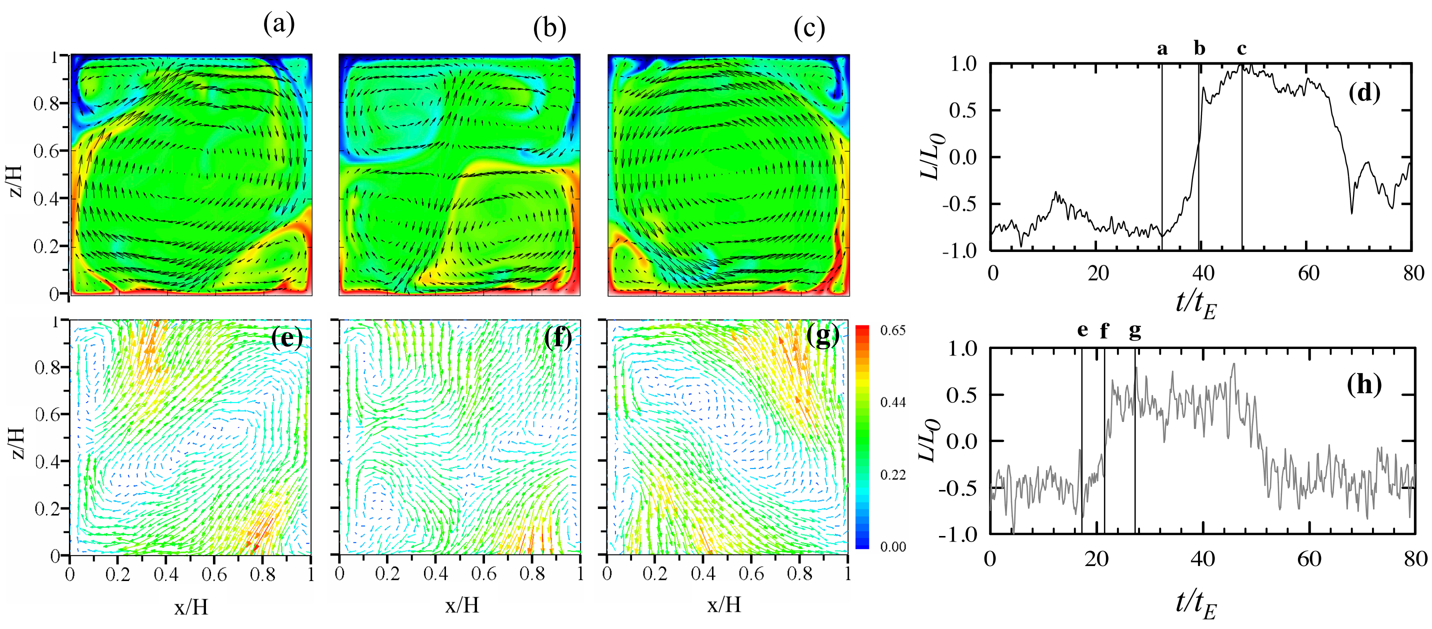

Figure 14.1: Top panel: Snapshots of the temperature (color) and velocity (arrows) field and time trace of angular momentum from numerical simulations ($Ra = 10^8$ and $Pr = 4.3$). Bottom panel: Snapshots of the velocity field and time trace of angular momentum from experiment ($Ra = 3.8 \times 10^8$ and $Pr = 5.7$). (a), (b), and (c) show the instantaneous dimensionless temperature $(T - T_t)/\Delta$ distribution. (d) shows the temporal change of the dimensionless angular momentum $L(t)/L_0$, where L_0 is the maximum of the absolute value of L. The positive and negative signs indicate the anti-clockwise and clockwise circulations, respectively. (e), (f), and (g) show the PIV-measured instantaneous velocity field and (h) the normalized instantaneous angular momentum $L(t)/L_0$. The color bar indicates the magnitude of the velocity (in unit of cm/sec). The snapshots in (a), (b), and (c) give numerical, and those in (e), (f), and (g) give experimental examples of the large scale circulation before, during and after a reversal process, as indicated in (d) and (h) respectively. Note that (b) and (f) show clearly the key role played by the growth of the corner rolls in the reversal process. Corresponding movies are offered in the supplementary material [115].

The numerical code is based on a fourth-order finite-difference discretization of the incompressible Oberbeck-Bousinesq equations and has been described in [106]. The grid resolution has been chosen according to the strict requirements as formulated in chapter 2. As in experiment also the numerical flow is wall-bounded, i.e., we use no-slip boundary conditions at all solid boundaries: $\mathbf{u} = \mathbf{0}$ at the top $(z = H)$ and bottom $(z = 0)$ plates as well as on the side walls $x = 0$ and $x = H$. For the temperature at the side walls heat-insulating conditions are employed and $T_b - T_t = \Delta$ is the temperature drop across the whole cell. Times are given in multiples of the large eddy turnover time t_E, defined by $t_E := 4\pi / \langle|\omega_c(t)|\rangle$, where ω_c denotes the center vorticity.

14.3 Flow reversals

We start by showing qualitative features of the reversal process using examples from both numerical simulations and experiments. Fig.14.1 shows snapshots of the temperature and velocity fields from DNS and those of the velocity field from experiment just before, during, and after the large convection roll reversal. Corresponding videos can be viewed from the supplementary materials [115]. Visually, the reversal process can be easily detected. To automatize this we measure the *local* angular velocity at the center of the cell; however, with this method some plumes passing through the center can lead to erroneous reversal counting. A better way is to rely on a *global* quantity, e.g. the global angular momentum (which has been successfully used for reversal characterization in 2D Navier-Stokes turbulence [106, 224]). This is defined as $L(t) = \langle -(z - H/2)u_x(\boldsymbol{x},t) + (x - H/2)u_z(\boldsymbol{x},t)\rangle_V$, where $\langle ... \rangle_V$ represents averaging over the full volume. The time dependence of L from simulation and experiment, as shown respectively in Figs.14.1(d) and (h), indeed nicely reveals the reversal through a sign-change.

From the movies corresponding to Fig. 14.1 the basic role of the corner flows in the reversal process can be observed: While the main roll is diagonally orientated in the cell, smaller counter-rotating rolls develop in diagonally opposing corners. They are energetically fed by detaching plumes from the boundary layers trapped in the corner flows, leading to their growth. Once the two corner flows have reached a linear extension of $\approx H/2$ [Fig.14.1(b) and moment (b) in Fig.14.1(d) and Fig. 14.1(f) and moment (f) in Fig.14.1(h)], they destroy the main convection roll and establish another one circulating in opposite direction.

The heights $h(t)$ of the corner flows are measured by first fitting the temperature profile at the respective sidewall with splines, and then identifying the position of the steepest gradient of $T(z)$: From movies and snapshots we judge that this is an excellent measure for the height $h(t)$ of the corner-flow. Time series of $h(t)$, together with the (rescaled) center vorticity $\omega_c(t)$ as quantitative measure of the strength of the

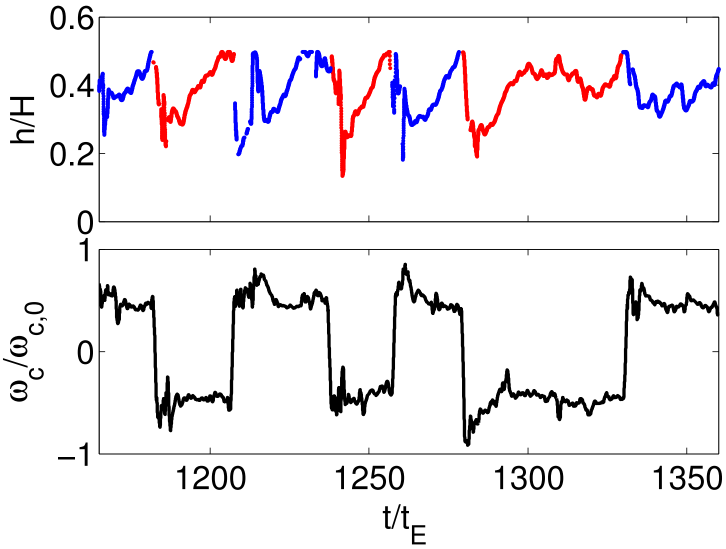

Figure 14.2: Time series of the center vorticity $\omega_c(t)$ (rescaled by its maximum) (lower panel) and the heights h(t) of the lower left (blue) and right (red) corner flows, revealing their approximate linear growth. Not all growth processes need to lead to an immediate successful reversal, as seen for $t/t_E \approx 1300$. $Ra = 10^8$, $Pr = 4.3$.

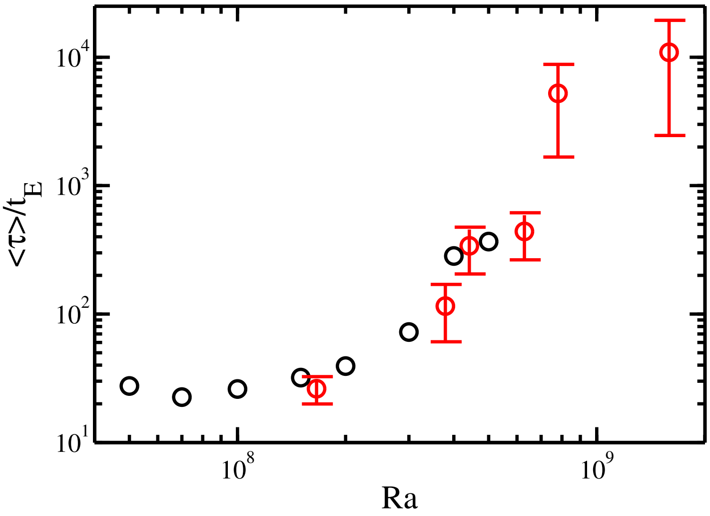

Figure 14.3: Log-log plot of the Ra-dependence of the mean time intervals $\langle\tau\rangle$ between reversals, normalized in terms of the large eddy turnover time t_E. Red symbols are from experiment and black ones from simulation. The error bar originates from the statistics of the reversals; for the numerical case it is smaller than the symbol size.

large scale convection roll, are shown in figure 14.2. It is seen that after a reversal (as indicated by a sign change in $\omega_c(t)$) the respective corner-flow grows roughly linearly in time, before it reaches the half-height $h(t)/H \approx 1/2$ and breaks down, leading to flow reversal. However, the growth of the corner-flow need not always lead to a reversal of the large scale convection roll: There are cases in which the corner-flow looses energy due to some plume detachment from it, leading to full recovery of the large scale convection roll in its orginal direction (e.g., at $t/t_E \approx 1300$ in figure 14.2). Also in experiment we have observed such unsuccessful build-ups of the corner-flow. Below we will try to quantify the energy gains and losses of the corner-flows.

The mean time interval $\langle\tau\rangle$ is shown in Fig. 14.3. Firstly, we clearly see that experiment and simulation are in very good agreement. The figure shows that $\langle\tau\rangle/t_E$ at most weakly depends on Ra up to $Ra \approx 2\times 10^8$, but for larger Ra rapidly increases with increasing Ra, i.e., reversals occur less and less frequently. The numbers mean that there are only very few reversals: of order one per hour in the $Ra \sim 10^8$ range down to one within two days in the $Ra \sim 10^9$ range. For Ra$\geq 5\times 10^8$ no reversals could be detected any more in our numerical simulations, even for an averaging time of 2600 large eddy turnovers. In experiment two reversals could still be observed at Ra$= 1.6\times 10^9$ (presumably due to the longer observation time in experiment which goes beyond 10000 large eddy turnovers, corresponding to four days), but these also cease for larger Ra.

14.4 Model

These findings led us to map out a considerable fraction of the Ra-Pr parameter space. The result is shown in figure 14.4, where the black symbols are from simulation and red symbols are from experiment. One sees a rather complicated structure. But given the limited amount of data, experiment and simulation are in general agreement, especially considering the fact that the simulations are for the true 2D case whereas the experiments run in a quasi-2D cell. It should again be pointed out that the experimental data point with the highest Ra ($= 1.6\times 10^9$) that still shows a reversal has an extremely low reversal rate (0.5/day), which corresponds to waiting for ~ 5500 large scale turn over time for a single reversal to occur.

From figure 14.4 we conclude that not only for too large Ra (as compared to above case of figure 1 with $Ra = 10^8$ and $Pr = 4.3$) the reversals do not occur any more, but also for too large or too small Pr. How to physically understand this complicated behavior? The key towards an understanding lies, from our point of view, in the role of the corner flows, and is based on a detailed observation of many movies at various Ra and Pr (see accompanying material [115]). As stated above, the corner flow rolls are fed by plumes detaching from the plates' boundary layers. For too small Pr (i.e., too large thermal diffusivity) the thermal energy they carry is lost through thermal

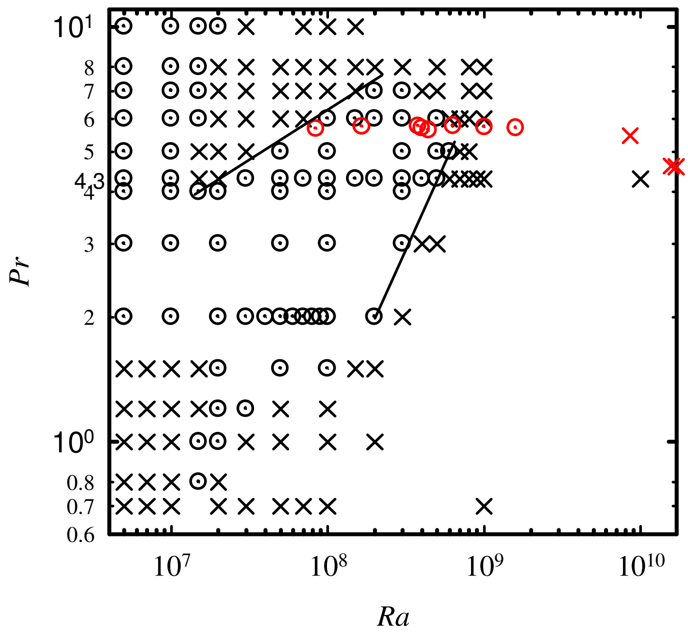

Figure 14.4: Phase diagrams in the Ra-Pr plane. Red symbols are from experiment and the black ones from DNS. Circles correspond to detected reversals, crosses to no detected reversals, in spite of excessive simulation (or observation) time. The straight lines are guides to the eye; they have (from left to right) slopes 0.25 and 1.00. Note that for small Ra and large Pr (upper left corner of the phase diagram) the flow is plume dominated, has a very large coherence length, and no developed rolls exist. However, the angular momentum has zeros.

diffusion.

On the other hand, for too large Pr (i.e., too large kinematic viscosity) the thermal BL is nested in the kinematic BL and the thermal coupling of the corner flow towards the thermal BL is hindered. In both cases the buildup of the corner flow and thus the reversals are suppressed. The situation is similar to the one in rotating RB, where Ekman vortices form, sucking heat out of the thermal BL and enhancing the heat flux: Also here there is an optimal $Pr \approx 10$ for which the Nusselt number is maximal, and for larger or smaller Pr the very same above mechanisms hinder efficient heat transport. This is discussed in chapter 7 of this thesis.

We now quantify this argument. The heat influx feeding the corner flow scales as $J_{in} \sim \kappa \Delta H^{-1} Nu$. The outflux of thermal and kinetic energy is either of diffusive or of convective origin. We model it as $J_{out} = J_{out}^{diff} + J_{out}^{conv}$. Flow reversal is prevented if $J_{out} > J_{in}$. The convective outflux, which is dominant for large Pr, is modeled by $J_{out}^{conv} \sim J_{in} \cdot \lambda_u / \lambda_\theta \sim \kappa \Delta H^{-1} Nu^2 / \sqrt{Re}$. The diffusive outflux is $J_{out}^{diff} \sim \kappa_t \Delta H^{-1} Nu$ with some effective, turbulent thermal diffusivity $\kappa_t = \nu_t / Pr \sim Pr^{-1} U^4 / \varepsilon \sim \kappa Pr^2 Re^4 / (Nu Ra)$, where we have assumed $Pr_t \approx Pr$ and employed the

k-ε-model [225] for the turbulent viscosity ν_t.

For dominant diffusive outflux (thus low Pr), suppression of reversals occurs at $\kappa_t \geq \kappa$. The threshold is given by the scaling relation $NuRa \sim Pr^2 Re^4$. Inserting $Nu(Ra,Pr)$ and $Re(Ra,Pr)$ either from experiment or from the unifying theory of Grossmann and Lohse [25–27], one obtains a relation between the critical Prandtl number Pr_{crit} and the critical Rayleigh number Ra_{crit} at which reversals stop. Depending on whether regime I_u, II_u, or IV_u of refs. [25] is dominant, we obtain $Pr_{crit} \sim Ra_{crit}^{\gamma}$, with $\gamma = 3/5$ or $2/3$, respectively, which correctly reflects the trend in Fig. 14.4.

For large Pr the convective outflux will be dominant. Here the threshold condition is $\kappa \sim \kappa Nu/\sqrt{Re}$, which with $Nu(Ra,Pr)$ and $Re(Ra,Pr)$ in regime I_u of refs. [25] leads to an Ra-independent Pr_{crit}, beyond which no reversals are possible. The reality of figure 14.4 is clearly more complicated, but at least the general trends are consistent with this explanation.

14.5 Conclusions

Finally, we note that we also performed experiments and simulations for $\Gamma = 0.85$. Even for this relatively small change in Γ the overall flow dynamics is very different and much more complex as compared to the case of $\Gamma = 1$. Just as the important role the corner flows play for reversals, this finding demonstrates the strong effect of the cell geometry on the overall flow dynamics in the $\Gamma = \mathcal{O}(\infty)$ regime. In full 3D geometries, it may be less pronounced, but it certainly is present, too, see also ref. [226]. It remains remarkably that the rich structure in the (Ra, Pr, Γ) parameter space for reversals is hardly reflected in Nu and Re.

Part IV

Conclusions

15

Conclusions and Outlook

In this thesis we studied various aspects of turbulent Rayleigh-Bénard (RB) convection using a combination of experimental, numerical, and theoretical techniques. We focused on three different aspect, namely (I) high Rayleigh number thermal convection, (II) rotating RB convection, and (III) two-dimensional RB convection. The most important conclusions for each part of this thesis are summarized below by answering the questions that were formulated in the introduction. At the end of this chapter we conclude with an outlook to the future research on turbulent RB.

15.1 Part I - High Rayleigh number thermal convection

- What effect causes the differences that are observed between the experimental and numerical results shown in figure 1.2?

The differences are due to underresolved plume dynamics in the simulations. In chapter 2 we showed that DNS with sufficient resolution using constant temperature boundary conditions for the horizontal plates are in good agreement with the experimental data of Niemela *et al.* [35–37] and Ahlers *et al.* [39–41]. Previous DNS results by Amati *et al.* [44] showed a Nusselt number that was up to 30% higher than the experimental results. The new simulations have been performed with much higher resolution than the previous ones to properly resolve the plume dynamics. Because in underresolved simulations the hot (cold) plumes travel further from the bottom (top) plate than in the better resolved ones, due to insufficient thermal dissipation close to the sidewall (where the grid cells are largest), the Nusselt number is overestimated in underresolved simulations.

- What numerical resolution should be used in the bulk and the boundary layers to assure that the flow in a DNS is properly resolved?

In chapter 2 we showed that it is crucial to properly resolve the plume dynamics to accurately determine the Nusselt number in DNS and based on these simulations we have defined general resolution criteria that have to be fulfilled to have a fully resolved DNS. Subsequently, we have used the laminar Prandtl-Blasius boundary layer theory in chapter 4 to find a lower bound estimate for the number of computational nodes that should be placed inside the kinetic and thermal boundary layers close to the horizontal plates.

- What effect causes the differences observed between the several experiments for $Ra \gtrsim 10^{11}$?

Although we do not yet know the full answer we can exclude Pr number effects or temperature boundary conditions at the bottom plate as a source for the differences. We have seen in chapter 3 that the practical realization of high Ra number thermal convection involves major technical difficulties (like the use of cryogenic gasses close to the critical point, pressurized fluids or large temperature differences due to which the Boussinesq approximation is not valid anymore, heat leakages, or simply very large systems) that make the correspondence between the experiments and the theoretical model problem uncertain. This has led to large differences between the experimentally measured heat transfers in the high Ra number regime in various labs, see figure 3.2. In chapter 2 and 3 we have used high resolution DNS to study the origin of these differences between the experiments. We presented results from simulations in an aspect ratio $\Gamma = 0.5$ sample with $Pr = 0.7$ up to Rayleigh number $Ra = 2 \times 10^{12}$, which includes the largest spatially resolved turbulent flow simulation ever performed in a closed system. These simulations show good agreement with the experimental results of Niemela *et al.* [35–37] and Ahlers *et al.* [39–41], while the measured heat transport in the experiments of Chavanne *et al.* [38, 53, 54] is visibly higher. In chapter 3 we showed that neither Pr number effects, nor a constant heat flux boundary condition at the bottom plate instead of constant temperature boundary conditions, lead to an increase in $Nu/Ra^{1/3}$. Therefore it is still unclear what imperfections exactly cause the differences between the experiments. However several issues, for example the finite conductivity and the temperature control of the sidewall in the experiments [178], still need to be investigated and we expect that DNS will play a leading roll in these future studies.

- How can one determine from experimental sidewall temperature measurements whether a large scale circulation is present?

In chapter 5 we introduced the relative large scale circulation (LSC) strength, which we define as the ratio between the energy in the first Fourier mode and the energy in all modes that can be determined from the azimuthal temperature and azimuthal vertical velocity profiles, to quantify the large-scale flow. For $Ra = 1 \times 10^8$ we find that this relative LSC strength is significantly lower in a $\Gamma = 1/2$ sample than in a $\Gamma = 1$ sample, reflecting that the LSC is much more pronounced in a $\Gamma = 1$ sample than in a $\Gamma = 1/2$ sample. The determination of the relative LSC strength can be applied directly to available experimental data to study the presence of the LSC in high *Ra* number thermal convection and rotating RB convection, as is shown in chapter 12.

15.2 Part II - Rotating Rayleigh-Bénard convection

- How does the effect of Ekman pumping depend on *Ra* and *Pr*?

We have found that Ekman pumping and associated heat transport enhancement is optimal for *intermediate Pr* numbers. However, its effect is reduced with increasing *Ra* number. In chapter 6 and chapter 7 we studied the effect of Ekman pumping as function of the *Ra*, and *Pr* with experiments, which were performed in the group of Guenter Ahlers in Santa Barbara and, by ourselves, at the Fluid Dynamics Laboratory in Eindhoven, and DNS of rotating RB convection. We found that at fixed *Ro* the effect of Ekman pumping is largest, and thus the observed heat transport enhancement with respect to the non-rotating case highest, at an *intermediate* Prandtl number. At lower *Pr* the effect of Ekman pumping is reduced as more hot fluid that enters the vertically-aligned-vortices at the base spreads out in the middle of the sample due to the large thermal diffusivity of the fluid. At higher *Pr* the thermal boundary layer becomes thinner with respect to the kinetic boundary layer. This means that the temperature of the fluid that enters the vortices at the base is lower for higher *Pr*, which limits the effect of Ekman pumping. In addition, we found that the effect of Ekman pumping reduces with increasing *Ra*. The reason for this is that the turbulent viscosity increases with increasing *Ra*, which means that more heat spreads out in the middle of the sample.

- What happens at the onset of heat transport enhancement?

In chapter 8 and 9 we showed that the heat transport enhancement only occurs above a bifurcation point at a critical inverse Rossby number $1/Ro_c$. We showed that this sharp onset is caused by a transition between two different turbulent states. For weak rotation we find a turbulent state dominated by a large convection roll in the whole cell, and for strong rotation we find a turbulent state dominated by heat transport in vertically-aligned vortices. The DNS showed that no vortices are formed close to the sidewall. This observation allowed us to explain this phenomenon by building on bifurcation theory from low-dimensional chaos, to show that the transition from one turbulent state to the other is a finite-size effect. For samples of infinite size the convection-roll dominated turbulent state does not exist at any finite rotation rate.

- What is the influence of the aspect ratio in rotating RB convection?

In chapter 9 we showed with a Ginzberg-Landau model that the rotation rate at the onset of heat transport enhancement depends on the aspect ratio due to the finite size of the system. It turns out that the onset of heat transport enhancement sets in at a lower rotation rate when the horizontal extent of the system is increased. Subsequently, we showed in chapter 10 that the heat transport becomes independent of the aspect ratio when a sufficiently strong rotation is applied. This is because the fraction of the horizontal area that is covered with vortices becomes independent of the aspect ratio for strong enough rotation. In this regime we found that the effect of the vortex depletion region (closest to the sidewall), and the vortex enhanced region (next to the vortex depletion region), on the average horizontal area that is covered with vortices approximately cancel out. At this moment it is not clear whether this is a general feature or that it depends on Ra and Pr.

- Can the Grossmann-Lohse model be extended in order to describe the heat transfer in rotating RB convection?

This issue is stil open but for the weakly rotating case at relatively low Ra number an extension of GL-theory has been derived. In chapter 11 we showed that the onset of heat transport enhancement does not always show up as a sharp transition, because we find a smooth onset of heat transport enhancement at relatively low Ra. This smooth onset can be understood from a model that extends the GL-theory to the weakly rotating case. However, we emphasize that the GL-theory cannot be extended to describe the heat transfer in the whole rotating phase space, since the framework of the GL-theory does not allow the description of the sharp transitions that are observed at the onset of heat transport enhancement at higher Ra. In addition, one of the main assumptions of the GL-theory, the presence of a domain filling LSC, is not valid anymore in the rotating regime as here vertically-aligned vortices are the dominant flow structures.

- How can changes in the flow structure due to rotation be detected from experimental sidewall temperature measurements?

The measure for the relative strength of the LSC introduced in chapter 5 turned out to be an excellent tool for this purpose. In chapter 12 we concluded that the LSC disappears when a strong enough rotation is applied by showing that the cosine profile in the azimuthal temperature profile, which normally indicates the presence of the LSC, disappears completely in the rotating regime. However, the vertical wall temperature gradient is still observed in the rotating regime. It turns out that the vertical wall temperature gradient in the rotating regime is caused by boundary layer dynamics characteristic for rotating flows, which drives a secondary flow that transports hot fluid up the sidewall in the lower part of the container and cold fluid downwards along the sidewall in the top part.

15.3 Part III - 2D Rayleigh-Bénard convection

- Do the boundary layer profiles in RB convection agree with the prediction of the Prandtl-Blasius theory?

In chapter 13 we used (quasi) 2D RB experiments and 2D simulations to show that the kinetic and thermal boundary layer profiles obtained in experiments and numerical simulation agree excellently with the Prandtl-Blasius profiles, once they are resampled in their respective dynamical reference frame. This result confirms that the boundary layers behave in a laminar way up to a certain *Ra*, as is assumed in the GL theory.

- What mechanism is responsible for the spontaneous flow reversals observed in 2D RB convection?

It is found that the corner rolls play a crucial role in the process of spontaneous reversals. In chapter 14 we also revealed that the presence of spontaneous flow reversals in 2D RB convection strongly depends on *Ra* and *Pr*. Just as heat transport enhancement due to Ekman pumping these flow reversals are only observed for *intermediate* Prandtl numbers. Then there is a diagonal large scale convection roll and two smaller secondary rolls in the two remaining corners diagonally opposing each other. These corner flow rolls play a crucial role for the large scale wind reversal: They grow in kinetic energy and thus also in size thanks to plume detachments from the boundary layers up to the time that they take over the main, large scale diagonal flow, thus leading to reversals. We find that flow reversals do not occur when the corner rolls loose too much energy, because then the corner rolls cannot become strong enough to destroy the main roll. The corner rolls can loose energy due to convective or diffusive outflux. The diffusive outflux increases with decreasing *Pr* or increasing *Ra*, while the convective outflux increases with increasing *Pr*. Therefore flow reversals are only observed for medium *Pr* numbers and not too large *Ra*.

15.4 Future research issues

Since the work of Kolmogorov in 1941 [144] scientists believed that there is only one state of fully developed turbulence. Therefore the sharp transition between different turbulent regimes in rotating RB convection is a paradigm shift in the turbulence community and this phenomenon must be investigated in detail.

Recently, sharp transitions between different turbulent states have also been found in the von Kármán experiment [129, 184] and in rotating turbulent flows with liquid sodium [182, 183], where the increase of the magnetic Reynolds number beyond a certain threshold leads to bifurcations between different turbulent states of the magnetic field. Recently, sharp transitions between different turbulent states have also been observed in high Reynolds number Taylor-Couette flow experiments performed with the Twente turbulent Taylor-Couette setup [227, 228]. It thus seems that for real turbulence, where finite-size effects are unavoidable, there are indeed different states of fully developed turbulence, with a sharp transition in between.

In addition, the recent experiments by Ahlers *et al.* [42] and Roche *et al.* [43] revealed the presence of different turbulent state for Rayleigh $Ra \gtrsim 10^{12}$. In this regime Ahlers *et al.* [42] found different scaling branches, which seem to be triggered by the temperature outside the cell, for the heat transfer as function of Ra. In contrast the experiments of Roche *et al.* [43] indicate the existence of different turbulent states for $Ra \gtrsim 10^{12}$ and $\Gamma = 0.23$. In this case the transition seems to be triggered by the density of the fluid as they find two different scaling branches for $Nu(Ra)$. An upper less steep branch for relatively low fluid density and a lower, but steeper branch for relatively high fluid density. Grossmann and Lohse [63] explained the existence of these different turbulent states by extending the GL-theory to the high Ra number regime by assuming that the kinetic boundary layers become turbulent. However, at this moment it is not clear why a different turbulent state would be triggered by changing the fluid density or the temperature outside the cell.

We must further explore the existence of different turbulent states in closed systems. Important questions are: what determines in what state the turbulent flow is? What are the roles of the boundary layers and how do boundary layers and bulk flow interact? What are the most appropriate observables to characterize the different turbulent states? When does a transition from one to another turbulent state occur? And finally: Can one trigger such a transition?

For RB convection these questions must be investigated by a combination of experimental and numerical work as both methods are complementary. In experiments the challenge would be to further develop the visualization and measurement techniques to be able to characterize the different turbulent flow states. For rotating RB convection, where the transition between the different turbulent states takes place at moderate Ra numbers, this can be obtained by applying direct visualization techniques. However, in high Ra number experiments the systems are not optically accessible. Therefore information from the flow field inside the sample has to be obtained with methods like hot-wire anemometry, which are invasive as a sensor has to be placed inside the flow. In addition, it would be an experimental challenge to exactly control the boundary conditions at the sidewall, which in fact may be the determining factor in which turbulent state the flow ends up.

When the transition between the different turbulent states is studied in DNS the full flow field is available for analysis, while the boundary conditions are exactly defined. However, in simulations the challenge is to obtain the relevant Ra number range, as the largest Ra number that is currently obtained in fully resolved DNS is $Ra = 2 \times 10^{12}$ at $Pr = 0.7$ in an aspect ratio $\Gamma = 0.5$ sample, see chapter 3, which is just below the Ra number range in which the transition between the different turbulent states is observed in experiments. Hence it is required to optimize the numerical codes for the next generation of supercomputers.

When simulations in the high Ra number regime come available the method introduced by Zhou and Xia to analyze the boundary layer profiles [34], which is also used in chapter 13, can be used to check whether the kinetic and/or thermal boundary layer become turbulent. In this case the Prandtl-Blasius profile should change towards a logarithmic profile. This analysis would reveal whether the main assumptions in the extension of the GL-theory to the very high Ra number regime [63], where the boundary layers are expected to become turbulent, are justified. Another effect in high Ra number convection that should be investigated is the effect of non-Oberbeck-Boussinesq effects. These effects come into play when a large temperature difference is applied between the bottom and the top of the sample, because then the fluid properties are different in the boundary layers close to the bottom and top horizontal plate. Fontenele-Araujo *et al.* [105, 136, 220] have already extended the Prandtl-Blasius boundary layer theory to include these non-Oberbeck-Boussinesq effects. To verify these theoretical predictions the resulting profiles should be compared with results from DNS in which the non-Oberbeck-Boussinesq effects are incorporated.

More insight on the mechanisms that cause sharp transitions between different turbulent states will be obtained when these transitions are studied in different systems. Just as RB convection, Taylor-Couette flow seems to be a good candidate to study the existence of different turbulent states. The benefit of both systems is that they are mathematically very well-defined by the Navier-Stokes equations and the appropriate boundary conditions, due to which a combination of theoretical, numerical, and experimental techniques can be applied to analyze the systems. In addition, for both systems several advanced experimental setups are already available. From a numerical point of view a combined study of these two systems is favorable due to the cylindrical geometry of both systems. Hence there is the possibility to transfer numerical procedures for codes that are developed for both systems.

A large part of this thesis was devoted to analyze rotated RB convection. However, as is shown in the rotating RB phase diagrams, see figure 10.1 and 11.1, still only a relatively small part of the rotating RB parameter regime is investigated. We especially note that up to now the rotating high *Ra* number regime has only been achieved in the experiments of Niemela *et al.* [81]. Because many natural phenomenon like the convection in the atmosphere [5] and oceans [6], including the global thermohaline circulation [7], are influence by rotation, while the *Ra* number is very high, it is very important to understand this regime better. It is especially important to know how rotation influenced the different turbulent states that are observed in the high *Ra* number regime.

Part V

Appendices

A

Effects in strongly rotated flows

In this appendix we discuss the Thermal wind balance and the Ekman boundary layer theory in order to familiarize the reader with these effects that come into play in rotating flows.

A.1 Thermal wind balance

Several effects of rotation, like the thermal wind balance and Ekman pumping close to the boundaries are described in textbooks, like Kundu [32] and Greenspan [229]. The thermal wind balance is effective under the influence of strong rotation, i.e. $Ro \ll 1$. Then the effect of viscosity becomes negligible away from the boundaries in the geostrophic interior. Several terms in equation 1.18 can then be discarded. If we in addition assume that there is steady flow, i.e. $\partial/\partial t = 0$ the primary balance of forces (in component form) becomes:

$$\begin{aligned} -2\Omega v &= -\frac{\partial p}{\partial x}, && \text{(A.1)} \\ 2\Omega u &= -\frac{\partial p}{\partial y}, && \text{(A.2)} \\ 0 &= -\frac{\partial p}{\partial z} + g\beta\theta. && \text{(A.3)} \end{aligned}$$

The horizontal balance described here is the geostrophic balance and states that isobars coincide with streamlines. In equation A.3 we recognize the hydrostatic balance, where the density is translated to temperature within the Boussinesq approximation.

Taking the derivative to y of equation A.1 and the derivative to x of equation A.2, we arrive at $-2\Omega(\partial u/\partial x+\partial v/\partial y)=0$. With the condition of incompressibility $\nabla\cdot\mathbf{u}=0$ it follows that

$$\frac{\partial w}{\partial z}=0. \tag{A.4}$$

After differentiating equations A.1 and A.2 with respect to z and using equation A.3, one obtains

$$2\Omega\frac{\partial v}{\partial z} = g\beta\frac{\partial\theta}{\partial x}, \tag{A.5}$$

$$2\Omega\frac{\partial u}{\partial z} = -g\beta\frac{\partial\theta}{\partial y}. \tag{A.6}$$

This is the thermal wind balance. It shows that in rotating flows the horizontal temperature gradients cause vertical gradients in the horizontal velocity components. It also shows that the vertical gradients of the vertical velocity component are always zero, but this does not mean that the vertical velocity has to be zero.

When we in addition assume that the temperature only depends on the vertical coordinate we get the Taylor Proudman case, where

$$\frac{\partial v}{\partial z}=\frac{\partial u}{\partial z}=0. \tag{A.7}$$

Equations A.4 and A.7 show that

$$\frac{\partial\mathbf{u}}{\partial z}=0, \tag{A.8}$$

which means that the velocity vector cannot vary in the direction of $\mathbf{\Omega}$, It shows that the vertical gradients of the velocity are prohibited away from the walls. Note however that the velocities do not have to be zero. This theorem was first derived by Taylor in 1916 and demonstrated experimentally by Taylor soon afterwards.

A.2 Ekman pumping

We consider now a rotating fluid (with the rotation axis vertical) above a horizontal flat plate. The Rossby number is much smaller than one and the flow is quasi-steady. The flow in the bulk is in geostrophic balance, with the velocity $\mathbf{u}_b$, while the velocity in the Ekman boundary layer is $\mathbf{u}_E$. There is a no-slip condition at the horizontal plates, i.e.

$$\mathbf{u}_E=0 \quad at \quad z=0, \tag{A.9}$$

while $\mathbf{u}_E$ is matched to the bulk flow, thus

$$\mathbf{u}_E = \mathbf{u}_b \quad at \quad z \rightarrow \infty. \tag{A.10}$$

Inside the Ekman boundary layer region (of typical thickness δ_E) the approximation is applied that in the viscous term only the vertical derivates are relevant:

$$\begin{aligned} -2\Omega v_E &= -\frac{\partial p_E}{\partial x} + \nu \frac{\partial^2 u_E}{\partial z^2}, & \text{(A.11)} \\ 2\Omega u_E &= -\frac{\partial p_E}{\partial y} + \nu \frac{\partial^2 v_E}{\partial z^2}, & \text{(A.12)} \\ 0 &= -\frac{\partial p_E}{\partial z} + \nu \frac{\partial^2 w_E}{\partial z^2}. & \text{(A.13)} \end{aligned}$$

With the incompressibility condition it is found that the vertical velocity component (w_E) is much smaller than the horizontal components. Furthermore, the vertical derivative of the pressure is assumed to be zero inside the boundary layer (as for the Prandtl-Blasius boundary layer). This allows the matching of p_E and p_b, which gives for p_E:

$$\begin{aligned} -2\Omega v_b = -\frac{\partial p_b}{\partial x} &= -\frac{\partial p_E}{\partial x}, & \text{(A.14)} \\ 2\Omega u_b = -\frac{\partial p_b}{\partial y} &= -\frac{\partial p_E}{\partial y}. & \text{(A.15)} \end{aligned}$$

Combining this with equation A.11 and A.12 gives

$$\begin{aligned} -2\Omega v_E &= -2\Omega v_b + \nu \frac{\partial^2 u_E}{\partial z^2}, & \text{(A.16)} \\ 2\Omega u_E &= +2\Omega u_b + \nu \frac{\partial^2 v_E}{\partial z^2}. & \text{(A.17)} \end{aligned}$$

Multiplying equation A.16 with i and adding equation A.17, gives

$$2i\Omega(u_E + iv_E) = 2i\Omega(u_b + iv_b) + \nu \frac{\partial^2 (u_E + iv_E)}{\partial z^2}. \tag{A.18}$$

Here i indicates the complex number. Solving the differential equation with respect to the boundary conditions gives the following solutions inside the Ekman layer

$$\begin{aligned} u_E &= u_b - [u_b \cos(z/\delta_E) + v_b \sin(z/\delta_E)] \exp(-z/\delta_E), & \text{(A.19)} \\ v_E &= v_b + [u_b \sin(z/\delta_E) - v_b \cos(z/\delta_E)] \exp(-z/\delta_E). & \text{(A.20)} \end{aligned}$$

With the incompressibility condition and $\partial w_b/\partial z = 0$, from assuming the bulk to be in the Taylor-Proudman regime, we find

$$\begin{aligned}
\frac{\partial w_E}{\partial z} &= -\frac{\partial u_E}{\partial x} - \frac{\partial v_E}{\partial y} = \\
&= -\left(\frac{\partial u_b}{\partial x} + \frac{\partial v_b}{\partial y}\right)[1 - \exp(-z/\delta_E)\cos(z/\delta_E)] \\
&\quad + \left(\frac{\partial v_b}{\partial x} - \frac{\partial u_b}{\partial y}\right)[\exp(-z/\delta_E)\sin(z/\delta_E)],
\end{aligned} \tag{A.21}$$

where the first term on the right hand side is zero due to incompressibility (as $\partial u_b/\partial x + \partial v_b/\partial y = 0$, because $\partial w_b/\partial z = 0$ as a result of Taylor Proudman). The term between the brackets in the second part is equal to the z-component of the vorticity ω_b. This simplifies the above to

$$\frac{\partial w_E}{\partial z} = \omega_b \exp(-z/\delta_E)\sin(z/\delta_E), \tag{A.22}$$

Thus the vertical velocity is

$$w_E = \tfrac{1}{2}\omega_b \delta_E \left(1 - \exp(-z/\delta_E)\left[\sin(z/\delta_E) + \cos(z/\delta_E)\right]\right). \tag{A.23}$$

The Ekman boundary layer produces a vertical flow in the bulk interior, which can be found by matching w_b and w_E at $z \to \infty$, which gives

$$w_b = \tfrac{1}{2}\omega_b \delta_E. \tag{A.24}$$

In this way the Ekman boundary layer actively influences the bulk flow. For a positive bulk vorticity this is known as Ekman pumping and for a negative bulk vorticity as Ekman suction.

B

Vortex identification in rotating Rayleigh-Bénard convection *

A major question in rotating Rayleigh-Bénard is how to exactly identify and characterize the vortices from experimentally or numerically obtained velocity maps. In this thesis we use the so-called Q_{2D}-criterion to determine the fraction of the horizontal area that is covered with vortices as function of the rotation rate to show that there is a strong increase in the number of vortices at the onset of heat transport enhancement, see chapter 9. In that chapter we find that the rotation rate at the onset of heat transport enhancement depends on the aspect ratio of the system. This is explained by a Ginzberg-Landau model, which takes the finite size effects of the system into account by assuming that no vortices are formed close to the sidewall. The assumptions of this model are confirmed by the analysis with this method which is explained in this appendix: The results in chapter 9 and 10 confirm that indeed no vortices are formed close to the sidewall.

To identify vortices, the vorticity itself may seem to be an obvious first-hand criterion. However, vorticity is also found in shear dominated regions. Therefore, more complicated quantities need to be used. Many others, e.g. Refs. [187, 230–235], have provided criteria that can be used for the detection of vortices, mostly based on the velocity gradient tensor $\nabla \mathbf{u}$. One can namely use the two-dimensional velocity

---

[*] Based on the EPAPS document of: R.J.A.M. Stevens, J.Q. Zhong, H.J.H. Clercx, G. Ahlers, and D. Lohse, Transitions between Turbulent States in Rotating Rayleigh-Bénard Convection, Phys. Rev. Lett. 103, 024503 (2009).

gradient tensor,

$$\nabla \mathbf{u} = \begin{pmatrix} \frac{\partial u}{\partial x} & \frac{\partial u}{\partial y} \\ \frac{\partial v}{\partial x} & \frac{\partial v}{\partial y} \end{pmatrix}. \tag{B.1}$$

This tensor can be split into a symmetric and antisymmetric part [187]:

$$\nabla \mathbf{u} = \frac{1}{2}\left[\nabla \mathbf{u} + (\nabla \mathbf{u})^T\right] + \frac{1}{2}\left[\nabla \mathbf{u} - (\nabla \mathbf{u})^T\right] = \mathbf{S} + \widetilde{\Omega} \tag{B.2}$$

where $\mathbf{S}$, the symmetric part, is also known as the rate-of-strain tensor, and $\widetilde{\Omega}$, the anitsymmetric part, is also known as the vorticity tensor.

A criterion introduced by Hunt *et al.* [232] (intended for three dimensional flows) is the so-called Q criterion, which defines a vortex as a spatial region where

$$Q \equiv \frac{1}{2}\left(\parallel \widetilde{\Omega} \parallel^2 - \parallel \mathbf{S} \parallel^2\right) > 0, \tag{B.3}$$

with the notation $\parallel A \parallel = \sqrt{\mathrm{Tr}(\mathbf{A}\mathbf{A}^T)}$ the Euclidean form.

Vorobieff & Ecke [74, 96] use a criterion based on the local flow topology: within vortices the eigenvalues of $\nabla \mathbf{u}$ are complex. Hence the vortex detection criterion is (Eq. 2 of Ref. [96]):

$$f \equiv [\mathrm{Tr}(\nabla \mathbf{u})]^2 - 4\det(\nabla \mathbf{u}) < 0 \tag{B.4}$$

The exact form we use in this thesis can be found in [187, 193]

$$Q_{2D} \equiv \left(\frac{\partial u}{\partial x} - \frac{\partial v}{\partial y}\right)^2 + \left(\frac{\partial v}{\partial x} + \frac{\partial u}{\partial y}\right)^2 - \left(\frac{\partial v}{\partial x} - \frac{\partial u}{\partial y}\right)^2 \tag{B.5}$$

In the space occupied by a vortex $Q_{2D} < 0$.

Previous results, based on experimental and numerical data, using the above analysis can be found in Kunnen *et al.* [92], where contour plots at the height $z = 0.5$ and $z = 0.8$ for $Ro = 0.45$ and volume representations for different Ro are given. In addition Kunnen *et al.* [92] determined the number and average size of the vortices close to the plates.

C

Bödewadt, Ekman, von Kármán model [*]

In this appendix the results obtained from the model with weak background rotation will be compared with analytic results obtained from Ekman BL theory [229], which uses a rotating reference frame. In the Ekman case the fluid at infinity is rotating at almost the same velocity as the disk, i.e. the limiting case of the model will be checked. We will indicate all quantities calculated in the rotating reference frame with an asterisk.

We will use the BEK (Bödewadt, Ekman, von Kármán) model, presented in [204, 236, 237], to derive a similar ODE as in section 11.3 for the temperature advection equation in the rotating reference frame. In the BEK model the following self-similarity assumption for the axial velocity is proposed:

$$w = \sqrt{\nu\Omega^*} Ro^* H^*(\xi), \tag{C.1}$$

where $\xi = z\sqrt{\Omega^*/\nu}$. Here, Ω^* is a system rotation rate, and Ro^* is a constant determined by the rotation rate. We call this still the Rossby number since it also represents a dimensionless inverse rotation. In the BEK model Ro^*, $\Delta\Omega$, and Ω^*, respectively, are defined as

$$Ro^* = \frac{\Delta\Omega}{\Omega^*}, \tag{C.2}$$

$$\Delta\Omega = \Omega_F - \Omega_D, \tag{C.3}$$

---

[*] Based on the appendix of: R.J.A.M. Stevens, H.J.H. Clercx, and D. Lohse, Boundary layers in rotating weakly turbulent Rayleigh-Bénard convection, Phys. Fluids, 22, 085103 (2010).

$$\Omega^* = \frac{\Omega_F}{2 - Ro^*} + \frac{\Omega_D}{2 + Ro^*}. \tag{C.4}$$

We obtain the following temperature advection equation in the BEK model

$$\widetilde{\theta}'' = PrH^*(\xi)Ro^*\widetilde{\theta}'. \tag{C.5}$$

From Eqs. (C.2)-(C.4) one obtains, after some algebra,

$$s = \frac{\Omega_F}{\Omega_D} = \left[\frac{2 + Ro^* - Ro^{*2}}{2 - Ro^* - Ro^{*2}}\right]. \tag{C.6}$$

This means for the Ekman case ($s \approx 1$, i.e. $Ro^* \to 0$) that $\Omega_F \simeq \Omega_D(1 + Ro^*)$. Thus when the fluid at infinity is rotating slower than the disk Ro^* is negative. From now on we assume Ro^* to be negative, i.e. $s < 1$.

Using Ekman BL theory [229] one can derive analytic solutions for the radial and tangential velocity profiles in the rotating reference frame. These analytical solutions read [229]:

$$u_E = -\Delta\Omega r e^{-\zeta}\sin\zeta = r\Omega^* Ro^* F^*(\zeta)\ , \tag{C.7}$$

$$v_E = \Delta\Omega r(1 - e^{-\zeta}\cos\zeta) = r\Omega^* Ro^* G^*(\zeta)\ , \tag{C.8}$$

with ζ as in (11.1). With the analytic expression for the radial velocity (C.7) and the continuity equation one obtains

$$\begin{aligned} w_E &= \Delta\Omega\sqrt{\frac{\nu}{\Omega_D}}\left(1 - e^{-\zeta}\left[\sin\zeta + \cos\zeta\right]\right) \\ &= \sqrt{\nu\Omega^*}Ro^* H^*(\zeta)\ . \end{aligned} \tag{C.9}$$

In the case $Ro^* \to 0$ it is found that $\Omega_D \approx \Omega^*$, thus $\xi \approx \zeta$. In particular, the expression for the axial flow reduces to $H^*(\xi) = \sqrt{\Omega^*/\Omega_D}(1 - e^{-\xi}\left[\sin\xi + \cos\xi\right])$, where $\sqrt{\Omega^*/\Omega_D} \approx 1$. We find that the analytic expressions and the above numerical solutions are identical within numerical accuracy for the limiting case (Ekman solution, $s \approx 1, Ro^* \to 0$). (Note that a coordinate transformation has to be applied as the Ekman solution is expressed in the corotating reference frame, whereas the numerical solution has been defined in the laboratory frame.)

Now we use this approach to calculate the BL characteristics for the Ekman layer. With the temperature advection equation (C.5) and the analytic expression $H^*(\xi)$ for the axial velocity we determine the effective scaling exponent γ in $\overline{\lambda}_\theta \sim Pr^\gamma$ as function of Pr for $Ro^* = -10^{-3}$ and $Ro^* = -10^{-5}$. Fig. 11.13 shows that when Ro^* goes to zero the low Pr regime ($\overline{\lambda}_\theta \gg \overline{\lambda}_u$) is extended to higher Pr, because the kinetic BL thickness becomes thinner and the axial velocity becomes smaller, i.e. the thermal BL becomes thicker.

Substitution of $H^*(\xi)$ in (C.5) yields the following expression for the temperature gradient in the Ekman layer

$$\frac{d\widetilde{\theta}}{d\xi} = C_1 e^{\left[\left(e^{-\xi}\cos\xi + \xi\right)PrRo^*\right]}, \tag{C.10}$$

where C_1 is a constant of integration which does not depend on ξ. To determine the constant C_1, and thereby Nu, one needs to integrate Eq. (C.10). An analytic result can be derived by substituting $\cos\xi = (e^{i\xi} + e^{-i\xi})/2$, $A = PrRo^*$, $z = A\xi$, $B = (i-1)/A$ (and $\overline{B}$ the complex conjugate of B), and evaluate the integral

$$\widetilde{\theta}(z) = \frac{C_1}{A} \int e^{z} e^{\frac{1}{2}Ae^{Bz}} e^{\frac{1}{2}Ae^{\overline{B}z}} dz + C_2 \, . \tag{C.11}$$

The integration constants C_1 and C_2 are determined by the boundary conditions $\widetilde{\theta}(\xi = 0) = 1$ and $\widetilde{\theta}(\xi \to \infty) = 0$: $C_2 = 0$ and, for small A,

$$\frac{1}{C_1} \approx \frac{1}{A} - \frac{1}{2}A - \frac{3}{16}A^2 + \mathcal{O}(A^3) \, . \tag{C.12}$$

The thermal BL thickness scales according to $\overline{\lambda}_\theta \propto e^{-A}/C_1$. With (C.12) we immediately see that in the small Prandtl number limit: $\overline{\lambda}_\theta \propto Pr^{-1}$. Comparison with Fig. 11.13b reveals that the analytic results are in good agreement with the numerical data for $\overline{\lambda}_\theta$ represented by the solid lines. Moreover, it predicts the scaling for $Ro^* = -1$ (the von Kármán case, thus far outside the regime of applicability of the Ekman analysis) surprisingly well, see Fig. 11.13b.

References

References

[1] S. Chandrasekhar, *Hydrodynamic and Hydromagnetic Stability* (Dover, New York) (1981).

[2] P. Drazin and W. H. Reid, *Hydrodynamic stability* (Cambridge University Press, Cambridge) (1981).

[3] A. V. Getling, *Rayleigh-Bénard convection: Structures and dynamics* (World Scientific, Singapore) (1998).

[4] E. Bodenschatz, W. Pesch, and G. Ahlers, "Recent developments in Rayleigh-Bénard convection", Ann. Rev. Fluid Mech. **32**, 709–778 (2000).

[5] D. L. Hartmann, L. A. Moy, and Q. Fu, "Tropical convection and the energy balance at the top of the atmosphere", J. Climate **14**, 4495–4511 (2001).

[6] J. Marshall and F. Schott, "Open-ocean convection: Observations, theory, and models", Rev. Geophys. **37**, 1–64 (1999).

[7] S. Rahmstorf, "The thermohaline ocean circulation: A system with dangerous thresholds?", Climate Change **46**, 247–256 (2000).

[8] H. Bryden, H. Longworth, and S. Cunningham, "Slowing of the Atlantic meridional overturning circulation at 25° N", Nature **438**, 655657 (2005).

[9] Q. Schiermeier, "Climate change: A sea change", Nature **439**, 256–260 (2006).

[10] G. Hadley, "Concerning the cause of the general trade-winds", Phil. Trans. R. Soc. Lond. **39**, 58–62 (1735).

[11] A. P. Ingersoll, "Atmosphere dynamics of the outer planets", Science **248**, 308–315 (1990).

[12] M. Heimpel and J. Aurnou, "Turbulent convection in rapidly rotating spherical shells: a model for equatorial and high latitude jets on Jupiter and Saturn", Icarus **187**, 540–557 (2007).

[13] D. Hassler, I. Dammasch, P. Lemaire, P. Brekke, W. Curdt, H. Mason, J.-C. Vial, and K. Wilhelm, "Solar wind outflow and the chromospheric magnetic network", Science **283**, 810–813 (1999).

[14] G. A. Glatzmaier and P. H. Roberts, "A three-dimensional self-consistent computer simulation of a geomagnetic field reversal", Nature **377**, 203–209 (1995).

[15] J. P. Johnston, “Effects of system rotation on turbulence structures: a review relevant to turbomachinery flows”, Int. J. Rot. Mach. **4**, 97–112 (1998).

[16] R. van Wissen, M. Golombok, and J. J. H. Brouwers, “Gas centrifugation with wall condensation”, AIChE Journal **52**, 1271–1274 (2006).

[17] Lord Rayleigh, “On convection currents in a horizontal layer of fluid, when the higher temperature is on the under side”, Phil. Mag. **32**, 529–546 (1916).

[18] H. Bénard, “Les tourbillons cellulaires dans une nappe liquide”, Rev. Gén. Sci. Pur. Appl. **11**, 1261 (1900).

[19] H. Bénard, “Les tourbillons cellulaires dans une nappe liquide transportant de la chaleur par convection en régime permanent”, Ann. Chim. Phys. **23**, 62–144 (1901).

[20] G. Ahlers, S. Grossmann, and D. Lohse, “Heat transfer and large scale dynamics in turbulent Rayleigh-Bénard convection”, Rev. Mod. Phys. **81**, 503 (2009).

[21] D. Lohse and K. Q. Xia, “Small-scale properties of turbulent Rayleigh-Bénard convection”, Annu. Rev. Fluid Mech. **42**, 335–364 (2010).

[22] A. Oberbeck, “über die Wärmeleitung der Flüssigkeiten bei Berücksichtigung der Strömungen infolge von Temperaturdifferenzen”, Ann. Phys. Chem. **7**, 271 (1879).

[23] J. Boussinesq, *Theorie analytique de la chaleur, Vol. 2* (Gauthier-Villars, Paris) (1903).

[24] L. D. Landau and E. M. Lifshitz, *Fluid Mechanics* (Pergamon Press, Oxford) (1987).

[25] S. Grossmann and D. Lohse, “Scaling in thermal convection: A unifying view”, J. Fluid. Mech. **407**, 27–56 (2000).

[26] S. Grossmann and D. Lohse, “Thermal convection for large Prandtl number”, Phys. Rev. Lett. **86**, 3316–3319 (2001).

[27] S. Grossmann and D. Lohse, “Prandtl and Rayleigh number dependence of the Reynolds number in turbulent thermal convection”, Phys. Rev. E **66**, 016305 (2002).

[28] S. Grossmann and D. Lohse, “Fluctuations in turbulent Rayleigh-Bénard convection: The role of plumes”, Phys. Fluids **16**, 4462–4472 (2004).

[29] L. G. Loitsianski and W. Szablewski, *Laminare Grenzschichten*, 2nd edition (Akademie-Verlag, Berlin) (1967).

[30] H. Schlichting, *Boundary layer theory*, 7th edition (McGraw Hill book company, New York) (1979).

[31] E. Guyon, J. P. Hulin, L. Petit, and C. D. Mitescu, *Physical hydrodynamics* (Oxford university press) (2001).

[32] P. K. Kundu and I. M. Cohen, *Fluid mechanics*, 3th edition (Elsevier academic press) (2004).

[33] C. Sun, Y. H. Cheung, and K. Q. Xia, "Experimental studies of the viscous boundary layer properties in turbulent Rayleigh-Bénard convection", J. Fluid Mech. **605**, 79 – 113 (2008).

[34] Q. Zhou and K.-Q. Xia, "Measured instantaneous viscous boundary layer in turbulent Rayleigh-Bénard convection", Phys. Rev. Lett. **104**, 104301 (2010).

[35] J. Niemela, L. Skrbek, K. R. Sreenivasan, and R. Donnelly, "Turbulent convection at very high Rayleigh numbers", Nature **404**, 837–840 (2000).

[36] J. Niemela, L. Skrbek, K. R. Sreenivasan, and R. J. Donnelly, "The wind in confined thermal turbulence", J. Fluid Mech. **449**, 169–178 (2001).

[37] J. Niemela and K. R. Sreenivasan, "Turbulent convection at high Rayleigh numbers and aspect ratio 4", J. Fluid Mech. **557**, 411 – 422 (2006).

[38] X. Chavanne, F. Chilla, B. Chabaud, B. Castaing, and B. Hebral, "Turbulent Rayleigh-Bénard convection in gaseous and liquid he", Phys. Fluids **13**, 1300–1320 (2001).

[39] D. Funfschilling, E. Bodenschatz, and G. Ahlers, "Search for the "ultimate state" in turbulent Rayleigh-Bénard convection.", Phys. Rev. Lett. **103**, 014503 (2009).

[40] G. Ahlers, E. Bodenschatz, D. Funfschilling, and J. Hogg, "Turbulent Rayleigh-Bénard convection for a Prandtl number of 0.67", J. Fluid. Mech. **641**, 157–167 (2009).

[41] G. Ahlers, D. Funfschilling, and E. Bodenschatz, "Transitions in heat transport by turbulent convection at Rayleigh numbers up to 10^{15}", New J. Phys. **11**, 123001 (2009).

[42] G. Ahlers, January 2010, lecture at the Euromech Colloquium in Les Houches, see `http://www.hirac4.cnrs.fr/HIRAC4_-_Talks_files/Ahlers.pdf`

[43] P.-E. Roche, F. Gauthier, R. Kaiser, and J. Salort, "On the triggering of the ultimate regime of convection", New J. Phys. **12**, 085014 (2010).

[44] G. Amati, K. Koal, F. Massaioli, K. R. Sreenivasan, and R. Verzicco, "Turbulent thermal convection at high Rayleigh numbers for a constant-Prandtl-number fluid under Boussinesq conditions", Phys. Fluids **17**, 121701 (2005).

[45] R. H. Kraichnan, "Turbulent thermal convection at arbritrary Prandtl number", Phys. Fluids **5**, 1374–1389 (1962).

[46] E. A. Spiegel, "Convection in stars", Ann. Rev. Astron. Astrophys. **9**, 323–352 (1971).

[47] D. Lohse and F. Toschi, "The ultimate state of thermal convection", Phys. Rev. Lett. **90**, 034502 (2003).

[48] E. Calzavarini, D. Lohse, F. Toschi, and R. Tripiccione, "Rayleigh and Prandtl number scaling in the bulk of Rayleigh-Bénard turbulence", Phys. Fluids **17**, 055107 (2005).

[49] L. Schmidt, D. Lohse, E. Calzavarini, F. Toschi, and R. Verzicco, "Axially-periodic Rayleigh-Bénard convection in a cylindrical cell", submitted to J. Fluid Mech. (2011).

[50] M. Gibert, H. Pabiou, F. Chilla, and B. Castaing, "High-Rayleigh-number convection in a vertical channel", Phys. Rev. Lett. **96**, 084501 (2006).

[51] M. R. Cholemari and J. H. Arakeri, "Experiments and a model of turbulent exchange flow in a vertical pipe", Int. J. Heat Mass Transfer **48**, 4467 – 4473 (2005).

[52] M. R. Cholemari and J. H. Arakeri, "Axially homogeneous, zero mean flow buoyancy-driven turbulence in a vertical pipe", J. Fluid Mech. **621**, 69–102 (2009).

[53] X. Chavanne, F. Chillá, B. Chabaud, B. Castaing, J. Chaussy, and B. Hébral, "High Rayleigh number convection with gaseous helium at low temperature", J. Low Temp. Phys. **104**, 109–129 (1996).

[54] X. Chavanne, F. Chilla, B. Castaing, B. Hebral, B. Chabaud, and J. Chaussy, "Observation of the ultimate regime in Rayleigh-Bénard convection", Phys. Rev. Lett. **79**, 3648–3651 (1997).

[55] J. J. Niemela, L. Skrbek, C. Swanson, S. Hall, K. R. Sreenivasan, and R. J. Donnelly, "New results in cryogenic helium flows at ultra-high Reynolds and Rayleigh numbers", J. Low Temp. Phys. **121**, 417–422 (2000).

[56] J. Niemela and K. R. Sreenivasan, "The use of cryogenic helium for classical turbulence: Promises and hurdles", J. Low Temp. Phys. **143**, 163 – 212 (2006).

[57] R. Verzicco and K. R. Sreenivasan, "A comparison of turbulent thermal convection between conditions of constant temperature and constant heat flux", J. Fluid Mech. **595**, 203–219 (2008).

[58] H. Johnston and C. R. Doering, "Comparison of turbulent thermal convection between conditions of constant temperature and constant flux", Phys. Rev. Lett. **102**, 064501 (2009).

[59] G. Ahlers, "Turbulent convection", Physics **2**, 74 (2009).

[60] P. E. Roche, B. Castaing, B. Chabaud, and B. Hebral, "Observation of the 1/2 power law in Rayleigh-Bénard convection", Phys. Rev. E **63**, 045303 (2001).

[61] P. E. Roche, B. Castaing, B. Chabaud, and B. Hebral, "Prandtl and Rayleigh numbers dependences in Rayleigh-Bénard convection", Europhys. Lett. **58**, 693–698 (2002).

[62] P. E. Roche, B. Castaing, B. Chabaud, and B. Hebral, "Heat transfer in turbulent Rayleigh-Bénard convection below the ultimate regime", J. Low. Temp. Phys. **134**, 1011–1042 (2004).

[63] S. Grossmann and D. Lohse, "Multiple scaling in the ultimate regime of thermal convection", Phys. Fluids **23**, 045108 (2011).

[64] Y. Nakagawa and P. Frenzen, "A theoretical and experimental study of cellular

convection in rotating fluids", Tellus **7**, 1–21 (1955).

[65] P. J. Lucas, J. Pfotenhauer, and R. Donnelly, "Stability and heat transfer of rotating cryogens. part 1. influence of rotation on the onset of convection in liquid ^{4}he", J. Fluid Mech. **129**, 254–264 (1983).

[66] J. M. Pfotenhauer, P. G. J. Lucas, and R. J. Donnelly, "Stability and heat transfer of rotating cryogens. part 2. effects of rotation on heat-transfer properties of convection in liquid He", J. Fluid Mech. **145**, 239–252 (1984).

[67] J. Pfotenhauer, J. Niemela, and R. Donnelly, "Stability and heat transfer of rotating cryogens. part 3. effects of finite cylindrical geometry and rotation on the onset of convection", J. Fluid Mech. **175**, 85–96 (1987).

[68] F. Zhong, R. E. Ecke, and V. Steinberg, "Rotating Rayleigh-Bénard convection: asymmetrix modes and vortex states", J. Fluid Mech. **249**, 135–159 (1993).

[69] J. Lopez, A. Rubio, and F. Marques, "Travelling circular waves in axisymmetric rotating convection", J. Fluid Mech. **569**, 331–348 (2006).

[70] J. Lopez and F. Marques, "Centrifugal effects in rotating convection: nonlinear dynamics", J. Fluid Mech. **628**, 269–297 (2009).

[71] A. Rubio, J. Lopez, and F. Marques, "Onset of Küppers-Lortz-like dynamics in finite rotating thermal convection", J. Fluid Mech. **644**, 337357 (2010).

[72] H. T. Rossby, "A study of Bénard convection with and without rotation", J. Fluid Mech. **36**, 309–335 (1969).

[73] K. Julien, S. Legg, J. McWilliams, and J. Werne, "Hard turbulence in rotating Rayleigh–Bénard convection", Phys. Rev. E **53**, R5557–R5560 (1996).

[74] P. Vorobieff and R. E. Ecke, "Turbulent rotating convection: an experimental study", J. Fluid Mech. **458**, 191–218 (2002).

[75] R. P. J. Kunnen, H. J. H. Clercx, and B. J. Geurts, "Breakdown of large-scale circulation in turbulent rotating convection", Europhys. Lett. **84**, 24001 (2008).

[76] E. M. King, S. Stellmach, J. Noir, U. Hansen, and J. M. Aurnou, "Boundary layer control of rotating convection systems", Nature **457**, 301 (2009).

[77] K. Julien, S. Legg, J. McWilliams, and J. Werne, "Rapidly rotating Rayleigh-Bénard convection", J. Fluid Mech. **322**, 243–273 (1996).

[78] Y. Liu and R. E. Ecke, "Heat transport scaling in turbulent Rayleigh-Bénard convection: effects of rotation and Prandtl number", Phys. Rev. Lett. **79**, 2257–2260 (1997).

[79] Y. Liu and R. E. Ecke, "Heat transport measurements in turbulent rotating Rayleigh-Bénard convection", Phys. Rev. E **80**, 036314 (2009).

[80] J.-Q. Zhong and G. Ahlers, "Heat transport and the large-scale circulation in rotating turbulent Rayleigh-Bénard convection", J. Fluid Mech. **665**, 300–333 (2010).

[81] J. Niemela, S. Babuin, and K. Sreenivasan, “Turbulent rotating convection at high rayleigh and taylor numbers”, J. Fluid Mech. **649**, 509 (2010).

[82] S. Raasch and E. Etling, “Numerical simulation of rotating turbulent thermal convection”, Beitr. Phys. Atmosph. **64**, 185–199 (1991).

[83] K. Julien, S. Legg, J. McWilliams, and J. Werne, “Plumes in rotating convection. part 1. ensemble statistics and dynamical balances”, J. Fluid Mech. **391**, 151–187 (1999).

[84] S. Legg, K. Julien, J. McWilliams, and J. Werne, “Vertical transport by convection plumes: modification by rotation”, Phys. Chem. Earth (B) **26**, 259–262 (2001).

[85] R. P. J. Kunnen, H. J. H. Clercx, and B. J. Geurts, “Heat flux intensification by vortical flow localization in rotating convection”, Phys. Rev. E **74**, 056306 (2006).

[86] R. Kunnen, B. Geurts, and H. Clercx, “Turbulence statistics and energy budget in rotating Rayleigh-Bénard convection”, Eur. J. Mech. B/Fluids **28**, 578 – 589 (2009).

[87] M. Sprague, K. Julien, E. Knobloch, and J. Werne, “Numerical simulation of an asymptotically reduced system for rotationally constrained convection”, J. Fluid Mech. **551**, 141–174 (2006).

[88] S. Schmitz and A. Tilgner, “Heat transport in rotating convection without Ekman layers”, Phys. Rev. E **80**, 015305 (2009).

[89] S. Schmitz and A. Tilgner, “Transitions in turbulent rotating Rayleigh-Bénard convection”, Geophysical and Astrophysical Fluid Dynamics **104**, 481–489 (2010).

[90] P. Oresta, G. Stingano, and R. Verzicco, “Transitional regimes and rotation effects in Rayleigh-Bénard convection in a slender cylindrical cell”, Eur. J. Mech. **26**, 1–14 (2007).

[91] R. P. J. Kunnen, B. J. Geurts, and H. J. H. Clercx, “Experimental and numerical investigation of turbulent convection in a rotating cylinder”, J. Fluid Mech. **82**, 445–476 (2010).

[92] R. P. J. Kunnen, B. J. Geurts, and H. J. H. Clercx, “Vortex statistics in turbulent rotating convection”, Phys. Rev. E **82**, 036306 (2010).

[93] B. M. Boubnov and G. S. Golitsyn, “Temperature and velocity field regimes of convective motions in a rotating plane fluid layer”, J. Fluid Mech. **219**, 215–239 (1990).

[94] S. Sakai, “The horizontal scale of rotating convection in the geostrophic regime”, J. Fluid Mech. **333**, 85–95 (1997).

[95] H. J. S. Fernando, R. Chen, and D. L. Boyer, “Effects of rotation on convective turbulence”, J. Fluid Mech. **228**, 513–547 (1991).

[96] P. Vorobieff and R. E. Ecke, “Vortex structure in rotating Rayleigh–Bénard

convection", Physica D **123**, 153–160 (1998).

[97] R. P. J. Kunnen, H. J. H. Clercx, and B. J. Geurts, "Enhanced vertical inhomogeneity in turbulent rotating convection", Phys. Rev. Lett. **101**, 174501 (2008).

[98] E. Brown and G. Ahlers, "Rotations and cessations of the large-scale circulation in turbulent Rayleigh-Bénard convection", J. Fluid Mech. **568**, 351–386 (2006).

[99] H.-D. Xi, Q. Zhou, and K.-Q. Xia, "Azimuthal motion of the mean wind in turbulent thermal convection", Phys. Rev. E **73**, 056312 (2006).

[100] J. E. Hart, S. Kittelman, and D. R. Ohlsen, "Mean flow precession and temperature probability density functions in turbulent rotating convection", Phys. Fluids **14**, 955–962 (2002).

[101] J. W. Portegies, R. P. J. Kunnen, G. J. F. van Heijst, and J. Molenaar, "A model for vortical plumes in rotating convection", Phys. Fluids **20**, 066602 (2008).

[102] I. Grooms, K. Julien, J. Weiss, and E. Knobloch, "Model of convective Taylor Columns in rotating Rayleigh-Bénard convection", Phys. Rev. Lett. **104**, 224501 (2010).

[103] J. Schmalzl, M. Breuer, S. Wessling, and U. Hansen, "On the validity of two-dimensional numerical approaches to time-dependent thermal convection", Europhys. Lett. **67**, 390–396 (2004).

[104] K. Sugiyama, E. Calzavarini, S. Grossmann, and D. Lohse, "Non-Oberbeck-Boussinesq effects in Rayleigh-Bénard convection:beyond boundary-layer theory", Europhys. Lett. **80**, 34002 (2007).

[105] G. Ahlers, E. Calzavarini, F. Fontenele Araujo, D. Funfschilling, S. Grossmann, D. Lohse, and K. Sugiyama, "Non-Oberbeck-Boussinesq effects in turbulent thermal convection in ethane close to the critical point", Phys. Rev. E **77**, 046302 (2008).

[106] K. Sugiyama, E. Calzavarini, S. Grossmann, and D. Lohse, "Flow organization in two-dimensional non-Oberbeck-Boussinesq Rayleigh-Bénard convection in water", J. Fluid Mech. **637**, 105135 (2009).

[107] R. Verzicco and P. Orlandi, "A finite-difference scheme for three-dimensional incompressible flow in cylindrical coordinates", J. Comput. Phys. **123**, 402–413 (1996).

[108] R. Verzicco and R. Camussi, "Prandtl number effects in convective turbulence", J. Fluid Mech. **383**, 55–73 (1999).

[109] R. Verzicco and R. Camussi, "Numerical experiments on strongly turbulent thermal convection in a slender cylindrical cell", J. Fluid Mech. **477**, 19–49 (2003).

[110] G. Grötzbach, "Spatial resolution for direct numerical simulations of Rayleigh-Bénard convection", J. Comp. Phys. **49**, 241–264 (1983).

[111] J. Schumacher, K. R. Sreenivasan, and P. K. Yeung, "Very fine structures in

scalar mixing", J. Fluid. Mech. **531**, 113–122 (2005).

[112] O. Shishkina and C. Wagner, "Local heat fluxes in turbulent Rayleigh–Bénard convection", Phys Fluids. **19**, 085107 (2007).

[113] B. I. Shraiman and E. D. Siggia, "Heat transport in high-Rayleigh number convection", Phys. Rev. A **42**, 3650–3653 (1990).

[114] X. D. Shang, P. Tong, and K.-Q. Xia, "Scaling of the local convective heat flux in turbulent Rayleigh-Bénard convection", Phys. Rev. Lett. **100**, 244503 (2008).

[115] See the online supplementary material on `http://stilton.tnw.utwente.nl/people/stevensr/`

[116] M. S. Emran and J. Schumacher, "Fine-scale statistics of temperature and its derivatives in convective turbulence", J. Fluid Mech. **611**, 13–34 (2008).

[117] R. P. J. Kunnen, H. J. H. Clercx, B. J. Geurts, L. A. van Bokhoven, R. A. D. Akkermans, and R. Verzicco, "Numerical and experimental investigation of structure function scaling in turbulent Rayleigh-Bénard convection", Phys. Rev. E **77**, 016302 (2008).

[118] O. Shishkina and C. Wagner, "Analysis of sheetlike thermal plumes in turbulent Rayleigh–Bénard convection", J. Fluid Mech. **599**, 383–404 (2008).

[119] M. Kaczorowski and C. Wagner, "Analysis of the thermal plumes in turbulent RayleighBénard convection based on well-resolved numerical simulations", J. Fluid. Mech. **618**, 89–112 (2009).

[120] J. Niemela and K. Sreenivasan, "Does confined turbulent convection ever attain the 'asymptotic scaling' with $1/2$ power?", New J. Phys. **12**, 115002 (2010).

[121] R. J. A. M. Stevens, R. Verzicco, and D. Lohse, "Radial boundary layer structure and Nusselt number in Rayleigh-Bénard convection", J. Fluid. Mech. **643**, 495–507 (2010).

[122] G. Ahlers and X. Xu, "Prandtl-number dependence of heat transport in turbulent Rayleigh-Bénard convection", Phys. Rev. Lett. **86**, 3320–3323 (2001).

[123] K.-Q. Xia, S. Lam, and S. Q. Zhou, "Heat-flux measurement in high-Prandtl-number turbulent Rayleigh-Bénard convection", Phys. Rev. Lett. **88**, 064501 (2002).

[124] R. Verzicco and R. Camussi, "Transitional regimes of low-prandtl thermal convection in a cylindrical cell", Phys. Fluids **9**, 1287–1295 (1997).

[125] R. J. A. M. Stevens, H. J. H. Clercx, and D. Lohse, "Boundary layers in rotating weakly turbulent Rayleigh-Bénard convection.", Phys. Fluids **22**, 085103 (2010).

[126] O. Shishkina, R. J. A. M. Stevens, S. Grossmann, and D. Lohse, "Boundary layer structure in turbulent thermal convection and its consequences for the required numerical resolution", New J. Phys. **12**, 075022 (2010).

[127] X. L. Qiu and K.-Q. Xia, "Viscous boundary layers at the sidewall of a convection cell", Phys. Rev. E **58**, 486–491 (1998).

[128] Q. Zhou, R. J. A. M. Stevens, K. Sugiyama, S. Grossmann, D. Lohse, and K.-Q. Xia, "Prandtl-Blasius temperature and velocity boundary layer profiles in turbulent Rayleigh-Bénard convection", J. Fluid. Mech. **664**, 297312 (2010).

[129] P. Cortet, A. Chiffaudel, F. Daviaud, and B. Dubrulle, "Experimental evidence of a phase transition in a closed turbulent flow", Phys. Rev. Lett. **105**, 214501 (2010).

[130] L. Prandtl, "über flüssigkeitsbewegung bei sehr kleiner reibung", in *Verhandlungen des III. Int. Math. Kongr., Heidelberg, 1904*, 484–491 (Teubner, Leipzig) (1905).

[131] H. Blasius, "Grenzschichten in Flüssigkeiten mit kleiner Reibung", Z. Math. Phys. **56**, 1–37 (1908).

[132] K. Pohlhausen, "Zur nährungsweisen Integration der Differentialgleichung der laminaren Grenzschicht", Z. Angew. Math. Mech. **1**, 252–268 (1921).

[133] D. Meksyn, *New Methods in Laminar Boundary Layer Theory* (Pergamon Press, Oxford) (1961).

[134] R. Kerr, "Rayleigh number scaling in numerical convection", J. Fluid Mech. **310**, 139–179 (1996).

[135] R. Kerr and J. R. Herring, "Prandtl number dependence of nusselt number in direct numerical simulations", J. Fluid Mech. **419**, 325–344 (2000).

[136] G. Ahlers, E. Brown, F. Fontenele Araujo, D. Funfschilling, S. Grossmann, and D. Lohse, "Non-Oberbeck-Boussinesq effects in strongly turbulent Rayleigh-Bénard convection", J. Fluid Mech. **569**, 409–445 (2006).

[137] O. Shishkina and A. Thess, "Mean temperature profiles in turbulent Rayleigh–Bénard convection of water", J. Fluid Mech. **633**, 449–460 (2009).

[138] X. L. Qiu and P. Tong, "Onset of coherent oscillations in turbulent Rayleigh-Bénard convection", Phys. Rev. Lett **87**, 094501 (2001).

[139] E. E. DeLuca, J. Werne, R. Rosner, and F. Cattaneo, "Numerical simulations of soft and hard turbulence - preliminary results for two-dimensional convection", Phys. Rev. Lett. **64**, 2370–2373 (1990).

[140] A. S. Monin and A. M. Yaglom, *Statistical Fluid Mechanics* (The MIT Press, Cambridge, Massachusetts) (1975).

[141] O. Shishkina, A. Shishkin, and A. Thess, "Simulations of turbulent thermal convection in complicated domains", J. Comput. and Appl. Math. **226**, 336–344 (2009).

[142] J. Verdoold, M. van Reeuwijk, M. J. Tummers, H. J. J. Jonker, and K. Hanjalić, "Spectral analysis of boundary layers in Rayleigh–Bénard convection", Phys. Rev. E **77**, 016303 (2008).

[143] E. D. Siggia, "High Rayleigh number convection", Annu. Rev. Fluid Mech.

26, 137–168 (1994).

[144] A. N. Kolmogorov, “The local structure of turbulence in incompressible viscous fluid for very large Reynolds numbers”, CR. Acad. Sci. USSR. **30**, 299 (1941).

[145] G. K. Batchelor, “Small-scale variation of convected quantities like temperature in turbulent fluid. Part 1: General discussion and the case of small conductivity”, J. Fluid Mech. **5**, 113 (1959).

[146] J. Niemela and K. R. Sreenivasan, “Confined turbulent convection”, J. Fluid Mech. **481**, 355–384 (2003).

[147] C. Sun, L.-Y. Ren, H. Song, and K.-Q. Xia, “Heat transport by turbulent Rayleigh-Bénard convection in 1m diameter cylindrical cells of widely varying aspect ratio”, J. Fluid Mech. **542**, 165–174 (2005).

[148] E. Brown, A. Nikolaenko, and G. Ahlers, “Reorientation of the large-scale circulation in turbulent Rayleigh-Bénard convection”, Phys. Rev. Lett. **95**, 084503 (2005).

[149] H. D. Xi, S. Q. Zhou, Q. Zhou, T. S. Chan, and K. Q. Xia, “Origin of temperature oscillations in turbulent thermal convection”, Phys. Rev. Lett. **102**, 044503 (2009).

[150] K.-Q. Xia, C. Sun, and S. Q. Zhou, “Particle image velocimetry measurement of the velocity field in turbulent thermal convection”, Phys. Rev. E **68**, 066303 (2003).

[151] D. Funfschilling and G. Ahlers, “Plume motion and large scale circulation in a cylindrical Rayleigh-Bénard cell”, Phys. Rev. Lett. **92**, 194502 (2004).

[152] C. Sun, K. Q. Xia, and P. Tong, “Three-dimensional flow structures and dynamics of turbulent thermal convection in a cylindrical cell”, Phys. Rev. E **72**, 026302 (2005).

[153] C. Sun, H. D. Xi, and K. Q. Xia, “Azimuthal symmetry, flow dynamics, and heat transport in turbulent thermal convection in a cylinder with an aspect ratio of 0.5”, Phys. Rev. Lett. **95**, 074502 (2005).

[154] E. Brown and G. Ahlers, “Effect of the Earth’s Coriolis force on turbulent Rayleigh-Bénard convection in the laboratory”, Phys. Fluids **18**, 125108–1 – 15 (2006).

[155] H. D. Xi and K. Q. Xia, “Cessations and reversals of the large-scale circulation in turbulent thermal convection”, Phys. Rev. E **75**, 066307 (2007).

[156] E. Brown and G. Ahlers, “Large-scale circulation model for turbulent Rayleigh-Bénard convection”, Phys. Rev. Lett. **98**, 134501 (2007).

[157] E. Brown and G. Ahlers, “A model of diffusion in a potential well for the dynamics of the large-scale circulation in turbulent rayleighbnard convection”, Phys. Fluids **20**, 075101 (2008).

[158] E. Brown and G. Ahlers, “Azimuthal asymmetries of the large-scale circulation

in turbulent RayleighBénard convection", Phys. Fluids **20**, 105105 (2008).

[159] D. Funfschilling, E. Brown, and G. Ahlers, "Torsional oscillations of the large-scale circulation in turbulent Rayleigh-Bénard convection", J. Fluid Mech. **607**, 119139 (2008).

[160] H. D. Xi and K. Q. Xia, "Flow mode transitions in turbulent thermal convection", Phys. Fluids **20**, 055104 (2008).

[161] H. D. Xi and K. Q. Xia, "Azimuthal motion, reorientation, cessation, and reversal of the large-scale circulation in turbulent thermal convection: A comparison between aspect ratio one and one-half geometries", Phys. Rev. E **78**, 036326 (2008).

[162] Q. Zhou, H. D. Xi, S. Q. Zhou, C. Sun, and K. Q. Xia, "Oscillations of the large-scale circulation in turbulent Rayleigh-Bénard convection: the sloshing mode and its relationship with the torsional mode", J. Fluid Mech. **630**, 367–390 (2009).

[163] E. Brown and G. Ahlers, "The origin of oscillations of the large-scale circulation of turbulent Rayleigh-Bénard convection", J. Fluid Mech. **638**, 383–400 (2009).

[164] G. Stringano and R. Verzicco, "Mean flow structure in thermal convection in a cylindrical cell of aspect-ratio one half", J. Fluid Mech. **548**, 1–16 (2006).

[165] P. Mishra, A. De, M. Verma, and V. Eswaran, "Dynamics of reorientations and reversals of large-scale flow in Rayleigh-Bénard convection", J. Fluid. Mech. **668**, 480–499 (2011).

[166] K. R. Sreenivasan, A. Bershadskii, and J. Niemela, "Mean wind and its reversals in thermal convection", Phys. Rev. E **65**, 056306 (2002).

[167] R. Benzi, "Flow reversal in a simple dynamical model of turbulence", Phys. Rev. Lett. **95**, 024502 (2005).

[168] F. Fontenele Araujo, S. Grossmann, and D. Lohse, "Wind reversals in turbulent Rayleigh-Bénard convection", Phys. Rev. Lett. **95**, 084502 (2005).

[169] C. Resagk, R. du Puits, A. Thess, F. V. Dolzhansky, S. Grossmann, F. Fontenele Araujo, and D. Lohse, "Oscillations of the large scale wind in turbulent thermal convection", Phys. Fluids **18**, 095105 (2006).

[170] S. Weiss and G. Ahlers, "Turbulent Rayleigh-Bénard convection in a cylindrical container with aspect ratio Γ=0.50 and Prandtl number Pr = 4.38", J. Fluid. Mech. **x**, y (2011).

[171] J. Bailon-Cuba, M. Emran, and J. Schumacher, "Aspect ratio dependence of heat transfer and large-scale flow in turbulent convection", J. Fluid Mech. **655**, 152–173 (2010).

[172] E. Villermaux, "Memory-induced low frequency oscillations in closed convection boxes", Phys. Rev. Lett. **75**, 4618–4621 (1995).

[173] B. Castaing, G. Gunaratne, F. Heslot, L. Kadanoff, A. Libchaber, S. Thomae,

X. Z. Wu, S. Zaleski, and G. Zanetti, “Scaling of hard thermal turbulence in Rayleigh-Bénard convection”, J. Fluid Mech. **204**, 1–30 (1989).

[174] J.-Q. Zhong, R. J. A. M. Stevens, H. J. H. Clercx, R. Verzicco, D. Lohse, and G. Ahlers, “Prandtl-, Rayleigh-, and Rossby-number dependence of heat transport in turbulent rotating Rayleigh-Bénard convection”, Phys. Rev. Lett. **102**, 044502 (2009).

[175] E. Brown, D. Funfschilling, A. Nikolaenko, and G. Ahlers, “Heat transport by turbulent Rayleigh-Bénard convection: Effect of finite top- and bottom conductivity”, Phys. Fluids **17**, 075108 (2005).

[176] D. Funfschilling, E. Brown, A. Nikolaenko, and G. Ahlers, “Heat transport by turbulent Rayleigh-Bénard convection in cylindrical cells with aspect ratio one and larger”, J. Fluid Mech. **536**, 145–154 (2005).

[177] G. M. Homsy and J. L. Hudson, “Centrifugally driven thermal convection in a rotating cylinder”, J. Fluid Mech. **35**, 33–52 (1969).

[178] R. Verzicco, “Effect of non-perfect thermal sources in turbulent thermal convection”, Phys. Fluids **16**, 1965–1979 (2004).

[179] G. Ahlers, “Effect of sidewall conductance on heat-transport measurements for turbulent Rayleigh-Bénard convection”, Phys. Rev. E **63**, 015303–1 – 4 (2000).

[180] H. G. Schuster, *Deterministic Chaos* (VCH, Weinheim) (1988).

[181] L. Trefethen, A. Trefethen, S. Reddy, and T. Driscol, “Hydrodynamic stability without eigenvalues”, Science **261**, 578–584 (1993).

[182] R. Monchaux, M. Berhanu, M. Bourgoin, M. Moulin, P. Odier, J. F. Pinton, R. Volk, S. Fauve, N. Mordant, F. Petrelis, A. Chiffaudel, F. Daviaud, B. Dubrulle, C. Gasquet, L. Marie, and F. Ravelet, “Generation of a magnetic field by dynamo action in a turbulent flow of liquid sodium”, Phys. Rev. Lett. **98**, 044502 (2007).

[183] F. Ravelet, M. Berhanu, R. Monchaux, S. Aumaitre, A. Chiffaudel, F. Daviaud, B. Dubrulle, M. Bourgoin, P. Odier, N. Plihon, J. F. Pinton, R. Volk, S. Fauve, N. Mordant, and F. Petrelis, “Chaotic dynamos generated by a turbulent flow of liquid sodium”, Phys. Rev. Lett. **101**, 074502 (2008).

[184] F. Ravelet, L. Marié, A. Chiffaudel, and F. Daviaud, “Multistability and memory effect in highly turbulent flow: Experimental evidence for a global bifurcation”, Phys. Rev. Lett. **93**, 164501 (2004).

[185] B. Dubrulle, “Scaling in large prandtl number turbulent thermal convection”, Eur. Phys. J. B **28**, 361–367 (2002).

[186] E. Brown and G. Ahlers, “Temperature gradients, and search for non-boussinesq effects, in the interior of turbulent Rayleigh-Bénard convection”, Europhys. Lett. **80**, 14001 (2007).

[187] R. P. J. Kunnen, “Turbulent rotating convection”, Ph.D. thesis, University of

Eindhoven (2008).

[188] B. M. Boubnov and G. S. Golitsyn, "Experimental study of convective structures in rotating fluids", J. Fluid Mech. **167**, 503–531 (1986).

[189] J. C. McWilliams, "The emergence of isolated coherent vortices in turbulent flow", J. Fluid Mech. **146**, 21 (1984).

[190] G. Ahlers, M. C. Cross, P. C. Hohenberg, and S. Safran, "The amplitude equation near the convective threshold: application to time-dependent experiments", J. Fluid Mech. **110**, 297 (1981).

[191] L. J. A. van Bokhoven, "Experiments on rapidly rotating turbulent flows", Ph.D. thesis, Eindhoven University of Technology (2007).

[192] S. Weiss and G. Ahlers, "Heat transport by turbulent rotating Rayleigh-Bénard convection", submitted to J. Fluid. Mech. (2011).

[193] J. C. McWilliams, "The emergence of isolated coherent vortices in turbulent flow", J. Fluid Mech. **146**, 21–43 (1984).

[194] R. J. A. M. Stevens, J.-Q. Zhong, H. J. H. Clercx, G. Ahlers, and D. Lohse, "Transitions between turbulent states in rotating Rayleigh-Bénard convection", Phys. Rev. Lett. **103**, 024503 (2009).

[195] S. Lam, X. D. Shang, S. Q. Zhou, and K. Xia, "Prandtl-number dependence of the viscous boundary layer and the Reynolds number in Rayleigh-Bénard convection", Phys. Rev. E **65**, 066306 (2002).

[196] M. H. Rogers and G. Lance, "The rotationally symmetric flow of a viscous fluid in the presence of an infinite rotating disk", J. Fluid. Mech. **7**, 617–631 (1960).

[197] L. van Wijngaarden, "On multiple solutions and other phenomena in rotating fluids", Fluid Dyn. Trans. **12**, 157–179 (1985).

[198] P. J. Zandbergen and D. Dijkstra, "Non-unique solutions of the Navier-Stokes equations for the Kármán swirling flow", J. Eng. Math **11**, 167–188 (1977).

[199] E. M. Sparrow and J. L. Gregg, "Heat transfer from a rotating disk to fluids of any Prandtl number", J. Heat Transfer **81**, 249–251 (1959).

[200] N. R. Vira and D. N. Fan, "Temperature distribution in generalized von Karman rotating flows", Numerical heat transfer **3**, 483–497 (1980).

[201] K. Millsaps and K. Pohlhausen, "Heat transfer by laminar flow from a rotating disk", J. of the Aeronautical Sciences **19**, 120–126 (1952).

[202] R. J. Lingwood, "Absolute instability of the boundary layer on a rotating disk", J. Fluid Mech. **299**, 17–33 (1995).

[203] R. J. Lingwood, "An experimental study of absolute instabilities of the rotating-disk boundary-layer flow", J. Fluid Mech. **314**, 373–405 (1996).

[204] R. J. Lingwood, "Absolute instability of the Ekman layer and the related rotating flows", J. Fluid Mech. **331**, 405–428 (1997).

[205] A. J. Colley, P. J. Thomas, P. W. Carpenter, and A. J. Cooper, "An experimen-

tal study of boundary-layer transition over a rotating compliant disk", Phys. Fluids **11**, 3340–3352 (1999).

[206] F. Zoueshtiagh, R. Ali, A. J. Colley, P. J. Thomas, and P. W. Carpenter, "Laminar-turbulent boundary-layer transition over a rough rotating plate", Phys. Fluids **15**, 2441–2444 (2003).

[207] F. H. Busse, "Thermal instabilities in rapidly rotating flows", J. Fluid Mech. **44**, 441–460 (1970).

[208] X. L. Qiu and P. Tong, "Large scale velocity structures in turbulent thermal convection", Phys. Rev. E **64**, 036304 (2001).

[209] K. Stewartson, "On almost rigid rotations", J. Fluid Mech. **3**, 17–26 (1957).

[210] K. Stewartson, "On almost rigid rotations. Part 2", J. Fluid Mech. **26**, 131–144 (1966).

[211] D. W. Moore and P. G. Saffman, "The shear-layer structure in a rotating fluid near a differentially rotating sidewall", Phil. Trans. R. Soc. A **264**, 597 – 634 (1969).

[212] G. J. F. van Heijst, "The shear-layer structure in a rotating fluid near a differentially rotating sidewall", J. Fluid Mech. **130**, 1 – 12 (1983).

[213] G. J. F. van Heijst, "Source-sink flow in a rotating cylinder", J. Engng. Math **18**, 247 – 257 (1984).

[214] G. J. F. van Heijst, "Fluid flow in a partially-filled rotating cylinder", J. Engng. Math. **20**, 233 – 250 (1986).

[215] J. E. Hart and D. R. Olsen, "On the thermal offset in turbulent rotating convection", Phys. Fluids **11**, 2101–2107 (1999).

[216] R. E. Ecke and Y. Liu, "Traveling-wave and vortex states in rotating Rayleigh–Bénard convection", Int. J. Eng. Sci. **36**, 1471–1480 (1998).

[217] E. S. C. Ching, "Heat flux and shear rate in turbulent convection", Phys. Rev. E **55**, 1189–1192 (1997).

[218] M. V. R. Malkus, "The heat transport and spectrum of thermal turbulence", Proc. R. Soc. London A **225**, 196–212 (1954).

[219] B. Dubrulle, "Momentum transport and torque scaling in Taylor-Couette flow from an analogy with turbulent convection", Eur. Phys. J. B **21**, 295 (2001).

[220] G. Ahlers, F. Fontenele Araujo, D. Funfschilling, S. Grossmann, and D. Lohse, "Non-Oberbeck-Boussinesq effects in strongly turbulent Rayleigh-Bénard convection", Phys. Rev. Lett. **98**, 054501 (2007).

[221] R. du Puits, C. Resagk, and A. Thess, "Mean velocity profile in confined turbulent convection", Phys. Rev. Lett. **99**, 234504 (2007).

[222] H. Schlichting and K. Gersten, *Boundary layer theory*, 8th edition (Springer Verlag, Berlin) (2000).

[223] J. Schmalzl, M. Breuer, and U. Hansen, "The influence of the Prandtl number on the style of vigorous thermal convection", Geophys. Astrophys. Fluid Dyn.

96, 381–403 (2002).

[224] G. J. F. van Heijst, H. J. H. Clercx, and D. Molenaar, “The effects of solid boundaries on confined two-dimensional turbulence,”, J. Fluid Mech. **554**, 411–431 (2006).

[225] S. B. Pope, *Turbulent Flow* (Cambridge University Press, Cambridge) (2000).

[226] Z. A. Daya and R. E. Ecke, “Does turbulent convection feel the shape of the container?”, Phys. Rev. Lett. **87**, 184501 (2001).

[227] D. van Gils, S. Huisman, G. W. Bruggert, C. Sun, and D. Lohse, “Torque scaling in turbulent Taylor-Couette flow with co- and counter-rotating cylinders”, Phys. Rev. Lett. **106**, 024502 (2011).

[228] D. van Gils, G. W. Bruggert, D. P. Lathrop, C. Sun, and D. Lohse, “The Twente turbulent Taylor-Couette (t^3c) facility: strongly turbulent (multi-phase) flow between independently rotating cylinders”, Rev. Sci. Instr. **82**, 025105 (2011).

[229] H. P. Greenspan, *The theory of rotating flows* (Breukelen Press, Brookline) (1990).

[230] M. S. Chong, A. E. Perry, and B. J. Cantwell, “A general classification of three-dimensional flow fields”, Phys. Fluids A **2**, 765–777 (1990).

[231] G. Haller, “An objective definition of a vortex”, J. Fluid Mech. **525**, 1–26 (2005).

[232] J. C. R. Hunt, A. Wray, and P. Moin, “Eddies, stream, and convergence zones in turbulent flows”, Report CTR-S88, Center for Turbulence Research (1988).

[233] J. Jeong and F. Hussain, “On the identification of a vortex”, J. Fluid Mech. **285**, 69–94 (1995).

[234] A. Okubo, “Horizontal dispersion of floatable trajectories in the vicinity of velocity singularities such as convergencies”, Deep-Sea Res. **17**, 445–454 (1970).

[235] J. Weiss, “The dynamics of enstrophy transfer in 2-dimensional hydrodynamics”, Physica D **48**, 273–294 (1991).

[236] A. J. Faller, “Instability and transition of disturbed flow over a rotating disk”, J. Fluid Mech. **230**, 245–269 (1991).

[237] H. A. Jasmine and J. S. B. Gajjar, “Absolute instability of the von Kármán, Bödewadt and Ekman flows between a rotating disc and a stationary lid”, Phil. Trans. R. Soc. A **363**, 1131–1144 (2005).

Summary

Turbulent convection in a layer of fluid contained between two parallel plates heated from below and cooled from above, known as RB convection, continues to be a topic of intense research. RB convection is highly relevant to better understand many problems in which heat transfer plays a crucial role. Key-examples include convection in the arctic ocean, in Earth's outer core, in the interior of gaseous giant planets, and in the outer layer of the Sun. Thus the problem is of interest in a wide range of sciences, including geology, oceanography, climatology, and astrophysics. Furthermore, there are various industrial applications, which can only be optimized when heat transfer, and particularly its interplay with rotation, is understood better. Because the RB problem is very cleanly defined it offers unique possibilities to combine experimental, theoretical, and numerical techniques and is hence ideally suited to test new concepts in fluid dynamics.

This thesis covers three main topics: Part I - High Rayleigh number thermal convection, Part II - Rotating RB convection, and Part III - 2D RB convection.

In part I we studied high Ra number thermal convection. There have been several experiments in which the heat transfer in the high Ra number regime was measured. Unfortunately, there are considerable disagreements between some of these experiments. These differences might be caused by the practical difficulties that arise in these measurements. In an attempt to find the effect that is responsible we compare the experimental results with accurate DNS. In chapter 2 we showed that there is a good agreement between experiments and DNSs up to $Ra = 2 \times 10^{11}$ when a sufficient numerical resolution is used. However, when a simulation is underresolved the measured heat transport in the simulations is too high, due to insufficient dissipation of the plumes close to the sidewall. This effect explains the difference observed between experiments and earlier DNS. Based on this experience we formulated general resolution criteria that should be satisfied in a properly resolved DNS. In chapter 3 we extend the simulations presented in chapter 2 up to $Ra = 2 \times 10^{12}$, which is the largest simulation of bounded turbulent flow up to date. In addition, we study the effect of the Pr number and the temperature boundary condition at the bottom plate on the heat transport. The numerical results at $Ra = 2 \times 10^{12}$ are in good agreement with the results of Ahlers et al. and Niemela et al. while there is a visible difference with the Chavanne et al. measurements. The simulations do not show any increase in

$Nu/Ra^{1/3}$, neither due to *Pr* number effects, nor due to a constant heat flux boundary condition at the bottom plate instead of constant temperature boundary conditions. In chapter 4 we determine, based on the laminar Prandtl-Blasius boundary layer theory, a lower bound for the number of computational grid nodes that should be placed inside the boundary layers in DNSs. These estimates have been used throughout this thesis to make sure that the presented simulations are properly resolved. Finally, in chapter 5 we introduce a new method, which uses the data of (numerical) probes placed inside the sidewall (close to the boundary), to determine whether the LSC is present. The method can be applied directly to available experimental data of high *Ra* number experiments to determine the relative LSC strength. In part II we used this method to determine what rotation rate is needed to destroy the LSC in rotating RB convection.

In part II we study rotating RB convection. When the rotation rate is increased the heat transport first increases, before it rapidly decreases due to a suppression of the vertical velocity fluctuations. The initial increase in the heat transport is due to Ekman pumping. In chapter 6 and 7 we show that the effect of Ekman pumping depends strongly on *Ra* and *Pr*. We found that at fixed *Ro* number the effect of Ekman pumping is largest, and thus the observed heat transport enhancement with respect to the non-rotating case highest, at an *intermediate* Prandtl number. At lower *Pr* the effect of Ekman pumping is reduced as more hot fluid that enters the vertically-aligned vortices at the base spreads out in the middle of the sample due to the large thermal diffusivity of the fluid. At higher *Pr* the thermal boundary layer becomes thinner with respect to the kinetic boundary layer. This means that the temperature of the fluid that enters the vortices at the base is lower for higher *Pr*, which limits the effect of Ekman pumping. The effect of Ekman pumping also reduces when *Ra* is increased. This is because the turbulent viscosity increases with increasing *Ra*, which means that more heat spreads out in the middle of the sample. In chapter 8 we find that the onset of heat transport enhancement occurs with a sharp transition, which coincides with a transition between two different turbulent flow states, one dominated by a large convection roll in the whole cell for weak rotation, and one dominated by heat transport in local vertically-aligned vortices for strong rotation. Such a sharp transition is uncommon in turbulence as normally the large random fluctuations in space and time assure that the phase-space is always fully explored by the dynamics, and then transitions between potentially different states that might be explored as a control parameter is changed are washed out. In chapter 9 we find that this sharp transition between the different turbulent states in rotating RB convection is caused by the finite size of the system. Here we show that the rotation rate at onset decreases with increasing aspect ratio. In chapter 10 we study the influence of the aspect ratio on the heat transport for stronger rotation and we find that the heat transport becomes independent of the aspect ratio when the rotation is sufficiently strong. In chapter 11 we study the influence of rotation on the boundary layers close to the horizontal plates. Based on these results we formulate a model to explain the *smooth* heat transport enhancement that is observed for relatively low *Ra* numbers. Finally, in chapter 12 we show, based on numerical simulations and experimental sidewall measurements, that the LSC disappears when a strong enough rotation is applied. However, the vertical wall temperature gradient is still observed. It turns out that the vertical wall temperature gradient in the rotating regime is caused by boundary layer dynamics characteristic for rotating flows. It drives a secondary flow that transports hot fluid up the sidewall in the lower part of the container and cold fluid downwards along the sidewall in the top part.

In part III we study (quasi) 2D RB convection in experiments and DNS. In chapter 13 we characterize the boundary layer profiles close to the horizontal plates. The results show that both the temperature and velocity profiles agree well with the classical Prandtl-Blasius boundary layer profiles. This result further confirms that one of the key assumptions of the Grossmann-Lohse theory is justified. In chapter 14 we analyze the spontaneous flow reversals of the large scale flow in a (quasi) 2D RB system with flow visualization experiments and DNS. For *intermediate Pr* numbers there is a diagonal large scale convection roll and two smaller secondary rolls in the two remaining corners diagonally opposing each other. These corner flow rolls play a crucial role for the large scale wind reversal: They grow in kinetic energy and thus also in size thanks to plume detachments from the boundary layers up to the time that they take over the main large scale diagonal flow, thus leading to reversal.

Samenvatting

In Rayleigh-Bénard convectie wordt een laag vloeistof, die zich tussen twee parallelle platen bevindt, van onderen verwarmd en van boven gekoeld. Er wordt veel onderzoek gedaan aan RB convectie, omdat het probleem zeer relevant is om veel situaties waarin warmte-overdracht een cruciale rol speelt beter te begrijpen. Belangrijke voorbeelden zijn convectie in de Arctische Oceaan, in de buitenste kern van de aarde, in het binnenste van gasvormige planeten, en in de buitenste laag van de zon. Het fenomeen is dus van belang in een breed scala van wetenschappen, zoals geologie, oceanografie, klimatologie en astrofysica. Daarnaast zijn er diverse industriële toepassingen die alleen geoptimaliseerd kunnen worden wanneer warmte-overdracht, en met name de interactie met rotatie, beter begrepen wordt. Het RB probleem is zeer precies omschreven en dit biedt unieke mogelijkheden om experimentele, theoretische en numerieke technieken te combineren. Daardoor is RB convectie bij uitstek geschikt om nieuwe concepten in de stromingsleer te testen.

Dit proefschrift omvat drie hoofdonderwerpen: deel I - Thermische convectie bij hoge Ra getallen, deel II - Roterende RB convectie, en deel III - 2D RB convectie.

In deel I onderzoeken we thermische convectie in het hoge Ra getal regime. Er zijn verschillende experimenten waarbij de warmte-overdracht in dit regime is gemeten. Helaas zijn er aanzienlijke verschillen tussen een aantal van deze experimenten. Deze verschillen kunnen veroorzaakt worden door de praktische moeilijkheden die zich voordoen bij deze metingen. In een poging om het effect dat verantwoordelijk is voor deze verschillen te vinden vergelijken we de experimentele resultaten met nauwkeurige simulaties. In hoofdstuk 2 laten we zien dat er een goede overeenkomst is tussen de experimenten en de simulaties tot $Ra = 2 \times 10^{11}$ wanneer de numerieke resolutie voldoende is. Maar in simulaties die zijn uitgevoerd met een te lage numerieke resolutie is het gemeten warmte-transport te hoog, omdat de pluimen dicht bij de zijwand dan onvoldoende gedissipeerd worden. Dit effect verklaart het verschil tussen experimenten en eerdere simulaties. Op basis van deze ervaring hebben we algemene resolutie criteria geformuleerd waaraan een voldoende opgeloste simulatie moet voldoen. In hoofdstuk 3 breiden we de simulaties gepresenteerd in hoofdstuk 2 uit tot $Ra = 2 \times 10^{12}$, momenteel de grootste simulatie van een turbulente stroming in een volledig afgesloten domein. Daarnaast bestuderen we het effect van Pr en de temperatuur randvoorwaarde aan de bodemplaat op het warmte-transport. De numerieke resultaten voor $Ra = 2 \times 10^{12}$ zijn in goede overeenstemming met de experimentele resultaten van Ahlers et al. en Niemela et al., terwijl er met de metingen van Chavanne et al. een zichtbaar verschil is. De simulaties tonen geen verhoging van $Nu/Ra^{1/3}$, noch als gevolg van Pr effecten, noch als gevolg van een constante warmte-aanvoer bij de bodemplaat in plaats van constante temperatuur. In hoofdstuk 4 bepalen we, op basis van de laminaire Prandtl-Blasius grenslaag theorie, een ondergrens voor het aantal rooster punten dat in de grenslaag geplaatst moet worden. Deze schatting is gebruikt in de rest van dit proefschrift om ervoor te zorgen dat de resolutie in de gepresenteerde simulaties voldoende is. In hoofdstuk 5 introduceren we een nieuwe methode, waarin de gegevens van (numerieke) sensoren geplaatst in (dicht bij) de zijwand, gebruikt worden om te bepalen of de LSC aanwezig is. Deze methode kan direct worden toegepast op beschikbare data van experimenten die zijn uitgevoerd voor hoge Ra getallen om de relatieve LSC sterkte te bepalen. In deel II hebben we deze methode gebruikt om te bepalen bij welke rotatie snelheid de LSC verdwijnt in roterende RB convectie.

In deel II onderzoeken we roterende RB convectie. Als de rotatiesnelheid wordt verhoogd dan neemt het warmte transport eerst toe, voordat het snel afneemt als gevolg van de onderdrukking van de verticale snelheidsvariaties. De aanvankelijke toename van het warmte transport wordt veroorzaakt door Ekmantransport. In hoofdstuk 6 en 7 laten we zien dat het effect van Ekmantransport sterk afhangt van Ra en Pr. We laten zien dat voor vaste Ro het effect van Ekmantransport, en dus de toename in het warmtetransport met betrekking tot het niet-roterende geval, het grootste is voor *tussenliggende* Pr. Bij lagere Pr wordt het effect van Ekmantransport verminderd doordat meer hete vloeistof die de verticaal uitgelijnde wervels binnenkomt bij de basis zich uitspreidt in het midden van de container. Oorzaak is de grotere thermische diffusie van de vloeistof bij lage Pr. Bij hogere Pr is de thermische grenslaag dunner in verhouding tot de kinetische grenslaag. Dit betekent dat de temperatuur van de vloeistof die de wervels bij de basis binnengaat lager is voor hogere Pr. Dit beperkt het effect van Ekmantransport. Het effect van Ekmantransport wordt ook lager wanneer Ra wordt verhoogd. Dit komt doordat de turbulente viscositeit toeneemt met Ra, waardoor meer warmte zich verspreidt in het midden van de container. In hoofdstuk 8 laten we zien dat de toename van het warmtetransport plotseling inzet. Dit komt door een overgang tussen twee verschillende turbulente regimes. Bij zwakke rotatie wordt de stroming gedomineerd door een grote convectie rol in de gehele cel en bij sterke rotatie wordt de stroming gedomineerd door warmtetransport in de lokale verticaal uitgelijnde wervels. Een scherpe overgang tussen verschillende turbulente regimes is ongewoon in turbulentie, omdat meestal de grote willekeurige fluctuaties in ruimte en tijd ervoor zorgen dat de overgangen tussen potentieel verschillende regimes worden afgevlakt. In hoofdstuk 9 laten we zien dat deze scherpe overgang tussen de verschillende turbulente toestanden in roterende RB convectie wordt veroorzaakt door de eindige grootte van het systeem. Hier laten we zien dat de rotatie snelheid waarbij de toename in het warmtetransport begint lager is als het systeem breder is. In hoofdstuk 10 bestuderen we de invloed van de breedte van het systeem op het warmtetransport bij sterkere rotatie en we laten zien dat het warmtetransport niet meer van de breedte afhangt als de rotatie voldoende sterk is. In hoofdstuk 11 bestuderen we de invloed van rotatie op de grenslagen dicht bij de horizontale platen. Op basis van deze resultaten formuleren we een model om de geleidelijke toename in het warmtetransport, die is waargenomen voor relatief lage *Ra*, te verklaren. In hoofdstuk 12 tonen we, op basis van numerieke simulaties en experimentele zijwand metingen, aan dat de LSC verdwijnt wanneer het systeem snel genoeg wordt geroteerd. Maar de verticale temperatuurgradiënt aan de wand wordt nog steeds waargenomen. Het blijkt dat de verticale temperatuurgradiënt aan de wand in het roterende regime wordt veroorzaakt door grenslaag dynamiek, die kenmerkend is voor roterende stromingen. Hierdoor wordt een secundaire stroming, die warme vloeistof omhoog brengt langs de zijwand in het onderste deel van de container en koude vloeistof naar beneden in het bovenste deel van de container, gecreeërd.

In deel III onderzoeken we (quasi) 2D RB convectie in experimenten en simulaties. In hoofdstuk 13 karakteriseren we de grenslaag profielen dicht bij de horizontale platen. De resultaten tonen aan dat de temperatuur en snelheid profielen goed overeenkomen met de klassieke Prandtl-Blasius grenslaag profielen. Dit resultaat bevestigt dat een van de belangrijkste aannames van de Grossmann-Lohse theorie gerechtvaardigd is. In hoofdstuk 14 analyseren we de spontane omkering van de grootschalige wervel in een (quasi) 2D RB systeem door middel van simulaties en experimenten waarin de stroming wordt gevisualiseerd. Voor *tussenliggende Pr* is er een diagonale grootschalige wervel en zwakkere wervels in de resterende twee hoeken schuin tegenover elkaar. Deze wervels in de hoeken spelen een cruciale rol in de omkering van de grootschalige wervel. De kracht van de wervel in de hoeken neemt langzaam toe door pluimen die van de onderplaat loskomen totdat de wervel in de hoek sterk genoeg is om de grootschalige diagonale wervel over te nemen en dit leidt tot een omdraaiing van de grootschalige diagonale wervel.

Scientific output

Publications in peer-reviewed journals

1. J.Q. Zhong, R.J.A.M. Stevens, H.J.H. Clercx, R. Verzicco, D. Lohse, G. Ahlers,
   Prandtl-, Rayleigh-, and Rossby-Number Dependence of Heat Transport in Turbulent Rotating Rayleigh-Bénard Convection,
   Phys. Rev. Lett. 102, 044502 (2009),
   Selected as cover illustration,
   see chapter 6 of this thesis.

2. R.J.A.M. Stevens, J.Q. Zhong, H.J.H. Clercx, G. Ahlers, D. Lohse,
   Transitions between Turbulent States in Rotating Rayleigh-Bénard Convection,
   Phys. Rev. Lett. 103, 024503 (2009),
   see chapter 8 of this thesis.

3. R.J.A.M. Stevens, R. Verzicco, D. Lohse,
   Radial boundary layer structure and Nusselt number in Rayleigh-Bénard convection,
   J. Fluid Mech. 643, 495-507 (2010),
   Most cited J. Fluid Mech. article published since 2010,
   see chapter 2 of this thesis.

4. O. Shishkina, R.J.A.M Stevens, S. Grossmann, D. Lohse,
   Boundary layer structure in turbulent thermal convection and its consequences for the required numerical resolution,
   New J. Phys. 12, 075022 (2010),
   see chapter 4 of this thesis.

5. R.J.A.M. Stevens, H.J.H. Clercx, D. Lohse,
   Optimal Prandtl number for heat transfer enhancement in rotating turbulent Rayleigh-Bénard convection,
   New J. Phys. 12, 075005 (2010),
   Selected as one of New J. of Phys. best papers in 2010,
   see chapter 7 of this thesis.

6. S. Weiss, R.J.A.M. Stevens, J.Q. Zhong, H.J.H. Clercx, D. Lohse, G. Ahlers,
   Finite-size effects lead to supercritical bifurcations in turbulent rotating Rayleigh-Bénard convection,
   Phys. Rev. Lett. 105, 224501 (2010),
   see chapter 9 of this thesis.

7. R.J.A.M. Stevens, H.J.H. Clercx, D. Lohse,
   Boundary layers in rotating weakly turbulent Rayleigh-Bénard convection,
   Phys. Fluids 22, 085103 (2010),
   see chapter 11 of this thesis.

8. Q. Zhou, R. J. A. M. Stevens, K. Sugiyama, S. Grossmann, D. Lohse, K. Q. Xia,
   Prandtl-Blasius temperature and velocity boundary layer profiles in turbulent Rayleigh-Bénard convection,
   J. Fluid Mech. 664, 297312 (2010),
   see chapter 13 of this thesis.

9. K. Sugiyama, R. Ni, R.J.A.M. Stevens, T.S. Chan, S.-Q. Zhou, H.-D Xi, C. Sun, S. Grossmann, K.-Q. Xia, D. Lohse,
   Flow reversals in thermally driven turbulence,
   Phys. Rev. Lett. 105, 034503 (2010),
   see chapter 14 of this thesis.

10. R.J.A.M. Stevens, H.J.H. Clercx, D. Lohse,
    Warmtetransport in een roterende turbulente stroming,
    Nederlands Tijdschrift voor Natuurkunde, February 2010.

11. R.J.A.M. Stevens, H.J.H. Clercx, D. Lohse,
    Effect of Plumes on Measuring the Large Scale Circulation in Turbulent Rayleigh-Bénard Convection,
    submitted to Phys. Fluids (2011),
    see chapter 5 of this thesis.

12. R.J.A.M. Stevens, D. Lohse, R. Verzicco,
    Prandtl and Rayleigh number dependence of heat transport in high Rayleigh number thermal convection,
    submitted to J. Fluid Mech. (2011),
    see chapter 3 of this thesis.

13. R.J.A.M. Stevens, J. Overkamp, D. Lohse, H.J.H. Clercx,
    Disappearance of aspect-ratio dependence of heat transport with increasing rotation rate in turbulent Rayleigh-Bénard convection,
    submitted to Phys. Rev. E (2011),
    see chapter 10 of this thesis.

14. R.P.J.Kunnen, R.J.A.M. Stevens, J. Overkamp, C. Sun, G.J.F. van Heijst, H.J.H. Clercx,
    The role of Stewartson and Ekman layers in turbulent rotating Rayleigh-Bénard convection,
    submitted to J. Fluid Mech. (2011),
    see chapter 12 of this thesis.

Peer reviewed conference proceedings

1. R.J.A.M. Stevens, J.Q. Zhong, H.J.H. Clercx, R. Verzicco, D. Lohse, G. Ahlers, Prandtl-, Rayleigh-, and Rossby-number dependence of heat transport in turbulent rotating Rayleigh-Bnard convection,
   Advances in Turbulence XII, Proceedings of the 12th EUROMECH European Turbulence Conference, Editor: B. Eckhardt, 7-10 September, Marburg, Germany (2009).

2. R.J.A.M. Stevens, H.J.H. Clercx, D. Lohse,
   Euromech, Numerical simulations of Rotating Rayleigh-Bénard convection,
   ERCOFTAC workshop DLES8, Direct and Large-Eddy Simulation 8, Eindhoven (NL), 7 - 9 July 2010, Springer Proceedings, in press (2010).

3. R.J.A.M. Stevens, D. Lohse, R. Verzicco,
   Prandtl and Rayleigh number dependence of heat transport in high Rayleigh number thermal convection,
   Proceedings of the 13th EUROMECH European Turbulence Conference, 12-15 september, Warshaw, Poland (2011), in press.

4. J. Overkamp, R.J.A.M. Stevens, D. Lohse, H.J.H. Clercx,
   Disappearance of aspect-ratio dependence of heat transport with increasing rotation rate in turbulent Rayleigh-Bénard convection,
   Proceedings of the 13th EUROMECH European Turbulence Conference, 12-15 september, Warshaw, Poland (2011), in press.

5. E.P. van der Poel, R.J.A.M. Stevens, D. Lohse,
   Aspect-ratio dependence of heat transport and roll state stability in 2D turbulent Rayleigh-Bénard convection,
   Proceedings of the 13th EUROMECH European Turbulence Conference, 12-15 september, Warshaw, Poland (2011), in press.

Invited and refereed talks

- Numerical simulations of (non)rotating high Ra Rayleigh-Bénard convection, KITP program: The Nature of Turbulence, Santa Barbara, The Netherlands. (April 2011)

- Direct numerical simulations of (rotating) Rayleigh-Bénard convection, Direct and Large-Eddy Simulation 8, Eindhoven, The Netherlands. (July 2010)

- Performing direct numerical simulations of very high Rayleigh number turbulent convection in fully confined geometries, Huygens user day, Amsterdam, The Netherlands. (May 2010)

- Measuring the large scale circulation in (rotating) Rayleigh-Bénard convection, Euromech Colloqium 520, High Ra convection, Les Houches, France. (January 2010)

- Prandtl and Rossby-number dependence of heat transport in Rayleigh-Bénard convection, Annual Meeting of Stichting FOM, Veldhoven, The Netherlands. (January 2010)

- Transitions between different turbulent states in rotating Rayleigh-Bénard Convection, 12^{th} European Turbulence Conference, Marburg, Germany. (September 2009)
- Heat transport in rotating turbulent flow, Finale Shell Bachelor Master Prijs 2008, Enschede, The Netherlands. (March 2009)

Contributed talks

- Two- and three-dimensional high Rayleigh number Rayleigh-Bénard simulations, 63^{th} meeting of the Division of Fluid Dynamics, Long Beach, USA. (November 2010)
- Aspect ratio dependence of heat transport in rotating turbulent Rayleigh-Bénard convection for $Pr = 4.38$, 63^{th} meeting of the Division of Fluid Dynamics, Long Beach, USA. (November 2010)
- Prandtl and Rossby-number dependence of heat transport in Rayleigh-Bénard convection, EuroMech Colloquium 519 Mixing and dispersion in flows dominated by rotation and buoyancy, Kerkrade, The Netherlands. (June 2010)
- Direct numerical simulations of (rotating) Rayleigh-Bénard convection, Taylor Couette workshop, Enschede, The Netherlands. (June 2010)
- Prandtl and Rossby-number dependence of heat transport in Rayleigh-Bénard convection, Annual turbulence contact day, Delft, The Netherlands. (June 2010)
- Optimal Prandtl number for heat transfer in rotating Rayleigh-Bénard convection, 62^{nd} meeting of the Division of Fluid Dynamics, Minneapolis, USA. (November 2009)
- Radial boundary layer structure and Nusselt number in Rayleigh-Bénard convection, International symposium on turbulence, Beijing, China. (September 2009)
- Radial boundary layer structure and Nusselt number in Rayleigh-Bénard convection, Solving the Riddle of Turbulence: What, Why and How?, Göttingen, Germany. (May 2009)
- Prandtl-, Rayleigh-, and Rossby-number dependence of heat transport in Rayleigh-Bénard convection, Burgerdag, Eindhoven, The Netherlands. (January 2009)
- Prandtl-, Rayleigh-, and Rossby-number dependence of heat transport in turbulent rotating Rayleigh-Bénard convection, 61^{st} meeting of the Division of Fluid Dynamics, San Antonio, USA. (November 2008)
- Rotating turbulent Rayleigh-Bénard convection: Effect of weak rotation on boundary layers and heat transfer, 7^{th} European Fluid Mechanics Conference, Manchester, UK. (September 2008)
- Rotating turbulent Rayleigh-Bénard convection: Effect of weak rotation on boundary layers and heat transfer, 28^{th} Dynamics Days, Delft, The Netherlands. (August 2008)

- Rotating turbulent Rayleigh-Bénard convection: Effect of weak rotation on boundary layers and heat transfer, Annual turbulence contact day, Enschede, The Netherlands. (June 2008)

Posters

- DEISA PRACE Symposium 2011, Helsinki, Finland. (April 2011)
- Annual Meeting of Stichting FOM, Veldhoven, The Netherlands. (January 2011)
- Annual Meeting of Stichting FOM, Veldhoven, The Netherlands. (January 2010)

Supervised student projects

- Erwin van der Poel, Wind reversal in thermally driven turbulence, Master Thesis. (since 12/10)
- Daniel Albernaz, Direct numerical simulations of turbulent Taylor-Couette, Scientific internship. (08/10-10/10)
- Jim Overkamp, Rotating Rayleigh-Bénard convection in cylindrical cells with aspect ratios one and two, Master thesis. (09/09-07/10)

Teaching experience

- Lecturer and teaching assistent for the 1^{st} year Master course ”Turbulence” for the study Applied Physics in Twente. (2008-2011)
- Teaching assistant for the 1^{st} year Bachelor course ”Experimenteren 2” for the study Applied Physics in Twente. (2006-2008)
- Teaching assistant for the 1^{st} year Bachelor course ”Herstelonderwijs wiskunde” for the studies Applied Physics and Applied Mathematics in Twente. (2006-2007)
- Teaching assistant for the 1^{st} year Bachelor course ”Calculus 1” for the study Mechanical Engineering in Twente. (2006)
- Teaching assistant for the 1^{st} year Bachelor course ”Experimenteren 1” for the study Applied Physics in Twente. (2006)

Grants

- Computation time at Lisa, Amsterdam, The Netherlands. (2010-2011)
- Large-Scale Project at High Performance Computing Center Stuttgart, Stuttgart, Germany. (2010-2011)
- DEISA (Distributed European Infrastructure for Supercomputing) grant for computation time at Huygens, Amsterdam, The Netherlands, and at the Leibniz-Rechenzentrum, München, Germany. (2009-2010)
- Computation time at Huygens, Amsterdam, The Netherlands. (2008-2011)
- Traveling grant EuroMech Colloquium 519. (2010)

Acknowledgements

The completion of the work that is presented in this thesis was only possible due to the great support of many people. Even when the investigation itself is interesting and challenging, it is your environment that determines whether your promotion becomes a success. Therefore, I gratefully thank everyone who has played a role in the completion of this thesis. A number of people I would like to mention particularly:

First of all I would like to thank my supervisors Detlef Lohse and Herman Clercx.

Detlef, I want to thank you for giving me the opportunity to do my PhD work in your group and for being my daily supervisor. It was a privilege to do science under your guidance and I learned a lot from you. Whenever I had question I always could discuss these with you. Our conversations and discussions were always very illuminating. Detlef, thanks for all the lessons learned and fine cooperation.

Herman, I want to thank you for the full trust and continuous support in good as well as in more difficult moments. Your knowledge about the influence of rotation on turbulent flow is tremendous, and in many cases I got new ideas and further insights in the very rich phenomenon that we observed in rotating thermal convection. Herman, I very much enjoyed our stimulating discussions and I appreciated all your motivating suggestions. It has been a pleasure to work with you.

I am very grateful for the work of the thesis committee, consisting of the promoters and GertJan van Heijst, Roberto Verzicco, Guenter Ahlers, Siegfried Grossmann, Bernard Geurts, and Bene Poelsema.

I would like to express my gratitude to my co-authors for the collaborations:

Roberto Verzicco for generously providing his 3D RB code to me. Roberto, you explained to me a lot about numerical techniques and high performance computing and you have a remarkable ability to point out the main physical effects that play a role. I always loved our discussions very much.

Guenter Ahlers, Stephan Weiss, and Jin-Qiang Zhong for performing many of the rotating RB experiments presented in this thesis. I valued our collaboration very much and I learnt a lot from you what is important in performing high accuracy measurements. Moreover it became clear to me that a deep physical insight is absolutely necessary.

Siegfried Grossmann for the discussions we had on several chapters that are presented in this thesis. Your ability to identify the key physical aspects of a problem is impressive. For me, it has been an honor to work together with you.

GertJan van Heijst, for his continued interest and many suggestions on the work about rotating RB convection. I thank you very much for introducing me to the concepts of the formation of Stewartson layers in rotating flows.

Ke-Qing Xia and Quan Zhou for analyzing the boundary layer profile in part III of this thesis. I would also like to thank all people from the group of Ke-Qing Xia in Hong Kong, i.e. Rui Ni, Tak Shing Chan, Sheng-Qi Zhou, Heng-Dong Xi and Chao Sun, that have contributed to the wonderful quasi 2D flow visualization experiments described in this thesis.

Chao Sun for the many (non)-scientific discussion that we have had. Your enthusiasm for doing research is simply contagious. Your knowledge and advice has turned out to be invaluable in setting up the experiments in Eindhoven. I will always remember some of the special places you have shown me in Beijing.

Olga Shiskina for your analysis that revealed the minimum number of computation nodes that should be placed inside the boundary layer. This result was very important to perform some of the high *Ra* number simulations. It was great to discuss the verifications and implications of this result with you.

Kazuyasu Sugiyama for providing his 2D RB code to me and for carefully checking the parallel version of his code that I have made. I very much liked our discussions on the flow reversals and the boundary layer dynamics in 2D RB convection.

Rudie Kunnen for the initial explaining of the code of Roberto Verzicco and for advising me in the initial design phase of the experimental setup in Eindhoven.

For the successful completion of the experiments in Eindhoven the support of the entire technical staff has turned out to be crucial. I would especially like to mention two names here: Gerald Oerlemans for the design and manufacturing of the experiment, and Freek van Uittert for the design of the software and electronics. I would like to express my gratitude to both of you for helping with the testing and optimization of the setup. For the calibration and advice on the temperature measurements I would like to thank Jaap van Wensveen from Tempcontrol.

I especially would like to thank Wim Rijks of SARA for making an optimized MPI version of our 3D RB code. The simulations presented in this thesis have been performed on several local clusters and supercomputers, i.e. LRZ (Leibniz-Rechenzentrum), HLRS (High Performance Computing Center Stuttgart), CASPUR (Consorzio interuniversitario per le Applicazioni di Supercalcolo Per Universit e Ricerca), and Huygens. I gratefully thank these computer centers and NCF (National Computing Facilities Foundation) and DEISA (Distributed European Infrastructure for Supercomputing Applications) for providing generous computational grants. Also the continuous technical support from people at the several supercomputing sites is gratefully acknowledged.

During my PhD I had the pleasure of getting several students under my guidance and I very much liked the close interaction I had with all of you. I thank Jim Overkamp (master student) for his work on the experiments in Eindhoven, which resulted in two publications in collaboration with Herman Clercx, GertJan van Heijst and Rudie Kunnen. I also thank Erwin van der Poel (master student) for the work he did on the aspect ratio dependence in 2D RB simulations. I am sure that this work will be published soon. Furthermore, I would like to thank Daniel Albernaz (internship student) for his work on Turbulent Taylor Couette simulations. The experience that we gained in this project will certainly be used in the future.

Furthermore, I would like to thank all people from the Physics of Fluids group in Enschede and the Turbulence and Vortex Dynamics group in Eindhoven. I very much enjoyed all conferences, trips, parties, lunch brakes that we have shared together. I would like to thank Bas Benschop for helping me with technical difficulties with my laptop during my PhD and Joanita Leferink you helping with administrative difficulties. From this group, I have a specific word of thanks to my (ex)-office mates in Enschede (Dennis, Julien, Edip, Sander and Marine) and Eindhoven (Michel, Marly, Geert, Alejandro): Thanks for the good laughs, great help and nice company, it was a pleasure sharing an office with you guys! In many lunch breaks I also enjoyed playing cards with Stefan, Dieter, Alexander and Lammert. I always looked forward to our card games.

A special thanks I would like to express to my paranymphs, Menno and Maarten, for being there for me. We share a lot and therefore I am very grateful that you will be very close at this special occasion.

Finally, I would like to thank all my friends and family for their support. I am especially grateful to my closest family members, my brother and my parents. You have always supported me with wise advice and help. Without your support I would never have come so far.

For financial support I want to acknowledge the Foundation for Fundamental Research on Matter (FOM) who funded this project

About the author

Richard Stevens was born in Nijmegen, The Netherlands, on November 15, 1984. He attended primary school and secondary school ’het Stedelijk Gymnasium Johan van Oldenbarnevelt’ in Amersfoort and graduated from high school in June 2003. In August 2003 he started to study Applied Physics at the University of Twente. During his study he was involved in organization of activities for the study association of Applied Physics ’Arago’ and the games association ’Fanaat’. In 2007 he spent a 3 month internship at Océ Technologies B.V. in Venlo. In March 2008 he obtained his master degree with honors in Applied Physics working with Prof. Detlef Lohse on the effect of rotation on heat transport. For this research he was awarded Shell Master prize in March 2009 for the best master thesis on a sustainable development and energy in the Netherlands. After obtaining his masters degree he continued as PhD student with Prof. Detlef Lohse and Prof. Herman Clercx at the Physics of Fluids group in Twente in close cooperation with the Turbulence and vortex dynamics group in Eindhoven.